

EUROPEAN ORGANIZATION FOR NUCLEAR RESEARCH  
STANFORD LINEAR ACCELERATOR CENTER

CERN-EP-2001-xxxx  
SLAC-PUB xxxx  
DRAFT of May 25, 2001

# Precision Electroweak Measurements on the Z Resonance

The ALEPH, DELPHI, L3, OPAL and SLD  
Collaborations,  
the LEP Electroweak Working Group,\* and  
the SLD Electroweak and Heavy Flavor Groups†

WORKING DRAFT May 25, 2001

---

\*some really hardworking people

†some more hardworking people

## Abstract

We report on the electroweak measurements performed with data taken at the Z resonance by the LEP and SLC experiments. The data consist of 17 million Z decays accumulated by the ALEPH, DELPHI, L3 and OPAL experiments at LEP, and 600 thousand Z decays by the SLD experiment at SLC. The measurements include cross sections, forward-backward asymmetries and polarized asymmetries. The mass and width of the Z boson and its couplings to fermions are precisely determined. The results are compared to the predictions of the Standard Model. The data are also used to determine, via radiative corrections, the mass of the top quark and of the W boson. These indirect measurements are compared to direct measurements and provide a stringent test of the Standard Model. In this context, data are used to set limits on the mass of the Higgs boson.

To be submitted to *Physics Reports*

### Note on DRAFT 1

This is the first draft released by the electroweak working group to all members of all five collaborations. As it is a draft, do not use the material presented here outside the five collaborations! Questions only should be addressed to the responsible section editors: Chapter 1: Robert Clare; 2: Günter Quast; 3: Peter Rowson; 4: Mike Roney; 5: Klaus Moenig; 6.1: Roger Jones; 6.2: Pippa Wells; rest: Martin Grünewald. However, in general all comments and other feedback from individuals is expected to be processed and combined by the review board of their experiment assigned to this draft first. We request that the reply of each of the five review boards on this draft is sent to us by e-mail not later than **July 10th, 2001**. Of course, earlier responses are greatly appreciated!

We are most interested in comments concerning the physics presentation of the results. The numerical results in this draft are not always final but correspond to the status of winter-2001. Some later updates such as the final tau-polarisation combination procedure or new topics such as tagged light flavour results are included but not yet propagated to the subsequent analysis chapters. In particular, this draft contains the recent b-quark forward-backward asymmetry measurements and the resulting necessary discussions. No qualitative and only minor quantitative changes are expected for final results.




# Contents

<b>1</b>	<b>Introduction</b>	<b>10</b>
1.1	LEP and SLC data . . . . .	10
1.1.1	LEP . . . . .	12
1.1.2	SLC . . . . .	14
1.2	LEP/SLC Detectors . . . . .	15
1.3	Standard Model relations . . . . .	17
1.4	The process $e^+e^- \rightarrow f\bar{f}$ . . . . .	21
1.5	Polarized cross-sections and asymmetries . . . . .	27
1.6	Pseudo-observables and Standard Model remnants . . . . .	28
<b>2</b>	<b>The Z lineshape</b>	<b>29</b>
2.1	Measurements of total cross-sections and forward-backward asymmetries . . . . .	29
2.1.1	Event selection . . . . .	29
2.1.2	Cross-section measurements . . . . .	32
2.1.3	Measurements of the lepton forward-backward asymmetries . . . . .	35
2.1.4	Systematic errors . . . . .	35
2.1.5	Energy calibration . . . . .	38
2.2	Experimental results . . . . .	42
2.3	Common uncertainties . . . . .	44
2.3.1	Common energy uncertainties . . . . .	47
2.3.2	Common $t$ -channel uncertainties . . . . .	47
2.3.3	Common luminosity uncertainties . . . . .	48
2.3.4	Common theory uncertainties . . . . .	49
2.4	Combination of results . . . . .	51
2.4.1	Multiple- $m_Z$ fits . . . . .	52
2.4.2	Shifts for halved experimental errors . . . . .	52
2.4.3	Influence of the $\gamma$ -Z interference term . . . . .	54
2.4.4	Direct Standard Model fits to the measured cross-sections and forward-backwards asymmetries . . . . .	55
2.4.5	Combined results . . . . .	56
2.5	Parameters derived from line shape results . . . . .	57
<b>3</b>	<b>Measurement of <math>A_{LR}</math> and the Lepton Asymmetries at the SLC</b>	<b>60</b>
3.1	The $A_{LR}$ Measurement . . . . .	60
3.1.1	Electron Polarization at the SLC . . . . .	61
3.1.2	Polarimetry at the SLC . . . . .	61
3.1.3	Energy Spectrometry . . . . .	65

3.1.4	Event Selection . . . . .	67
3.1.5	Control of Systematic Effects . . . . .	67
3.2	Measurement of the Lepton Asymmetries $A_e$ , $A_\mu$ and $A_\tau$ at the SLC . . . . .	69
3.2.1	The Analysis Method . . . . .	73
3.2.2	Systematic Errors . . . . .	74
3.2.3	Results . . . . .	76
3.3	Combined Results for $\sin^2 \theta_W^{\text{eff}}$ . . . . .	76
<b>4</b>	<b>The <math>\tau</math> Polarisation Measurements</b>	<b>78</b>
4.1	Introduction . . . . .	78
4.2	Experimental Methods . . . . .	78
4.3	Systematic Errors . . . . .	85
4.4	Results . . . . .	88
<b>5</b>	<b>Results from b and c quarks</b>	<b>93</b>
5.1	Introduction . . . . .	93
5.2	Heavy flavour tagging methods . . . . .	94
5.2.1	Lifetime Tagging . . . . .	94
5.2.2	Lepton tagging . . . . .	99
5.2.3	D-meson tags . . . . .	100
5.3	Partial width measurements . . . . .	103
5.3.1	$R_b$ measurements . . . . .	104
5.3.2	$R_c$ measurements . . . . .	105
5.4	Asymmetry measurements . . . . .	106
5.4.1	Asymmetry measurements used in the combination . . . . .	110
5.5	Auxiliary measurements . . . . .	111
5.6	External inputs to the heavy flavour combination . . . . .	111
5.6.1	The heavy quark fragmentation . . . . .	112
5.6.2	Heavy quarks from gluon splitting . . . . .	112
5.6.3	Multiplicities in heavy flavour decays . . . . .	113
5.6.4	Heavy flavour lifetimes . . . . .	114
5.6.5	Charmed hadron decays to exclusive final states . . . . .	114
5.6.6	Heavy flavour leptonic decays . . . . .	115
5.6.7	Hemisphere correlations in double-tag methods . . . . .	116
5.6.8	Light quark background in lifetime tagged samples . . . . .	118
5.7	Corrections to the measured electroweak parameters . . . . .	118
5.7.1	Corrections to $R_b$ , $R_c$ . . . . .	118
5.7.2	QCD corrections to the heavy flavour forward-backward asymmetries . . . . .	118
5.7.3	Other corrections to the asymmetries . . . . .	120
5.8	Combination procedure . . . . .	120
5.9	Results . . . . .	122
<b>6</b>	<b>Results from inclusive and light flavours</b>	<b>129</b>
6.1	Inclusive flavour hadronic events . . . . .	129
6.1.1	Systematic Uncertainties . . . . .	130
6.1.2	Combination Procedure . . . . .	131
6.1.3	Results and Interpretation . . . . .	131
6.2	Light flavour tagging . . . . .	132

6.2.1	Asymmetry measurements . . . . .	132
6.2.2	Partial width measurements . . . . .	135
<b>7</b>	<b>Additional Correlations between Results</b>	<b>139</b>
<b>8</b>	<b>Effective Couplings of the Neutral Weak Current</b>	<b>140</b>
8.1	The Asymmetry Parameters $\mathcal{A}_f$ . . . . .	140
8.2	The Effective Vector and Axial-Vector Coupling Constants . . . . .	142
8.3	The $\rho_f$ Parameters and the Effective Electroweak Mixing Angles . . . . .	144
8.4	The Leptonic Effective Electroweak Mixing Angle . . . . .	146
8.5	Discussion . . . . .	148
<b>9</b>	<b>Constraints on the Standard Model</b>	<b>150</b>
9.1	Parameters of the Minimal Standard Model . . . . .	150
9.2	Hadronic Vacuum Polarisation . . . . .	151
9.3	Additional Measurements . . . . .	152
9.3.1	Mass of the Top Quark . . . . .	153
9.3.2	Mass of the W Boson . . . . .	153
9.3.3	On-Shell Electroweak Mixing Angle . . . . .	153
9.3.4	Atomic Parity Violation Parameters . . . . .	153
9.4	Sensitivities and Uncertainties . . . . .	154
9.4.1	QCD Uncertainties . . . . .	155
9.5	Analysis Procedure . . . . .	156
9.6	Sensitivity to Radiative Corrections Beyond QED . . . . .	156
9.7	Tests of Electroweak Radiative Corrections . . . . .	157
9.7.1	Parametrisations . . . . .	157
9.7.2	Results . . . . .	159
9.8	Standard-Model Analyses . . . . .	163
9.8.1	Z-Pole Results . . . . .	163
9.8.2	The mass of the top quark and of the W boson . . . . .	164
9.8.3	The mass of the Higgs boson . . . . .	164
9.9	Discussion . . . . .	170
<b>10</b>	<b>Summary and Conclusions</b>	<b>176</b>
<b>A</b>	<b>The Measurements used in the Heavy Flavour Averages</b>	<b>177</b>

# List of Figures

1.1	The lowest-order $s$ -channel Feynmann diagrams for $e^+e^- \rightarrow f\bar{f}$ .	11
1.2	The hadronic cross-section as a function of energy.	11
1.3	The LEP storage ring	12
1.4	The SLC linear collider	15
1.5	Longitudinal polarization at SLC	16
1.6	An example LEP/SLC detector.	16
1.7	Event display pictures of $q\bar{q}$ , $e^+e^-$ , $\mu^+\mu^-$ and $\tau^+\tau^-$	18
1.8	Side view of $Z \rightarrow b\bar{b}$	19
1.9	Higher order corrections to the gauge boson propagators	20
1.10	QED corrections to fermion-pair production.	23
1.11	QED corrections to the hadronic cross-section and muon forward-backward asymmetry 	25
2.1	Separation of final states 	30
2.2	Luminosity measurement 	33
2.3	Hadronic cross-section measurements	36
2.4	$t$ -channel contribution to $e^+e^-$ final states	37
2.5	$\mu^+\mu^-$ differential cross-section	38
2.6	With of the depolarizing spin resonance	41
2.7	Measurements of $m_Z, \Gamma_Z, \sigma_{\text{had}}^0, R_\ell^0$ and $A_{\text{FB}}^{0,\ell}$	46
2.8	Multiple $m_Z$ fits	53
2.9	$R_\ell^0$ vs. $A_{\text{FB}}^{0,\ell}$	58
3.1	The SLC Compton polarimeter setup	63
3.2	Compton scattering asymmetry as a function of channel position. The horizontal axis gives the distance in mm from the center of the detector channels (1 cm wide each) to the path of the hypothetical undeflected electron beam (neutral-beam line). The inset shows the seven inner detector channels, sized to match the horizontal scale. The per channel data is plotted as open circles, and the corrected asymmetry function is the solid curve. The size of the correction from the theoretical QED calculation is indicated by the dashed curve.	64
3.3	The SLC extraction-line energy spectrometer	66
3.4	History of the SLD $A_{\text{LR}}^0$ measurements.	72
3.5	Polarization dependent angular distributions for leptons	75
4.1	ALEPH $\tau$ polarisation: $\tau \rightarrow \rho\nu$ optimal variable spectrum	81
4.2	OPAL $\tau$ polarisation: $\tau \rightarrow \pi\nu$ momentum spectrum	82
4.3	L3 $\tau$ polarisation: $\tau \rightarrow e\nu\bar{\nu}$ energy spectrum	83
4.4	DELPHI $\tau$ polarisation: $\tau \rightarrow \mu\nu\bar{\nu}$ momentum spectrum	84

4.5	Measured $\tau$ polarisation <i>vs</i> $\cos\theta_\tau$ for all LEP experiments . . . . .	90
4.6	Comparison of $\tau$ polarisation measurements of $\mathcal{A}_\tau$ and $\mathcal{A}_e$ . . . . .	91
5.1	Impact parameter significance from DELPHI for data and simulation. . . . .	96
5.2	Impact parameter b-tag from L3. . . . .	97
5.3	Decay length significance and neural network tagging variable for the OPAL secondary vertex based b-tag. . . . .	98
5.4	Reconstructed vertex mass from SLD for data and simulation. . . . .	99
5.5	Momentum and transverse momentum spectrum from L3 compared to the different sources from simulation. . . . .	100
5.6	$D^{*\pm}$ momentum spectrum for all events and for $b\bar{b}$ and $c\bar{c}$ events from OPAL normalised to the beam energy after subtraction of combinatorial background. . . . .	100
5.7	Mass spectra for $D^0 \rightarrow K^-\pi^+$ , $D^+ \rightarrow K^-\pi^+\pi^+$ , $D_s^+ \rightarrow K^+K^-\pi^+$ and $\Lambda_b^0 \rightarrow pK^-\pi^+$ obtained by ALEPH. . . . .	101
5.8	$m(K^-\pi^+) - m(K^-\pi^+\pi^+)$ mass difference spectrum from OPAL in different channels. . . . .	102
5.9	$p_t$ spectrum opposite a high energy $D^{*\pm}$ for pions with the opposite and same sign as the $D^{*\pm}$ . . . . .	103
5.10	Reconstructed $\cos\theta$ distribution from the ALEPH b-asymmetry measurement with leptons for a) the b-enriched and b) the c-enriched sample. . . . .	107
5.11	Reconstructed $\cos\theta$ distribution from the SLD vertex charge analysis with left- and right-handed beam polarisation. . . . .	108
5.12	Charge separation of the ALEPH neural net tag using jet charge, vertex charge and charged Kaons. . . . .	110
5.13	$R_b^0$ , $R_c^0$ , $A_{FB}^{0,b}$ , $A_{FB}^{0,c}$ , $\mathcal{A}_b$ and $\mathcal{A}_c$ measurements used in the heavy flavour combination. . . . .	123
5.14	Energy dependence of $A_{FB}^b$ and $A_{FB}^c$ . . . . .	125
5.15	Contours in the $R_c^0$ - $R_b^0$ and $\mathcal{A}_c$ - $\mathcal{A}_b$ planes from the LEP and SLD data. . . . .	128
6.1	A schematic illustration of the charge flow for an individual flavour of $Z^0 \rightarrow q\bar{q}$ decay. The sum of the hemisphere charges helps control any detector-induced biases, as this should be zero on average. . . . .	130
6.2	The input values and derived average of $\sin^2\theta_{\text{eff}}^{\text{lept}}$ from $\langle Q_{FB} \rangle$ measurements. . . . .	132
6.3	DELPHI RICH . . . . .	133
6.4	SLD measurement of $\mathcal{A}_s$ . . . . .	136
8.1	Comparison of the asymmetry parameters $A_i$ . . . . .	142
8.2	Comparison of the effective coupling constants . . . . .	145
8.3	Comparison of $\rho$ and the effective electroweak mixing angle . . . . .	147
8.4	Comparison of the effective electroweak mixing angle $\Delta$ . . . . .	149
9.1	Contour curve in the $(\rho_\ell, \sin^2\theta_{\text{eff}}^{\text{lept}})$ plane . . . . .	158
9.2	Model-independent $\epsilon$ Parametrisation . . . . .	161
9.3	Model-independent <i>STU</i> Parametrisation . . . . .	162
9.4	Comparison of results on the mass of the W boson . . . . .	165
9.5	Comparison of top-quark and W-boson mass determinations . . . . .	166
9.6	Constraints on the Higgs mass from $m_t$ , $m_W$ and $\Delta\alpha_{\text{had}}^{(5)}(m_Z^2)$ . . . . .	167
9.7	The “blue-band” plot $\Delta\chi^2(m_H)$ . . . . .	168

9.8	Measurements and pulls . . . . .	172
9.9	Higgs sensitivity of $\Gamma_Z$ , $\sigma_h^0$ , $R_\ell^0$ , $A_{\text{FB}}^{0,\ell}$ , $A_{\text{FB}}^{0,b}$ and $A_{\text{FB}}^{0,c}$ . . . . .	173
9.10	Higgs sensitivity of $\mathcal{A}_\tau(P_\tau)$ , $\mathcal{A}_e(P_\tau)$ , $\mathcal{A}_\ell(\text{SLD})$ , $\sin^2 \theta_{\text{eff}}^{\text{lept}}(\langle Q_{\text{FB}} \rangle)$ and $m_W(\text{LEP-2})$ . . . . .	174
9.11	Higgs sensitivity of $R_b$ , $R_c$ , $\mathcal{A}_b$ and $\mathcal{A}_c$ . . . . .	175



# List of Tables

1.1	▲ Beam energies and integrated luminosities . . . . .	13
1.2	Recorded event statistics ▲ . . . . .	13
1.3	The weak-isospin structure of the fermions in the Standard Model. . . . .	19
2.1	Selection efficiencies and backgrounds . . . . .	34
2.2	Experimental systematic errors . . . . .	39
2.3	Summary of errors on the centre-of-mass energy . . . . .	42
2.4	Nine parameter results . . . . .	43
2.5	Five parameter results . . . . .	45
2.6	Common energy errors for nine-parameter fits . . . . .	47
2.7	Common $t, s - t$ uncertainties . . . . .	48
2.8	TOPAZ0-ZFITTER differences . . . . .	50
2.9	QED-related common errors . . . . .	51
2.10	Covariance matrix of combined line shape and asymmetry measurements . . . . .	52
2.11	Shifts in central values with halved experimental errors . . . . .	54
2.12	Direct SM fits . . . . .	56
2.13	Combined results . . . . .	57
2.14	Partial Z widths ▲ . . . . .	59
2.15	Z branching fractions . . . . .	59
3.1	▲ . . . . .	66
3.2	▲ . . . . .	70
3.3	Luminosity-weighted mean electron polarization, $A_{LR}$ and $\sin^2\theta_w^{eff}$ measurements: summary of results for all SLD runs. . . . .	71
3.4	Summary of event selections, efficiency, and purity for $e^+e^- \rightarrow \ell^+\ell^-$ for the 1997-1998 SLD data . . . . .	73
3.5	Summary of statistical and systematic uncertainties in units of $10^{-4}$ for the 1997-1998 data. The superscript on each asymmetry refers to the lepton sample from which it was derived (electrons, muons or taus). . . . .	76
3.6	Correlation coefficients between $\mathcal{A}_e$ , $\mathcal{A}_\mu$ and $\mathcal{A}_\tau$ . . . . .	77
4.1	Tau polarisation decay channel sensitivity . . . . .	79
4.2	Common systematic errors in $\tau$ polarisation measurements . . . . .	89
4.3	LEP results for $\mathcal{A}_\tau$ and $\mathcal{A}_e$ . . . . .	92
4.4	Tau polarisation error correlation matrix for $\mathcal{A}_\tau$ and $\mathcal{A}_e$ . . . . .	92
5.1	Vertex detector characteristics and experimental resolutions . . . . .	95
5.2	b-Tagging performance of the different experiments at the working points of the $R_b$ analyses. . . . .	98

5.3	Correlation between the lepton charge and the quark charge at decay time. . . . .	108
5.4	Topological rates for the different charm meson species, with estimated errors and correlation coefficients. The subscripts indicate the number of charged particles produced. . . . .	114
5.5	Error sources for the QCD corrections to the forward-backward asymmetries. . . . .	119
5.6	Corrections to be applied to the quark asymmetries as $A_{\text{FB}}^{0,q} = A_{\text{FB}}^{q\bar{q}}(\text{pk}) + \delta A_{\text{FB}}$ . . . . .	120
5.7	The measurements of $R_b^0$ . All measurements use a lifetime tag enhanced by other features like invariant mass cuts or high $p_T$ leptons. . . . .	124
5.8	The correlation matrix for the set of the 14 heavy flavour parameters. . . . .	126
5.9	The dominant error sources for the electroweak parameters from the 14-parameter fit. . . . .	127
6.1	$\sin^2 \theta_{\text{eff}}^{\text{lept}}$ from inclusive hadronic charge asymmetry . . . . .	131
6.2	▲ . . . . .	132
6.3	Comparison of direct photon analyses . . . . .	137
8.1	Results on the leptonic asymmetry parameters $\mathcal{A}_\ell$ . . . . .	141
8.2	Results on the asymmetry parameters $\mathcal{A}_f$ . . . . .	143
8.3	Results on the effective coupling constants for leptons . . . . .	143
8.4	Results on the effective coupling constants . . . . .	144
8.5	Results on $\rho$ and $\sin^2 \theta_{\text{eff}}^f$ . . . . .	146
9.1	Theoretical Uncertainties . . . . .	155
9.2	Results on all $\epsilon$ parameters . . . . .	160
9.3	Results on the three Z-pole $STU\gamma_b$ parameters . . . . .	160
9.4	Results on Standard Model parameters from Z-pole measurements . . . . .	163
9.5	Results on Standard Model parameters . . . . .	169
9.6	Overview of results . . . . .	171
A.1	The measurements of $R_b^0$ . All measurements use a lifetime tag enhanced by other features like invariant mass cuts or high $p_T$ leptons. . . . .	178
A.2	The measurements of $R_c^0$ . “c-count” denotes the determination of $R_c^0$ from the sum of production rates of weakly decaying charmed hadrons. “D meson” denotes any single/double tag analysis using exclusive and/or inclusive D meson reconstruction. . . . .	178
A.3	The measurements of $A_{\text{FB}}^{\text{bb}}(-2)$ . All numbers are given in %. . . . .	179
A.4	The measurements of $A_{\text{FB}}^{\text{cc}}(-2)$ . All numbers are given in %. . . . .	180
A.5	The measurements of $A_{\text{FB}}^{\text{bb}}(\text{pk})$ . All numbers are given in %. . . . .	181
A.6	The measurements of $A_{\text{FB}}^{\text{cc}}(\text{pk})$ . All numbers are given in %. . . . .	182
A.7	The measurements of $A_{\text{FB}}^{\text{bb}}(+2)$ . All numbers are given in %. . . . .	183
A.8	The measurements of $A_{\text{FB}}^{\text{cc}}(+2)$ . All numbers are given in %. . . . .	184
A.9	The measurements of $\mathcal{A}_b$ . . . . .	185
A.10	The measurements of $\mathcal{A}_c$ . . . . .	186
A.11	The measurements of $\text{BR}(b \rightarrow \ell)$ . All numbers are given in %. . . . .	187
A.12	The measurements of $\text{BR}(b \rightarrow c \rightarrow \ell)$ . All numbers are given in %. . . . .	188
A.13	The measurements of $\text{BR}(c \rightarrow \ell)$ . All numbers are given in %. . . . .	188
A.14	The measurements of $\bar{\chi}$ . . . . .	189
A.15	The measurements of $\text{P}(c \rightarrow D^{*+}) \times \text{BR}(D^{*+} \rightarrow \pi^+ D^0)$ . . . . .	189

A.16 The measurements of $R_c f_{D^+}$ . . . . .	190
A.17 The measurements of $R_c f_{D_s}$ . . . . .	191
A.18 The measurements of $R_c f_{\Lambda_c}$ . . . . .	191
A.19 The measurements of $R_c f_{D^0}$ . . . . .	192
A.20 The measurements of $R_c P(c \rightarrow D^{*+}) \times BR(D^{*+} \rightarrow \pi^+ D^0)$ . . . . .	192

# Chapter 1

## Introduction

\$Id: physrep\_intro.tex,v 1.27 2001/05/23 22:24:22 clare Exp \$

With the observation of neutral current interactions in neutrino-electron scattering [1] and the discovery of the W and Z bosons in  $p\bar{p}$  collisions [2, 3], the Standard Model [4] was well established experimentally. The LEP and SLC accelerators were designed to copiously produce Z bosons via  $e^+e^-$  annihilation, allowing detailed studies of the properties of the Z boson to be performed in a very clean environment.

The accumulated data are used to determine the properties of the Z boson with high precision: its mass, its partial and total widths, and its couplings to fermion pairs. These results are compared to the predictions of the Standard Model. The experimental precision is sufficient to demonstrate the existence of higher-order electroweak radiative corrections with high significance. Via the effects of these corrections, the properties of particles not produced at LEP and SLC, most notably the top quark and the Higgs boson, is inferred.

After a brief introduction to the LEP and SLC programs and the Standard Model, detailed discussions of the measurements follow. These are the Z lineshape and leptonic asymmetries in Chapter 2, the left-right polarised asymmetry (Chapter 3), tau polarisation (Chapter 4), heavy quark (b and c) measurements (Chapter 5), light quark measurements (Chapter 6) and correlations between measurements (Chapter 7). Chapter 8 discusses the derivations of the effective neutral weak coupling constants, and Chapter 9 reviews the electro-weak measurements presented here and elsewhere and the constraints on the Standard Model that these measurements imply.

### 1.1 LEP and SLC data

The process under study is  $e^+e^- \rightarrow f\bar{f}$ , which proceeds in lowest order via photon and Z boson exchange, as shown in Figure 1.1. Between the years of 1989 and 1998, the LEP [5] and SLC [6]  $e^+e^-$  accelerators operated at energies of approximately 91 GeV, close to the mass of the Z boson. The hadronic cross-section as a function of the centre-of-mass energy is shown in Figure 1.2. There are two prominent features in the hadronic cross-section. The first is the  $1/s$  fall-off, due to photon exchange (the left diagram in Figure 1.1), which leads to the peak at low energies, and the second is the peak at 91 GeV, due to Z exchange (the right diagram of Figure 1.1). Thus, at LEP and SLC, Z bosons were copiously produced.

The LEP accelerator ran from 1989 to 2000. However, only during the first years, until 1995, was the running dedicated to the Z boson region. From 1996 until 2000, the machine

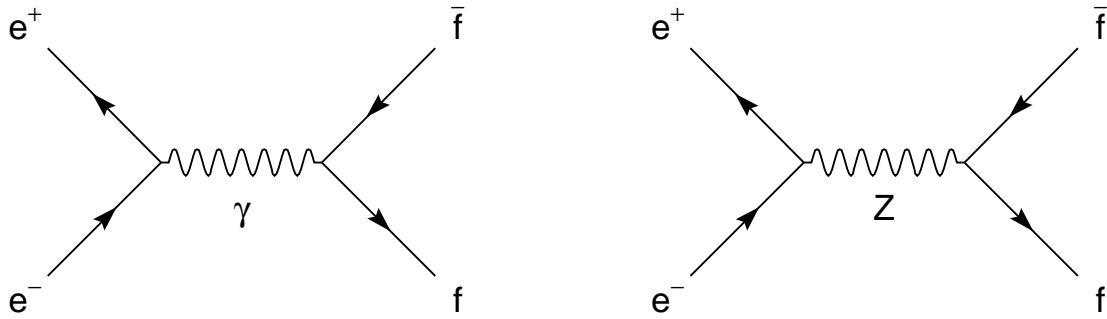


Figure 1.1: The lowest-order  $s$ -channel Feynmann diagrams for  $e^+e^- \rightarrow f\bar{f}$ . For  $e^+e^-$  final states, the photon and the  $Z$  boson can also be exchanged via the  $t$ -channel.

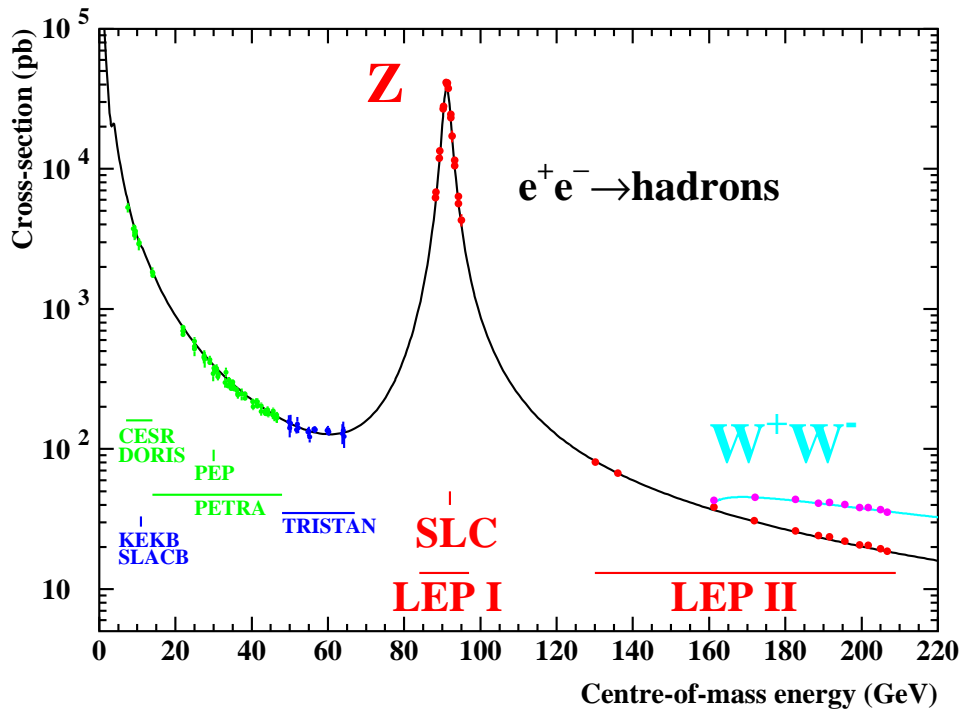


Figure 1.2: The hadronic cross-section as a function of center-of-mass energy. The solid line is the prediction of the Standard Model, and the points are the experimental measurements. Also indicated are the energy ranges of various  $e^+e^-$  accelerators. The cross-sections have been corrected for the effects of photon radiation.

was operated at energies at and above 160 GeV, allowing the production of pairs of  $W$  bosons,  $e^+e^- \rightarrow W^+W^-$ , as indicated in Figure 1.2. Although some results from this later running will be used in this report, the bulk of the data stems from the  $Z$  period. When needed, the  $Z$  period will be denoted “LEP-I”, and the period beginning in 1996 “LEP-II”.

During the six years of running at LEP-I, the four experiments ALEPH [7], DELPHI [8], L3 [9] and OPAL [10] collected approximately 17 million  $Z$  decays in total distributed over seven points in centre-of-mass energy in the range of the  $Z$  mass plus or minus 3 GeV.

The SLC accelerator started running in 1989 and the MarkII collaboration published the first observations of  $Z$  production in  $e^+e^-$  collisions [11]. However, it was not until 1992 that a significant longitudinal polarization of the SLC electron beam was established. By then the SLD [12–14] detector had replaced MarkII. From 1992 until 1998, when the accelerator was shut down, SLD accumulated approximately 600 thousand  $Z$  decays. Although the data set is much smaller than that of LEP, the presence of longitudinal polarization allows complementary and competitive measurements of the  $Z$  couplings. Other properties of the accelerator, for example the extremely small luminous volume of the interaction point, have been used to improve the statistical power of the data.

### 1.1.1 LEP

LEP is a electron-positron storage ring with a circumference of approximately 27 km. Four interaction regions are situated around the ring (L3, ALEPH, OPAL and DELPHI), as shown in Figure 1.3. In summer 1989 the first  $Z$  bosons were produced at LEP and observed by the

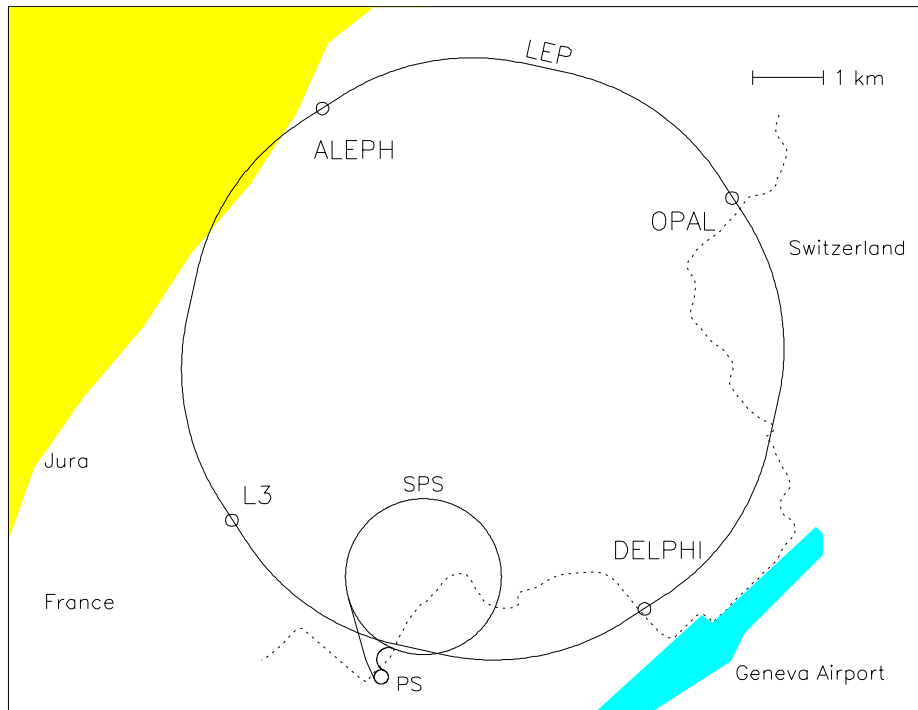


Figure 1.3: The LEP storage ring, showing the locations of the four experiments, and the existing accelerators (PS, SPS) used as pre-accelerators for the electron and positron bunches.

four experiments. Since then the operation of the machine and its performance were steadily

improved. At the end of LEP data taking around the Z resonance in autumn 1995 the peak luminosity had reached nearly twice its design value. At this luminosity, approximately 1000 Z bosons were recorded every hour by each of the four experiments, making LEP a true Z factory. Table 1.1 summarises the data taking periods, the approximate centre-of-mass energies and the delivered integrated luminosities.

year	beam energy range [GeV]	integrated luminosity [pb <sup>-1</sup> ]
1989	88.2 – 94.2	1.7
1990	88.2 – 94.2	8.6
1991	88.5 – 93.7	18.9
1992	91.3	28.6
1993	89.4, 91.2, 93.0	40.0
1994	91.2	64.5
1995	89.4, 91.3, 93.0	39.8

Table 1.1: Approximate centre-of-mass energies and integrated luminosities delivered per experiment. In 1990 and 1991, a total of about 7 pb<sup>-1</sup> was taken at off-peak energies, and 20 pb<sup>-1</sup> per year in 1993 and in 1995. The total luminosity used by the experiments in the analyses was smaller by 10–15% due to data taking inefficiencies.

The data collected in 1989 constitute only a very small subset of the total statistics and are of lower quality, and therefore these have not been used in the final analyses. In the years 1990 and 1991 “energy scans” were performed at seven different centre-of-mass energies around the peak of the Z resonance, placed about one GeV apart. In 1992 and 1994 there were high-statistics runs only at the peak energy. In 1993 and 1995 data taking took place at three centre-of-mass energies, about 1.8 GeV below and above the peak and at the peak. The accumulated event statistics amounts to about 17 million Z decays recorded by the four experiments. A detailed break-down is given in Table 1.2.

q $\bar{q}$						$\ell^+\ell^-$					
year	A	D	L	O	all	year	A	D	L	O	all
'90/91	433	357	416	454	1660	'90/91	53	36	39	58	186
'92	633	697	678	733	2741	'92	77	70	59	88	294
'93	630	682	646	649	2607	'93	78	75	64	79	296
'94	1640	1310	1359	1601	5910	'94	202	137	127	191	657
'95	735	659	526	659	2579	'95	90	66	54	81	291
total	4071	3705	3625	4096	15497	total	500	384	343	497	1724

Table 1.2: The q $\bar{q}$  and  $\ell^+\ell^-$  event statistics, in units of 10<sup>3</sup>, used for Z analyses by the experiments ALEPH (A), DELPHI (D), L3 (L) and OPAL (O).

Much effort was dedicated to the determination of the energy of the colliding beams, which reached a precision of about  $20 \times 10^{-6}$  on the absolute energy scale. This level of accuracy was vital for the precision of the measurements of the mass and width of the Z. In particular the

off-peak energies in the 1993 and 1995 scans were carefully calibrated employing the technique of resonant depolarisation of the transversely polarised beams [15–18]. In order to minimise the effects of any long-term instabilities during the energy scans, the centre-of-mass energy was changed for every new fill of the machine. A fill of the machine typically provided luminosity for approximately 10 hours. Thus the data samples taken above and below the resonance are well balanced within each year. The data recorded within a year around one centre-of-mass energy were combined to give one measurement at this “energy point”.

All the experiments replaced their first-generation luminosity detectors, which had systematic uncertainties around the percent level, by high-precision devices capable of pushing systematic errors on the acceptance of small-angle Bhabha scattering events below one per-mil. Silicon vertex detectors were also added to the tracking systems, which greatly improved the identification of secondary decay vertices accompanying the production of b and c quarks. As a consequence of these improvements during LEP-I running, statistical and systematic errors are much smaller for the last three years of data taking, which hence dominate the precision achieved on the Z parameters.

### 1.1.2 SLC

The SLC was the first  $e^+e^-$  linear collider. As such, it operated in a somewhat different mode than LEP. It used the SLAC linear accelerator to accelerate alternate bunches of electrons and positrons, a set of two damping rings to reduce the size and energy spread of the electron and positron bunches, and two separate arcs to guide the bunches to a single interaction region, as shown in Figure 1.4. The repetition rate was 120 Hz (compared to either 45 kHz or 90 kHz, depending on the mode, for LEP).

The standard operating cycle began with the production of two closely spaced (61 ns) electron bunches, the first of which was longitudinally polarised. These bunches were accelerated part way down the linac before being stored in the specially designed electron damping rings. Before storage in the damping rings, the longitudinal polarisation was rotated to be transverse. After damping for 8.3 ms (1/120 s), the two bunches were extracted, the polarization of the first bunch rotated back to longitudinal, and accelerated in the linac. At 30 GeV, the second bunch was diverted to a target, where positrons were created. The positrons were captured, accelerated to 200 MeV and sent back to the beginning of the linac, where they were then stored in the positron damping ring. As the spatial and momentum spreads of the positrons were large, the positron bunch was stored in the damping ring for 16.6 ms. The positron bunch was then extracted just before (60 ns) the next two electron bunches, and accelerated. At 30 GeV, the third bunch was diverted to create positrons, while the remaining positron and electron bunches were accelerated to the final energy of  $\approx 46.5\text{GeV}$  to be transported in the arcs to the final focus and interaction point, [loosing](#) approximately 1 GeV in the arcs due to synchrotron radiation, leading to a centre-of-mass energy of 91.25 GeV, the maximum of the annihilation cross-section.

The era of high-precision measurements at SLC started in 1992 with the first longitudinally polarized beams. The polarization was achieved by shining circularly polarized laser light on the gallium arsenide electron source. At that time, the polarization was only 22%. Shortly thereafter, “strained lattice” photocathodes were introduced, and the polarization increased significantly, as can be seen in Figure 1.5, which shows the polarization as a function of time. Much work was invested in the SLC machine to maintain the electron polarization at a very high value throughout the production, damping, acceleration and transfer through the arcs. In



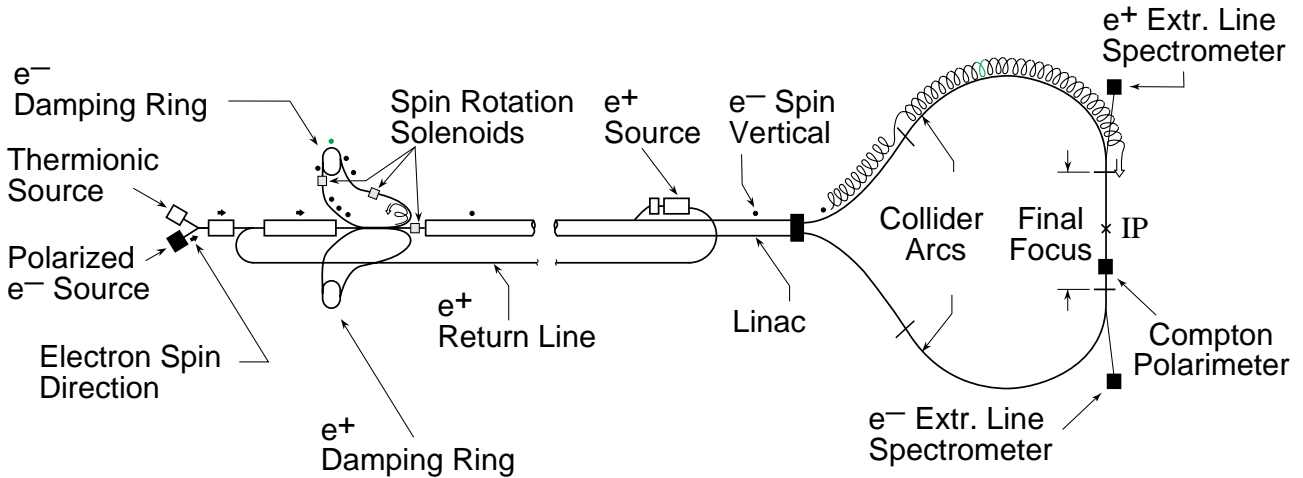


Figure 1.4: The SLC linear collider complex, showing the electron source, the damping rings, the positron source, the linac and arcs and the final focus.

addition, to avoid as much as possible any correlations in the SLC machine or SLD detector, the electron helicity was randomly changed on a pulse-to-pulse basis by changing the circular polarization of the laser.

Also evident in Figure 1.5 is that almost 60% of the data were collected in the last two years of SLC running, from 1997 to 1998, with the second to last week of running producing more than 20000 Z bosons.

## 1.2 LEP/SLC Detectors

The designs of the LEP and SLC detectors are quite similar, although the details **very** significantly among them. As an example, the OPAL detector is shown in Figure 1.6. Starting radially from the interaction point, there is first a vertex detector, typically composed of multilayered silicon devices followed by a gas drift chamber to measure the parameters of charged tracks. The silicon detector significantly improves the ability to measure impact parameters and to identify secondary vertices with a resolution of approximately  $300 \mu\text{m}$ . As the typical B hadron produced in Z decays will move about 3 mm from the primary vertex before decaying, the use of these detectors allows the selection of a heavy quark sample with high purity. All five detectors had almost complete solid angle coverage; the only holes being at very small angle due to the beam pipe.

Surrounding the tracking system is a calorimeter system, usually divided into two sections. The first section is designed to measure the position and energy of electromagnetic showers from photons (including those from  $\pi^0$  decay) and electrons. The electromagnetic calorimeter is followed by a hadronic calorimeter to measure the energy flow of hadronic particles. Finally, an outer tracking system designed to measure the parameters of penetrating particles (muons) completes the system.

The central part of the detector (at least the tracking chamber) is immersed in a solenoidal magnetic field to allow the measurement of the momentum of charged particles. In addition, particle identification systems may be installed, including ionisation loss measurements ( $dE/dx$ ) in the central chamber, time-of-flight, and ring-imaging Čerenkov detectors. These measure-

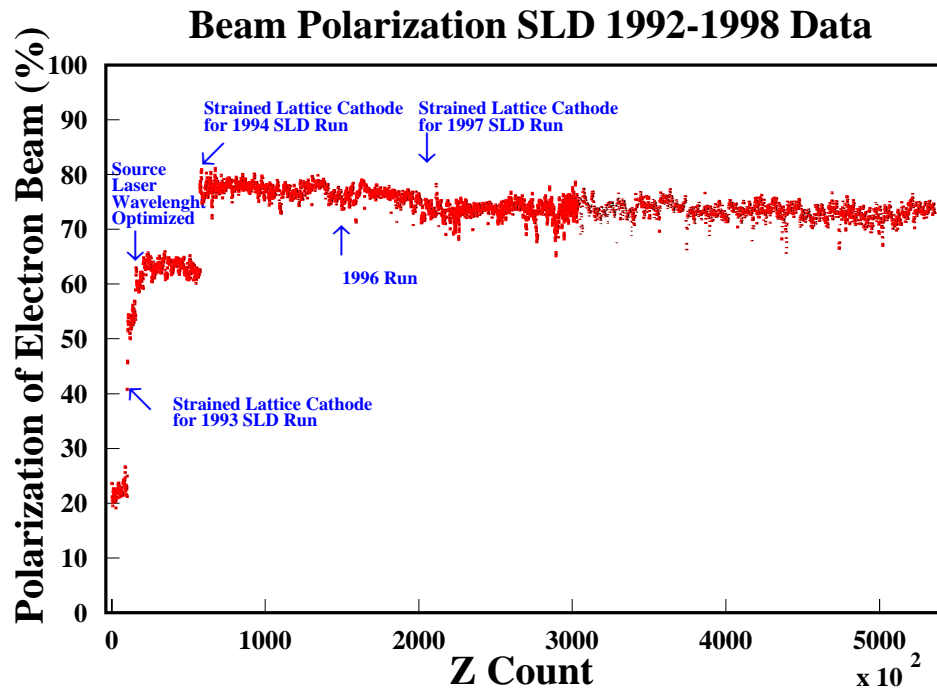


Figure 1.5: The amount of longitudinal electron polarisation as a function of time at SLC.

Figure 1.6: A cut-away view of the OPAL detector, as an example LEP/SLC detector.

ments can be used to determine the velocity of particles; these coupled with the momentum measurements yield the particle masses. Special detectors are placed at small polar angles to detect Bhabha scattering events, used to determine the luminosity.

The somewhat different conditions at the SLC allowed some improvements to the basic design for the SLD detector. As the dimensions of the SLC beams were much smaller than the LEP beams, the vertex detectors were placed at a smaller radius. Because of the low repetition rate, slow, but very high-resolution, CCD arrays were employed instead of the micro-strip devices used at LEP. Both features allowed an improved vertex reconstruction.

A few typical Z decays, as seen in the detectors are shown in Figure 1.7. As can be seen, the events at LEP are extremely clean with practically no background allowing high-efficiency and high-purity selections to be made.

Shown in Figure 1.8 is a side view of an event interpreted as the decay of a Z into a  $b\bar{b}$ . The displaced vertex from the decay of a B hadron is clearly visible. This event also shows the definition of a “forward” event, as the b-quark goes into hemisphere defined by the direction of the electron beam ( $\theta < \pi/2$ ).

Total cross-sections for a given process are determined by counting selected events,  $N_{\text{sel}}$ , subtracting background,  $N_{\text{bg}}$ , and normalising by the selection efficiency,  $\epsilon_{\text{sel}}$ , and the luminosity,  $\mathcal{L}$ :

$$\sigma = \frac{N_{\text{sel}} - N_{\text{bg}}}{\epsilon_{\text{sel}} \mathcal{L}}. \quad (1.1)$$

The expected background and the selection efficiencies are determined using Monte-Carlo event generators. The generated events are typically passed through a program that simulates the detector response and then processed by the same reconstruction program as used for the data.

Another important measurement is that of forward-backward asymmetries. The asymmetry is defined as the number of produced fermions (as opposed to anti-fermions) which travel in the same direction as the incoming electron beam (forward events) minus the number of fermions produced in the backward direction, divided by the total number of produced events:

$$A_{\text{FB}} = \frac{N_{\text{F}} - N_{\text{B}}}{N_{\text{F}} + N_{\text{B}}} \quad (1.2)$$

$$N_{\text{F}} \equiv \sigma(\theta < \pi/2) \epsilon_{\text{se}} \mathcal{L} \quad (1.3)$$

$$N_{\text{B}} \equiv \sigma(\theta > \pi/2) \epsilon_{\text{se}} \mathcal{L}, \quad (1.4)$$

where  $\theta$  is the scattering angle of the outgoing fermion with respect to the direction of the electron beam.

### 1.3 Standard Model relations

In the Standard Model, the relationship between the weak and electromagnetic couplings is given by

$$G_{\text{F}} = \frac{\pi\alpha}{\sqrt{2}m_{\text{W}}^2 \sin^2 \theta_{\text{W}}}, \quad (1.5)$$

where  $G_{\text{F}}$  is the Fermi constant determined in muon decay,  $\alpha$  is the electromagnetic fine-structure constant,  $m_{\text{W}}$  is the W boson mass, and  $\sin^2 \theta_{\text{W}}$  is the electro-weak mixing angle. In



An SLD figure will go here when I get it...

Figure 1.8: Side view of an event classified as  $Z \rightarrow b\bar{b}$ . The displaced vertex is visible in the expanded view of the vertex. From the charge of the tracks at the vertex, this event has a b-quark in the forward hemisphere, and is thus a “forward” event.

in addition, the relationship between the neutral and charged weak couplings fixes the ratio of the W and Z boson masses:

$$\rho = \frac{m_W^2}{m_Z^2 \cos^2 \theta_W}. \quad (1.6)$$

The  $\rho$  parameter is determined by the Higgs structure of the theory; in the Minimal Standard Model containing only Higgs doublets,  $\rho$  is unity.

The fermions are arranged in weak-isospin doublets for left-handed particles and weak-isospin singlets for right-handed particles, as shown in Table 1.3. The interaction of the Z

Family			$T$	$T^3$	$Q$
$\begin{pmatrix} \nu_e \\ e \end{pmatrix}_L$	$\begin{pmatrix} \nu_\mu \\ \mu \end{pmatrix}_L$	$\begin{pmatrix} \nu_\tau \\ \tau \end{pmatrix}_L$	1/2	+1/2 -1/2	0 -1
$\nu_{eR}$	$\nu_{\mu R}$	$\nu_{\tau R}$	0	0	0
$e_R$	$\mu_R$	$\tau_R$	0	0	-1
$\begin{pmatrix} u \\ d \end{pmatrix}_L$	$\begin{pmatrix} c \\ s \end{pmatrix}_L$	$\begin{pmatrix} t \\ b \end{pmatrix}_L$	1/2	+1/2 -1/2	+2/3 -1/3
$u_R$	$c_R$	$t_R$	0	0	+2/3
$d_R$	$s_R$	$b_R$	0	0	-1/3

Table 1.3: The weak-isospin structure of the fermions in the Standard Model. “L” and “R” stands for left-handed and right-handed fermions,  $T$  and  $T^3$  are the total weak-isospin and the third component, and  $Q$  is the charge. Right-handed neutrinos can exist only if the neutrinos have non-zero masses. Note that the results presented in this report are insensitive to, and independent of, any small ( $< \text{MeV}$ ) neutrinos masses.

boson with fermions is given by the left- and right-handed couplings:

$$g_L = \sqrt{\rho}(T^3 - Q \sin^2 \theta_W) \quad (1.7)$$

$$g_R = \sqrt{\rho} Q \sin^2 \theta_W, \quad (1.8)$$

or, equivalently in terms of vector and axial-vector couplings:

$$g_V \equiv g_L - g_R = \sqrt{\rho}(T^3 - 2Q \sin^2 \theta_W) \quad (1.9)$$

$$g_A \equiv g_L + g_R = \sqrt{\rho} T^3. \quad (1.10)$$

These tree-level quantities are modified by radiative corrections to the propagators as shown in Figure 1.9. The bulk of the electro-weak corrections can be absorbed into the definitions of

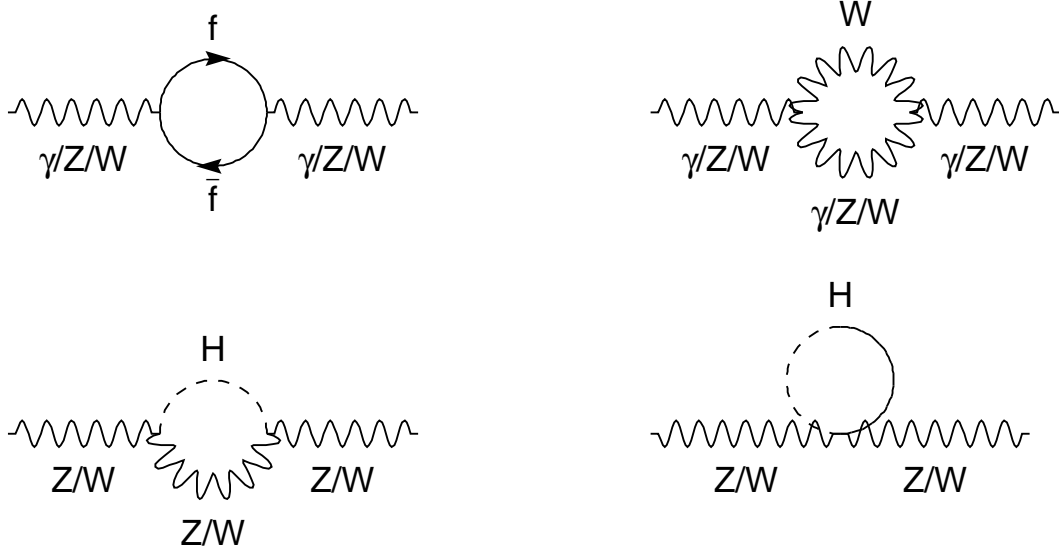


Figure 1.9: Higher order corrections to the gauge boson propagators due to boson and fermion loops.

the  $\rho$  parameter and the couplings, resulting in “effective” quantities:

$$\bar{\rho} = 1 + \Delta\rho \quad (1.11)$$

$$g_V^{\text{eff}} = \sqrt{\bar{\rho}}(T^3 - 2Q \sin^2 \theta_{\text{eff}}) \quad (1.12)$$

$$g_A^{\text{eff}} = \sqrt{\bar{\rho}} T^3 \quad (1.13)$$

$$\sin^2 \theta_{\text{eff}} = \left( 1 + \frac{\cos^2 \theta_W}{\sin^2 \theta_W} \Delta\rho + \dots \right) \sin^2 \theta_W, \quad (1.14)$$

where we use the minimal Higgs structure resulting in  $\rho = 1$ . In addition, the effective couplings acquire small imaginary components, resulting in complex couplings, which are denoted by  $\mathcal{G}_V$  and  $\mathcal{G}_A$ . In the remainder of this report, only the effective couplings will be used and thus, for simplicity, we denote

$$g_V = g_V^{\text{eff}} \equiv \Re(\mathcal{G}_V) \quad (1.15)$$

$$g_A = g_A^{\text{eff}} \equiv \Re(\mathcal{G}_A). \quad (1.16)$$

The distinction, however, will be kept between  $\sin^2 \theta_W$  given by the ratio of bosons masses, and the effective parameter  $\sin^2 \theta_{\text{eff}}$ .

In principle, the corrections are specific to each fermion flavor, so when necessary, the parameters will be labelled, for example,  $\rho_b$  indicates the effective  $\rho$  parameter for the  $b\bar{b}$  vertex, and  $\sin^2 \theta_{\text{eff}}^{\text{lept}}$  indicates the effective mixing angle for lepton vertices (assuming lepton universality).

The relationship between the couplings and the boson masses is also modified by radiative corrections:

$$G_F = \frac{\pi\alpha}{\sqrt{2}m_W^2 \sin^2 \theta_W} \frac{1}{1 - \Delta r}, \quad (1.17)$$

where  $\Delta r$  is given by

$$\Delta r = \Delta\alpha + \Delta r_w. \quad (1.18)$$

The  $\Delta\alpha$  term incorporates the running of the electromagnetic coupling due to fermion loops in the photon propagator. These effects can be absorbed into  $\alpha$ :

$$\alpha(s) = \frac{\alpha(0)}{1 - \Delta\alpha}. \quad (1.19)$$

At LEP/SLC energies,  $\alpha$  is increased from the Thompson limit of  $1/137.036$  to  $1/128.945$ . The dominant term in  $\Delta r_w$  is given by  $\Delta\rho$ , defined above:

$$\Delta r_w = -\frac{\cos^2 \theta_W}{\sin^2 \theta_W} \Delta\rho + \Delta r_{\text{remainder}}. \quad (1.20)$$

The leading-order contributions to  $\Delta r_w$  depend on the top quark mass and the Higgs boson mass:

$$\Delta r^t = -3 \frac{G_F m_W^2}{8\sqrt{2}\pi^2} \frac{m_t^2}{m_W^2} \cot^2 \theta_W + \dots \quad (1.21)$$

$$\Delta r^H = \frac{11}{3} \frac{G_F m_W^2}{8\sqrt{2}\pi^2} \left( \ln \frac{m_H^2}{m_W^2} - \frac{5}{6} \right) + \dots \quad (1.22)$$

The radiative corrections thus have a quadratic dependence on the top quark mass and a weaker logarithmic dependence on the Higgs mass. By measuring the effects of these corrections, the top quark mass can be determined indirectly and compared to the direct measurements. Using the measured top quark mass, information on the Higgs mass can be inferred.

## 1.4 The process $e^+e^- \rightarrow f\bar{f}$

The differential cross-sections for fermion pair production (see Figure 1.1) around the Z resonance can be cast into a Born-type structure using the complex-valued effective coupling constants given in the previous section. Effects from photon vacuum polarisation are taken into account by the running electromagnetic coupling constant (Equation 1.19), which also acquires a small imaginary piece. Neglecting initial and final state photon radiation, final state

gluon radiation and fermion masses, the electroweak kernel cross-section can thus be written as the sum of three contributions, from  $\gamma$  and Z exchange and from their interference,

$$\begin{aligned}
\frac{2s}{\pi} \frac{1}{N_c^f} \frac{d\sigma_{ew}}{d\cos\theta}(e^+e^- \rightarrow f\bar{f}) = & \\
& \underbrace{|\alpha(s)Q_f|^2(1 + \cos^2\theta)}_{\sigma^\gamma} \\
& - 8\Re \left\{ \alpha^*(s)Q_f\chi(s) \left[ \mathcal{G}_{Ve}\mathcal{G}_{Vf}(1 + \cos^2\theta) + 2\mathcal{G}_{Ae}\mathcal{G}_{Af}\cos\theta \right] \right\} \\
& \underbrace{\hspace{10em}}_{\gamma - Z \text{ interference}} \\
& + 16|\chi(s)|^2 \left[ (|\mathcal{G}_{Ve}|^2 + |\mathcal{G}_{Ae}|^2)(|\mathcal{G}_{Vf}|^2 + |\mathcal{G}_{Af}|^2)(1 + \cos^2\theta) \right. \\
& \quad \left. + 8\Re \{ \mathcal{G}_{Ve}\mathcal{G}_{Ae}^* \} \Re \{ \mathcal{G}_{Vf}\mathcal{G}_{Af}^* \} \cos\theta \right] \\
& \underbrace{\hspace{10em}}_{\sigma^Z}
\end{aligned} \tag{1.23}$$

with

$$\chi(s) = \frac{G_F m_Z^2}{8\pi\sqrt{2}} \frac{s}{s - m_Z^2 + is\Gamma_Z/m_Z}. \tag{1.24}$$

where  $\theta$  is the scattering angle of the out-going fermion with respect to the direction of the  $e^-$  and the colour factor  $N_c^f$  is one for leptons ( $f=e, \mu, \tau$ ) and three for quarks ( $f=u, d, s, c, b$ ), and  $\chi(s)$  is the propagator term with a Breit-Wigner denominator with an  $s$ -dependent width.

The  $1 + \cos^2\theta$  terms in the above formula contribute to the total cross-section, whereas the terms multiplying  $\cos\theta$  contribute only to the forward-backward asymmetries for an experimental acceptance symmetric in  $\cos\theta$ . The total cross-section is completely dominated by Z exchange. The  $\gamma$ -Z interference determines the energy dependence of the forward-backward asymmetries and dominates at off-peak energies, but the leading contribution from the real parts of the couplings vanishes at  $\sqrt{s} = m_Z$ .

In Bhabha final states,  $e^+e^- \rightarrow e^+e^-$ , also the  $t$ -channel diagrams contribute to the cross-sections, with a very dominant photon contribution at large  $\cos\theta$ , *i.e.*, in the forward direction. This contribution, and also its interference with the  $s$ -channel, add to the pure  $s$ -channel cross section for  $e^+e^- \rightarrow e^+e^-$ . (See Sec. 2.3.2 for details.)

The definition of the mass and width with an  $s$ -dependent width term in the Breit-Wigner denominator is suggested by phase-space and the structure of the electroweak radiative corrections within the Standard Model. It is different from another commonly used definition, the real part of the pole position in the energy-squared plane, where the propagator term takes the form  $\chi(s) \propto s/(s - \bar{m}_Z^2 + i\bar{m}_Z\bar{\Gamma}_Z)$ . It should be noted, however, that this fundamental choice of definition has limited consequences to the analysis. Under the transformations  $\bar{m}_Z = m_Z/\sqrt{1 + \Gamma_Z^2/m_Z^2}$  and  $\bar{\Gamma}_Z = \Gamma_Z/\sqrt{1 + \Gamma_Z^2/m_Z^2}$ , the two formulations lead to *exactly* equivalent resonance shapes.

Photon radiation (Figure 1.10) from the initial and final states, and their interference, is conveniently treated by convoluting the electroweak kernel cross-section,  $\sigma_{ew}(s)$ , with a QED radiator,  $H_{\text{QED}}^{\text{tot}}$ ,

$$\sigma(s) = \int_{4m_f^2/s}^1 dz H_{\text{QED}}^{\text{tot}}(z, s) \sigma_{ew}(zs). \tag{1.25}$$

The difference between the forward and backward cross-sections entering into the determination of the forward-backward asymmetries,  $\sigma_F - \sigma_B$ , is treated in the same way using a radiator



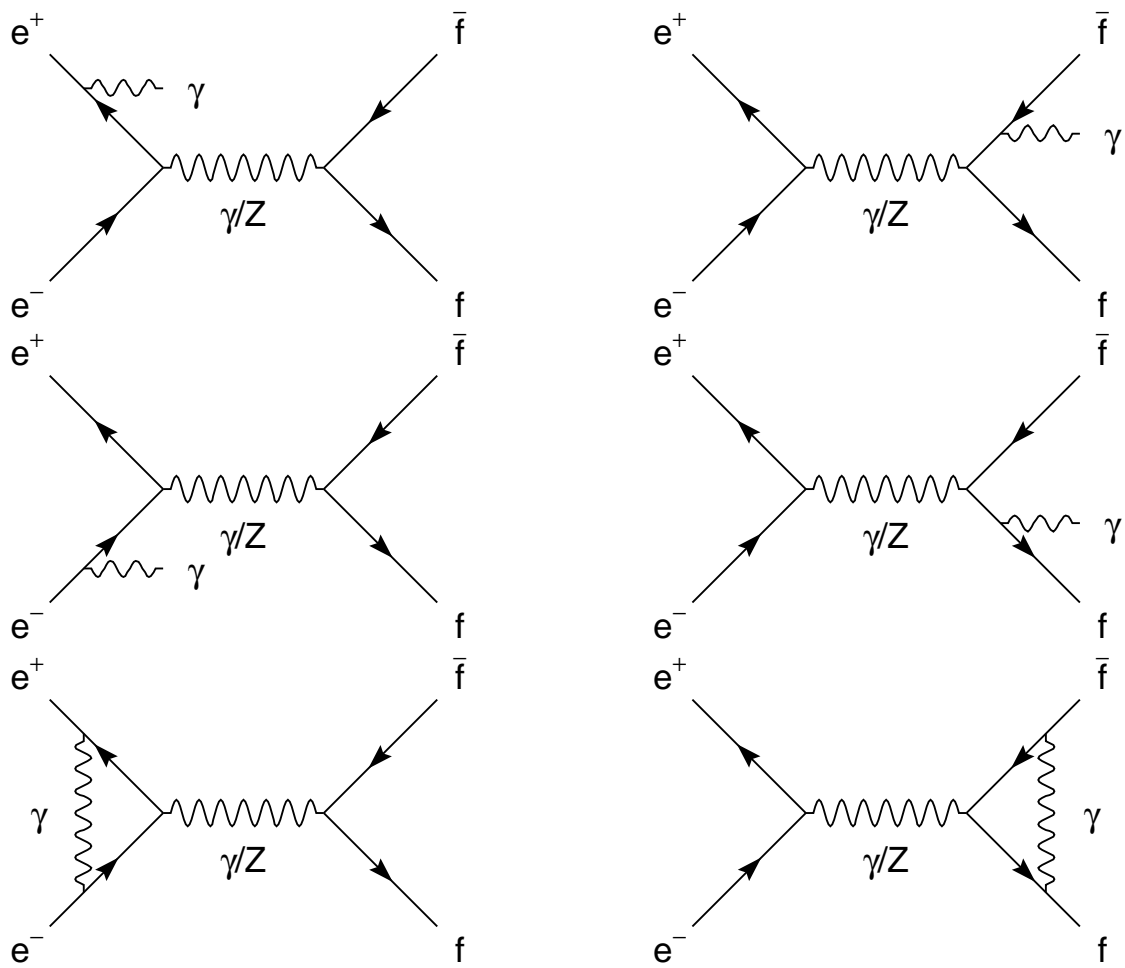


Figure 1.10: QED corrections to fermion-pair production.

function  $H_{\text{QED}}^{\text{FB}}$ . The effects of these QED corrections on the cross-sections and asymmetries are shown in Figure 1.11. At the peak the QED de-convoluted cross-section is 36% larger than the measured one, and the peak position is shifted downwards by about 100 MeV. The estimated precision of these important corrections is discussed in Section 2.3.4.

The partial Z decay widths are defined inclusively, *i.e.* they contain QED and QCD final state corrections and the contribution from the imaginary parts of the effective couplings,

$$\Gamma_{\text{ff}} = N_c^f \frac{G_F m_Z^3}{6\sqrt{2}\pi} \left( |\mathcal{G}_{Af}|^2 R_{Af} + |\mathcal{G}_{Vf}|^2 R_{Vf} \right) + \Delta_{ew/QCD}. \quad (1.26)$$

The radiator factors  $R_{Vf}$  and  $R_{Af}$  take into account final state QED and QCD corrections as well as non-zero fermion masses;  $\Delta_{ew/QCD}$  accounts for non-factorisable electroweak/QCD corrections. The inclusion of the imaginary parts of the couplings in the definition of the leptonic width,  $\Gamma_{\ell\ell}$ , leads to changes of 0.15 per-mil corresponding to only 15% of the LEP-combined experimental error on  $\Gamma_{\ell\ell}$ . The primary reason to define the partial widths including final state corrections and the contribution of the imaginary terms of the couplings is to allow the straightforward addition of the partial widths to yield the full width of the Z boson.

The total cross-section arising from the  $\cos\theta$ -symmetric Z production term can also be written in terms of the partial decay widths into the initial and final states,  $\Gamma_{ee}$  and  $\Gamma_{\text{ff}}$ ,

$$\sigma_{\text{ff}}^Z = \sigma_{\text{ff}}^{\text{peak}} \frac{s\Gamma_Z^2}{(s - m_Z)^2 + s^2\Gamma_Z^2/m_Z^2}, \quad (1.27)$$

where

$$\sigma_{\text{ff}}^{\text{peak}} = \frac{1}{1 + \delta_{\text{QED}}} \sigma_{\text{ff}}^0 \quad (1.28)$$

$$\text{and} \quad (1.29)$$

$$\sigma_{\text{ff}}^0 = \frac{12\pi}{m_Z^2} \frac{\Gamma_{ee}\Gamma_{\text{ff}}}{\Gamma_Z^2}. \quad (1.30)$$

The term  $1/(1 + \delta_{\text{QED}})$  removes the final state QED correction included in the definition of  $\Gamma_{ee}$ , and is given by  $\delta_{\text{QED}} = \frac{3}{4}Q_f^2\alpha/\pi + \dots$ .

The overall hadronic cross-section is parameterised in terms of the hadronic width given by the sum over all quark final states,

$$\Gamma_{\text{had}} = \sum_{q, q \neq t} \Gamma_{q\bar{q}}. \quad (1.31)$$

The invisible width from Z decays to neutrinos,  $\Gamma_{\text{inv}} = N_\nu\Gamma_{\nu\nu}$ , where  $N_\nu$  is the number of light neutrino species, can be determined from the measurements of the decay widths to all visible final states and the total width,

$$\Gamma_Z = \Gamma_{ee} + \Gamma_{\mu\mu} + \Gamma_{\tau\tau} + \Gamma_{\text{had}} + \Gamma_{\text{inv}}. \quad (1.32)$$

Because the measured cross-sections depend on products of the partial widths and also on the total width, the widths constitute a highly correlated parameter set. In order to reduce correlations among the fit parameters an experimentally-motivated set of six parameters is used to describe the total hadronic and leptonic cross-sections around the Z peak. These are

- the mass of the Z,  $m_Z$ , and the total width,  $\Gamma_Z$ ;

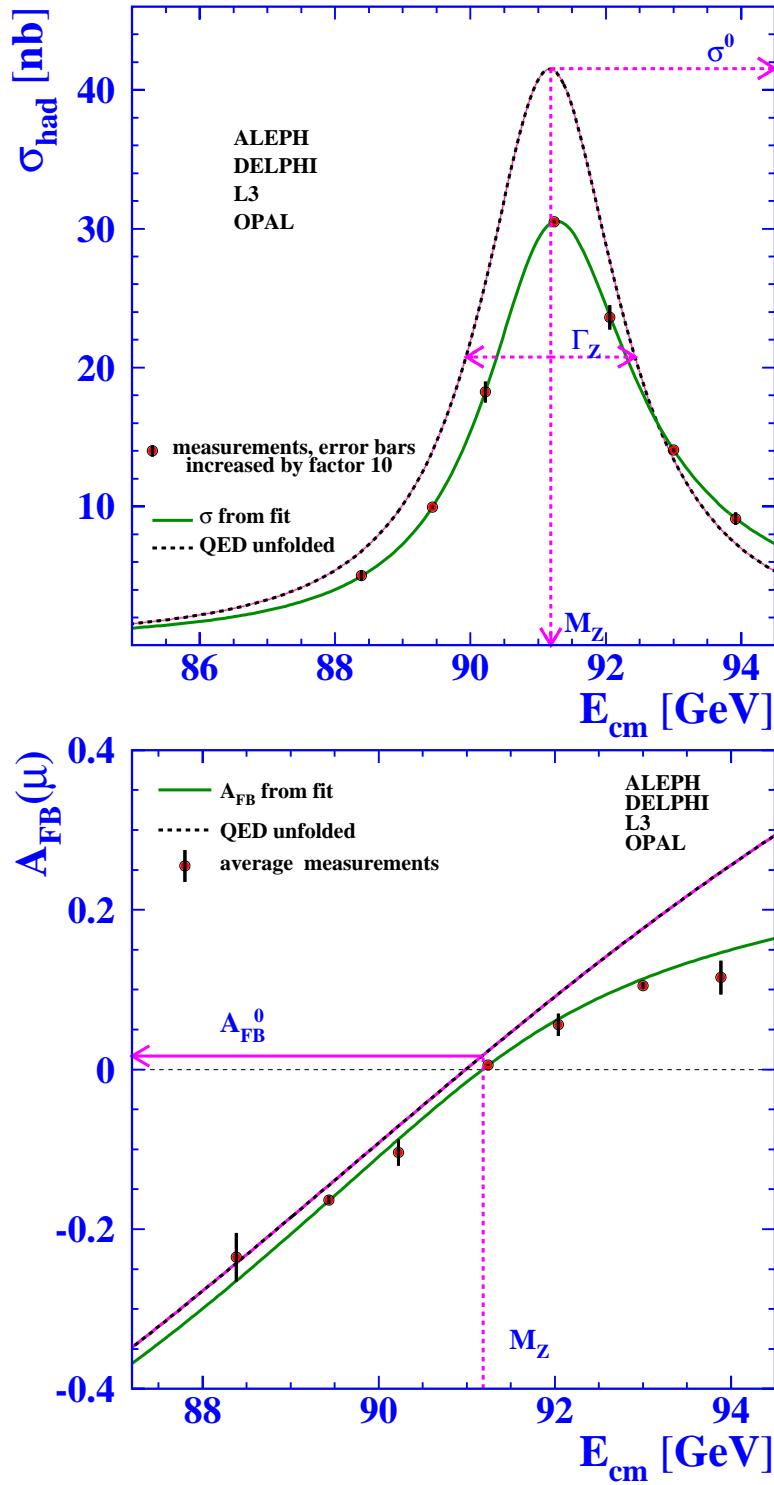


Figure 1.11: Average over measurements of the hadronic cross-sections (top) and of the muon forward-backward asymmetry (bottom) by the four experiments, as a function of centre-of-mass energy. The full line represents the results of model-independent fits to the measurements, as outlined in Sec. 1.4. Unfolding of photonic effects yields the dashed curves, which define the Z parameters described in the text.

- the “hadronic pole cross-section”,

$$\sigma_h^0 \equiv \frac{12\pi}{m_Z^2} \frac{\Gamma_{ee}\Gamma_{\text{had}}}{\Gamma_Z^2}; \quad (1.33)$$

- the ratios

$$R_e^0 \equiv \Gamma_{\text{had}}/\Gamma_{ee}, \quad R_\mu^0 \equiv \Gamma_{\text{had}}/\Gamma_{\mu\mu} \quad \text{and} \quad R_\tau^0 \equiv \Gamma_{\text{had}}/\Gamma_{\tau\tau}. \quad (1.34)$$

- for those hadronic final states where the primary quarks can be identified, additional ratios can be defined:

$$R_q^0 \equiv \Gamma_{q\bar{q}}/\Gamma_{\text{had}}, \quad e.g. \quad R_b^0 = \Gamma_{b\bar{b}}/\Gamma_{\text{had}}. \quad (1.35)$$

These ratios have traditionally been treated independently of the above set, as described in Chapters 5 and 6.

▲ The leading contribution from  $\gamma$ - $Z$  interference is proportional to the product of the vector couplings of the initial and final states and vanishes at  $\sqrt{s} = m_Z$ , but becomes noticeable at off-peak energies and therefore affects the  $Z$  mass. Because a determination of all quark couplings is not possible, the  $\gamma$ - $Z$  interference term in the hadronic final state is fixed to its Standard Model value. The implications of this are discussed in Sec. 2.4.3.

Three additional parameters are needed to describe the leptonic forward-backward asymmetries. These are the “pole asymmetries”,  $A_{\text{FB}}^{0,e}$ ,  $A_{\text{FB}}^{0,\mu}$  and  $A_{\text{FB}}^{0,\tau}$  for the processes  $e^+e^- \rightarrow e^+e^-$ ,  $e^+e^- \rightarrow \mu^+\mu^-$  and  $e^+e^- \rightarrow \tau^+\tau^-$ . Contrary to the case of the partial widths which are defined using the full complex couplings in order to ensure that the sum over all partial widths equals the total width, the pole asymmetries are defined purely in terms of the real parts of the effective  $Z$  couplings,

$$A_{\text{FB}}^{0,f} \equiv \frac{3}{4} \mathcal{A}_e \mathcal{A}_f \quad \text{with} \quad (1.36)$$

$$\mathcal{A}_f = \frac{2g_{Vf}g_{Af}}{g_{Vf}^2 + g_{Af}^2}. \quad (1.37)$$

Due to the smallness of the leptonic forward-backward asymmetry at  $\sqrt{s} = m_Z$ , QED corrections are as large as  $A_{\text{FB}}^{0,\ell}$  itself. Off-peak the contributions from  $\gamma - Z$  interference to the asymmetries become even larger. Since the slope of the asymmetry as a function of energy is proportional to the axial-vector couplings of the  $Z$ , which are well-determined by the measured cross sections, only the small imaginary parts of the couplings remain to give asymmetry contributions which must be calculated rather than experimentally determined. Here it must be noted that although only the real parts of the couplings are used in the definition of the pole asymmetries, the complete complex couplings are used in the extraction of the pole asymmetries from the measured asymmetries.

As with the widths, the forward-backward asymmetries for hadronic states with identified quarks can also be measured, resulting in determinations of  $A_{\text{FB}}^{q\bar{q}}$ . Also, as for the purely leptonic case, although the widths are inclusive (including QED and QCD effects), the parameters used in the fits ( $A_{\text{FB}}^{0,q}$ ) are corrected for QCD effects, QED radiation,  $\gamma$  exchange and  $\gamma$ - $Z$  interference to arrive at the pole asymmetries defined above.

## 1.5 Polarized cross-sections and asymmetries

The above neglects any information concerning helicities of the incoming or outgoing particles. There are, however, four helicity configurations which are involved: left- or right-handed incoming electrons and left- or right-handed outgoing fermions. These configurations must be taken into account when dealing with any processes where polarized initial or final states are important. Taking only the Z exchange diagrams and only real couplings\*, one can define the following four differential cross-sections:

$$\frac{d\sigma_{ll}}{d\cos\theta} \propto g_{Le}^2 g_{Lf}^2 (1 + \cos\theta)^2 \quad (1.38)$$

$$\frac{d\sigma_{rr}}{d\cos\theta} \propto g_{Re}^2 g_{Rf}^2 (1 + \cos\theta)^2 \quad (1.39)$$

$$\frac{d\sigma_{lr}}{d\cos\theta} \propto g_{Le}^2 g_{Rf}^2 (1 - \cos\theta)^2 \quad (1.40)$$

$$\frac{d\sigma_{rl}}{d\cos\theta} \propto g_{Re}^2 g_{Lf}^2 (1 - \cos\theta)^2. \quad (1.41)$$

From these, a set of four independent cross-sections can be measured:

$$\sigma_{\text{tot}} = \sigma_{ll} + \sigma_{rr} + \sigma_{lr} + \sigma_{rl} \quad (1.42)$$

$$\sigma_{\text{LR}} = \sigma_{ll} + \sigma_{lr} - \sigma_{rl} - \sigma_{rr} \quad (1.43)$$

$$\sigma_{\text{pol}} = \sigma_{ll} + \sigma_{rl} - \sigma_{lr} - \sigma_{rr} \quad (1.44)$$

$$\sigma_{\text{FB}} = \sigma_{ll} + \sigma_{rr} - \sigma_{lr} - \sigma_{rl} \quad (1.45)$$

These correspond to the total cross-section, the difference in cross-sections between left and right-handed incoming electrons, the difference in cross-sections between left and right-handed outgoing fermions, and the difference in cross-sections between outgoing fermions in the forward hemisphere and in the backward hemisphere.

From these cross-sections, several asymmetries can be extracted, which can be related directly to  $g_L$  and  $g_R$  (or, as is used in this report,  $g_V$  and  $g_A$ ). Using the same definition of  $\mathcal{A}$  as given in Equation 1.37, the asymmetries are

$$A_{\text{FB}} = \frac{3}{4} \frac{\sigma_{\text{FB}}}{\sigma_{\text{tot}}} = \frac{3}{4} \mathcal{A}_e \mathcal{A}_f \quad (1.46)$$

$$A_{\text{LR}} = \frac{\sigma_{\text{LR}}}{\sigma_{\text{tot}}} = \mathcal{A}_e \quad (1.47)$$

$$A_{\text{pol}} = \frac{\sigma_{\text{pol}}}{\sigma_{\text{tot}}} = \mathcal{A}_f (= -\mathcal{P}_f). \quad (1.48)$$

$\mathcal{P}_f$  is the polarization of the final state, and the minus sign is a historical definition. The factor 3/4 in  $A_{\text{FB}}$  arises from the integration of the angular form in Equations 1.38–1.41. By comparing the polarized cross-sections  $\sigma_{\text{pol}}$  and  $\sigma_{\text{LR}}$  in the forward and backward hemispheres, two additional asymmetries can be measured:

$$A_{\text{FB}}^{\text{pol}} = A_{\text{pol}}(F) - A_{\text{pol}}(B) = \frac{3}{4} \mathcal{A}_e \quad (1.49)$$

$$A_{\text{FBLR}} = A_{\text{LR}}(F) - A_{\text{LR}}(B) = \frac{3}{4} \mathcal{A}_f. \quad (1.50)$$

---

\*As in the previous section, the effects of radiative corrections, including the imaginary parts of couplings are taken into account in the analysis. They are neglected here to allow a clearer view of the helicity structure.

The measurement of any of the polarized asymmetries requires the determination of the polarization of either the initial state or the final state. The final state polarization can only be determined for tau final states, where the charged current tau decay serves as a polarization analyzer. Thus,  $\mathcal{A}_\tau$  and  $\mathcal{A}_e$  can be determined at LEP using measurements of tau polarization. In contrast, with the initial state polarization available at SLC,  $\mathcal{A}_e$  can be measured using all final states and  $\mathcal{A}_f$  can be measured for each final state that can be isolated. These include the electron, muon, tau, b-quark, c-quark and s-quark final states. Using the measurements of  $\mathcal{A}_e$ , the parameters  $\mathcal{A}_\mu$ ,  $\mathcal{A}_\tau$ ,  $\mathcal{A}_b$  and  $\mathcal{A}_c$  can be inferred from forward-backward asymmetry measurements at LEP. Thus, the LEP and SLC results form a complementary and practically complete set of  $\mathcal{A}$  measurements.

## 1.6 Pseudo-observables and Standard Model remnants

The parameters introduced in Sections 1.4 and 1.5 describing the main features of all measurements around the Z resonance are not “realistic observables” as the underlying measurements themselves, but are defined quantities with significant theoretical corrections. Therefore they are commonly named “pseudo-observables”. Where necessary, the pseudo-observables will be denoted by a superscript 0, *e.g.*,  $\sigma_{\text{had}}$  is the measured hadronic cross-section, whereas  $\sigma_{\text{h}}^0$  is the pole-cross-section derived from the measurements. Similarly,  $R_b$  is the measured b quark cross-section divided by the hadronic cross-section ( $\sigma_{b\bar{b}}/\sigma_{\text{had}}$ ) and  $R_b^0$  is the derived ratio of Z boson partial widths,  $\Gamma_{b\bar{b}}/\Gamma_{\text{had}}$ .

The bulk of the differences between the realistic and pseudo-observables is due to QED effects; differences between the pseudo-observables and the QED de-convoluted observables at  $\sqrt{s} = m_Z$ , arising from the interference between photon and Z diagrams and from the interplay between the real and imaginary parts of the photon and Z couplings, are small in the Standard Model.  $\sigma_{\text{ff}}^0$ , given in terms of the partial decay widths, agrees to better than 0.05% for both hadrons and leptons with the QED de-convoluted cross-sections without the photon exchange contribution at  $\sqrt{s} = m_Z$ . This is only a fraction of the LEP combined experimental error. The difference between  $A_{\text{FB}}^{0,\ell}$  and the QED de-convoluted forward-backward asymmetry at the peak amounts to 0.0013, which is slightly larger than the LEP combined error on  $A_{\text{FB}}^{0,\ell}$ . It is therefore important to treat the imaginary parts correctly, but there is no sensitivity of the measurements to Standard Model parameters entering through the imaginary parts.

However, these pseudo-observables cannot be considered as truly model-independent, because imaginary parts of the couplings as well as the  $\gamma$ -Z interference in the hadronic final state need to be fixed to their Standard Model values. This leads to small “Standard Model remnants” in any attempted “model-independent” definition of the pseudo-observables. More details about the treatment of imaginary parts and Standard Model remnants in the theory programs TOPAZ0 [19] and ZFITTER [20] are given in Reference 21. These computer codes include the best up-to-date knowledge on QED and electroweak corrections within the minimal Standard Model and thus provide the connection between the realistic observables and the pseudo-observables. In addition, they are used to determine the important Standard Model parameters, such as the Higgs boson mass, given the pseudo- or realistic observables.

# Chapter 2

## The Z lineshape

The analyses described in this section focus on the measurements of the total production cross-sections in the four channels  $e^+e^- \rightarrow q\bar{q}$ ,  $e^+e^-$ ,  $\mu^+\mu^-$  and  $\tau^+\tau^-$  at different centre-of-mass energies within  $\pm 3$  GeV around  $\sqrt{s} = m_Z$ . Decays to neutrinos escape direct detection and are referred to as “invisible decays”. Since quark flavours cannot be completely separated, an inclusive selection of all hadronic final states is performed here. The expected approximate branching fractions of the Z are 70%, 20% and 10% to hadrons, neutrinos and charged leptons, respectively. The full LEP-I data set consists of about  $4 \times 200$  measurements of hadronic and leptonic cross-sections and of leptonic forward-backward asymmetries at different centre-of-mass energies. Only the forward-backward asymmetries in the leptonic channels are considered here, because asymmetry measurements in  $q\bar{q}$  final states require dedicated flavour tagging techniques, see Chapter 5, or inclusive methods as described in Chapter 6.

From the measurements of the cross-sections and asymmetries each experiment has extracted a set of pseudo-observables describing the differential cross-section around the Z resonance, which include the mass,  $m_Z$ , and width,  $\Gamma_Z$ , of the Z, the total pole cross-section for  $q\bar{q}$  production,  $\sigma_h^0$ , and the leptonic forward-backward asymmetry at the peak,  $A_{FB}^{0,\ell}$ , as defined in Section 1.3. The combination of the results by the four experiments is based on this set of parameters.

### 2.1 Measurements of total cross-sections and forward-backward asymmetries

The main features of the event selection procedures for measurements of the total hadronic and the leptonic cross-sections and of the leptonic forward-backward asymmetries are briefly described below. Detailed descriptions of the individual experimental analyses are given in References 22–25.

#### 2.1.1 Event selection

The event selection for  $q\bar{q}$ ,  $e^+e^-$ ,  $\mu^+\mu^-$  and  $\tau^+\tau^-$  final states in each of the experiments is aimed at high selection efficiencies within the largest possible acceptance in order to keep corrections small.

The design of the detectors and the cleanliness of the LEP beams allowed the experiments to trigger on hadronic and leptonic Z decays with high redundancy and essentially 100% efficiency.

ALEPH

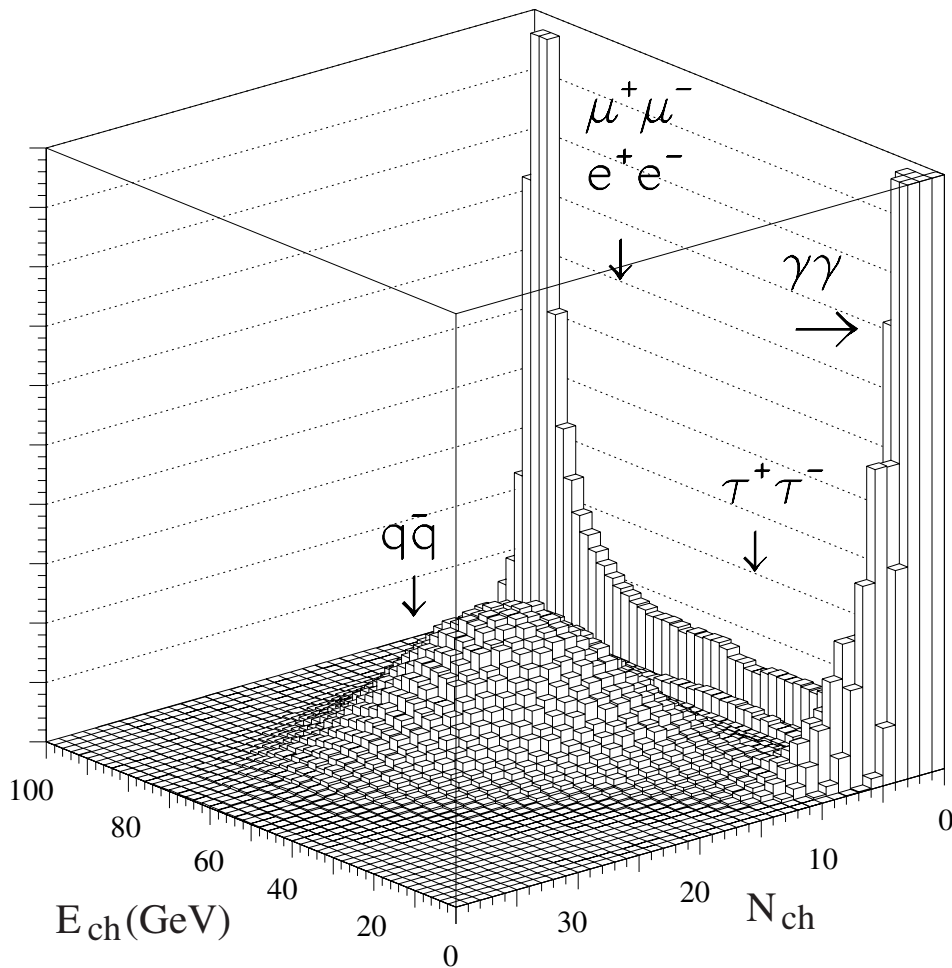


Figure 2.1: Separation of the final states from only two variables, the sum of the track momenta and the track multiplicity, in the central detector of the ALEPH experiment.

The selections accept events with initial and final state radiation as much as possible in order to benefit from cancellations between real and virtual particle emission. Good discrimination of  $q\bar{q}$  from  $\ell^+\ell^-$  final states is mandatory, and excellent separation of  $e^+e^-$ ,  $\mu^+\mu^-$  and  $\tau^+\tau^-$  permits checks of the universality of the Z couplings to the different lepton species to be carried out. Machine-induced backgrounds at LEP-I were small, and background from  $e^+e^-$  processes are restricted to two-photon reactions ( $\gamma\gamma$ ). Event pictures of each of the final states are shown in Figure 1.7 in Chapter 1.

The separation between leptonic and hadronic events and their distinction from two-photon reactions ( $\gamma\gamma$ ) are exemplified in Figure 2.1, in a two-dimensional distribution of the number of charged tracks and the energy sum of all tracks calculated from the measured momentum assuming the pion mass. A peak from  $e^+e^-$  and  $\mu^+\mu^-$  events at high momenta and low multiplicities is clearly separated from two-photon background at relatively low multiplicities and momenta. The intermediate momentum region at low multiplicities is populated by  $\tau^+\tau^-$  events. Hadronic events populate the high multiplicity region at energies below the centre-of-mass energy, since neutral particles in the jets are not measured in the central detector. The



separation of electrons and muons is achieved using also the information from the electromagnetic and hadron calorimeters and from the muon chambers.

The experiments use very detailed detector simulations [26, 27] to understand the selection efficiencies. Owing to the high redundancy of the detectors, cross-checks using the data themselves are possible by comparing event samples identified with different selection criteria. Various Monte Carlo generators are interfaced to the detector simulations and are used to describe the kinematics of the physics reactions of interest:  $q\bar{q}$  production with gluon radiation including phenomenological modelling of the non-perturbative hadronisation process [28–30], production of  $\mu^+\mu^-$  and  $\tau^+\tau^-$  final states [31, 32],  $e^+e^-$  final states including the  $t$ -channel contribution [33–35], and finally  $e^+e^-$  scattering in the forward direction [36], which is dominated by  $t$ -channel photon exchange and serves as the normalisation reaction for the determination of the luminosity of the colliding  $e^+e^-$  beams. The Monte Carlo generators are used to apply corrections at the edges of the experimental acceptance, and for small extrapolations of the measured cross-sections and forward-backward asymmetries from the true experimental cuts to a simple **sets** of cuts that can be handled at the fitting stage. In the case of  $q\bar{q}$  final states, the only remaining cut after all corrections is  $s' > 0.01 s$ , where  $\sqrt{s'}$  is the effective centre-of-mass energy after initial-state photon radiation. The treatment of the lepton channels differs in detail among the experiments; the results are specified either with an  $s'$  cut only, within a given acceptance in the fermion production angle **w.r.t. the incident electron direction,  $\cos\theta$** , and the minimal fermion energy, or additionally with a cut on the maximum allowed acollinearity of the final state fermion pair. The results quoted for the  $e^+e^-$  final state either include contributions originating from  $t$ -channel diagrams, or the  $t$  and  $s$ - $t$  interference effects are explicitly subtracted, allowing the same treatment of  $e^+e^-$  and  $\mu^+\mu^-$  or  $\tau^+\tau^-$  final states in the fits for the  $Z$  parameters.

Hadronic events in the detectors are characterised by a large number of particles arising from the hadronisation process of the originally produced quark pair. This leads to high track multiplicities in the central detectors and high cluster multiplicities in the electromagnetic and hadron calorimeters. For  $Z \rightarrow q\bar{q}$  events, the deposited energy is balanced along the beam line, which is generally not the case for hadronic events produced in  $\gamma\gamma$  reactions. In addition,  $\gamma\gamma$  events have an almost constant production **cross-sections** around the  $Z$  resonance. It is thus possible to estimate the  $\gamma\gamma$  fraction directly **from the data** by studying the energy dependence of two event samples, one with an enriched  $\gamma\gamma$  contribution and another **one** with tight selection cuts for genuine  $Z \rightarrow q\bar{q}$  events, which show a resonant behaviour. Background from  $\tau\tau$  events is subtracted using  $\tau\tau$  Monte Carlo.

Lepton pairs are selected by requiring low track and cluster multiplicities. Electrons are characterised by energy deposits in the electromagnetic calorimeters **matching well** the measured momentum in the tracking detectors. Muons have only minimum ionising energy deposits in the electromagnetic and hadron calorimeters and signals in the outer muon chambers. Tau leptons decay before reaching any detector component. Their visible decay products are either a single electron, muon or hadron, or a collimated jet consisting of three or five charged hadrons and a few neutral hadrons; in addition energy is missing due to the undetectable neutrinos.  $\tau^+\tau^-$  events are therefore selected by requiring the total energy and momentum sums to be below the centre-of-mass energy **to discriminate** against  $e^+e^-$  and  $\mu^+\mu^-$ , and to be above a minimum energy **to reject lepton pairs** arising from two-photon reactions. The approximate direction of flight **of the  $\tau$**  is taken to be the momentum sum of the visible decay products.

Leptonic events with photons or fermion pairs radiated from the **initial or final state** leptons are contained in the signal definition. Initial-state pairs typically remain in the beam pipe

and are therefore experimentally indistinguishable from initial state photon radiation. Final-state pairs may change the selection efficiencies, which is studied using four-fermion event generators [37, 38]. The classification of such four-fermion events into one of the three lepton categories is made by choosing the pair with the highest invariant mass.

### 2.1.2 Cross-section measurements

The total cross-section,  $\sigma_{\text{tot}}$ , is determined from the number of selected events in a final state,  $N$ , the number of background events,  $N_{\text{bg}}$ , the selection efficiency,  $\epsilon$ , and the integrated luminosity,  $\mathcal{L}$ .  $\sigma_{\text{tot}} = (N - N_{\text{bg}})/(\epsilon\mathcal{L})$ .

#### Measurement of the luminosity

The luminosity of the beams is measured from the process of small-angle Bhabha scattering. Events with forward going electrons are recorded concurrently with all other processes, thus ensuring that they correctly reflect any data-taking inefficiencies arising from read-out dead-times and detector down-times. Furthermore, the statistical precision of this process is high, matching well even the high statistics of hadronic events at the Z resonance. The luminosity measurement requires the detection of back-to-back energy deposits by electrons and positrons close to the beam direction. Their positions and energies are precisely measured by calorimeters placed at small angles with respect to the beam line, typically covering a polar range from 25 mrad to 60 mrad from the beam line. Depending on the experiment, the accepted cross-section in the luminosity devices is at least twice as large as the hadronic on-peak cross-section, and therefore the statistical errors arising from the luminosity determination are small. The typical experimental signature of luminosity events is shown in Figure 2.2. The main experimental systematic error arises from the definition of the geometrical acceptance for this process. Since the angular distribution is steeply falling with increasing scattering angle ( $\propto \theta^{-3}$ ), the precise definition of the inner radius of the acceptance region is most critical. Background arises from random coincidences between the calorimeters at the two sides and is largely beam-induced. The integrated luminosity is given by the ratio of the number of observed small-angle  $e^+e^-$  events and the calculated cross-section for this process within a given acceptance. The Bhabha cross-section at small scattering angles is dominated by the well-known QED process of  $t$ -channel scattering, but nonetheless this gives rise to an important theoretical error of about 0.5 per-mil affecting all experiments coherently, as is discussed in Section 2.3.3. Typical experimental systematic errors on the luminosity are well below 0.1 %.

#### Event selection efficiency and background levels

In the hadronic channel the selection efficiencies within the acceptance are high, typically above 99 %. Backgrounds are dominated by  $Z \rightarrow \tau^+\tau^-$  and non-resonant  $q\bar{q}$  production from  $\gamma\gamma$  reactions. At the peak of the resonance these together contribute at a level of a few per-mil. Backgrounds in the lepton selections are typically around 1 % for  $e^+e^-$  and  $\mu^+\mu^-$  and slightly larger for  $\tau^+\tau^-$  final states. The dominant background in  $e^+e^-$  and  $\mu^+\mu^-$  final states arises from  $\tau^+\tau^-$  events, which plays no role if the total leptonic cross-section is measured. Backgrounds other than  $\tau^+\tau^-$  in the  $e^+e^-$  and  $\mu^+\mu^-$  channels are at a level of  $\mathcal{O}(0.1\%)$ .

An overview of the selection efficiencies within the acceptance and of the background levels is presented in Table 2.1. The acceptances quoted in the table are ideal ones suitable as input to the electroweak program libraries used for fitting, while the actual set of experimental cuts is more complicated. Monte Carlo event generators and detailed detector simulations in com-

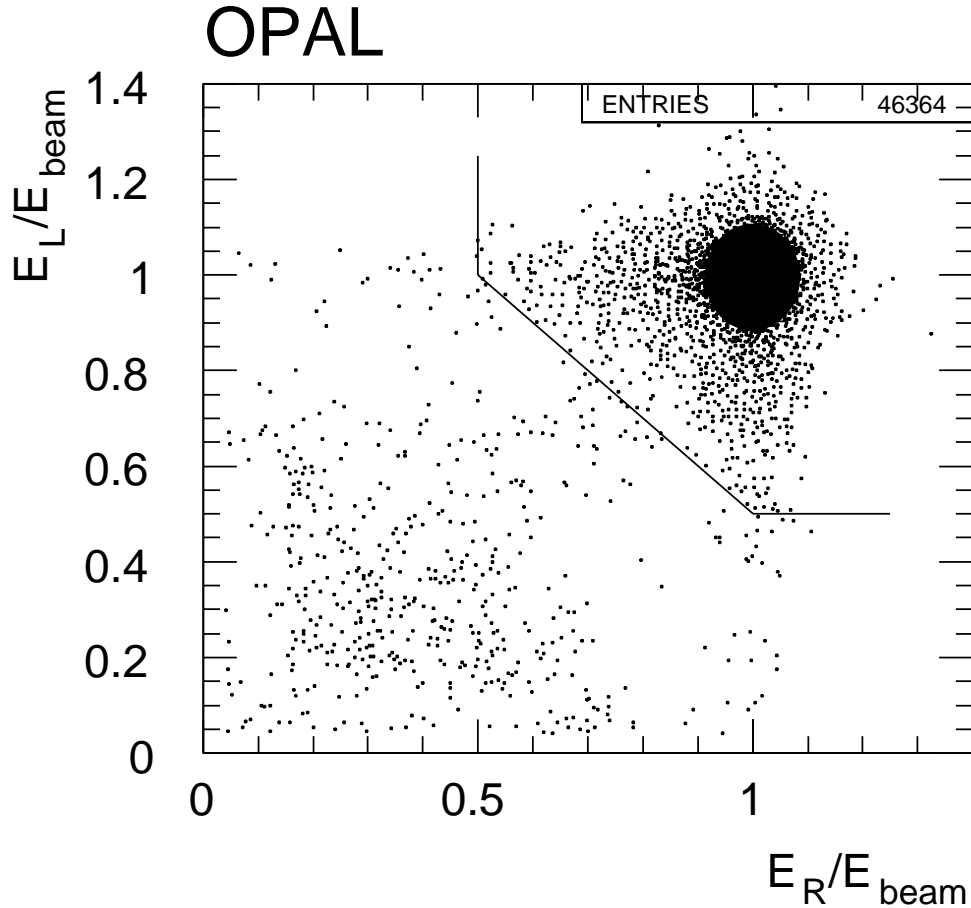


Figure 2.2: Fraction of the beam energy observed in the left and right luminosity calorimeters of the OPAL experiment, after all cuts except the one on the deposited energies. The lines indicate the acceptance region for the signal events. Initial state photon radiation leads to tails towards lower deposited energies. Background events from accidental coincidences populate the low-energy regions in both calorimeters.

bination with dedicated corrections are used to transform the true experimental acceptances to the ideal ones. As is shown in the Table, the selection efficiencies are high, above 95% in  $e^+e^-$  and  $\mu^+\mu^-$  and slightly lower, 70–90% in  $\tau^+\tau^-$  final states.  $\blacktriangle$

The idealised acceptances are defined by the scattering angle,  $\theta$ , of the negatively charged lepton in the laboratory frame, and also require a cut-off for initial-state photon radiation. The latter may either be given by a cut on the acollinearity of the two final-state leptons,  $\eta$ , or by an explicit cut on the invariant mass of the final-state leptons,  $m_{\ell\bar{\ell}}$ ; alternatively, the effective centre-of-mass energy after photon radiation off the initial state,  $s'$ , may be used. The experimental efficiencies for low values of  $m_{\ell\bar{\ell}}$  or  $s'$  are small. Despite the differing definitions the efficiencies given in the Table are still comparable, because the acceptance difference between the wider definition  $s'/s > 4m_\tau^2$  and a tight definition using an acollinearity cut at  $\eta < 10^\circ$  is only 2%.  $\blacktriangle$

### Total cross-section

The total cross-section for the production of each final state is obtained from the efficiency and background corrected numbers of selected events normalised to the luminosity. Data taken at

	ALEPH	DELPHI	L3	OPAL
$q\bar{q}$ final state				
acceptance	$s'/s > 0.01$	$s'/s > 0.01$	$s'/s > 0.01$	$s'/s > 0.01$
efficiency [%]	99.1	94.8	99.3	99.5
background [%]	0.7	0.5	0.3	0.3
$e^+e^-$ final state				
acceptance	$-0.9 < \cos\theta < 0.7$ $s' > 4m_\tau^2$	$ \cos\theta  < 0.72$ $\eta < 10^\circ$	$ \cos\theta  < 0.72$ $\eta < 25^\circ$	$ \cos\theta  < 0.7$ $\eta < 10^\circ$
efficiency [%]	97.4	97.0	98.0	99.0
background [%]	1.0	1.1	1.1	0.3
$\mu^+\mu^-$ final state				
acceptance	$ \cos\theta  < 0.9$ $s' > 4m_\tau^2$	$ \cos\theta  < 0.94$ $\eta < 20^\circ$	$ \cos\theta  < 0.8$ $\eta < 90^\circ$	$ \cos\theta  < 0.95$ $m_{\text{ff}}^2/s > 0.01$
efficiency [%]	98.2	95.0	92.8	97.9
background [%]	0.2	1.2	1.5	1.0
$\tau^+\tau^-$ final state				
acceptance	$ \cos\theta  < 0.9$ $s' > 4m_\tau^2$	$0.035 <  \cos\theta  < 0.94$ $s' > 4m_\tau^2$	$ \cos\theta  < 0.92$ $\eta < 10^\circ$	$ \cos\theta  < 0.9$ $m_{\text{ff}}^2/s > 0.01$
efficiency [%]	92.1	72.0	70.9	86.2
background [%]	1.7	3.1	2.3	2.7

Table 2.1: Acceptances, selection efficiencies\* within an idealised acceptance, and background contribution at the peak of the resonance (1994 data).

\*The selection efficiencies given by the experiments were in some cases quoted for full acceptance in  $\cos\theta$ ; here, these were corrected to the fiducial cuts in  $\cos\theta$  actually used in the analyses, assuming a shape of the differential cross-section according to  $(1 + \cos^2\theta)$ .

the same energy point and within the same year are combined into a single cross-section measurement at the average energy. As an example, the measurements of the hadronic cross-section around the three principal energies are shown in Figure 2.3. Because the hadron statistics are almost ten times larger than the lepton statistics, these measurements dominate the determination of the mass and the width of the  $Z$ .

The energy dependence of the hadronic cross-section (the “line shape”) is shown in the left-hand plot of Figure 1.11 in Section 1.3. The energy dependence of the muon and tau cross-section is nearly identical in shape to the hadronic one. In  $e^+e^-$  final states however, diagrams involving photon exchange in the  $t$ -channel and their interference with the  $s$ -channel diagrams also contribute. The different contributions are shown as a function of centre-of-mass energy in the left-hand plot of Figure 2.4.

### 2.1.3 Measurements of the lepton forward-backward asymmetries

The forward-backward asymmetry,  $A_{\text{FB}}$ , is defined by the numbers of events in which the final state lepton goes forward ( $\cos(\theta_{\ell^-}) > 0$ ) or backward ( $\cos(\theta_{\ell^-}) < 0$ ) with respect to the direction of the incoming electron,  $N_f$  and  $N_b$ , respectively:  $A_{\text{FB}} = (N_f - N_b)/(N_f + N_b)$ . This definition of  $A_{\text{FB}}$  depends on the acceptance cuts applied on the production polar angle,  $\cos\theta$ , of the leptons. The measurements of  $A_{\text{FB}}(\ell^+\ell^-)$  require the determination of  $\cos\theta$  and the separation of leptons and anti-leptons based on their electric charges, which are determined from the curvature of the lepton tracks in the magnetic fields of the central detectors. For  $\mu^+\mu^-$  and  $\tau^+\tau^-$  final states,  $A_{\text{FB}}$  is determined from un-binned maximum-likelihood fits to the differential cross-section distributions of the form  $d\sigma/d\cos\theta \propto 1 + \cos^2\theta + 8/3 A_{\text{FB}} \cos\theta$ . This procedure makes better use of the available information and hence leads to slightly smaller statistical errors. Determined this way the  $A_{\text{FB}}$  measurements are insensitive of any detection inefficiencies as long as these are symmetric in  $\cos\theta$ . Examples of the measured angular distributions for the  $e^+e^-$  and  $\mu^+\mu^-$  final states are shown in Figure 2.5.

The shape of the differential cross-section in the electron final state is more complex due to the contributions from the  $t$ -channel and the  $s$ - $t$ -interference, which lead to a large contribution of events in which the electron is scattered in the forward direction. A maximum-likelihood fit to obtain  $A_{\text{FB}}(e^+e^-)$  may be performed after subtracting the  $t$  and  $s$ - $t$  contributions, but usually the asymmetry is determined from the efficiency-corrected numbers of events with forward and backward going electrons, according to the above definition.

The energy dependence of the forward-backward asymmetry in  $\mu^+\mu^-$  final state is shown in the right-hand plot of Figure 1.11 above. The forward-backward asymmetry as a function of centre-of-mass energy in the  $e^+e^-$  final state including the  $t$ ,  $s$ - $t$  contributions is illustrated in the right-hand plot of Figure 2.4

### 2.1.4 Systematic errors

In general, the systematic errors arising from the selection procedures are small and so the accumulated statistics can be fully exploited. Furthermore, the purely experimental errors arising from the limited understanding of detector acceptances are uncorrelated among the experiments. An overview of the experimental systematic errors is given in Table 2.2. Statistical errors per experiment are only around 0.5 per-mil in the hadronic channel and around 2.5 per-mil in each of the three lepton channels. Statistical errors from the number of small-angle Bhabha events affect all channel in a correlated way, but even on-peak they are smaller than

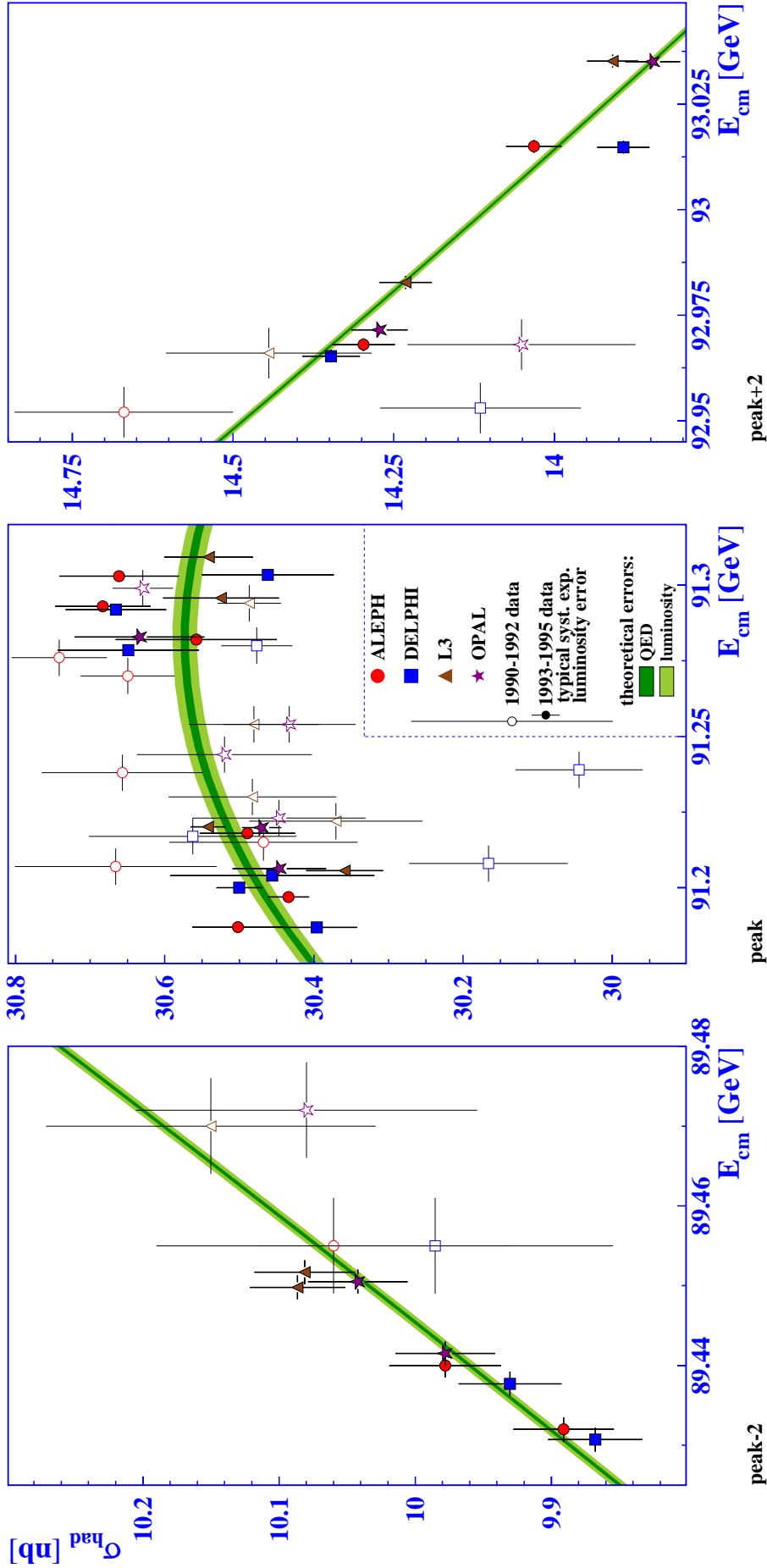


Figure 2.3: Measurements by the four experiments of the hadronic cross-sections around the three principal energies. The vertical error bars show the statistical errors only. The open symbols represent the early measurements with typically much larger systematic errors than the later ones, shown as full symbols. Typical experimental systematic errors on the determination of the luminosity are indicated in the legend; these are almost fully correlated within each experiment, but uncorrelated among the experiments. The horizontal error bars show the uncertainties in LEP centre-of-mass energy, where the errors for the period 1993–1995 are smaller than the symbol size in some cases. The bands represent the result of the model-independent fit to all data, including the two most important common theoretical errors from initial-state photon radiation and from the [calculations](#) of the small-angle Bhabha cross-section.

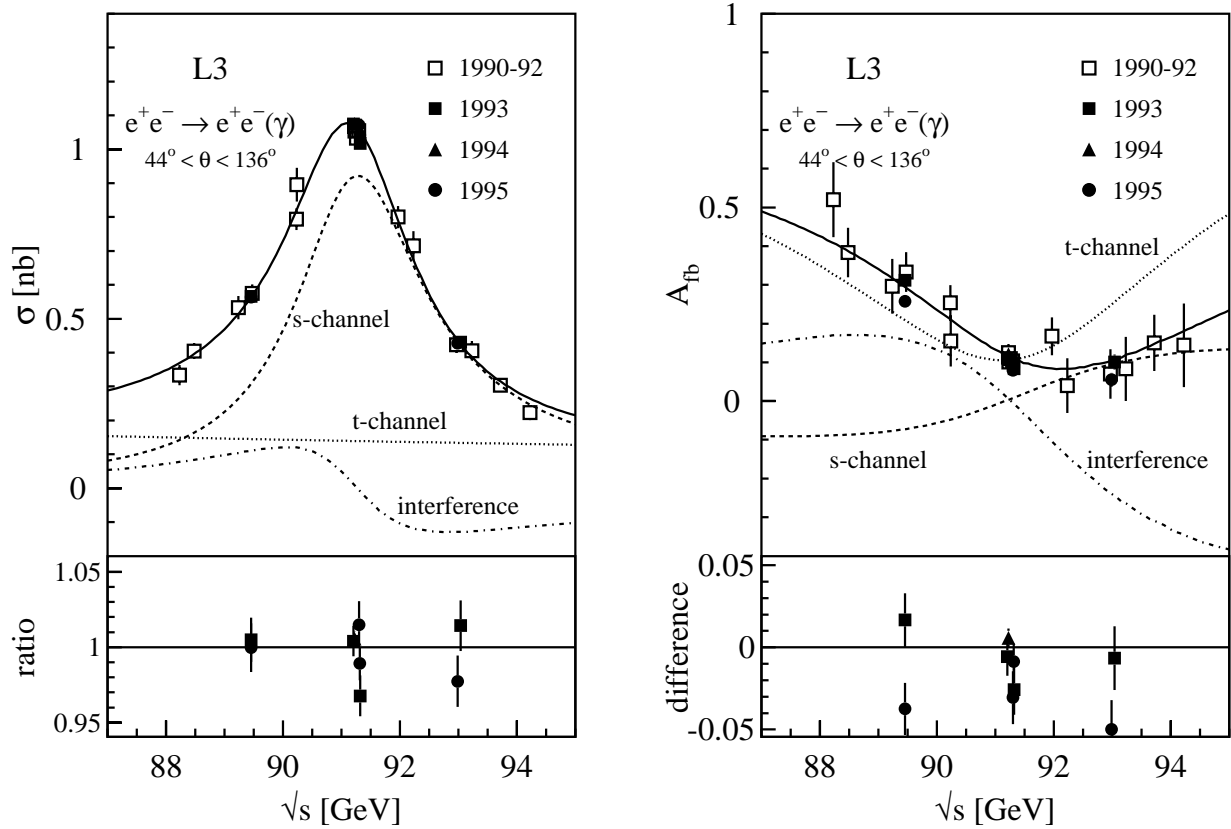


Figure 2.4: The energy dependence and the contributions from the  $s$  and  $t$ -channel diagrams and from the  $s$ - $t$  interference for observables in the  $e^+e^-$  channel. Shown are the total cross-section (left) and the difference between the forward and backward cross-sections after normalisation to the total cross section (right). The data points measured by the L3 collaboration refer to an angular acceptance of  $|\cos \theta| < 0.72$ , an acollinearity  $\xi < 25^\circ$  and a minimum energy of 1 GeV. The lines represent the model-independent fit to all L3 data.

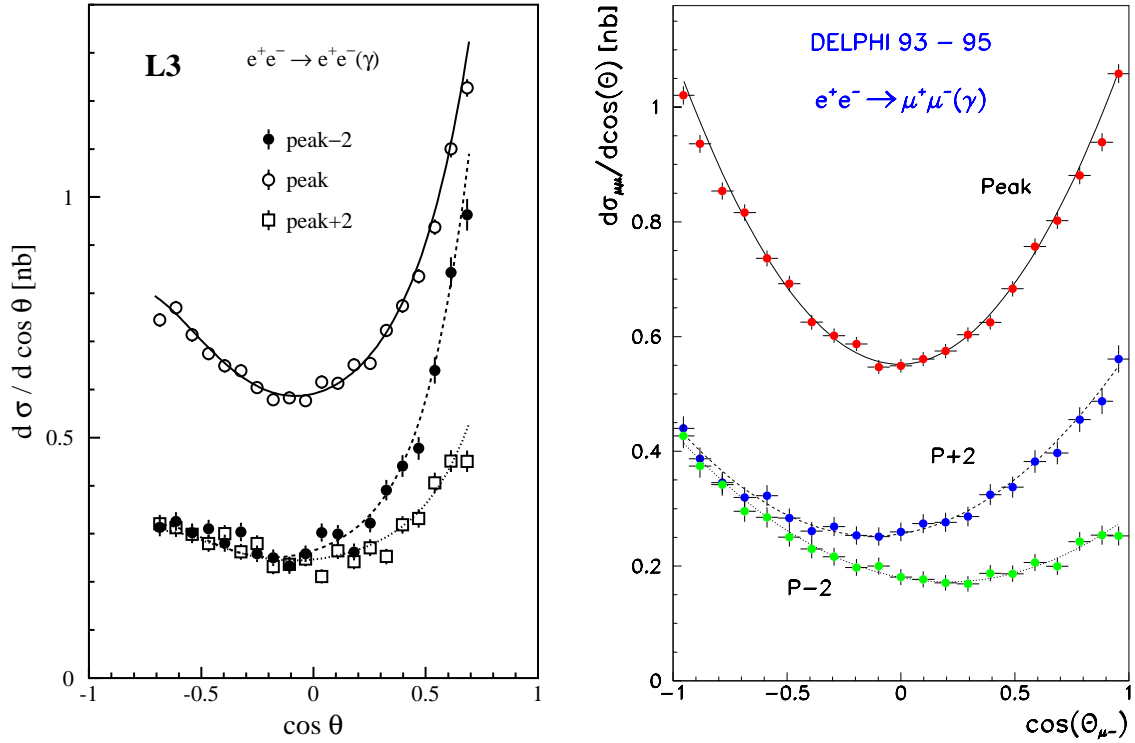


Figure 2.5: Distribution of the production polar angle,  $\cos\theta$ , for  $e^+e^-$  and  $\mu^+\mu^-$  events at the three principal energies during the years 1993–1995, measured in the L3 (left) and DELPHI (right) detectors, respectively. The curves show the Standard Model prediction from ALIBABA for  $e^+e^-$  and a fit to the data for  $\mu^+\mu^-$  assuming the lowest-order functional form of the differential cross-section given in the text.

those in the hadronic channel by at least a factor of  $\sqrt{2}$ .

Errors arising from limitations in theoretical precision, such as the calculation of the small-angle Bhabha cross-section, the  $t$ -channel contribution in the  $e^+e^-$  final state or pure QED corrections to the cross-section, are common to all experiments. They are discussed in detail in Section 2.3.

### 2.1.5 Energy calibration

Precise knowledge of the centre-of-mass energy is essential for the determination of the mass and width of the  $Z$  resonance. The uncertainty in the absolute energy scale, *i. e.* uncertainties correlated between the energy points, directly affect the mass, whereas the  $Z$  width is only influenced by the error in the difference in energy between energy points. The determination of the mass and width are completely dominated by the high-statistics scans taken at the  $\text{peak}\pm 2$  points in 1993 and 1995 and the errors are therefore approximately given by

$$\begin{aligned} \Delta m_Z &\approx 0.5 \cdot \Delta(E_{+2} + E_{-2}) \text{ and} \\ \Delta \Gamma_Z &\approx \frac{\Gamma_Z}{E_{+2} - E_{-2}} \Delta(E_{+2} - E_{-2}). \end{aligned} \quad (2.1)$$



	ALEPH			DELPHI		
	'93	'94	'95	'93	'94	'95
$\mathcal{L}^{\text{exp.}}$	0.067%	0.073%	0.080%	0.24%	0.09%	0.09%
$\sigma_{\text{had}}$	0.069%	0.072%	0.073%	0.10%	0.11%	0.10%
$\sigma_e$	0.15%	0.13%	0.15%	0.46%	0.52%	0.52%
$\sigma_\mu$	0.11%	0.09%	0.11%	0.28%	0.26%	0.28%
$\sigma_\tau$	0.26%	0.18%	0.25%	0.60%	0.60%	0.60%
$A_{\text{FB}}^e$	0.0006	0.0006	0.0006	0.0026	0.0021	0.0020
$A_{\text{FB}}^\mu$	0.0005	0.0005	0.0005	0.0009	0.0005	0.0010
$A_{\text{FB}}^\tau$	0.0009	0.0007	0.0009	0.0020	0.0020	0.0020

	L3			OPAL		
	'93	'94	'95	'93	'94	'95
$\mathcal{L}^{\text{exp.}}$	0.086%	0.064%	0.068%	0.033%	0.033%	0.034%
$\sigma_{\text{had}}$	0.042%	0.041%	0.042%	0.073%	0.073%	0.085%
$\sigma_e$	0.24%	0.17%	0.28%	0.17%	0.14%	0.16%
$\sigma_\mu$	0.32%	0.31%	0.40%	0.16%	0.10%	0.12%
$\sigma_\tau$	0.68%	0.65%	0.76%	0.49%	0.42%	0.48%
$A_{\text{FB}}^e$	0.0025	0.0025	0.0025	0.001	0.001	0.001
$A_{\text{FB}}^\mu$	0.0008	0.0008	0.0015	0.0007	0.0004	0.0009
$A_{\text{FB}}^\tau$	0.0032	0.0032	0.0032	0.0012	0.0012	0.0012

Table 2.2: Experimental systematic errors for the Z analyses at the Z peak. The errors are relative for the cross-sections and absolute for the forward-backward asymmetries. None of the common errors discussed in Section 2.3 are included here.

The average momentum of particles circulating in a storage ring is proportional to the magnetic bending field integrated over the path of the particles. The very accurate determination of the average energy of the beams in LEP was based on the technique of resonant spin depolarisation [39,40], which became available in 1991, after transverse polarisation of the electron beam in LEP had first been observed in 1990 [41] with a Compton polarimeter [42]. Transverse polarisation of the beams in LEP occurs after a careful adjustment of the beam orbit in order to avoid any static depolarising resonances, with single or separated beams. The same magnetic bending field seen by the particles along their path leads to precession of the average spin vector of the polarised bunches. The beam energy is proportional to the number of spin precessions per turn, the “spin tune”  $\nu$ . The spin precession frequency is measured by observing the depolarisation which occurs when an artificial spin resonance is excited with the help of a weak oscillating radial magnetic field. This method offers a very high precision as good as  $\pm 0.2$  MeV on the beam energy at the time of the measurement. The resolution of the method is illustrated in Figure 2.6, which shows the observed drop in polarisation as a function of the fractional tune of the oscillating depolarising magnetic field.

Measurements with resonant depolarisation were only possible outside normal data taking, typically at the end of fills. About 40% of the recorded off-peak luminosity in the 1993 scan and about 70% in the 1995 scan was taken during fills with at least one such precise calibration of the beam energy. Other techniques had to be employed to trace this back to earlier times in a fill and to those fills where no calibrations by resonant depolarisation could be made. This required precise knowledge of the values and time evolutions of numerous parameters and careful modeling of their impacts on the beam energy [15–18].

For particles on central orbit the magnetic bending field is given by the field produced by the bending dipoles and corrector magnets and by small contributions from the Earth’s magnetic field and from remnant fields in the beam pipe. In addition, magnetic fields originating from leakage currents produced by trains in the Geneva area must be taken into account. The magnetic field of the dipoles was measured with a nuclear magnetic resonance probe (“NMR”) in a reference dipole on the surface. In 1995, two NMR probes were installed in two of the tunnel dipoles, which measured the magnetic field directly above the beam pipe.

Contributions from the quadrupoles and sextupoles also must be considered for non-central orbits, which arise from geological deformations of the LEP tunnel. Among the identified origins of such deformations were tidal effects from the Sun and the Moon, the water level in the Geneva Lake and rain fall in the Jura Mountains. These could all be tracked by frequent and precise measurements of the beam orbit position inside the LEP beam pipe.

In order to obtain the energy of the particles colliding at an interaction point (“IP”), additional effects from the radio frequency system (“RF”) and from a possible energy-dependence of the distribution of particle positions in a bunch, so-called “dispersion effects”, had to be considered. For each experiment a value of the beam energy was provided every 15 minutes. These values were determined from a model taking into account the time evolutions of the effects mentioned above. Errors on the centre-of-mass energy are largely dominated by the uncertainties in this model. A summary of the error contributions and an indication of the typical size of the effects is shown in Table 2.3.

The energy errors vary slightly among the interaction points, mainly due to different configurations of the radio frequency cavities. The energy errors for different experiments and data taking periods have large common parts, and therefore the use of a full correlation matrix is necessary. Assuming that all experiments contribute with the same weight allows all the LEP energy errors to be conveniently summarised in a single error matrix, common to all interaction

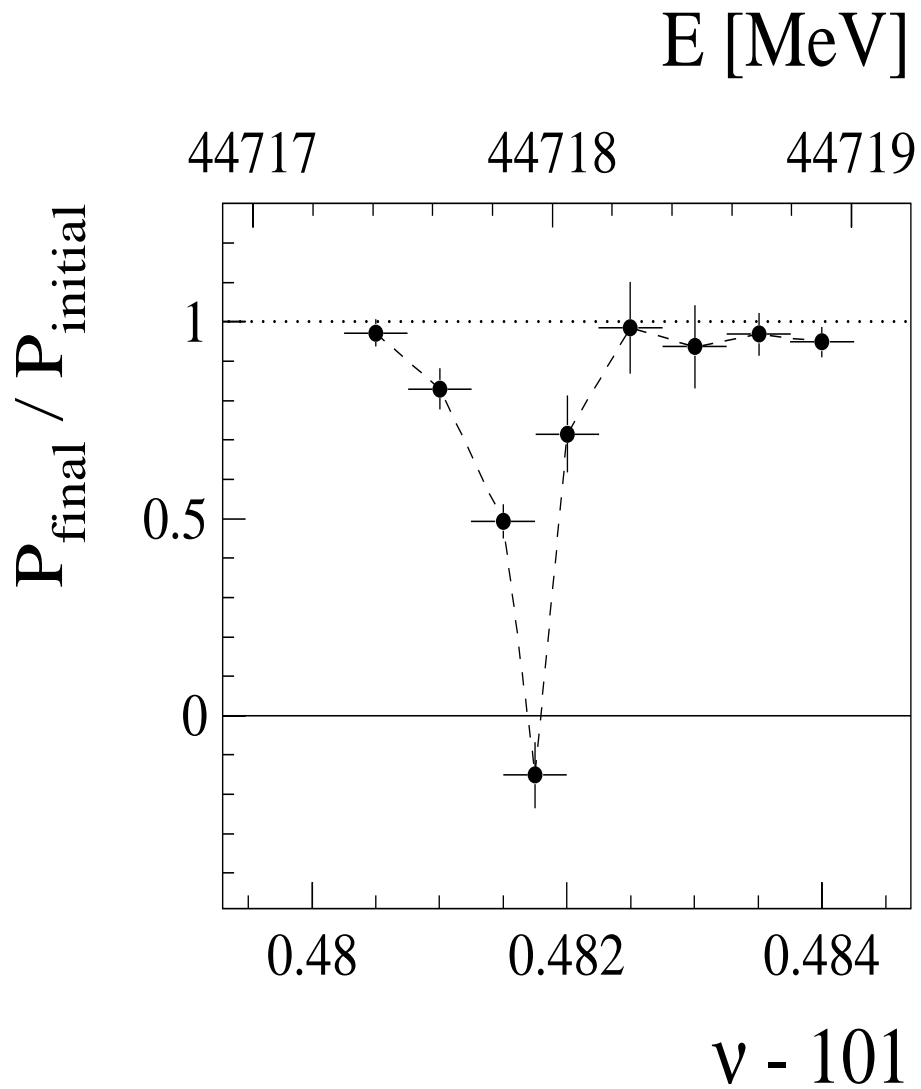


Figure 2.6: Measurement of the width of the artificially excited spin resonance which is used for the energy calibration of LEP (from Reference 40).

origin of correction	contribution to $E_{CM}$		$\Delta m_Z$ [MeV]	$\Delta \Gamma_Z$ [MeV]
	size [MeV]	error [MeV]		
energy measurement by resonant depolarisation		0.5	0.4	0.5
mean fill energy, from uncalibrated fills		[0.5–5.0]	0.5	0.8
dipole field changes	up to 20	[1.3–3.3]	1.7	0.6
tidal deformations	$\pm 10$	[0.0–0.3]	0.0	0.1
$e^+$ energy difference	$< 0.3$	0.3	0.2	0.1
bending field from horizontal correctors	[0–2]	[0.0–0.5]	0.2	0.1
IP dependent RF corrections	[0–20]	[0.5–0.7]	0.4	0.2
dispersion at IPs	0.5	[0.4–0.7]	0.2	0.1

Table 2.3: Breakdown of effects on the centre-of-mass energy, for illustrative purpose only. The last two columns give the approximate contribution of each effect to the error on  $m_Z$  and  $\Gamma_Z$ . The full evaluation of the energy errors used values specific to each year and energy and also took into account their correlations. (See Reference 18 for a complete discussion.)

points, as given in Reference 18. Details on the energy calibration for the earlier years can be found in References 15–17.

The energy of individual beam particles is usually not at the mean value considered above, but oscillates around the mean energy. Therefore observables are not measured at a sharp energy,  $E_{cm}^0$ , but instead their values are averaged over a range in energies  $E_{cm}^0 \pm \delta E_{cm}$ . With the assumption of a Gaussian shape of the energy distribution, the total cross-sections receive a correction proportional to  $\delta E_{cm}^2$  and the second derivative of  $\sigma(E_{cm})$  w.r.t.  $E_{cm}$ . At LEP-I, typical values of the centre-of-mass energy spread are around 50 MeV. The effects of the correction lead to an increase of the cross-section at the peak of the  $Z$  resonance by 0.16% and a decrease of the width by about 5 MeV. The uncertainties on the energy spread, around  $\pm 1$  MeV in 1993–1995, constitute a negligible source of error common to all experiments.

In addition to the natural energy spread, changes in the mean beam energy due to changes of machine parameters have a similar effect. Data taking periods with a very similar centre-of-mass energy were combined into a single energy point in the experimental analyses by performing a luminosity-weighted average. The additional energy spread resulting from this was only around 10 MeV, which is added in quadrature to the natural beam energy spread of the accelerator.

Uncertainties from the energy calibration as described in this sub-section and corrections for the beam energy spread were taken into account by all experiments in the fits from which the  $Z$  parameters were extracted; the related common uncertainties are discussed in Section 2.3.1.

## 2.2 Experimental results

Each experiment performed fits [22–25] to their measured cross-sections and forward-backward asymmetries in order to extract the common set of parameters used for the largely model-independent parametrisation of the differential cross-section described in the introduction. The results presented here deviate slightly from those published by the experiments in order to facilitate the combination procedure. The four dedicated sets of fit results for the combination are summarised in Table 2.4.

All fits are based on versions 6.23 of ZFITTER and 4.4 of TOPAZ0. The published ALEPH

		correlations								
		$m_Z$	$\Gamma_Z$	$\sigma_h^0$	$R_e^0$	$R_\mu^0$	$R_\tau^0$	$A_{\text{FB}}^{0,e}$	$A_{\text{FB}}^{0,\mu}$	$A_{\text{FB}}^{0,\tau}$
$\chi^2/N_{\text{df}} = 169/176$		ALEPH								
$m_Z$ [GeV]	$91.1891 \pm 0.0031$	1.00								
$\Gamma_Z$ [GeV]	$2.4959 \pm 0.0043$	.038	1.00							
$\sigma_h^0$ [nb]	$41.558 \pm 0.057$	-.091	-.383	1.00						
$R_e^0$	$20.690 \pm 0.075$	.102	.004	.134	1.00					
$R_\mu^0$	$20.801 \pm 0.056$	-.003	.012	.167	.083	1.00				
$R_\tau^0$	$20.708 \pm 0.062$	-.003	.004	.152	.067	.093	1.00			
$A_{\text{FB}}^{0,e}$	$0.0184 \pm 0.0034$	-.047	.000	-.003	-.388	.000	.000	1.00		
$A_{\text{FB}}^{0,\mu}$	$0.0172 \pm 0.0024$	.072	.002	.002	.019	.013	.000	-.008	1.00	
$A_{\text{FB}}^{0,\tau}$	$0.0170 \pm 0.0028$	.061	.002	.002	.017	.000	.011	-.007	.016	1.00
$\chi^2/N_{\text{df}} = 177/168$		DELPHI								
$m_Z$ [GeV]	$91.1864 \pm 0.0028$	1.00								
$\Gamma_Z$ [GeV]	$2.4876 \pm 0.0041$	.047	1.00							
$\sigma_h^0$ [nb]	$41.578 \pm 0.069$	-.070	-.270	1.00						
$R_e^0$	$20.88 \pm 0.12$	.063	.000	.120	1.00					
$R_\mu^0$	$20.650 \pm 0.076$	-.003	-.007	.191	.054	1.00				
$R_\tau^0$	$20.84 \pm 0.13$	.001	-.001	.113	.033	.051	1.00			
$A_{\text{FB}}^{0,e}$	$0.0171 \pm 0.0049$	.057	.001	-.006	-.106	.000	-.001	1.00		
$A_{\text{FB}}^{0,\mu}$	$0.0165 \pm 0.0025$	.064	.006	-.002	.025	.008	.000	-.016	1.00	
$A_{\text{FB}}^{0,\tau}$	$0.0241 \pm 0.0037$	.043	.003	-.002	.015	.000	.012	-.015	.014	1.00
$\chi^2/N_{\text{df}} = 158/166$		L3								
$m_Z$ [GeV]	$91.1897 \pm 0.0030$	1.00								
$\Gamma_Z$ [GeV]	$2.5025 \pm 0.0041$	.065	1.00							
$\sigma_h^0$ [nb]	$41.535 \pm 0.054$	.009	-.343	1.00						
$R_e^0$	$20.815 \pm 0.089$	.108	-.007	.075	1.00					
$R_\mu^0$	$20.861 \pm 0.097$	-.001	.002	.077	.030	1.00				
$R_\tau^0$	$20.79 \pm 0.13$	.002	.005	.053	.024	.020	1.00			
$A_{\text{FB}}^{0,e}$	$0.0107 \pm 0.0058$	-.045	.055	-.006	-.146	-.001	-.003	1.00		
$A_{\text{FB}}^{0,\mu}$	$0.0188 \pm 0.0033$	.052	.004	.005	.017	.005	.000	.011	1.00	
$A_{\text{FB}}^{0,\tau}$	$0.0260 \pm 0.0047$	.034	.004	.003	.012	.000	.007	-.008	.006	1.00
$\chi^2/N_{\text{df}} = 155/194$		OPAL								
$m_Z$ [GeV]	$91.1858 \pm 0.0030$	1.00								
$\Gamma_Z$ [GeV]	$2.4948 \pm 0.0041$	.049	1.00							
$\sigma_h^0$ [nb]	$41.501 \pm 0.055$	.031	-.352	1.00						
$R_e^0$	$20.901 \pm 0.084$	.108	.011	.155	1.00					
$R_\mu^0$	$20.811 \pm 0.058$	.001	.020	.222	.093	1.00				
$R_\tau^0$	$20.832 \pm 0.091$	.001	.013	.137	.039	.051	1.00			
$A_{\text{FB}}^{0,e}$	$0.0089 \pm 0.0045$	-.053	-.005	.011	-.222	-.001	.005	1.00		
$A_{\text{FB}}^{0,\mu}$	$0.0159 \pm 0.0023$	.077	-.002	.011	.031	.018	.004	-.012	1.00	
$A_{\text{FB}}^{0,\tau}$	$0.0145 \pm 0.0030$	.059	-.003	.003	.015	-.010	.007	-.010	.013	1.00

Table 2.4: Results on Z parameters and their correlation coefficients.

results were derived using vers. 6.10 of ZFITTER, which did not yet contain the improved treatment of fermion pairs radiated from the initial state [43]. For the combination presented here, the ALEPH measurements were reanalysed using version 6.23 of ZFITTER, leading to small changes at the level of a few tenths of  $MeV$  in  $m_Z$  and  $\Gamma_Z$ .

Each experiment used the combined energy error matrix described above. This makes a small difference at the level of  $0.1 MeV$  on  $m_Z$  and  $\Gamma_Z$  and their errors only for L3, where uncertainties arising from the modelling of the radio frequency cavities are largest.

The  $s$ - $t$  interference in the Bhabha final state has a small dependence on the value of the  $Z$  mass. Although this is practically negligible for a single experiment, a consistent treatment becomes important for the combination. Despite some different choices in the publications of the individual analyses, all experiments evaluate the  $t$ , $s$ - $t$  channel correction at their own value of the  $Z$  mass for the results presented here. The resulting interdependencies between the  $Z$  mass and the parameters from the Bhabha final state are explicitly included in the error correlation coefficients between  $m_Z$  and  $R_e^0$  or  $A_{FB}^{0,e}$ .

The LEP experiments agreed to use a standard set of parameters used for the calculation of the Standard Model remnants in the theory programs. The important parameters are the  $Z$  mass,  $m_Z = 91.187 GeV$ , the Fermi constant,  $G_F = 1.16637 \times 10^{-5} GeV^{-2}$ , the electromagnetic coupling constant,  $\alpha^{(5)}(m_Z) = 1/128.877^*$ , the strong coupling constant,  $\alpha_s(m_Z) = 0.119$ , the top quark mass,  $m_t = 175 GeV$ , and finally the Higgs mass,  $m_H = 150 GeV$ . The dependence of the fit results arising from uncertainties in these parameters is negligible except for  $m_H$ , as is discussed in Section 2.3.4.

All experiments also provide fits to their measured cross-sections and asymmetries with lepton universality imposed, *i.e.*  $R_e^0$ ,  $R_\mu^0$  and  $R_\tau^0$  are replaced by  $R_\ell^0$  and  $A_{FB}^{0,e}$ ,  $A_{FB}^{0,\mu}$  and  $A_{FB}^{0,\tau}$  get replaced by  $A_{FB}^{0,\ell}$  in the model-independent parametrisation of the differential cross-section. Here  $R_\ell^0$  is defined for massless leptons. The individual experimental results and the correlation matrices are given in Table 2.5. A graphical overview of the results is given in Figure 2.7; the averages are those discussed in Section 2.4 below.

Comparing with the nine-parameter results of Table 2.4, there is a noticeable change in  $m_Z$  of a few tenth of  $MeV$  in all experiments. This is a consequence of the dependence of the  $t$ -channel correction on  $m_Z$ , as discussed in Section 2.3.2. When  $R_e^0$  and  $A_{FB}^{0,e}$  are replaced by the leptonic quantities  $R_\ell^0$  and  $A_{FB}^{0,\ell}$ , their correlation with the  $Z$  mass leads to a shift, which is driven by the (statistical) difference between  $R_e^0$  and  $R_\ell^0$  and  $A_{FB}^{0,e}$  and  $A_{FB}^{0,\ell}$ . Similarly, replacing  $R_e^0$  and  $A_{FB}^{0,e}$  from the values of a single experiment by the LEP average introduces a shift in  $m_Z$  in the presence of these particular correlation coefficients. Such shifts should become smaller when averaged over the four experiments. Indeed, the average of the shifts is only  $-0.2 MeV$ .

## 2.3 Common uncertainties

Important common errors among the results from all LEP experiments arise from several sources. These include the calibration of the beam energy, the theoretical error on the calculation of the small-angle Bhabha cross-section used as the normalisation reaction, the theoretical uncertainties in the  $t$ -channel and  $s$ - $t$  interference contribution to the differential large-angle Bhabha cross-section, the theoretical uncertainties in the calculations of QED radiative effects

---

\* $\alpha^{(5)}(m_Z)$  is the electromagnetic coupling constant at the scale of the  $Z$  mass for five quark flavours; the value and error given correspond to a value of the correction due to hadronic vacuum polarisation of  $\Delta\alpha_{had}^{(5)} = 0.02804 \pm 0.00065$ .

		correlations				
		$m_Z$	$\Gamma_Z$	$\sigma_h^0$	$R_\ell^0$	$A_{\text{FB}}^{0,\ell}$
$\chi^2/N_{\text{df}} = 172/180$		ALEPH				
$m_Z$ [GeV]	$91.1893 \pm 0.0031$	1.00				
$\Gamma_Z$ [GeV]	$2.4959 \pm 0.0043$	.038	1.00			
$\sigma_h^0$ [nb]	$41.559 \pm 0.057$	-.092	-.383	1.00		
$R_\ell^0$	$20.729 \pm 0.039$	.033	.011	.246	1.00	
$A_{\text{FB}}^{0,\ell}$	$0.0173 \pm 0.0016$	.071	.002	.001	-.076	1.00
$\chi^2/N_{\text{df}} = 183/172$		DELPHI				
$m_Z$ [GeV]	$91.1863 \pm 0.0028$	1.00				
$\Gamma_Z$ [GeV]	$2.4876 \pm 0.0041$	.046	1.00			
$\sigma_h^0$ [nb]	$41.578 \pm 0.069$	-.070	-.270	1.00		
$R_\ell^0$	$20.730 \pm 0.060$	.028	-.006	.242	1.00	
$A_{\text{FB}}^{0,\ell}$	$0.0187 \pm 0.0019$	.095	.006	-.005	.000	1.00
$\chi^2/N_{\text{df}} = 163/170$		L3				
$m_Z$ [GeV]	$91.1894 \pm 0.0030$	1.00				
$\Gamma_Z$ [GeV]	$2.5025 \pm 0.0041$	.068	1.00			
$\sigma_h^0$ [nb]	$41.536 \pm 0.055$	.014	-.348	1.00		
$R_\ell^0$	$20.809 \pm 0.060$	.067	.020	.111	1.00	
$A_{\text{FB}}^{0,\ell}$	$0.0192 \pm 0.0024$	.041	.020	.005	-.024	1.00
$\chi^2/N_{\text{df}} = 158/198$		OPAL				
$m_Z$ [GeV]	$91.1853 \pm 0.0029$	1.00				
$\Gamma_Z$ [GeV]	$2.4947 \pm 0.0041$	.051	1.00			
$\sigma_h^0$ [nb]	$41.502 \pm 0.055$	.030	-.352	1.00		
$R_\ell^0$	$20.822 \pm 0.044$	.043	.024	.290	1.00	
$A_{\text{FB}}^{0,\ell}$	$0.0145 \pm 0.0017$	.075	-.005	.013	-.017	1.00

Table 2.5: Results on Z parameters and error correlation matrices by the four experiments with lepton universality imposed.

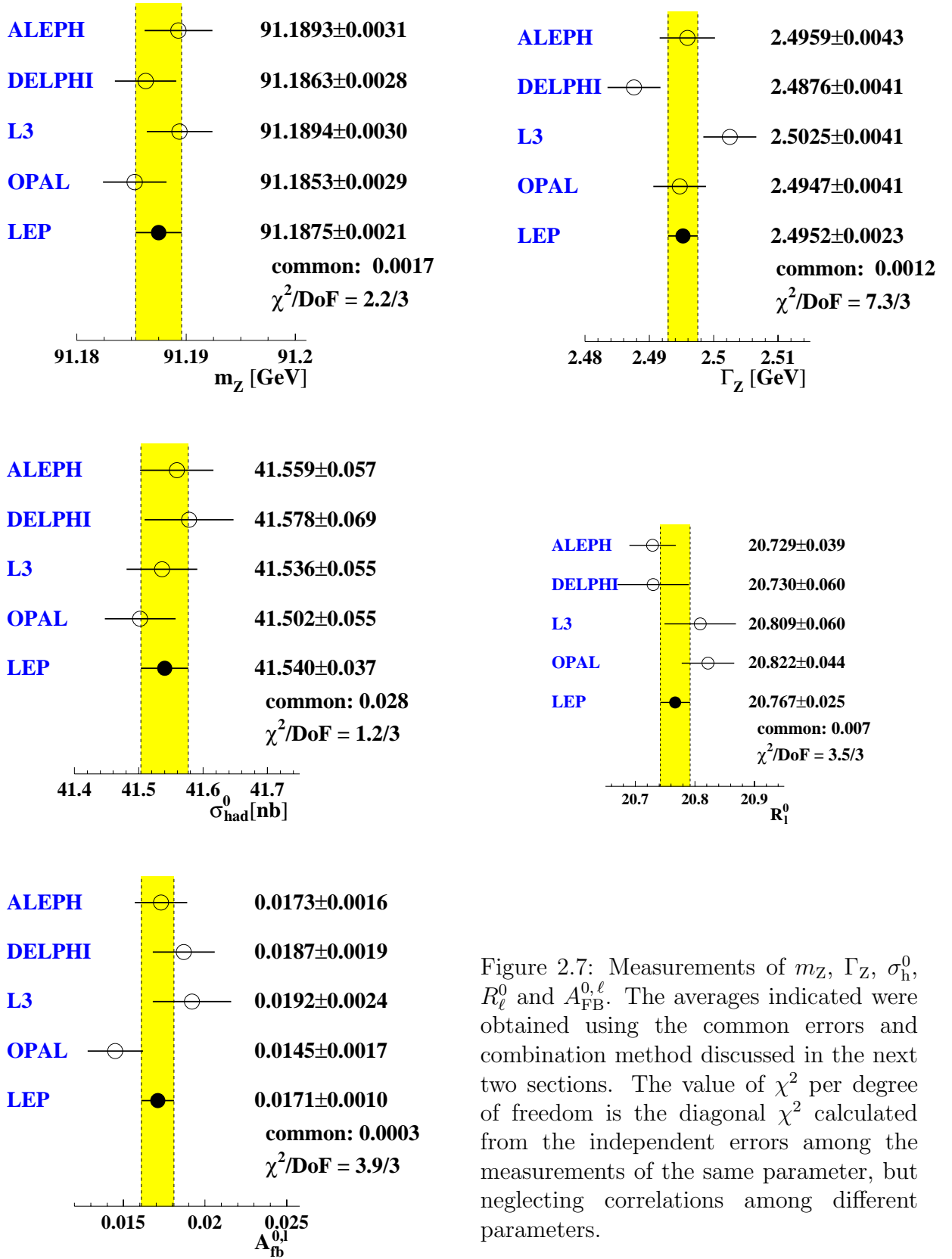


Figure 2.7: Measurements of  $m_Z$ ,  $\Gamma_Z$ ,  $\sigma_{\text{had}}^0$ ,  $R_\ell^0$  and  $A_{\text{FB}}^{0,\ell}$ . The averages indicated were obtained using the common errors and combination method discussed in the next two sections. The value of  $\chi^2$  per degree of freedom is the diagonal  $\chi^2$  calculated from the independent errors among the measurements of the same parameter, but neglecting correlations among different parameters.



	$m_Z$	$\Gamma_Z$	$\sigma_h^0$	$R_e^0$		$A_{\text{FB}}^{0,e}$	$A_{\text{FB}}^{0,\mu}$	$A_{\text{FB}}^{0,\tau}$
$m_Z$ [GeV]	0.0017				$A_{\text{FB}}^{0,e}$	0.0004		
$\Gamma_Z$ [GeV]	-0.0006	0.0012			$A_{\text{FB}}^{0,\mu}$	-0.0003	0.0003	
$\sigma_h^0$ [nb]	-0.0018	-0.0027	0.011		$A_{\text{FB}}^{0,\tau}$	-0.0003	0.0003	0.0003
$R_e^0$	0.0017	-0.0014	0.0073	0.013				

Table 2.6: Common energy errors for nine-parameter fits. Values are given as the signed square root of the covariance matrix elements; elements above the diagonal have been omitted for simplicity. The anti-correlation between electron and muon or tau asymmetries arises from the different energy dependence of the electron asymmetry due to the  $t$ -channel contribution.

and, finally, from small uncertainties in the parametrisation of the electroweak cross-section near the Z resonance in terms of the standard set of pseudo-observables. These common errors are quantified below and are used in the combination.

Other sources of common errors may arise from the use of common Monte Carlo generators and detector simulation programs. However, each experiment uses its own tuning procedures and event selections which best suit their detector, and therefore the related errors are treated as uncorrelated among the experiments.

### 2.3.1 Common energy uncertainties

For the purpose of combining the experimental results at the parameter level, the errors on the centre-of-mass energy of each individual cross-section or asymmetry measurement need to be transformed into errors on the extracted pseudo-observables. Special fits have been performed by each experiment to achieve this. The first step is to scale the energy errors by factors of  $1 \pm \epsilon$ , while maintaining the experimental errors fixed. Typical values of  $\epsilon$  used are between 5% and 20%. Performing the standard fits with these scaled errors generates two pseudo-observable covariance matrices,  $V_{\pm}$ , from which the covariance matrix due to energy errors,  $V_E$ , can be separated from the other errors,  $V_{\text{exp}}$ , using the relation  $(V_{\pm}) = (1 \pm \epsilon)^2(V_E) + (V_{\text{exp}})$ . The validity of this procedure was verified using a data set restricted to the hadronic cross-section measurements of the years 1993–1995, which were combined both at the cross-section level and at the parameter level.

The estimated energy errors differ slightly depending on which experimental data set is used to derive them. Combinations may be attempted based on each of them, or on the average. The central values and errors of each of the averaged parameters agree to well within 5% of the error on that average. It is therefore most appropriate to take the average of the error estimates over the experiments as the common energy errors, which are shown in Table 2.6.

### 2.3.2 Common $t$ -channel uncertainties

The  $t$  channel and  $s$ - $t$  interference contributions are calculated in the Standard Model using the program ALIBABA [33]. The theoretical uncertainty on the  $t$ -channel correction is discussed in detail in Reference 44. The size of the uncertainty is typically 1.1 pb for the forward cross-section and 0.3 pb for the backward cross-section and depends slightly on the acceptance cuts [45]. All collaborations incorporate the theory uncertainty as an additional error on the electron pair cross-section and asymmetry. In order to evaluate the common error due to the

	$R_e^0$	$A_{\text{FB}}^{0,e}$
$R_e^0$	0.024	
$A_{\text{FB}}^{0,e}$	-0.0054	0.0014

Table 2.7: Common uncertainties arising from the  $t$  channel and  $s$ - $t$  interference contribution to the  $e^+e^-$  final states, given as the signed square root of the covariance matrix elements.

$t$ ,  $s$ - $t$  theory error, each collaboration performed two fits, with and without the theory error, and the quadratic differences of the covariance matrix elements for  $R_e^0$  and  $A_{\text{FB}}^{0,e}$  are taken as an estimate of the common error. The unknown error correlation between energy points below and above the peak are included in the error estimates by adding in quadrature the observed shifts in mean values of  $R_e^0$  and  $A_{\text{FB}}^{0,e}$  when varying these correlations between  $-1$  and  $+1$ . The  $t$ ,  $s$ - $t$  related errors estimated by individual experiments are all very similar, and therefore the average is taken as the common error matrix, as shown in Table 2.7.

The  $s$ - $t$  interference contribution to the  $t$ -channel correction in Bhabha final states depends on the value of the  $Z$  mass. For the purpose of this combination, all experiments parametrise the  $t$  and  $s$ - $t$  contributions as a function of  $m_Z$ . This allows the  $t$ ,  $s$ - $t$  correction to follow the determination of  $m_Z$  in the fits, which results in a correlation between  $m_Z$  and  $R_e^0$  or  $A_{\text{FB}}^{0,e}$ . The change in correlation coefficients introduced by explicitly taking into account in the fits the  $m_Z$  dependence of the  $t$ -channel is about  $+10\%$  for the correlation  $m_Z$ - $R_e^0$  and  $-10\%$  for  $m_Z$ - $A_{\text{FB}}^{0,e}$ . These correlation coefficients properly take into account the changes in  $R_e^0$  and  $A_{\text{FB}}^{0,e}$  when  $m_Z$  takes its average value in the combination of the four experiments.

### 2.3.3 Common luminosity uncertainties

The four collaborations use similar techniques to measure the luminosity of their data samples by counting the number of small-angle Bhabha scattered electrons. The experimental details of the four measurements differ sufficiently that no correlation is believed to exist in the experimental component of the luminosity errors. All four collaborations, however, use BHLUMI 4.04 [36], the best available Monte Carlo generator of small-angle Bhabha scattering, to calculate the acceptance of their luminosity counters. Therefore significant correlations exist in the errors assigned to the scale of the measured cross-sections due to the uncertainty in this common theoretical calculation.

This uncertainty is estimated to be  $0.061\%$  [46] without applying a correction for the production of light fermion pairs, which are not calculated in BHLUMI, and enter as a contribution to the estimated error. A recent calculation of the contribution of light pairs [47] has allowed OPAL to explicitly correct for light pairs and reduce its theoretical luminosity uncertainty to  $0.054\%$ . This  $0.054\%$  error is taken to be correlated with the errors of the other three experiments, which among themselves share a mutual correlated error of  $0.061\%$ .

These errors almost exclusively affect the hadronic pole cross-section, and contribute about half its total error after combination. The common luminosity error also introduces a small contribution to the covariance matrix element between  $\Gamma_Z$  and  $\sigma_h^0$ . This was neglected in the common error tables given above, as it had no noticeable effect on the combined result.

### 2.3.4 Common theory uncertainties

An additional class of common theoretical errors arises from the approximations and special choices made in the fitting codes. These comprise contributions from QED radiative corrections, including initial-state pair radiation, and the parametrisation of the differential cross-section around the Z resonance in terms of pseudo-observables defined precisely at the peak and for pure Z exchange only. In order to estimate the uncertainties from the parametrisation of the electroweak cross-sections near the Z resonance the two most advanced calculational tools, ZFITTER [20], and TOPAZ0 [19] were compared. In addition, there are “parametric uncertainties” arising from parameters of the Standard Model that are needed to fix the Standard Model remnants.

#### QED uncertainties

The effects of initial state radiation (ISR) and the radiation of fermion pairs (ISPP) lead to large corrections in the vicinity of the Z resonance and therefore play a central role in the extraction of the pseudo-observables from the measured cross-sections and asymmetries. Such large radiative effects have to be seen in contrast to the experimental precision, which is below the per-mil level in the case of the hadronic cross-section.

The most up-to-date evaluations of photonic corrections to the measurements are complete in  $\mathcal{O}(\alpha^2)$  and for the total cross-sections also include the leading contributions up to  $\mathcal{O}(\alpha^3)$ . Two different schemes are available to estimate the remaining uncertainties:

1. KF:  $\mathcal{O}(\dots \alpha^2 L^2, \alpha^2 L, \alpha^2 L^0)$  calculations [48] including the exponentiation scheme of Kuraev-Fadin [49] with  $\mathcal{O}(\alpha^3 L^3)$  [50].<sup>†</sup>
2. YFS: the 2<sup>nd</sup> order inclusive exponentiation scheme of Reference 51, 52, based on the YFS approach [53]. Third order terms are also known and have only a small effect [54].

Differences between these schemes, which are both implemented in ZFITTER, TOPAZ0 and MIZA [55], and uncertainties due to missing higher order corrections [54], amount to at most  $\pm 0.1$  MeV on  $m_Z$  and  $\Gamma_Z$ , and  $\pm 0.01\%$  on  $\sigma_h^0$ .

The influence of the interference between initial and final state radiation on the extracted parameters has also been studied recently [56], and uncertainties on  $m_Z$  of at most  $\pm 0.1$  MeV from this source are expected for the experimental results given with only a small cut on  $s'$ , the effective squared centre-of-mass energy after photon radiation from the initial state. The uncertainties due to the extrapolation of the leptonic  $s$ -channel cross-sections to full angular acceptance and from large to small  $s'$  differ among the experiments and are believed to be largely uncorrelated.

QED related uncertainties are dominated by the radiation of fermion pairs from the initial state. Starting from the full second order pair radiator [48, 57], a simultaneous exponentiation scheme for radiated photons and pairs was proposed in Reference [58]. A third-order pair radiator was calculated recently [43] and compared with the other existing schemes, which are all available in the latest version of ZFITTER. Independent implementations of some schemes exist in TOPAZ0 and in MIZA. The largest uncertainty arises from the contribution of hadronic pairs. The maximum differences are 0.3 MeV on  $m_Z$ , 0.2 MeV on  $\Gamma_Z$  and 0.015% on  $\sigma_h^0$ .

In summary, comparing the different options for photonic and fermion pair radiation leads to error estimates of  $\pm 0.3$  MeV on  $m_Z$  and  $\pm 0.2$  MeV on  $\Gamma_Z$ . The observed differences in  $\sigma_h^0$  are

<sup>†</sup>Third-order terms for the KF scheme had also been calculated earlier [51].

$\Delta m_Z$ [GeV]	$\Delta \Gamma_Z$ [GeV]	$\Delta \sigma_h^0$ [nb]	$\Delta R_\ell^0$	$\Delta A_{\text{FB}}^{0,\ell}$
0.0001	0.0001	0.001	0.004	0.0001

Table 2.8: Differences in fit results obtained with TOPAZ0 and ZFITTER, taken as common systematic errors.

slightly smaller than the error estimate of  $\pm 0.02\%$  in Reference 54, which is therefore taken as the error for the QED-related uncertainties.

### Parametrisation of line shape and asymmetries

In a recent very detailed comparison of TOPAZ0 and ZFITTER [21], cross-sections from Standard Model calculations and from differing choices in the model-independent parametrisation were considered. Uncertainties on the pseudo-observables arise from the parametrisation of the electroweak cross-sections near the Z resonance. In order to determine the TOPAZ0-ZFITTER differences, each of the two codes has been used. For practical reasons, cross-sections and forward-backward asymmetries were calculated with TOPAZ0 and then fitted with ZFITTER. Errors were assigned to the calculated cross-sections and forward-backward asymmetries which reflected the integrated luminosity taken at each energy, thus ensuring that each energy point entered with the appropriate weight.

The dominant part of the small differences between the two codes results from details of the implementation of the cross-section parametrisation in terms of the pseudo-observables. This is particularly visible for the off-peak points, where the assignment of higher-order corrections to the Z resonance or to the Standard Model remnants is not in all cases unambiguous. The size of the differences also depends on the particular values of the pseudo-observables, since these do not necessarily respect the exact Standard Model relations. Slightly different choices are made in the two codes if the Standard Model relations between the pseudo-observables are not fulfilled. Finally, variations of factorisation schemes and other options in the electroweak calculations may affect the fit results through the Standard Model remnants, but were found to have a negligible effect.

In Table 2.8 differences between TOPAZ0 and ZFITTER are shown, which are taken as systematic uncertainties. They were evaluated around the set of pseudo-observables representing the average of the four experiments; cross-sections and asymmetries were calculated for full acceptance with only a cut on  $s' > 0.01 s$ . The only important systematic error of this kind is the one on  $R_\ell^0$ , which amounts to 15% of the combined error.

Putting all sources together, the overall theoretical errors as listed in Table 2.9 are obtained, and these are used in the combination.

### Parametric uncertainties

Through the Standard Model remnants the fit results depend slightly on the values of some Standard Model parameters. Varying these within their present experimental errors, or between 100 GeV and 1000 GeV in case of the Higgs boson mass, leads to observable effects only on the Z mass, which is affected through the  $\gamma$ -Z interference term. The dominant dependence is on  $m_H$ , followed by  $\alpha^{(5)}(m_Z)$ .

	$m_Z$	$\Gamma_Z$	$\sigma_h^0$	$R_e^0$	$R_\mu^0$	$R_\tau^0$	$A_{\text{FB}}^{0,e}$	$A_{\text{FB}}^{0,\mu}$	$A_{\text{FB}}^{0,\tau}$
$m_Z[\text{GeV}]$	0.0003								
$\Gamma_Z[\text{GeV}]$		0.0002							
$\sigma_h^0[\text{nb}]$			0.008						
$R_e^0$				0.004					
$R_\mu^0$				0.004	0.004				
$R_\tau^0$				0.004	0.004	0.004			
$A_{\text{FB}}^{0,e}$							0.0001		
$A_{\text{FB}}^{0,\mu}$							0.0001	0.0001	
$A_{\text{FB}}^{0,\tau}$							0.0001	0.0001	0.0001

Table 2.9: Theoretical errors from fit programs, i.e. photon and fermion-pair radiation and model-independent parametrisation, given as the signed square root of the covariance matrix elements.

The effect on  $m_Z$  from a variation of  $1/\alpha^{(5)}(m_Z)$  by its error of  $\pm 0.090$  is  $\mp 0.05$  MeV, which is negligibly small compared to the systematic error on  $m_Z$  arising from other QED-related uncertainties (see Table 2.9). The change in  $m_Z$  due to  $m_H$  amounts to  $+0.23$  MeV per unit change in  $\log_{10}(m_H/\text{GeV})$ . Note that this is small compared to the total error on  $m_Z$  of  $\pm 2.1$  MeV and is not considered as an error, but rather as a correction to be applied once the Higgs boson mass is known. The consequences of a completely model-independent treatment of the  $\gamma$ -Z interference in the hadronic channel are discussed in Section 2.4.3.

## 2.4 Combination of results

The combination of results on the Z parameters is based on the nine parameters  $m_Z$ ,  $\Gamma_Z$ ,  $\sigma_h^0$ ,  $R_e^0$ ,  $R_\mu^0$ ,  $R_\tau^0$ ,  $A_{\text{FB}}^{0,e}$ ,  $A_{\text{FB}}^{0,\mu}$  and  $A_{\text{FB}}^{0,\tau}$  and the common errors given in the previous chapter.

For this purpose it is necessary to construct the full  $(4 \times 9) \times (4 \times 9)$  covariance matrix of the errors. The four diagonal  $9 \times 9$  matrices consist of the four error matrices specified by each experiment (Table 2.4). The  $9 \times 9$  common error matrices build the off-diagonal elements.

A symbolic representation of the full error matrix is shown in Table 2.10. Each table element represents a  $9 \times 9$  matrix;  $(\mathcal{C}_{exp})$  for  $exp = A, D, L$  and  $O$  are the covariance matrices of the experiments (see Table 2.4), and  $(\mathcal{C}_c) = (\mathcal{C}_E) + (\mathcal{C}_L) + (\mathcal{C}_t) + (\mathcal{C}_{\text{QED,th}})$  is the matrix of common errors.  $(\mathcal{C}_E)$  (Table 2.6) is the error matrix due to LEP energy uncertainties,  $(\mathcal{C}_L)$  (Section 2.3.3) arises from the theoretical error on the small-angle Bhabha cross-section calculations,  $\mathcal{C}_t$  (Table 2.7) contains the errors from the  $t$ -channel treatment in the  $e^+e^-$  final state, and  $(\mathcal{C}_{\text{QED,th}})$  contains the errors from initial state photon and fermion pair radiation and from the model-independent parametrisation (Table 2.9). Since the latter errors were not included in the experimental error matrices, they were also added to the block matrices in the diagonal of Table 2.10.

The combined parameter set and its covariance matrix are obtained from a  $\chi^2$  minimisation, with

$$\chi^2 = (\mathbf{X} - \mathbf{X}_m)^T (\mathcal{C})^{-1} (\mathbf{X} - \mathbf{X}_m); \quad (2.2)$$

$(\mathbf{X} - \mathbf{X}_m)$  is the vector of residuals of the combined parameter set to the individual results.

( $\mathcal{C}$ )	ALEPH	DELPHI	L3	OPAL
A	$(\mathcal{C}_A) + (\mathcal{C}_{\text{QED,th}})$			
D	$(\mathcal{C}_c)$	$(\mathcal{C}_D) + (\mathcal{C}_{\text{QED,th}})$		
L	$(\mathcal{C}_c)$	$(\mathcal{C}_c)$	$(\mathcal{C}_L) + (\mathcal{C}_{\text{QED,th}})$	
O	$(\mathcal{C}_c)$	$(\mathcal{C}_c)$	$(\mathcal{C}_c)$	$(\mathcal{C}_O) + (\mathcal{C}_{\text{QED,th}})$

Table 2.10: Symbolic representation of the covariance matrix, ( $\mathcal{C}$ ), used to combine the line shape and asymmetry results of the four experiments. Elements above the diagonal are the same as those below, but are left blank for simplicity. The components of the matrix are explained in the text.

Some checks of the combination procedure outlined above are described in the following subsections, and the combined results are given in the tables of Section 2.4.5.

### 2.4.1 Multiple- $m_Z$ fits

In 1993 and 1995, the two years when LEP performed precision energy scans to measure the Z line shape, the experimental errors are very comparable, but the LEP energy was appreciably better understood in 1995 than in 1993. In determining the optimum value of  $m_Z$ , therefore, the four experiments combined should give more weight to the 1995 data than they each do in their independent determinations. To quantify this issue the measurements of each experiment were fit to determine independent values of  $m_Z$  for the periods 1990–1992, 1993–94 and 1995. In this “eleven-parameter fit”, each of the three mass values  $m_Z^{90-92}$ ,  $m_Z^{93-94}$  and  $m_Z^{95}$  has its specific energy error reflecting the different systematic errors on the absolute energy scale of LEP. In the combination, the relative importance of energy related and independent experimental errors on the mass values is properly treated.

When the three values of  $m_Z$  are condensed into a single one, the effects of the time dependence of the precision in the energy calibration is taken into account. The difference of  $-0.2$  MeV w.r.t. the  $m_Z$  value from the nine-parameter fits corresponds to 10% of the combined error. All other parameters are identical to their values from the nine-parameter fit to within less than 5% of the combined error. This result justifies using the standard combination based on the nine parameters.

The averages over the four experiments of the three values  $m_Z^{90-92}$ ,  $m_Z^{93-94}$  and  $m_Z^{95}$  also provide a cross-check on the consistency of the energy calibration, which dominates the errors on  $m_Z$  in each of the periods considered. The mass values for the three different periods and the correlated and uncorrelated parts of their errors are shown in Figure 2.8. The differences amount to  $|m_Z^{90-92} - m_Z^{93-94}| = 31\%$ ,  $|m_Z^{90-92} - m_Z^{95}| = 56\%$  and  $|m_Z^{93-94} - m_Z^{95}| = 43\%$  of the uncorrelated error, *i. e.* the three Z mass values are consistent.

### 2.4.2 Shifts for halved experimental errors

When the average over the experiments is performed at the parameter level, information on the individual contribution of particular data points to the average is lost. Performing the average over the data points instead may therefore lead to changes of the relative importance of independent experimental errors w.r.t. the common errors. The examples of  $m_Z$  and the importance of the  $t$ -channel errors for  $R_\ell^0$ , as discussed in the previous subsections, provide good

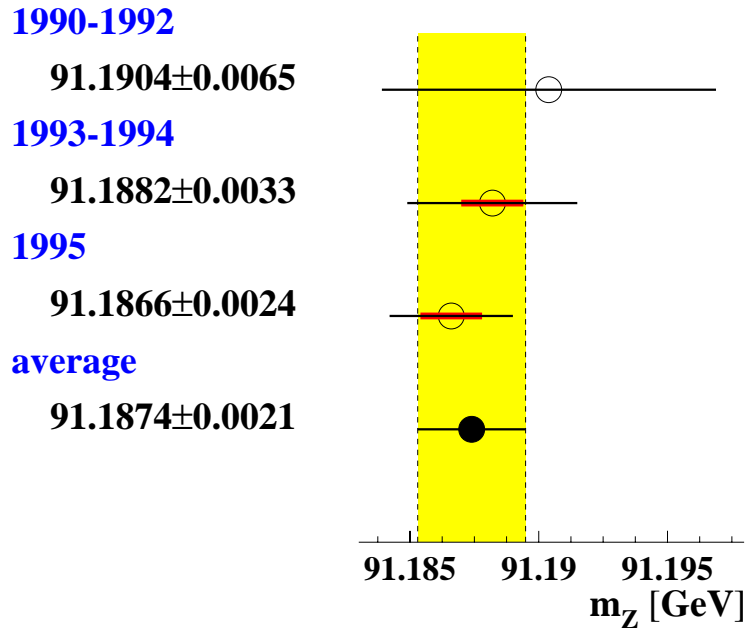


Figure 2.8:  $m_Z$  in GeV for different periods of data taking, before 1993, 1993–1994 and 1995. The second, smaller error bar represents the correlated error component of 1.2 MeV between  $m_Z^{93-94}$  and  $m_Z^{95}$ .  $m_Z^{90-92}$  is essentially uncorrelated with the other two.

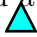
illustrations of such effects. It was demonstrated that averaging the shifts in  $m_Z$  which each experiment observed when halving its experimental errors to simulate the generic “combined” experiment also reproduced the results of the full fit to the combined hadronic cross-section measurements.

While  $m_Z$  is properly treated by the eleven-parameter fits, other pseudo-observables may suffer from similar changes due to weight shifts. Changes in central values when halving the independent experimental errors in each experiment can be used as a monitoring tool for these parameters as well. The average of these changes over the four LEP experiments serves to control the differences between an average at the parameter level compared to a full cross-section average. Of course, this assumes that all measurements from individual experiments enter into the average with the same weight. The observed shifts are summarised in Table 2.11. The shift downwards in  $m_Z$  of 0.3 MeV corresponds to the slightly smaller shift of 0.2 MeV already seen in the multiple- $m_Z$  fits.

Thus, the average changes in  $m_Z$ ,  $\sigma_h^0$ ,  $R_e^0$ ,  $A_{\text{FB}}^{0,\mu}$  and  $A_{\text{FB}}^{0,\tau}$  amount to about 10% of the combined errors, in all other cases they are even smaller. This is an estimate of the magnitude of the changes in the final results that would arise from a combination of the four experiments at the cross-section level w.r.t the averaging at the parameter level. Given the smallness of the observed effects it is obvious that the parameter-level average is adequate.



	A	D	L	O	average	% of error
$m_Z$ [GeV]	-0.0006	0.0000	-0.0004	-0.0001	-0.00028	13
$\Gamma_Z$ [GeV]	-0.0002	+0.0001	-0.0004	0.0000	-0.00013	5
$\sigma_h^0$ [nb]	+0.006	0.000	+0.008	+0.0036	+0.0037	10
$R_e^0$	+0.004	+0.017	0.000	+0.004	+0.0063	13
$R_\mu^0$	0.000	0.000	0.000	+0.001	0.0000	0
$R_\tau^0$	0.000	0.000	-0.001	+0.002	+0.0003	1
$A_{\text{FB}}^{0,e}$	-0.0001	-0.0003	0.0000	-0.0000	-0.00011	5
$A_{\text{FB}}^{0,\mu}$	+0.0002	+0.0003	0.0000	+0.0001	+0.00014	11
$A_{\text{FB}}^{0,\tau}$	+0.0002	+0.0003	0.0000	+0.0001	+0.00015	9

Table 2.11: Shifts in central values of the fitted pseudo-observables seen when halving the independent experimental errors, for individual experiments and average. 

### 2.4.3 Influence of the $\gamma$ -Z interference term

In the nine-parameter analyses discussed here, the  $\gamma$ -Z interference terms in the differential cross-sections for leptons are expressed using the effective coupling constants and the electric charges of the electron,  $Q^e$ , and the final state fermion,  $Q^f$  (see equation for the differential cross-section in Section 1.3). For the hadronic final state, however, the  $\gamma$ -Z interference terms **must** are fixed to the Standard Model values, as individual quark flavours are not separated. Fits with a free interference term are possible in the S-matrix scheme [59]. The OPAL collaboration [25] also studied a different approach based on an extension of the standard parameter set. In the S-Matrix approach the interference terms are considered as free and independent parameters. The hadronic interference term is described by the parameter  $j_{\text{tot}}^{\text{had}}$ , given in the Standard Model by

$$j_{\text{tot}}^{\text{had}} = \frac{G_F m_Z^2}{\sqrt{2}\pi\alpha(m_Z)} Q^e g_{V_e} \times 3 \sum_q Q^q g_{V_q}. \quad (2.3)$$

Note that the running of  $\alpha$  as well as final state QED and QCD corrections are also included in the definition of the S-matrix parameters. The Standard Model value of  $j_{\text{tot}}^{\text{had}}$  is  $0.21 \pm 0.01$ .

The dependence of the nine parameters on the hadronic  $\gamma$ -Z interference term is studied by considering a set of ten parameters consisting of the standard nine parameters extended by the parameter  $j_{\text{tot}}^{\text{had}}$  from the S-Matrix approach. The  $\gamma$ -Z interference terms in the lepton channels are fixed by the leptonic Z couplings. As already observed in S-Matrix analyses of the LEP-I data [24], a large anti-correlation between  $m_Z$  and  $j_{\text{tot}}^{\text{had}}$  appears, leading to errors on  $m_Z$  enlarged by a factor of almost three. The dependence of  $m_Z$  on  $j_{\text{tot}}^{\text{had}}$  is given by

$$\frac{dm_Z}{dj_{\text{tot}}^{\text{had}}} = -1.6 \text{ MeV}/0.1.$$

The changes in all other parameters are below 20% of their combined error for a change in  $j_{\text{tot}}^{\text{had}}$  of 0.1.

Better experimental constraints on the hadronic interference term are obtained by including measurements of the hadronic total cross-section at centre-of-mass energies further away from the Z pole than just the off-peak energies at LEP-I. Including the measurements of the TRISTAN collaborations at KEK, TOPAZ [60] and VENUS [61], at  $\sqrt{s}=58$  GeV, the error on



$j_{\text{tot}}^{\text{had}}$  is reduced to  $\pm 0.1$ , while its central value is in good agreement with the Standard Model expectation. Measurements at centre-of-mass energies above the Z resonance at LEP-II also provide constraints on  $j_{\text{tot}}^{\text{had}}$ , but in addition test modifications to the interference terms arising from the possible existence of a heavy Z' boson [62–65].

The available experimental constraints on  $j_{\text{tot}}^{\text{had}}$  thus lead to uncertainties on  $m_Z$ , independent of Standard Model assumptions in the hadronic channel, which are already smaller than its error. No additional error is assigned to the standard nine-parameter results from effects which might arise from a non-Standard Model behavior of the  $\gamma$ -Z interference.

#### 2.4.4 Direct Standard Model fits to the measured cross-sections and forward-backwards asymmetries

Since an important use of the combined results presented here is to determine parameters of the Standard Model and to test its validity, it is crucial to verify that the parameter set chosen for the combination represents the four sets of experimental measurements from which they were extracted in a manner adequate to this purpose. When the set of pseudo-observables is used in the framework of the Standard Model, the role of  $m_Z$  changes from an independent parameter to that of a Lagrangian parameter of the theory. This imposes additional constraints which can be expected to shift the value of  $m_Z$ .

To check whether the nine parameters adequately describe the reaction to these constraints, each collaboration provided results from direct Standard Model fits to their cross-section and asymmetry data. The comparison of these results with those obtained by using the set of pseudo-observables as fit input instead is shown in Table 2.12.  $m_H$  and  $\alpha_s$  were free parameters in these fits, while the additional inputs  $m_t = 174.3 \pm 5.1$  GeV and  $\Delta\alpha_{\text{had}}^{(5)} = 0.02804 \pm 0.00065$  (corresponding to  $1/\alpha^{(5)}(m_Z) = 128.877 \pm 0.090$ ) provided external constraints.

Most noticeably, significant shifts in  $m_Z$  are observed in some experiments, which cancel out to almost zero in the average over the four experiments. One anticipated source of these shift was already mentioned: the Z couplings defining the  $\gamma$ -Z interference term depends on  $m_H$ , which is allowed to move freely in the first fit, but is fixed to 150 GeV for the extraction of the pseudo-observables. The approximate values of  $m_H$  preferred by the Standard Model fit to the cross-sections and asymmetries are indicated in the second part of the table. Using the dependence of  $m_Z$  on the value of  $m_H$  given in Section 2.3.4, the differences in  $m_Z$  can be corrected to a common value of the Higgs mass of  $m_Z = 150$  GeV, as is shown in the last line of Table 2.12. Hence the net average difference in  $m_Z$  directly from the realistic observables or through the intermediary of the pseudo-observables is less than 0.1 MeV. Shifts in the other Standard Model parameters, in the individual data sets as well as in the average, are all well under 5% of the errors, and therefore also negligible.

The conclusion of this study is that Standard Model parameters extracted from the pseudo-observables are almost identical to the ones that would be obtained from the combined cross-sections and asymmetries. Within the Standard Model the combined set of pseudo-observables provides a description of the measurements of the Z parameters that is equivalent to the full set of cross-sections and asymmetries. This is also true for any theory beyond the Standard Model which leads to corrections that are absorbed in the pseudo-observables. An exception to this are those theories with an additional Z'-bosons which lead to significant modifications of the  $\gamma$ -Z interference term. (See the discussion in Section 2.4.3.)

	A	D	L	O	average	% of error
$\chi^2/N_{\text{df}}$	174/180	184/172	168/170	161/198		
$\Delta m_Z$ [MeV]	-0.7	+0.5	0.0	+0.1	-0.03	1
$\Delta m_t$ [GeV]	0.0	0.0	0.0	0.0	0.0	<2
$\Delta \log_{10}(m_H/\text{GeV})$	-0.01	+0.04	+0.02	+0.04	+0.02	4
$\Delta \alpha_s$	0.0000	-0.0002	+0.0002	+0.0002	+0.0001	4
$\Delta(\Delta \alpha_{\text{had}}^{(5)})$	+0.00002	-0.00004	0.00000	-0.00004	-0.00002	2
fit value of $m_H$ [GeV]	40.	10.	35.	390.		
$\Delta m_Z$ [MeV] corr. to 150 GeV $m_H$	-0.6	+0.7	+0.1	0.0	+0.05	2

Table 2.12: Shifts in Standard Model parameters, from direct Standard Model fit to the cross-sections and forward-backward asymmetries w.r.t. fits to the the nine-parameter results. The numbers in the last line of the table give the shifts in  $m_Z$  if the results from the first line are corrected to a common value of the Higgs mass of 150 GeV.

### 2.4.5 Combined results

The result of the combination of the four sets of nine pseudo-observables including the experimental and common error matrices is given in Table 2.13. The value of the Higgs boson mass is assumed to be 150 GeV and is relevant only for the value of  $m_Z$ , which changes by +0.23 MeV per unit change in  $\log_{10}(m_H/\text{GeV})$ . (See Section 2.3.4.)

The value of  $\chi^2$  per degree of freedom of the combination is 32.6/27 and corresponds to a probability of 21 % to find an agreement among the four sets of measurements which is worse than the one actually observed. The correlation matrix of the combined result shows significant correlations of  $\sigma_h^0$  with  $\Gamma_Z$  and  $R_e^0$ ,  $R_\mu^0$  and  $R_\tau^0$  and between  $R_e^0$  and  $A_{\text{FB}}^{0,e}$ .

A comparison of the leptonic quantities  $R_e^0$ ,  $R_\mu^0$  and  $R_\tau^0$  and of  $A_{\text{FB}}^{0,e}$ ,  $A_{\text{FB}}^{0,\mu}$  and  $A_{\text{FB}}^{0,\tau}$  shows that they agree within errors. Note that  $R_\tau^0$  is expected to be larger by 0.23 % because of  $\tau$  mass effects. Figure 2.9 shows the corresponding 68 % level contours in the  $R_\ell^0 - A_{\text{FB}}^{0,\ell}$  plane.

Imposing the additional requirement of lepton universality in the combination leads to the results shown in the second part of Table 2.13. Here  $R_\ell^0$  is not a simple average over the three lepton species, but refers to Z decays into pairs of one massless charged lepton species. The value of  $\chi^2/N_{\text{df}}$  of 36.5/31 for the combination of the four sets of nine pseudo-observables into the five parameters of Table 2.13 corresponds to a  $\chi^2$ -probability of 23 %. The central ellipse in Figure 2.9 shows the 68 %-CL contour for the combined values of  $R_\ell^0$  and  $A_{\text{FB}}^{0,\ell}$  determined from all three lepton species.

In principle, the average over the four experiments could also be performed at the level of the five-parameter results. When this is attempted, good agreement is seen with the results in the lower part of Table 2.13 except for  $R_\ell^0$ , where the difference amounts to 0.005 or 20 % of the total error. The origin of this shift are changes of weight for the  $e^+e^-$  final state due to the common  $t$ -channel error. If the average over the leptonic measurements is performed by each experiment individually, the weight given to the electron channel is larger than for the case where the averages over individual lepton species are averaged at the end. Extracting the results with lepton universality from the nine parameters is therefore the appropriate method.

without lepton universality		correlations									
$\chi^2/N_{\text{df}} = 32.6/27$		$m_Z$	$\Gamma_Z$	$\sigma_h^0$	$R_e^0$	$R_\mu^0$	$R_\tau^0$	$A_{\text{FB}}^{0,e}$	$A_{\text{FB}}^{0,\mu}$	$A_{\text{FB}}^{0,\tau}$	
$m_Z$ [GeV]	$91.1876 \pm 0.0021$	1.00									
$\Gamma_Z$ [GeV]	$2.4952 \pm 0.0023$	-.024	1.00								
$\sigma_h^0$ [nb]	$41.541 \pm 0.037$	-.044	-.297	1.00							
$R_e^0$	$20.804 \pm 0.050$	.078	-.011	.105	1.00						
$R_\mu^0$	$20.785 \pm 0.033$	.000	.008	.131	.069	1.00					
$R_\tau^0$	$20.764 \pm 0.045$	.002	.006	.092	.046	.069	1.00				
$A_{\text{FB}}^{0,e}$	$0.0145 \pm 0.0025$	-.014	.007	.001	-.371	.001	.003	1.00			
$A_{\text{FB}}^{0,\mu}$	$0.0169 \pm 0.0013$	.046	.002	.003	.020	.012	.001	-.024	1.00		
$A_{\text{FB}}^{0,\tau}$	$0.0188 \pm 0.0017$	.035	.001	.002	.013	-.003	.009	-.020	.046	1.00	

with lepton universality		$m_Z$	$\Gamma_Z$	$\sigma_h^0$	$R_\ell^0$	$A_{\text{FB}}^{0,\ell}$
$\chi^2/N_{\text{df}} = 36.5/31$		$m_Z$	$\Gamma_Z$	$\sigma_h^0$	$R_\ell^0$	$A_{\text{FB}}^{0,\ell}$
$m_Z$ [GeV]	$91.1875 \pm 0.0021$	1.00				
$\Gamma_Z$ [GeV]	$2.4952 \pm 0.0023$	-.023	1.00			
$\sigma_h^0$ [nb]	$41.540 \pm 0.037$	-.045	-.297	1.00		
$R_\ell^0$	$20.767 \pm 0.025$	.033	.004	.183	1.00	
$A_{\text{FB}}^{0,\ell}$	$0.0171 \pm 0.0010$	.055	.003	.006	-.056	1.00

Table 2.13: Result of the combination of the four sets of nine pseudo-observables from Table 2.4.

## 2.5 Parameters derived from line shape results

Additional pseudo-observables, more familiar than the experimentally motivated set of Table 2.13, can be obtained through parameter transformations. The partial Z decay widths are summarised in Table 2.14. Note that they have larger correlations than the original set of results. If lepton universality is imposed, a more precise value of  $\Gamma_{\text{had}}$  is obtained, because  $\Gamma_{ee}$  in the relation between the hadronic pole cross-section and the partial widths is replaced by the more precise value of  $\Gamma_{\ell\ell}$ . The invisible width,  $\Gamma_{\text{inv}} = \Gamma_Z - \Gamma_{\text{had}} - \Gamma_{ee} - \Gamma_{\mu\mu} - \Gamma_{\tau\tau}$ , is also shown in the table. The leptonic pole cross-section,  $\sigma_\ell^0$ , is shown in the last line of Table 2.14. Because  $\alpha_s$  appears quadratically in the denominator via  $\Gamma_Z$ ,  $\sigma_\ell^0$  has a higher sensitivity to  $\alpha_s$  than  $\sigma_h^0$  or  $R_\ell^0$ , where the dependence on  $\alpha_s$  is only linear.

Assuming only standard particles, the invisible width is compatible with the Standard Model hypothesis of decays into the three neutrino species,  $\Gamma_{\text{inv}} = 3\Gamma_{\nu\nu}$ . The “number of neutrinos”  $N_\nu$  is calculated according to

$$\blacktriangle \frac{\Gamma_{\text{inv}}}{\Gamma_{\ell\ell}} = N_\nu \left( \frac{\Gamma_{\nu\nu}}{\Gamma_{\ell\ell}} \right)_{\text{SM}}. \quad (2.4)$$

The Standard Model value for the ratio of the partial widths to neutrinos and to charged leptons is  $1.9912 \pm 0.0012$ , where the uncertainty arises from variations of the top quark mass within its experimental error and of the Higgs mass within  $100 \text{ GeV} < m_H < 1000 \text{ GeV}$ . With the measured value of  $\Gamma_{\text{inv}} / \Gamma_{\ell\ell} = 5.942 \pm 0.016$ , the number of light neutrino species is determined to be  $N_\nu = 2.984 \pm 0.008$ . This may also be turned into a quantitative limit on extra, non-standard contributions to the invisible width, *i.e.* not originating from  $Z \rightarrow \nu\bar{\nu}$ , by taking the difference between the value given in Table 2.14 and the Standard Model expectation of  $(\Gamma_{\text{inv}})_{\text{SM}} = 501.7_{-0.9}^{+0.1} \text{ MeV}$ . This gives  $\Gamma_{\text{inv}}^x = -2.7_{-1.5}^{+1.7} \text{ MeV}$ , or expressed as a limit,  $\Delta\Gamma_{\text{inv}}^z \ll$

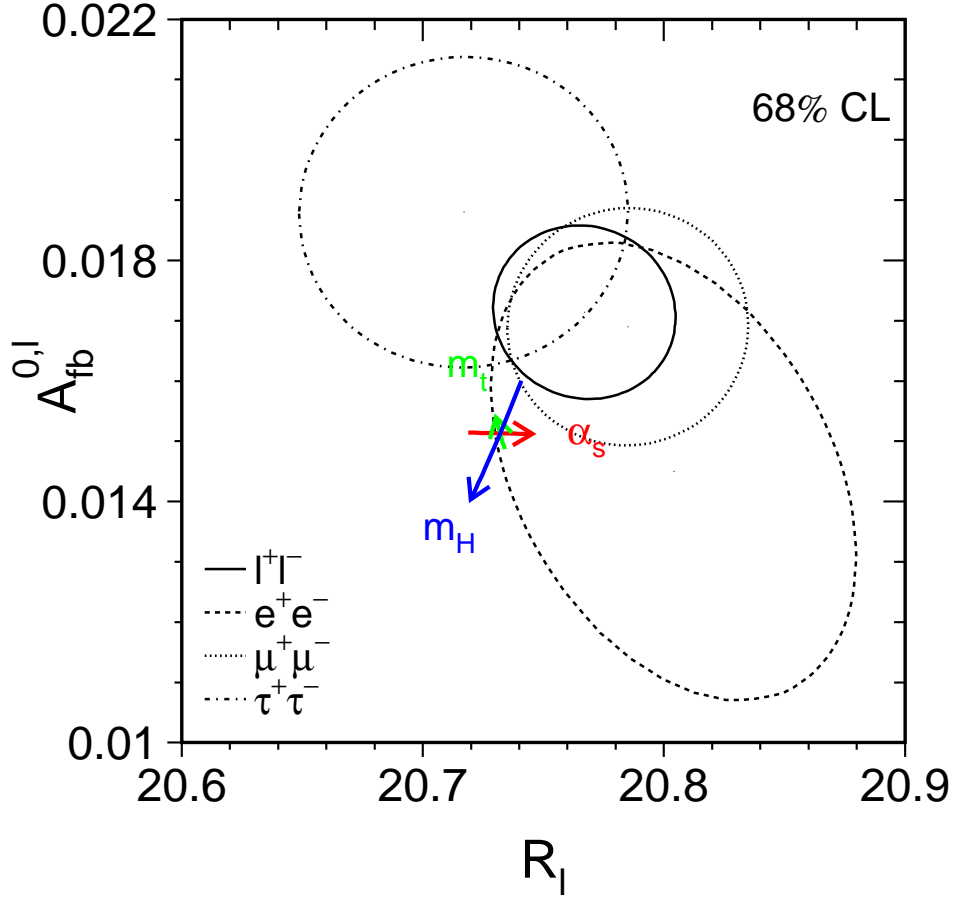


Figure 2.9: Contour lines (68 % CL) in the  $R_\ell^0 - A_{\text{FB}}^{0,\ell}$  plane for  $e^+e^-$ ,  $\mu^+\mu^-$  and  $\tau^+\tau^-$  final states and for all leptons combined. For better comparison the results for the  $\tau$  lepton are corrected to correspond to the massless case. The Standard Model prediction for  $m_Z = 91.1875$  GeV,  $m_t = 174.3$  GeV,  $m_H = 300$  GeV, and  $\alpha_S(m_Z^2) = 0.119$  is also shown. The lines with arrows correspond to the variation of the Standard Model prediction when  $m_t$ ,  $m_H$  and  $\alpha_S(m_Z^2)$  are varied in the intervals  $m_t = 174.3 \pm 5.1$  GeV,  $m_H = 300_{-200}^{+700}$  GeV, and  $\alpha_S(m_Z^2) = 0.119 \pm 0.002$ , respectively. The arrows point in the direction of increasing values of  $m_t$ ,  $m_H$  and  $\alpha_S$ .

2.0 MeV at 95% CL; here, the limit was conservatively calculated allowing only positive values of  $\Gamma_{\text{inv}}^x$ .

The Z branching fractions, *i. e.* the ratios of the partial decay widths to the individual final states and the total Z width, are shown in Table 2.15. The branching fraction to invisible particles is derived by constraining the sum of all branching fractions to one and therefore does not constitute an independent measurement.

without lepton universality		correlations
$\Gamma_{\text{had}}$ [MeV]	$1745.8 \pm 2.7$	
$\Gamma_{ee}$ [MeV]	$83.92 \pm 0.12$	-0.29
$\Gamma_{\mu\mu}$ [MeV]	$83.99 \pm 0.18$	0.66 -0.20
$\Gamma_{\tau\tau}$ [MeV]	$84.08 \pm 0.22$	0.54 -0.17 0.39

with lepton universality		
$\Gamma_{\text{inv}}$ [MeV]	$499.0 \pm 1.5$	
$\Gamma_{\text{had}}$ [MeV]	$1744.4 \pm 2.0$	-0.29
$\Gamma_{\ell\ell}$ [MeV]	$83.984 \pm 0.086$	0.49 0.39
$\Gamma_{\text{inv}}/\Gamma_{\ell\ell}$	$5.942 \pm 0.016$	
$\sigma_{\ell}^0$ [nb]	$2.0003 \pm 0.0027$	

Table 2.14: Partial Z decay widths and correlation coefficients.

without lepton universality		correlations
$B(Z \rightarrow q\bar{q})$	$0.69967 \pm 0.00093$	
$B(Z \rightarrow e^+e^-)$	$0.033632 \pm 0.000042$	-0.76
$B(Z \rightarrow \mu^+\mu^-)$	$0.033662 \pm 0.000066$	0.59 -0.50
$B(Z \rightarrow \tau^+\tau^-)$	$0.033696 \pm 0.000083$	0.48 -0.40 0.33
$B(Z \rightarrow \mu^+\mu^-) / B(Z \rightarrow e^+e^-)$	$1.0009 \pm 0.0028$	
$B(Z \rightarrow \tau^+\tau^-) / B(Z \rightarrow e^+e^-)$	$1.0019 \pm 0.0032$	0.63

with lepton universality		
$B(Z \rightarrow q\bar{q})$	$0.69911 \pm 0.00056$	
$B(Z \rightarrow e^+e^- + \mu^+\mu^- + \tau^+\tau^-)$	$0.100898 \pm 0.000069$	-0.29
$B(Z \rightarrow \text{invisible particles})$	$0.20000 \pm 0.00055$	

Table 2.15: Z branching fractions. Note that the branching fraction to invisible particles is fully correlated with the sum of the branching fractions to the visible final states.

# Chapter 3

## Measurement of $A_{LR}$ and the Lepton Asymmetries at the SLC

### 3.1 The $A_{LR}$ Measurement

The measurement of the left-right cross section asymmetry ( $A_{LR}$ ) by SLD [?] [?] at the SLC provides a systematically precise, statistics dominated, determination of the coupling  $\mathcal{A}_e$ , and is presently the most precise single measurement, with the smallest systematic error, of this quantity. In addition,  $A_{LR}$  is the most sensitive among the asymmetries to the effective weak mixing angle, with  $\delta A_{LR} \approx 7.85\delta(\sin^2 \theta_W^{\text{eff}})$ .

In principle the analysis is straightforward: one counts the numbers of Z bosons produced by left and right longitudinally polarised electrons, forms an asymmetry, and then divides by the luminosity-weighted  $e^-$  beam polarisation magnitude (the  $e^+$  beam is not polarised):

$$A_{LR} = \frac{N_L - N_R}{N_L + N_R} \frac{1}{\langle \mathcal{P}_e \rangle}. \quad (3.1)$$

The method requires no detailed final state event identification ( $e^+e^-$  final state events are removed due to non-resonant t-channel contributions, as are all other backgrounds not due to Z decay) and is insensitive to all acceptance and efficiency effects. In order to convert  $A_{LR}$  at a particular value of  $E_{cm}$  into a determination of the effective weak mixing angle, the result is converted into a “Z-pole” value by the application of a small (typically about 2.0%) correction for initial state radiation and  $\gamma - Z$  interference [?]

$$A_{LR}(E_{CM}) \rightarrow A_{LR}^0 \equiv \mathcal{A}_e. \quad (3.2)$$

This calculation requires accurate and precise knowledge of the luminosity-weighted average center-of-mass collision energy  $E_{cm}$ .

For the most recent data (1997-1998), the small total systematic error of 0.65% relative is dominated by the 0.50% relative systematic error in the determination of the luminosity weighted average  $e^-$  polarisation, with the second largest error (0.39%) arising from uncertainties in the determination of the luminosity-weighted average center-of-mass energy. A number of very much smaller contributions to the systematic error will be discussed below. The relative statistical error on  $A_{LR}$  from all data is about 1.3%.

In what follows, some of the details of the  $A_{LR}$  measurement will be described and some historical context for the  $A_{LR}$  program at SLC/SLD (1992-1998) will be provided.

### 3.1.1 Electron Polarization at the SLC

In section 1.1.2, the operation of the SLC was briefly outlined, and Figure 1.4 provided a schematic of the machine. The SLC produced longitudinally polarized electrons by illuminating a GaAs photocathode with a circularly polarized Ti-Sapphire laser. Following the advent of high polarisation “strained lattice” GaAs photocathodes (1994) [?], where mechanical strain induced in a thin (0.1 micron) GaAs layer lifts an angular momentum degeneracy in the valence band of the material, the average electron polarization at the  $e^+e^-$  interaction point (IP) (slightly lower than the value produced at the source) was in the range 73% to 77%. Corresponding values were about 22% in 1992 using a unstrained “bulk” GaAs cathode, and 63% in 1993 using a thicker (0.3 micron) strained layer cathode design. The electron helicity is chosen randomly pulse-to-pulse at the machine repetition rate of 120 Hz by controlling the circular polarization of the source laser.

The electron spin orientation is longitudinal at the source and remains longitudinal until it is transported to the damping ring (DR). In the linac-to-ring (LTR) transport line, the electron spins precess due to the dipole magnets, where the spin precession angle is given in terms of the anomalous magnetic moment  $g$  :  $\theta_{precession} = (\frac{g-2}{2})\frac{E}{m}\theta_{bend}$ . By design, the bend angle  $\theta_{bend}$  results in transverse spin orientation at the entrance to the LTR spin rotator magnet. This superconducting solenoid magnet is used to rotate the polarization about the beam direction into the vertical orientation for storage in the DR. This is necessary as any horizontal spin components precess rapidly and completely dissipate during the 8.3 msec (1/120 seconds) storage time due to energy spread in the bunch. The polarized electron bunches can be stored in one of two possible configurations by the reversal the LTR spin rotator solenoid magnet. These reversals, typically done **after** three month intervals, were useful for identifying and minimizing the small ( $\mathcal{O}(10^{-4})$ ) polarization asymmetries produced at the source.

Manipulation of the electron spin in the SLC north arc, necessary for maximal longitudinal polarization at the IP, was possible as the betatron phase advance closely matched the spin precession (1080 and 1085 degrees respectively) in each of the arc bend magnets - and hence the north arc operated close to a spin-tune resonance. As a result, excepting 1992 running, two additional SLC spin rotator solenoids were not necessary for spin orientation, and were used only in a series of specialized polarization experiments.

### 3.1.2 Polarimetry at the SLC

In Compton scattering of longitudinally polarized electrons from circularly polarized photons, the differential cross section in terms of the normalized scattered photon energy fraction  $x$  is given by

$$\frac{d\sigma}{dx} = \frac{d\sigma_0}{dx} [1 - \mathcal{P}_\gamma \mathcal{P}_e A(x)], \quad (3.3)$$

where  $\frac{d\sigma_0}{dx}$  is the unpolarized differential cross section,  $\mathcal{P}_{\gamma,e}$  are the photon and electron polarizations, and  $A(x)$  is the Compton asymmetry function. The asymmetry arises due to the difference between spin parallel and spin anti-parallel cross sections ( $j = 3/2 > j = 1/2$ ). In a polarimeter, the Compton scattered photons or electrons are detected, and the **requisite instrumental effects are incorporated into a detector response function**. The convolution of  $A(x)$  with  $\frac{d\sigma_0}{dx}$  and the response function (all functions of  $x$ ), normalized by the convolution of  $A(x)$  and  $\frac{d\sigma_0}{dx}$ , is known as the “analyzing power”. When  $\mathcal{P}_\gamma$  and the analyzing power are known, the **experimental determination of the  $j = 3/2$  to  $j = 1/2$  scattering asymmetry** determines



$\mathcal{P}_e$ , and hence the utility of this elementary QED process to electron polarimetry. The SLD precision Compton polarimeter detected beam electrons that had been scattered by photons from a circularly polarised laser. The choice of a Compton scattering polarimeter was dictated by the requirements that the device be operated continually while beams were in collision and that uncertainties in the physics of the scattering process not be a limiting factor in the systematic error; both troublesome issues for Møller scattering instruments due to their magnetic alloy targets. In addition, the pulse-to-pulse controllability of the laser polarization, as well as the high polarization (99.9%), are additional advantages over other options.

Figure 3.1 illustrates the essential features of the polarimeter : Frequency doubled (532 nm) Nd:YAG laser pulses of 8 ns duration and peak power of typically 25 MW were produced at 17 Hz, circularly polarized by a linear polarizer and a Pockels cell pair. The laser beam was transported to the SLC beamline by four sets of phase-compensating mirror pairs and into the vacuum chamber through a reduced-strain quartz window. About 30 meters downstream from the IP, the beam was brought into head-on collisions with the outgoing electron beam (10 mrad crossing angle) at the Compton Interaction Point (CIP), and then left the beampipe through a second window to an analysis station. The pair of Pockels cells on the optical bench allowed for full control of elliptical polarization and was used to automatically scan the laser beam polarization at regular intervals in order to monitor, and maximize, laser polarization at the CIP. Downstream from the CIP, a pair of bend magnets swept out the off-energy Compton scattered electrons (typically of order 1000 per laser pulse) which passed through a thin window out of the beamline vacuum and into a 9 channel (1 cm per channel) transversely segmented gas Cherenkov detector. By detecting scattered electrons with a threshold Cherenkov device, large beamstrahlung backgrounds in the SLC environment were dramatically reduced.

The minimum energy 17.4 GeV electrons, corresponding to full backscattering, generally fell into the 7th channel. At this point in the electron spectrum, known as the “Compton edge”, the polarization asymmetry function reached its maximum value of 0.748. Small deviations from the theoretical Compton energy dependent asymmetry function (of order 1%) were modeled using EGS simulations in a detailed Monte Carlo of the detector geometry and the magnetic spectrometer [?] [?]. The detector was mounted on a movable platform and the Compton Edge was scanned across several channels at regular intervals in order to monitor the location of the Compton edge and to experimentally determine the detector channel response functions. The procedure was essential for the precise determination of the analyzing power of the important outer channels. Representative data showing the corrected Compton asymmetry as well as the magnitude of the correction, as a function of position and scattered electron energy, is shown in Figure 3.2. There is good agreement between the corrected asymmetry and the data in each channel.

Starting in 1996, two additional polarimeters [?] [?] that were sensitive to the Compton-scattered photons and which were operated in the absence of positron beam, were used to verify the precision polarimeter calibration. These two devices were of different design (one was a gas Cherenkov detector and the other was a quartz-fiber calorimeter) with different systematic errors, and had in common with the primary electron polarimeter only the instrumental errors due to the polarized laser. The cross check provided by these photon detectors was used to establish a calibration uncertainty of 0.4%. The systematic errors due to polarimetry are summarized in Table 3.1. During the period 1992-1998, this total fractional systematic error decreased from 2.7% to its present value of 0.50%, with the most significant reductions coming from greatly improved understanding of the laser polarization and Cherenkov detector nonlinearities. The dominant error is now due to the analysing power calibration discussed



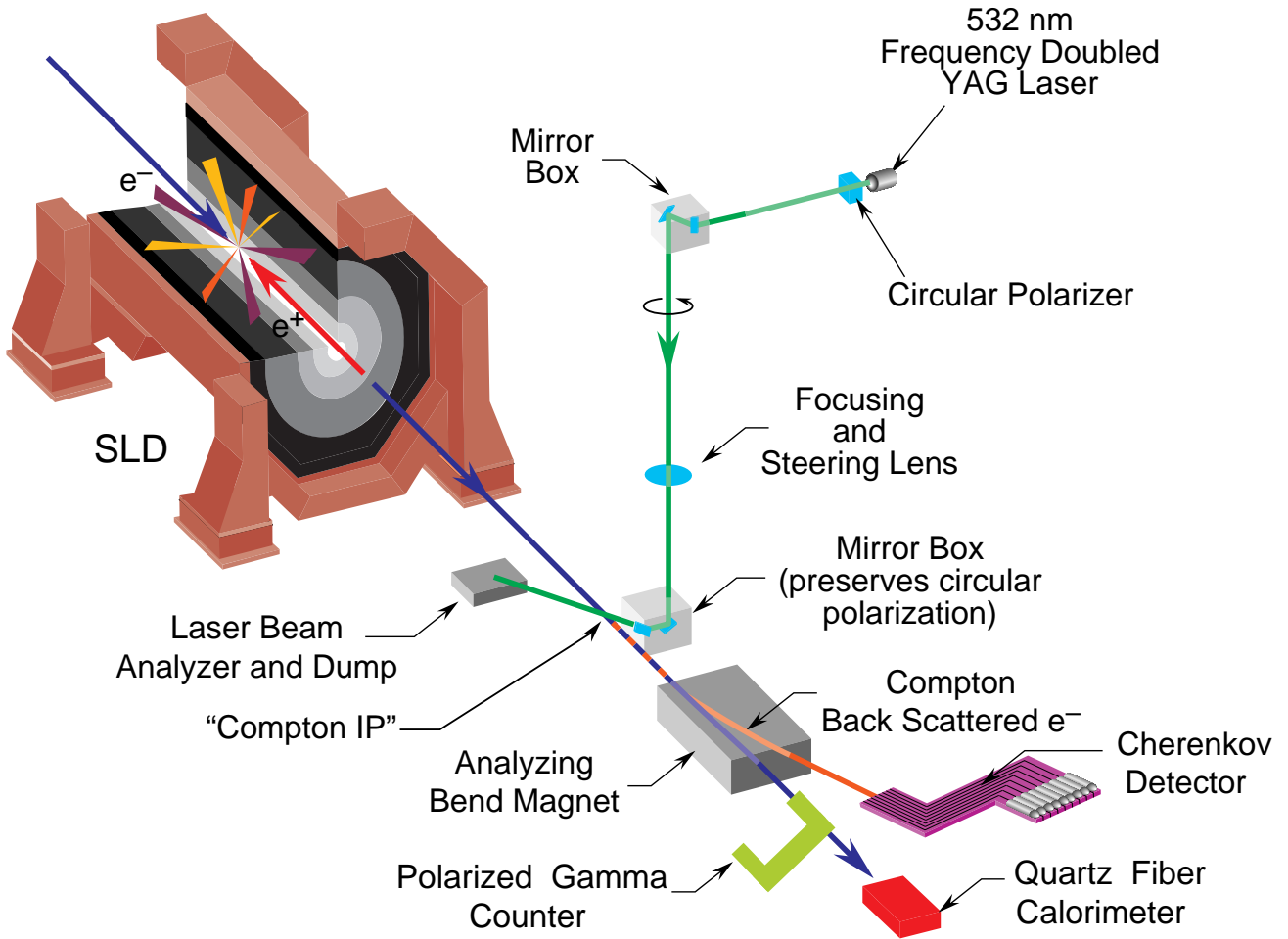


Figure 3.1: A conceptual diagram of the SLD Compton Polarimeter. The laser beam is circularly polarized and transported into head-on collision with the electron beam approximately 30 meters from the IP. Following the laser/electron-beam collision, the electrons and Compton scattered photons continue downstream until analyzing bend magnets deflect the Compton scattered electrons into a transversely segmented Cherenkov detector. The photons continue undeflected and are detected by a gamma counter and a calorimeter which are used to cross-check the polarimeter calibration.

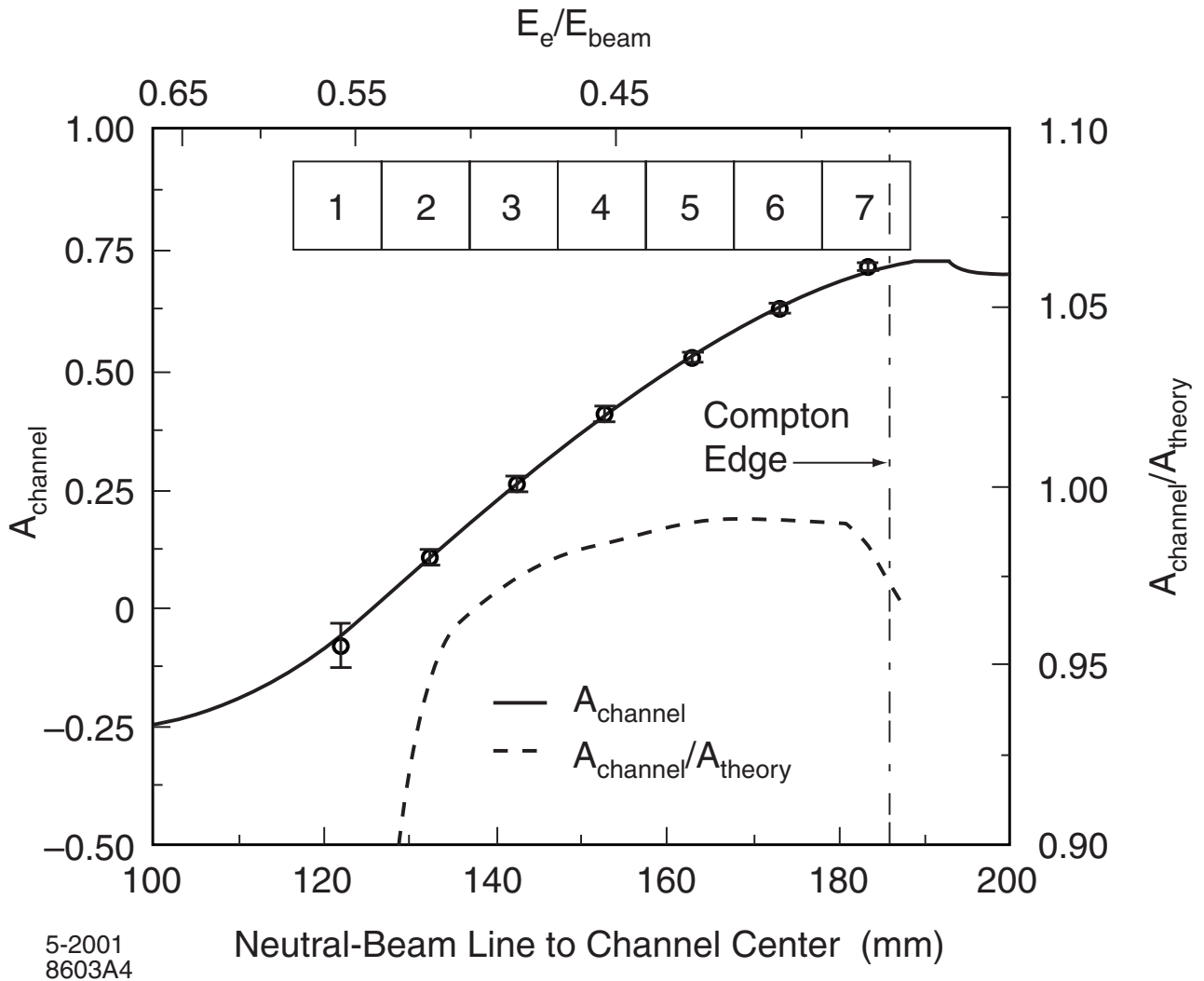


Figure 3.2: Compton scattering asymmetry as a function of channel position. The horizontal axis gives the distance in mm from the center of the detector channels (1 cm wide each) to the path of the hypothetical undeflected electron beam (neutral-beam line). The inset shows the seven inner detector channels, sized to match the horizontal scale. The per channel data is plotted as open circles, and the corrected asymmetry function is the solid curve. The size of the correction from the theoretical QED calculation is indicated by the dashed curve.

above.

The polarimeter result was corrected for higher order QED and accelerator-related effects (a total of  $-0.22 \pm 0.15\%$  for 1997-1998 data). The higher order QED offset was very small and well-determined ( $-0.1\%$ ) [?]. The primary accelerator-related effect arose from energy-to-polarization correlations that caused the average beam polarization measured by the Compton Polarimeter to differ slightly from the luminosity-weighted average beam polarization at the IP. In 1994-1998 a number of changes in the operation of the SLC and in monitoring procedures (smaller and better determined beam energy spread and polarization energy dependence) reduced the size of this *chromaticity* correction and its associated error to below  $0.2\%$  from its value of  $1.1 \pm 1.7\%$  when it was first observed in 1993. An effect of comparable magnitude arose due to the small precession of the electron spin in the final focusing elements between the IP and the polarimeter. The contribution of collisional depolarization was determined to be negligible as expected, by comparing polarimeter data taken with and without beams in collision. All effects combined yielded a correction with the uncertainty given in Table 3.1.

The luminosity-weighted average polarization  $\langle \mathcal{P}_e \rangle$  for each run was estimated from measurements of  $\mathcal{P}_e$  made when Z events were recorded,

$$\langle \mathcal{P}_e \rangle = (1 + \xi) \cdot \frac{1}{N_Z} \sum_{i=1}^{N_Z} \mathcal{P}_i \quad (3.4)$$

where  $N_Z$  is the total number of Z events,  $\mathcal{P}_i$  is the polarization measurement associated in time with the  $i^{\text{th}}$  event, and  $\xi$  is the small total correction described in the previous paragraph. The polarimeter was operated continually, where typically about three minutes were required to achieve a relative statistical precision of order  $1\%$  for each polarization measurement.

The fully corrected luminosity weighted average polarizations corresponding to each of the SLD runs are given in Table 3.3. The evolution of GaAs photocathode performance is evident in 1993 and again in 1994-1995. Changes in the achieved polarization in later years mainly reflect variations in photocathode manufacture.

### 3.1.3 Energy Spectrometry

The SLC employed a pair of energy spectrometers located in the electron and positron extraction lines (Figure 1.4). The **beam deflection by** a precision dipole magnet was detected and measured using synchrotron radiation swaths emitted by the beam in deflector magnets located before and after the bend (see Figure 3.3). These devices were first operated in their final configuration in 1989 by the Mark II experiment, and the calibration of the two precision spectrometer magnets was performed in 1988 [?]. Their expected precision was about  $\pm 20$  MeV on the measured center-of-mass collision energy  $E_{cm}$ . The importance of these devices to the  $A_{LR}$  measurement is quantified by the approximate rule of thumb that an 80 MeV uncertainty in  $E_{cm}$  corresponds to a  $1\%$  error on the Z-pole asymmetry  $A_{LR}^0$ . For this reason, in 1998 a Z peak scan was performed in order to calibrate the spectrometers to the LEP measurement of the Z mass. The scan used two optimized offpeak points at  $+0.88$  and  $-0.93$  GeV and approximately 9,000 Z equivalents of luminosity to reach a statistical precision on the peak position of 20 MeV. The results of a complete analysis of systematic effects determined an offset of  $-46$  MeV and a total  $E_{cm}$  uncertainty of 29 MeV (a  $0.39\%$  uncertainty on  $A_{LR}^0$ , as shown in Table [??] [?].

Uncertainty	$\delta\mathcal{P}_e/\mathcal{P}_e$ (%)	$\delta A_{LR}/A_{LR}$ (%)	$\delta A_{LR}^0/A_{LR}^0$ (%)
Laser polarization	0.10		
Detector linearity	0.20		
Analyzing power calibration	0.40		
Electronic noise	0.20		
Total polarimeter uncertainty	0.50	0.50	
Chromaticity and IP corrections		0.15	
Corrections in Eq. 3.5		0.07	
$A_{LR}$ Systematic uncertainty		0.52	0.52
Electroweak interference correction			0.39
$A_{LR}^0$ Systematic uncertainty			0.64

Table 3.1: Systematic uncertainties that affect the  $A_{LR}$  measurement for 1997/98. The uncertainty on the electroweak interference correction is caused by the uncertainty on the SLC energy scale.

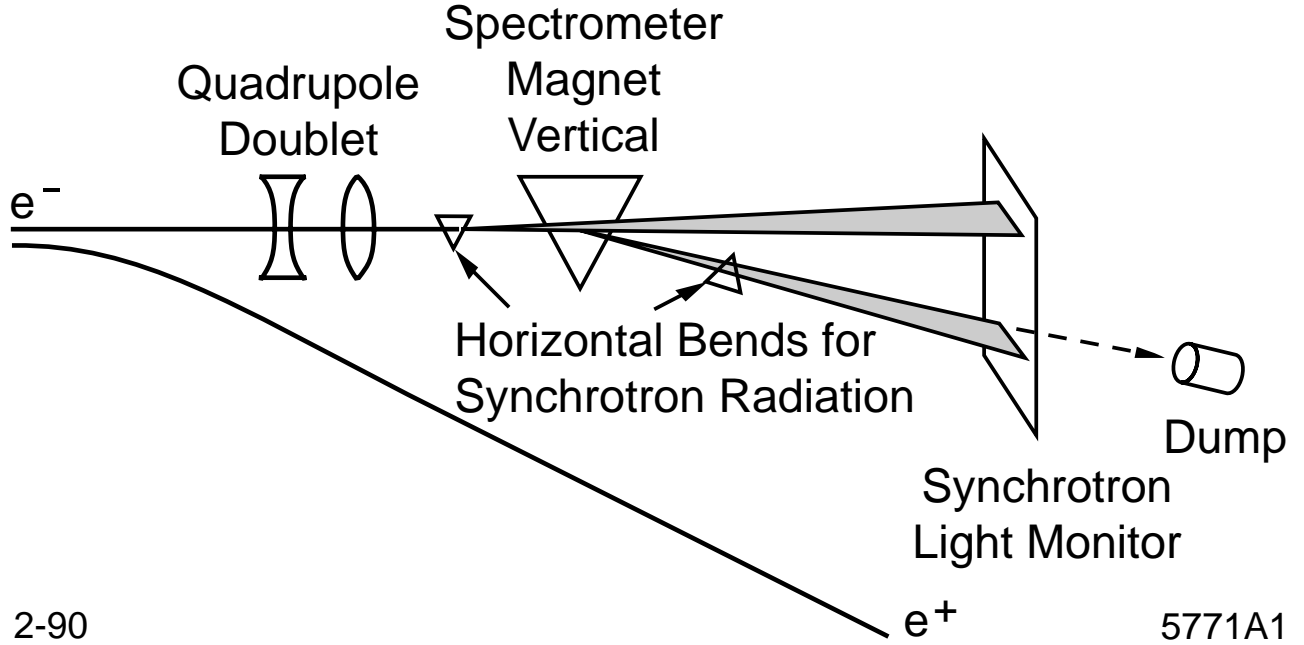


Figure 3.3: The energy spectrometer for electrons (a similar device is used on the positron side) uses a precision bend magnet and synchrotron-radiation-producing deflectors before and after the bend, in order to determine the beam deflection.

### 3.1.4 Event Selection

A simple calorimetric event selection in the LAC, supplemented by track multiplicity and topology requirements in the Central Drift Chamber, were used to select hadronic Z decays. For each event candidate, energy clusters were reconstructed in the LAC. Selected events were required to contain at least 22 GeV of energy observed in the clusters and to manifest a normalized energy imbalance of less than 0.6 [?]. The left-right asymmetry associated with final state  $e^+e^-$  events is expected to be diluted by the t-channel photon exchange subprocess. Therefore, we excluded  $e^+e^-$  final states by requiring that each event candidate contain at least 4 selected CDC tracks, with at least 2 tracks in each hemisphere (defined with respect to the beam axis), or at least 4 tracks in either hemisphere. This track topology requirement excludes Bhabha events which contain a reconstructed gamma conversion. Small backgrounds in the  $A_{LR}$  data sample were due to residual  $e^+e^-$  final state events, and to two-photon events, beam-related noise, and cosmic rays. For the most recent data (1996-98) the total background contamination was estimated to be  $< 0.05\%$  for a selection efficiency of  $91 \pm 1\%$ .

### 3.1.5 Control of Systematic Effects

The  $A_{LR}$  measurement is remarkably resistant to detector dependent systematic effects and monte carlo modeling uncertainties that are significant issues for all other electroweak precision measurements. By far the dominant systematic effects arise from polarimetry and from the determination of the collision energy, rather than from any details of the analysis or the operation of the SLD. The simple expression given in equation 3.1 applies to the ideal case in the absence of systematic effects, and as such it is a good approximation to better than a relative 0.2%.

Nevertheless, systematic left-right asymmetries in luminosity, polarization, beam energy, and acceptance, as well as background and positron polarization effects, can be incorporated into an extended expression for the cross section asymmetry. (Note that while the random helicity of the delivered electron bunches is exactly 50% righthanded, it is in principle possible that the magnitude of the luminosity is not helicity symmetric. In addition, the individual polarization measurements of equation 3.4 average over many beam crossings and over any systematic left-right polarization offset, and hence additional information is needed to make the required correction.) One finds the measured asymmetry  $A_m$  is related to  $A_{LR}$  by the following expression which incorporates a number of small correction terms in lowest-order approximation,

$$A_{LR} = \frac{A_m}{\langle \mathcal{P}_e \rangle} + \frac{1}{\langle \mathcal{P}_e \rangle} \left[ f_{bkg}(A_m - A_{bkg}) - A_{\mathcal{L}} + A_m^2 A_{\mathcal{P}} - E_{cm} \frac{\sigma'(E_{cm})}{\sigma(E_{cm})} A_E - A_\varepsilon + \langle \mathcal{P}_e \rangle \mathcal{P}_p \right], \quad (3.5)$$

where  $\langle \mathcal{P}_e \rangle$  is the mean luminosity-weighted polarization;  $f_{bkg}$  is the background fraction;  $\sigma(E)$  is the unpolarized Z boson cross section at energy  $E$ ;  $\sigma'(E)$  is the derivative of the cross section with respect to  $E$ ;  $A_{bkg}$ ,  $A_{\mathcal{L}}$ ,  $A_{\mathcal{P}}$ ,  $A_E$ , and  $A_\varepsilon$  are the left-right asymmetries [?] of the residual background, the integrated luminosity, the beam polarization, the center-of-mass energy, and the product of detector acceptance and efficiency, respectively; and  $\mathcal{P}_p$  is any longitudinal positron polarization which is assumed to have constant helicity. Since the colliding electron and positron bunches were produced on different machine cycles and since the electron helicity of each cycle was chosen randomly, any positron helicity arising from the polarization of the

production electrons was uncorrelated with electron helicity at the IP. The net effect of positron polarization from this process vanishes rigorously. However, **positron polarization of constant helicity** would affect the measurement.

The close ties between this measurement and the SLC accelerator complex is evident from numerous dedicated accelerator-based experiments dedicated to the SLD physics program, for which the energy-calibrating Z-peak scan is one example. Other examples include :

- *Communication of the  $e^-$  bunch helicity from the polarized source was verified by setting up a large current/helicity correlation in the SLC, allowing for the use of the SLD liquid-argon calorimeter (LAC) to verify data synchronization (1992-1993).* While the electron bunch polarization state is transmitted via reliable and redundant paths to the SLD detector/polarimeter complex, the SLD electroweak group proposed a series of independent tests of the synchronization of this data and the SLD event data. In one such test, the laser optics at the SLC polarized source were temporarily modified by the addition of a polarizer and quarter-wave plate so that photocathode illumination was nulled for one of the two circular polarization states. The positron beam was turned off, and the electron beam was delivered to the IP. Beam-related background in the LAC was detected, but only for the non-extinct pulses. By this means, the expected correlation between helicity and the **presence** of beam, and hence the LAC data stream, was verified [?].
- *Moderate precision Møller and Mott polarimeters confirmed the high precision Compton polarimeter result to  $\sim 3\%$  (1993-1995).* Møller polarimeters located at the end of the SLAC Linac and in the SLC electron extraction line were used to cross-check the Compton polarimeter. The perils of employing a less reliable method to test a precision device were apparent when large corrections for atomic electron momentum effects in the Møller target were discovered [?], after which, good agreement was obtained. In addition, a less direct comparison was provided by Mott polarimeter bench tests of the GaAs photocathodes [?].
- *SLC Arc spin transport was extensively studied (1993-1998), and was adjusted and frequently monitored.* A series of experiments were done that studied the beam polarization reported by the Compton polarimeter as a function of beam energy, beam energy spread and beam trajectory in the SLC arcs [?]. Two spin rotators (in the Linac, and in the ring-to-linac return line) were scanned in order to determine the IP polarization maximum. An important result of these experiments was the discovery that the SLC arcs operate near a spin tune resonance, leading to the advent of spin manipulation via “spin bumps” in the SLC arcs mentioned earlier. This procedure eliminated the need for the orientation spin rotators and allowed for minimization of the spin chromaticity ( $dP/dE$ ), reducing the resulting polarization correction from  $> 1\%$  in 1993 to  $< 0.2\%$  by 1995. In subsequent years the spin transport properties of the SLC arcs were monitored at regular intervals.
- *Positron polarization was experimentally constrained.* In 1998, a dedicated experiment was performed in order to directly test the expectation that accidental polarisation of the positron beam was negligible ; the positron beam was delivered to the SLAC End Station A (ESA) where a Møller polarimeter was **used**. Experimental control was assured by first delivering the polarized electron beam, and then an unpolarized electron beam (sourced from SLAC’s thermionic electron gun), to the ESA, confirming polarimeter operation. In addition, the spin rotator magnet located in the Linac was reversed halfway through the positron beam running, reversing the sense of polarization at the Møller target and

reducing systematic error. The final result verified that  $e^+$  polarisation was consistent with zero ( $-0.02 \pm 0.07\%$ ) [?].

The asymmetries in luminosity, polarization, and beam energy were all continually monitored using a small-angle radiative Bhabha counter located  $\approx 40\text{m}$  from the IP, beamstrahlung monitors, beam current monitors, the Compton polarimeter, and energy spectrometer data, and were limited to approximately  $10^{-4}$ ,  $10^{-3}$  and  $10^{-2}$  respectively. The long-term average values of all asymmetries of this type were reduced by the roughly tri-monthly reversal of the transverse polarization sense in the electron damping ring referred to in section [?]. The dominant cause of the observed asymmetries was the small current asymmetry produced at the SLC polarized source. This arose due to residual linear polarization in the source laser light that was correlated with the light helicity. This effect was minimized by a polarization control and intensity feedback system starting in 1993, and was generally maintained at below  $10^{-4}$ .

The value of  $A_{LR}$  is unaffected by decay-mode-dependent variations in detector acceptance and efficiency provided, for the simple case of Z decay to a fermion pair, that the efficiency for detecting a fermion at some polar angle (with respect to the electron direction) is equal to the efficiency for detecting an antifermion at the same polar angle. In hadronic Z decays, the fermions in question are the initial quark-antiquark pair, which materialize as multi-particle jets. These facts, and the high degree of polar symmetry in the SLD detector, render  $A_\epsilon$  completely negligible. Finally,  $\mathcal{P}_p$  was experimentally demonstrated to be consistent with zero to a precision of  $7 \times 10^{-4}$  as described above (calculations based on polarization buildup in the positron damping ring suggested a much smaller number,  $\mathcal{P}_p \leq \mathcal{O}(10^{-3})$ ); hence no correction for  $\mathcal{P}_p$  was applied to the data).

The systematic effects discussed in this section are summarized in Table 3.2. The corrections for backgrounds and accelerator asymmetries and the associated uncertainties, were much smaller than the leading systematic errors due to polarimetry and energy uncertainties, as can be seen by comparing the last three rows of Table 3.2.

The run-by-run  $A_{LR}$  results are shown in Table 3.3. The  $E_{cm}$  dependent radiative correction, and its uncertainty, is evident in the difference between  $A_{LR}$  and  $A_{LR}^0$ . These five results show a chi squared of 7.44 for 4 degrees of freedom, corresponding to a probability of 11.4% (Figure 3.4). The  $\overline{\sin^2\theta_W^{eff}}$  results derive from the equivalence  $A_{LR}^0 \equiv \mathcal{A}_e$ , which provides that

$$A_{LR}^0 = \frac{2(1 - 4\sin^2\theta_W^{eff})}{1 + (1 - 4\sin^2\theta_W^{eff})^2}. \quad (3.6)$$


The average for the complete SLD data sample is:

$$\begin{aligned} A_{LR}^0 &= 0.15138 \pm 0.00216 \\ \overline{\sin^2\theta_W^{eff}} &= 0.23097 \pm 0.00027. \end{aligned} \quad \blacktriangle$$

Note that small correlated systematic effects are accounted for in forming this average.

## 3.2 Measurement of the Lepton Asymmetries $A_e$ , $A_\mu$ and $A_\tau$ at the SLC

The SLD collaboration determined the individual lepton asymmetry parameters using lepton final-state events [?, ?]. Electron polarization allows one to *directly* measure the final state asymmetry parameter  $A_l$  for lepton  $l$  using the left-right forward-backward asymmetry ( $A_{FB}^{LR} =$

Table 3.2:  $Z^0$  event counts and corrections  from equation 3.5 for all SLD runs. **Italicized numbers** are not applied as corrections. Also shown are the total polarimetry errors (including chromaticity and IP effects), and the relative error due to the electroweak interference correction needed for the conversion of  $A_{LR}$  to  $A_{LR}^0$ . Note that due to low statistics, a number of effects were ignored for the 1992 run.

	1992	1993	1994/95	1996	1997/98
# $Z^0$ with LH $e^-$ beam $N_L$	5,226	27,225	52,179	29,016	183,335
# $Z^0$ with RH $e^-$ beam $N_R$	4,998	22,167	41,465	22,857	148,259
Measured asym. $A_m$	0.0223 $\pm 0.0099$	0.1024 $\pm 0.0045$	0.1144 $\pm 0.0032$	0.1187 $\pm 0.0044$	0.1058 $\pm 0.0017$
Bkgd fraction $f_{bkg}$ (%)	1.4 $\pm 1.4$	0.25 $\pm 0.10$	0.11 $\pm 0.08$	0.029 $\pm 0.021$	0.042 $\pm 0.032$
Bkgd asym. $A_{bkg}$		0.031 $\pm 0.010$	0.055 $\pm 0.021$	0.033 $\pm 0.026$	0.023 $\pm 0.022$
Luminosity asym. $A_L$ ( $10^{-4}$ )	1.8 $\pm 4.2$	0.38 $\pm 0.50$	-1.9 $\pm 0.3$	+0.03 $\pm 0.50$	-1.3 $\pm 0.7$
Polarization asym. $A_P$ ( $10^{-4}$ )	-29	-33 $\pm 1$	+24 $\pm 10$	+29 $\pm 43$	+28 $\pm 69$
<b>CM energy</b> asym. $A_E$ ( $10^{-4}$ )		0.0044 $\pm 0.0001$	0.0092 $\pm 0.0002$	-0.0001 $\pm 0.0035$	+0.0028 $\pm 0.0014$
$E_{cm} \frac{\sigma'(E_{cm})}{\sigma(E_{cm})}$		-1.9	0.0 $\pm 2.5$	2.0 $\pm 3.0$	4.3 $\pm 2.9$
Detection efficiency asym. $A_\epsilon$	0	0	0	0	0
Positron beam polariz. $\mathcal{P}_p$ ( $10^{-4}$ )	< 0.16	< 0.16	< 0.16	< 0.16	-2 $\pm 7$
Total correction, $\Delta A_{LR}/A_{LR}$ , (%)		+0.10 $\pm 0.08$	+0.2 $\pm 0.06$	+0.02 $\pm 0.05$	+0.16 $\pm 0.07$
$\delta \mathcal{P}_e/\mathcal{P}_e$ (%)	2.7	1.7	0.67	0.52	0.52
Electroweak Interference <b>Correction</b> (relative (%))		0.3	0.4	0.4	0.39



Table 3.3: Luminosity-weighted mean electron polarization,  $A_{LR}$  and  $\sin^2\theta_W^{eff}$  measurements: summary of results for all SLD runs. Statistical errors are listed first.

	$\langle \mathcal{P}_e \rangle$	$A_{LR}$	$A_{LR}^0$	$\sin^2\theta_W^{eff}$
1992	0.244 $\pm 0.006$	0.100 $\pm 0.044 \pm 0.004$	0.097 $\pm 0.044 \pm 0.004$	0.2378 $\pm 0.0056 \pm 0.0005$
1993	0.630 $\pm 0.011$	0.1628 $\pm 0.0071 \pm 0.0028$	0.1656 $\pm 0.0071 \pm 0.0028$	0.2292 $\pm 0.0009 \pm 0.0004$
1994/95	0.7723 $\pm 0.0052$	0.1485 $\pm 0.0042 \pm 0.0010$	0.1512 $\pm 0.0042 \pm 0.0011$	0.23100 $\pm 0.00054 \pm 0.00014$
1996	0.7616 $\pm 0.0040$	0.1559 $\pm 0.00572 \pm 0.00084$	0.15929 $\pm 0.00573 \pm 0.00101$	0.22996 $\pm 0.00073 \pm 0.00013$
1997/98	0.7292 $\pm 0.0038$	0.1454 $\pm 0.00237 \pm 0.00077$	0.14906 $\pm 0.00237 \pm 0.00096$	0.23126 $\pm 0.00030 \pm 0.00012$
All combined			$0.15138 \pm 0.00216$	$0.23097 \pm 0.00027$

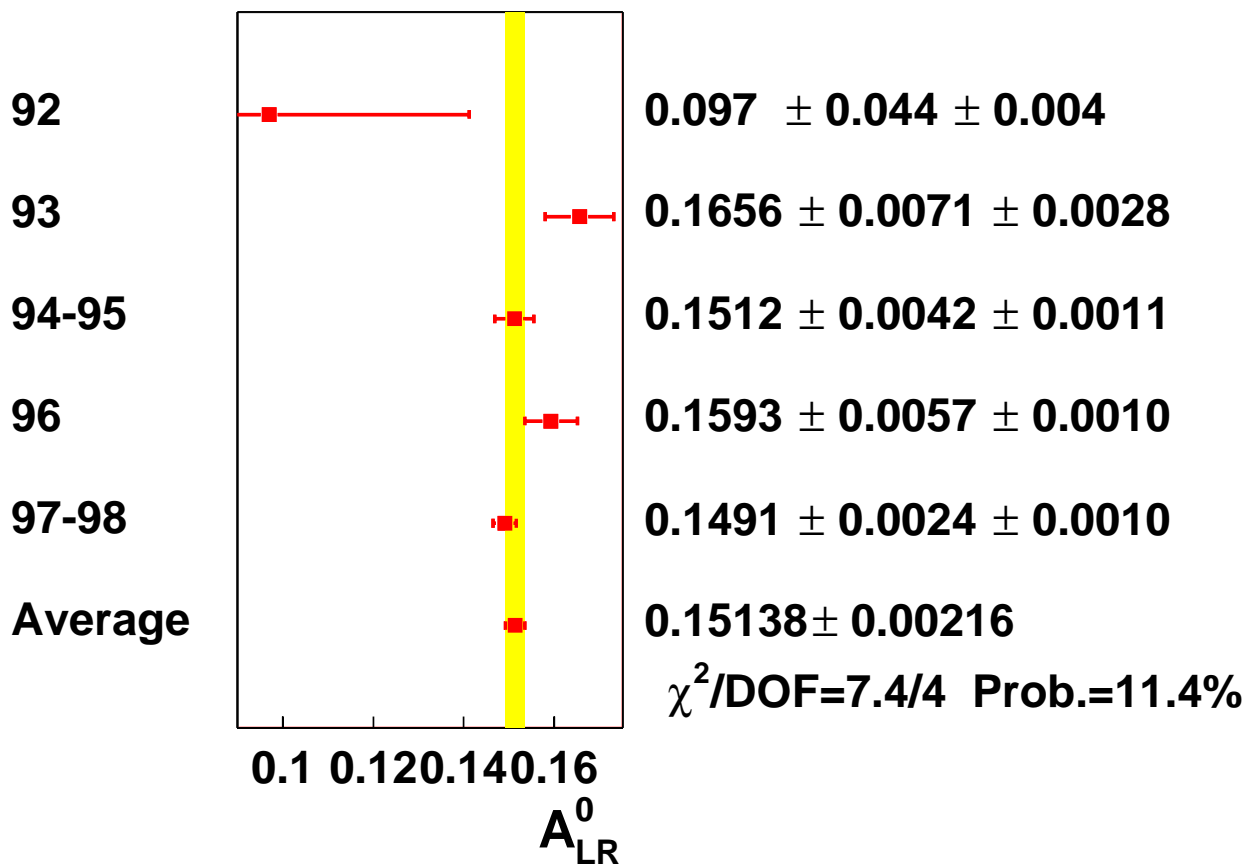


Figure 3.4: A compilation of the published SLD  $A_{LR}^0$  results, ordered by year. The final average is formed including correlations in systematic errors.

Table 3.4: Summary of event selections, efficiency, and purity for  $e^+e^- \rightarrow \ell^+\ell^-$  for the 1997-1998 SLD data

Event Sample	Background as % of Selected Events	Efficiency in $ \cos\theta  < 0.9$	# of Selected Events
$e^+e^- \rightarrow e^+e^-$	0.7% $\tau^+\tau^-$	75%	15675
$Z \rightarrow \mu^+\mu^-$	0.2% $\tau^+\tau^-$	77%	11431
$Z \rightarrow \tau^+\tau^-$	$e^+e^-:\mu^+\mu^-:2\text{-}\gamma:\text{had.}$ 0.9%:2.9%:0.9%:0.6%	70%	10841

$\frac{3}{4}|\mathcal{P}_e|A_l$ ), while the LEP experiments measure the product of initial and final state asymmetry parameters ( $A_{FB} = \frac{3}{4}A_e \cdot A_l$ ). The LEP measurements of the tau polarization yield  $A_e$  and  $A_\tau$  separately, but the SLD provided the only direct measurement of  $A_\mu$  (although errors are of order 10%). An additional advantage of polarization is that with  $\mathcal{P}_e = 75\%$ , the left-right forward-backward asymmetries yield a statistical precision equivalent to measurements of the unpolarized forward-backward asymmetry using a 25 times larger event sample.

If lepton universality is assumed, the results for all three lepton flavors can be combined to yield a determination of  $\sin^2\theta_W^{\text{eff}}$ , which in turn can be combined with the more precise result from  $A_{LR}$ . The event sample used for  $A_{LR}$  was purely hadronic (there is a very small  $0.3 \pm 0.1\%$  admixture of tau pair events) - and hence the left-right asymmetry of the lepton events was an independent measurement. While the lepton final state analysis described in what follows is more sophisticated than an  $A_{LR}$ -style counting measurement, essentially all the information on  $\sin^2\theta_W^{\text{eff}}$  is obtained from the left-right asymmetry of these events. The inclusion of the distributions in polar angle that are essential for the extraction of the final state asymmetries improves the resulting precision on  $\sin^2\theta_W^{\text{eff}}$ , but only to  $\pm 0.00076$  compared to about  $\pm 0.00078$  obtained from a simple left-right event count.

The differential cross section for the pure Z amplitude  $e^+e^- \rightarrow Z \rightarrow f\bar{f}$  is factorized as follows \*:

$$\begin{aligned} \frac{d}{dx}\sigma_Z(x, s, \mathcal{P}_e; A_e, A_l) &\equiv f_Z(s) \Omega_Z(x, \mathcal{P}_e, A_e, A_l) \\ &= f_Z(s) [(1 - \mathcal{P}_e A_e)(1 + x^2) + (A_e - \mathcal{P}_e)A_l 2x], \end{aligned} \quad (3.7)$$

where  $f_Z$  isolates dependence on  $s$ , the squared center-of-mass energy, and  $\Omega_Z$  contains the dependence on  $x = \cos\theta$ , which gives the direction of the outgoing lepton ( $l^-$ ) with respect to the electron-beam direction. For a complete description of lepton pair production, photon exchange terms and, if the final state leptons are electrons,  $t$ -channel contributions have to be taken into account, as we describe below.

### 3.2.1 The Analysis Method

Leptonic final state events are identified, and Table 3.4 summarizes the selection efficiencies, backgrounds and numbers of selected candidates for  $e^+e^-$ ,  $\mu^+\mu^-$ , and  $\tau^+\tau^-$  final states.

Figure 3.5 shows the  $\cos\theta$  distributions for  $e^+e^-$ ,  $\mu^+\mu^-$ , and  $\tau^+\tau^-$  candidates for the 1997-1998 data. The pre-1997 results are similar but have smaller acceptance ( $|\cos\theta| \leq 0.8$ ), reflecting the improved acceptance of an upgraded vertex detector used for the newer data, which

\*For  $\mathcal{P}_e$ , we use the convention that left-handed bunches have negative sign.

allowed for efficient track finding up to  $|\cos\theta| = 0.9$ . The SLD event totals including all data are 22,254, 16,844 and 16,084 for the electron-, muon- and tau-pair final states respectively).

An event-by-event maximum likelihood fit was used to incorporate the contributions of all the terms in the cross section and to include the effect of initial state radiation. There are three likelihood functions for individual lepton final states. All three lepton asymmetry parameters,  $A_e$  and  $A_l$  ( $A_\mu$ ), were obtained from  $\mu^+\mu^-$  ( $\tau^+\tau^-$ ) final states. The  $A_l$  results were combined with  $A_e$  obtained from the  $e^+e^-$  final state.

The likelihood function for muon- and tau-pair final states was defined as follows:

$$\mathcal{L}(x, s, \mathcal{P}_e; A_e, A_l) = \int ds' H(s, s') \left\{ \frac{d}{dx} \sigma_Z(x, s', \mathcal{P}_e; A_e, A_l) + \frac{d}{dx} \sigma_{Z\gamma}(x, s', \mathcal{P}_e; A_e, A_l) + \frac{d}{dx} \sigma_\gamma(x, s') \right\}, \quad (3.8)$$

where  $A_e$  and  $A_l$  ( $=A_\mu$  or  $A_\tau$ ) are free parameters and  $H(s, s')$  is a radiator function. The integration over  $s'$  is done with the program MIZA [?] to take into account the initial state radiation. The spread in the beam energy had a negligible effect.  $(d\sigma_Z/dx)$ ,  $(d\sigma_\gamma/dx)$ , and  $(d\sigma_{Z\gamma}/dx)$  are the tree-level differential cross sections for  $Z$  exchange, photon exchange, and their interference. The integration was performed before the fit to obtain the coefficients  $\bar{f}_Z$ ,  $\bar{f}_{Z\gamma}$ , and  $\bar{f}_\gamma$ , and the likelihood function becomes

$$\mathcal{L}(x, s, \mathcal{P}_e; A_e, A_l) = \bar{f}_Z(s) \Omega_Z(x, \mathcal{P}_e; A_e, A_l) + \bar{f}_{Z\gamma}(s) \Omega_{Z\gamma}(x, \mathcal{P}_e; A_e, A_l) + \bar{f}_\gamma(s) \Omega_\gamma(x), \quad (3.9)$$

where the differential cross sections have been factorized in analogy with equation 3.7. These coefficients gave the relative sizes of the three terms at the SLC center-of-mass energy (e.g.  $\sqrt{s} = 91.237 \pm 0.029$  GeV for the 1997-1998 run).

The  $e^+e^-$  final state includes both  $s$ -channel and  $t$ -channel  $Z$  and photon exchanges which yields four amplitudes and ten cross-section terms. All ten terms are energy-dependent. A maximum likelihood function for  $e^+e^-$  final states was defined by modifying Eqs. 3.8 and 3.9 to include all ten terms. The integration over  $s'$  was performed with DMIBA [?] to obtain the coefficients for the relative size of the ten terms.

### 3.2.2 Systematic Errors

Systematic uncertainties are summarized in Table 3.5, where it is made clear that this measurement is entirely statistics dominated. The errors for the 1997-98 dataset, which dominates the sample, are shown.

The uncertainty on the beam polarization is correlated among all the measurements and corresponds to an uncertainty on  $A_l$  of  $\pm 0.0008$ . The uncertainty in the amount of background and its effect on the fitted parameters are taken into account. The background contaminations have been derived from detailed Monte Carlo simulations as well as from studying the effect of cuts in background-rich samples of real data.

The radiative correction and their systematic errors are estimated using the MIZA [?] and DMIBA [?] programs whose inherent 1 per mil precision leads to negligible effects compared to our  $\sqrt{s}$  uncertainty. The uncertainty in the asymmetry parameters due to a  $\pm 1\sigma$  variation of  $\sqrt{s}$  (which affects radiative corrections) is of the order  $10^{-4}$ , except for the  $A_e$  determination from  $e^+e^-$  final states for which it is of order  $10^{-3}$ .

The dominant systematic error in the tau analysis results from the V-A structure of tau decay [?], which introduces a selection bias in the analysis. For example, if both taus decay to

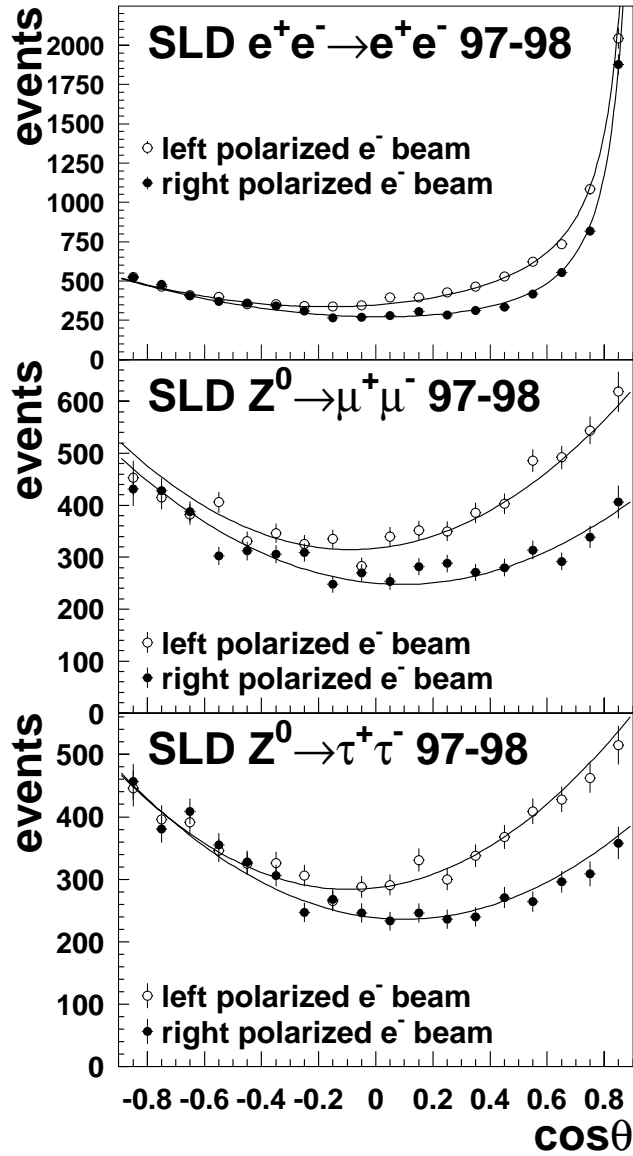


Figure 3.5: Polar-angle distributions for  $Z$  decays to  $e$ ,  $\mu$  and  $\tau$  pairs for the 1997-1998 SLD run. The solid line represents the fit, while the points with error bars show the data in bins of 0.1 in  $\cos\theta_{thrust}$ . For  $|\cos\theta_{thrust}| > 0.7$ , the data are corrected for a decrease in the detection efficiency with increasing  $|\cos\theta_{thrust}|$ .

Table 3.5: Summary of statistical and systematic uncertainties in units of  $10^{-4}$  for the 1997-1998 data. The superscript on each asymmetry refers to the lepton sample from which it was derived (electrons, muons or taus).

Source	$A_e^e$	$A_e^\mu$	$A_e^\tau$	$A_\mu^\mu$	$A_\tau^\tau$
Statistics	110	130	130	180	180
Polarization	8	8	8	8	8
Backgrounds	5	–	13	–	14
Radiative Correction	23	2	2	3	2
V-A	–	–	–	–	18
Charge Confusion	–	–	–	7	11
Detector asymmetry	–	–	–	–	4
Nonuniform efficiency	2	–	–	–	–

$\pi\nu$ , helicity conservation requires that both pions generally have lower momentum for a left-handed  $\tau^-$  and right-handed  $\tau^+$  and higher momentum otherwise. This effect, which biases the reconstructed event mass, is large at the SLD because the high beam polarization induces a very high and asymmetric tau polarization as a function of polar angle. The value of  $A_e$  extracted from  $\tau^+\tau^-$  final states is not affected since the overall relative efficiencies for left-handed beam and right-handed beam events are not changed significantly (only the polar angle dependence of the efficiencies are changed).

### 3.2.3 Results

Results for all SLD runs are combined while accounting for small effects due to correlations in systematic uncertainties (polarization and average SLD center-of-mass energy). From purely leptonic final states, one obtains  $A_e = 0.1544 \pm 0.0060$ . This  $A_e$  result is combined with the left-right asymmetry measurement in the final tabulation of SLD leptonic asymmetry results given below :

$$\begin{aligned}
 A_e &= 0.1516 \pm 0.0021 \text{ (with } A_{LR}^e \text{)} ; \\
 A_\mu &= 0.142 \pm 0.015 ; \text{ and} \\
 A_\tau &= 0.136 \pm 0.015.
 \end{aligned}
 \tag{3.10}$$

These results are consistent with lepton universality and hence can be combined into  $A_l$ , which in the context of the standard model is simply related to the electroweak mixing angle. The result is discussed in the following section.

## 3.3 Combined Results for $\sin^2 \theta_W^{\text{eff}}$

The final  $A_{LR}$  result is an average, formed while accounting for correlated systematic effects, of all SLD  $A_{LR}$  measurements (1992, 1993, 1994-1995, 1996, and 1997-1998). The combined result for  $A_{LR}$  is  $0.15138 \pm 0.00216$ .

Assuming lepton universality, the  $A_{LR}$  result and the results on the leptonic left-right forward-backward asymmetries can be combined, where small correlated systematics are ac-

counted for, yielding

$$\mathcal{A}_\ell = 0.15130 \pm 0.00207. \quad (3.11)$$

The correlation matrix is given in [Table 3.6](#). This measurement is equivalent to a determination

$$\sin^2 \theta_W^{\text{eff}} = 0.23098 \pm 0.00026, \quad (3.12)$$

where the total error and corresponding systematic error of  $\pm 0.00012$ , are more precise than those obtained by other techniques.

	$\mathcal{A}_e$	$\mathcal{A}_\mu$	$\mathcal{A}_\tau$
$\mathcal{A}_e$	1.000		
$\mathcal{A}_\mu$	0.038	1.000	
$\mathcal{A}_\tau$	0.033	0.007	1.000

[Table 3.6](#): Correlation coefficients between  $\mathcal{A}_e$ ,  $\mathcal{A}_\mu$  and  $\mathcal{A}_\tau$



# Chapter 4

## The $\tau$ Polarisation Measurements

### 4.1 Introduction

For pure Z exchange produced in the interaction of the unpolarised  $e^+e^-$  beams at LEP, the dependence of  $\mathcal{P}_\tau$  on  $\theta_{\tau^-}$  can be described by a simple relation expressed in terms of the two neutral current asymmetry parameters,  $\mathcal{A}_\tau$  and  $\mathcal{A}_e$ , and the forward-backward asymmetry of the tau,  $A_{\text{FB}}$ :

$$\mathcal{P}_\tau(\cos\theta_{\tau^-}) = -\frac{\mathcal{A}_\tau(1 + \cos^2\theta_{\tau^-}) + 2\mathcal{A}_e \cos\theta_{\tau^-}}{(1 + \cos^2\theta_{\tau^-}) + \frac{8}{3}A_{\text{FB}} \cos\theta_{\tau^-}}. \quad (4.1)$$

The four LEP experiments use kinematic distributions of the  $\tau$  decay products to measure the polarisation as a function of  $\cos\theta_{\tau^-}$  in data collected during the 1990-95 Z running period. Because the actual reaction does not only contain the pure Z propagator but also includes contributions from the photon propagator,  $\gamma$ -Z interference, and other photonic radiative corrections, the parameters obtained using Equation 4.1 are approximations to  $\mathcal{A}_\tau$  and  $\mathcal{A}_e$ . In order to distinguish between these pure Z parameters and those which include the small non-Z effects, the measured parameters are denoted as  $\langle\mathcal{P}_\tau\rangle$  and  $A_{\text{FB}}^{\text{pol}}$  in the literature.  $\langle\mathcal{P}_\tau\rangle$  is the  $\tau$  polarisation averaged over all production angles and  $A_{\text{FB}}^{\text{pol}}$  is the forward-backward polarisation asymmetry. If one had only pure Z exchange, these would be trivially related to the neutral current asymmetry parameters:  $\langle\mathcal{P}_\tau\rangle = -\mathcal{A}_\tau$  and  $A_{\text{FB}}^{\text{pol}} = -\frac{3}{4}\mathcal{A}_e$ . ZFITTER [20] is used to effectively convert from  $\langle\mathcal{P}_\tau\rangle$  and  $A_{\text{FB}}^{\text{pol}}$  to  $\mathcal{A}_\tau$  and  $\mathcal{A}_e$ , respectively, by correcting for the contributions of the photon propagator,  $\gamma$ -Z interference and electromagnetic radiative corrections for initial state and final state radiation. These corrections have a  $\sqrt{s}$  dependence which arise from the non-Z contributions to  $\langle\mathcal{P}_\tau\rangle$  and  $A_{\text{FB}}^{\text{pol}}$ . This latter feature is important since the off-peak data are included in the event samples for all experiments. Ultimately, all LEP collaborations express their  $\tau$  polarisation measurements in terms of  $\mathcal{A}_\tau$  and  $\mathcal{A}_e$ .

It is important to remark that this method of measuring  $\mathcal{P}_\tau(\cos\theta_{\tau^-})$  yields nearly independent determinations of  $\mathcal{A}_\tau$  and  $\mathcal{A}_e$ . Consequently, the  $\tau$  polarisation measurements provide not only a determination of  $\sin^2\theta_{\text{eff}}^{\text{lept}}$  but also test the hypothesis of the universality of the couplings of the Z to the electron and  $\tau$  lepton.

### 4.2 Experimental Methods

Each LEP experiment measures  $\mathcal{P}_\tau$  using the five  $\tau$  decay modes  $e\nu\bar{\nu}$ ,  $\mu\nu\bar{\nu}$ ,  $\pi\nu$ ,  $\rho\nu$  and  $a_1\nu$  [66–69]. The five decay modes do not all have the same sensitivity to the  $\tau$  polarisation. The



$\tau \rightarrow \pi\nu$  mode \* has a large sensitivity because it is a two body decay involving a spinless particle, whereas the  $\tau \rightarrow e\nu\bar{\nu}$  and  $\tau \rightarrow \mu\nu\bar{\nu}$  modes have substantially lower sensitivities because the  $\tau$  decays to three fermions, two of which are undetected neutrinos. The  $\tau \rightarrow \rho\nu$  and  $\tau \rightarrow a_1\nu$  decays are somewhat more complex because they involve spin-1 particles. If only the final-state particle energies are used to discriminate between helicity states there is a significant loss of sensitivity. Much of this sensitivity reduction can be regained by using those kinematic properties of the  $\rho$  and  $a_1$  decays which are related to the parent's spin orientation. The maximum sensitivity for each decay mode, defined as  $\frac{1}{\sqrt{N}\sigma}$  where  $\sigma$  is the statistical error on the polarisation measurement using  $N$  events for  $\mathcal{P}_\tau=0$ , is given in Table 4.1. It assumes that all the available information in the decay is used with full efficiency both for the case when the  $\tau$  direction information is not used and for the case when it is used. The additional information provided by the tau direction is an azimuthal angle of the decay of the hadronic system in the  $\tau$  rest frame [70]. When included in the decay distributions of spin-1 hadronic channels with even modest precision an improvement in the sensitivity is achieved. A measure of the weight with which a given decay mode ideally contributes to the overall measurement of the polarisation is given by that decay mode's sensitivity squared multiplied by its branching ratio. Normalised ideal weights, which are calculated assuming maximum sensitivity and perfect identification efficiency and purity, for each decay mode, are also given in Table 4.1. As can be seen, the  $\tau \rightarrow \rho\nu$  and  $\tau \rightarrow \pi\nu$  channels are expected to dominate the combined polarisation measurement, especially if information from the tau direction is not used. The actual sensitivity achieved by each experiment for its selected event sample is degraded because of inefficiencies in the process of selecting a sample of decays and by the presence of background in the sample. Much of the background, however, retains some polarisation information which is exploited by the fitting procedure.

	$\tau \rightarrow \rho\nu$	$\tau \rightarrow \pi\nu$	$\tau \rightarrow e\nu\bar{\nu}$	$\tau \rightarrow \mu\nu\bar{\nu}$	$\tau \rightarrow a_1\nu$ $a_1 \rightarrow \pi^\pm\pi^+\pi^-$
Branching ratio	0.25	0.12	0.18	0.17	0.09
Maximum Sensitivity (no $\tau$ direction)	0.49	0.58	0.22	0.22	0.45
(with $\tau$ direction)	0.58	0.58	0.27	0.27	0.58
Normalised ideal weight (no $\tau$ direction)	0.44	0.30	0.06	0.06	0.13
(with $\tau$ direction)	0.47	0.22	0.07	0.07	0.17

Table 4.1: The branching ratios, maximum sensitivity [70] and normalised ideal weight for the five decay modes used in the analysis. The ideal weight is calculated as the product of the branching ratio and the square of the maximum sensitivity. Presented in the last line of the table is the ideal weight for each channel divided by the sum of the ideal weights of the five channels.

In all analyses, a value of  $\mathcal{P}_\tau$  is extracted from the data by fitting linear combinations of positive and negative helicity distributions in kinematic variables appropriate to each  $\tau$  decay channel to the data, where the two distributions are obtained from Monte Carlo simulation.

\*As no experiment discriminates between charged pions and kaons, the  $\tau \rightarrow \pi\nu$  channel also includes  $\tau \rightarrow K\nu$  decays and the  $\tau \rightarrow \rho\nu$  channel also includes  $\tau \rightarrow K\pi^0\nu$  decays.

For example, in the  $\tau \rightarrow \mu\nu\bar{\nu}$ ,  $\tau \rightarrow e\nu\bar{\nu}$  and  $\tau \rightarrow \pi\nu$  channels, the energy of the charged particle decay divided by the beam energy is the appropriate kinematic variable. For the  $\tau \rightarrow \rho\nu$  and  $\tau \rightarrow a_1\nu$  channels, an ‘optimal variable’ [70],  $\omega$ , is employed by all experiments. Using Monte Carlo distributions in the fitting procedure allows for simple inclusion of detector effects and their correlations, efficiencies and backgrounds. Any polarisation dependence in the backgrounds from other  $\tau$  decays are automatically incorporated into these analyses. The systematic errors associated with the detector then amount to uncertainties in how well the detector response is modelled by the Monte Carlo simulation of the detector, whereas the errors associated with uncertainties in the underlying physics content in the distributions arise from uncertainties in the Monte Carlo generators of the signal and backgrounds. The spin correlations between the two  $\tau$ -leptons produced in a decay are treated differently in the different experiments and are discussed below.

The ALEPH [66] analysis also includes the  $\tau^- \rightarrow \pi^- 2\pi^0\nu$  decays in addition to those listed in Table 4.1 and uses information from the  $\tau$  direction for the semileptonic decays, as discussed in [70]. The addition of the tau direction information ideally increases the sensitivity of the  $\tau \rightarrow a_1\nu$  and  $\tau \rightarrow \rho\nu$  channels by the amounts indicated in Table 4.1.

To the analysis of the five channels listed in Table 4.1, DELPHI [67] and L3 [68] add an inclusive hadronic analysis in which the single charged track (one-prong) semileptonic decay modes are collectively analysed. This approach yields a high overall efficiency for these modes by sacrificing the optimal sensitivity characterizing the analysis of high purity channels. For DELPHI and L3 the correlations between the polarisation measurements from their inclusive hadronic analysis and measurements using separately identified single-track hadronic channels are small enough that significant improvements are achieved when both results are combined.

The OPAL [69]  $\mathcal{A}_\tau$  and  $\mathcal{A}_e$  results are based entirely on an analysis in which all five exclusive channels listed in Table 4.1 are combined in a global binned maximum likelihood analysis. A single fit to all distributions in the kinematic observables of all decay modes and  $\cos\theta_{\tau^-}$  yield  $\langle\mathcal{P}_\tau\rangle$  and  $A_{\text{FB}}^{\text{pol}}$ . When both  $\tau^+$  and  $\tau^-$  decays of a given event are identified, the event is analysed as a whole. This global analysis approach fully accounts for the intrinsic correlation between the helicities of the  $\tau^+$  and  $\tau^-$  produced in the same Z decay, an effect which is accounted for by the other experiments by applying a correction to the statistical errors of the fit results. In such a global analysis, the evaluation of the systematic errors automatically incorporate all correlations between the systematic uncertainties in the different channels. For the channel-by-channel analyses of ALEPH, L3 and DELPHI, the correlation in the systematic errors between channels are taken into account in the combination.

DELPHI [67] augments their exclusive five channel and inclusive one-prong analysis with a separate neural network analysis of its 1993-1995 one-prong data set. The neural network is used to classify all one-prong decays as either  $\tau \rightarrow \rho\nu$ ,  $\tau \rightarrow \pi\nu$ ,  $\tau \rightarrow e\nu\bar{\nu}$ ,  $\tau \rightarrow \mu\nu\bar{\nu}$  or  $\tau^- \rightarrow \pi^- 2\pi^0\nu$ . A simultaneous fit for  $\mathcal{P}_\tau$  as a function of  $\cos\theta_{\tau^-}$  is performed with  $\mathcal{A}_\tau$  and  $\mathcal{A}_e$  determined from a separate fit to the  $\mathcal{P}_\tau(\cos\theta_{\tau^-})$  functional form as described below. As with OPAL’s global analysis, the channel-to-channel correlated systematic errors are automatically evaluated in this analysis.

ALEPH [66] and L3 [68] complement their analyses of the kinematic distributions of the different decay modes, by including information from event acollinearity to measure the tau polarisation. This has the advantage of being sensitive to detector related systematics errors that are different from those associated with the measurements of spectra.

Examples of the different kinematic distributions from the different experiments are shown in Figures 4.1 to 4.4.

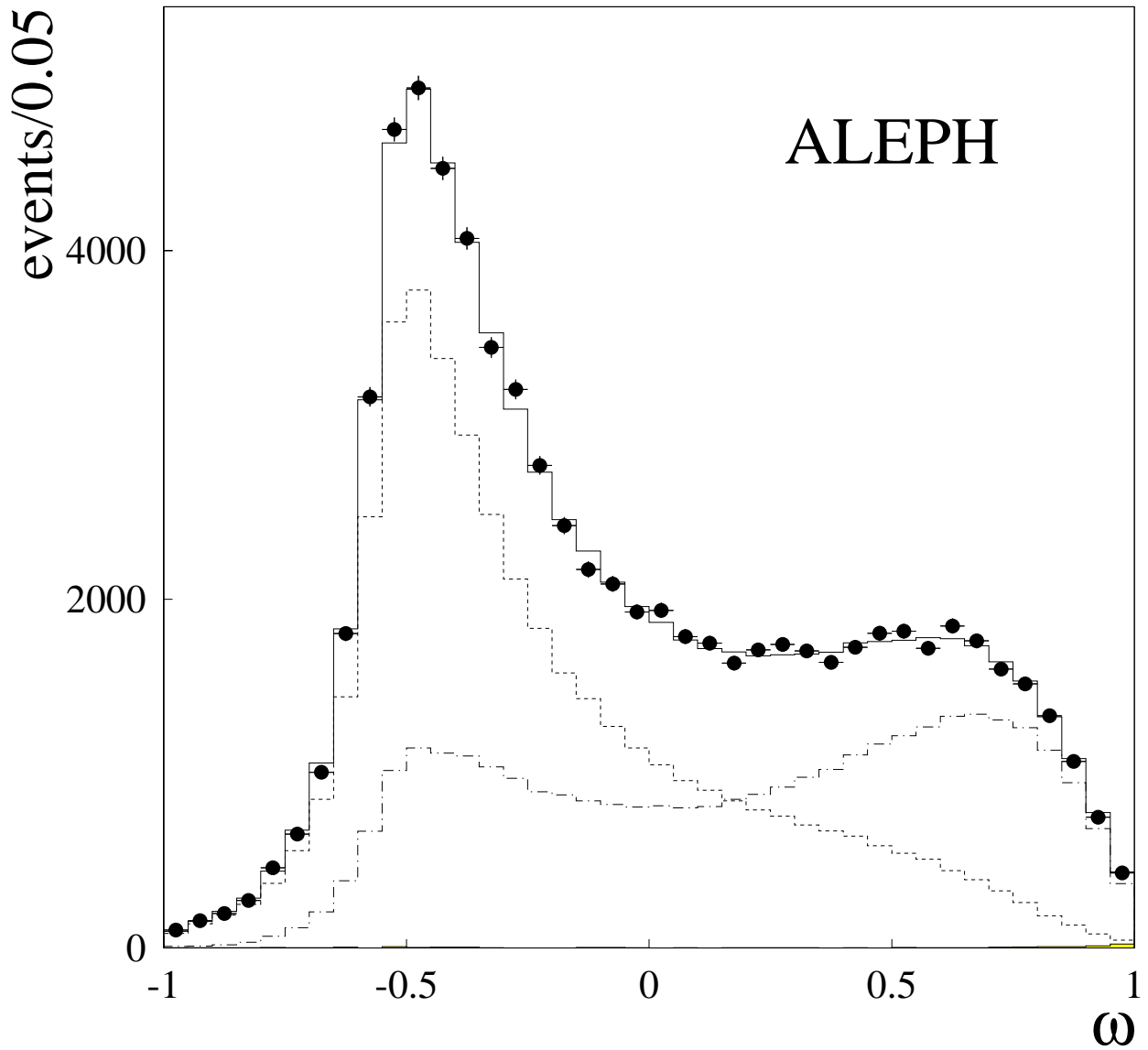


Figure 4.1: The measured spectrum of the polarisation-sensitive variable for the  $\tau \rightarrow \rho\nu$  decays in the ALEPH experiment. The variable is the optimal variable  $\omega$ . The dotted and dashed lines correspond to the contributions of left- and right-handed  $\tau$ 's respectively. The shaded area is the non- $\tau$  background contribution. ▲ ▲

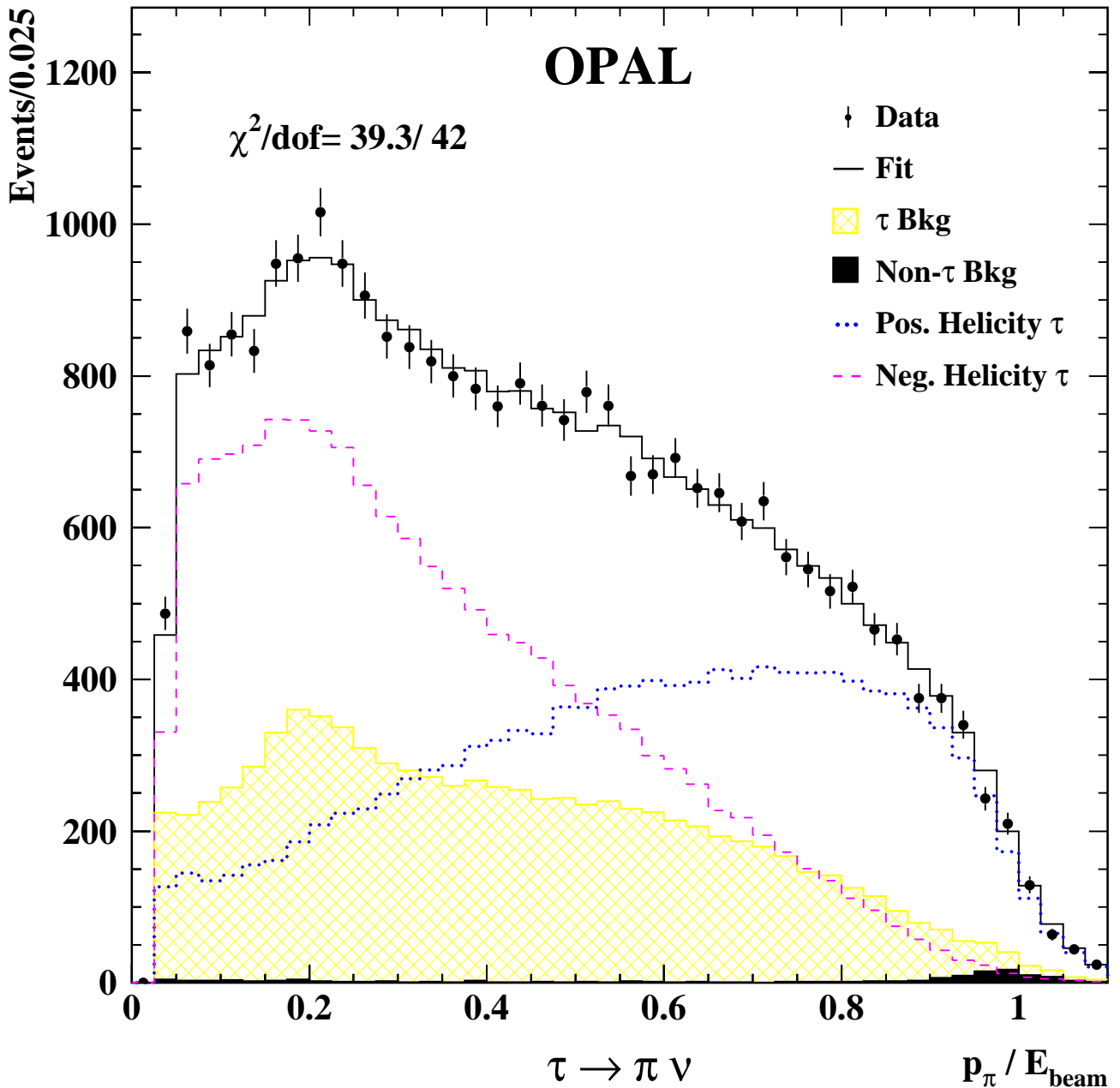


Figure 4.2: The measured distributions in the polarisation-sensitive variable for the  $\tau \rightarrow \pi \nu$  decays in the OPAL experiment. The variable is the ratio of the measured charged hadron momentum to the beam energy. The the data, shown by points with error bars, are integrated over the whole  $\cos \theta_{\tau^-}$  range. Overlaying this distribution are Monte Carlo distributions for the positive (dotted line) and negative (dashed line) helicity  $\tau$  leptons and for their sum including background, assuming a value for  $\langle \mathcal{P}_\tau \rangle$  equal to the fitted average polarisation. The hatched histogram represents the Monte Carlo expectations of contributions from cross-contamination from other  $\tau$  decays and the dark shaded histogram the background from non- $\tau$  sources. The level of agreement between the data and Monte Carlo distributions is quantified by quoting the  $\chi^2$  and the number of degrees of freedom.

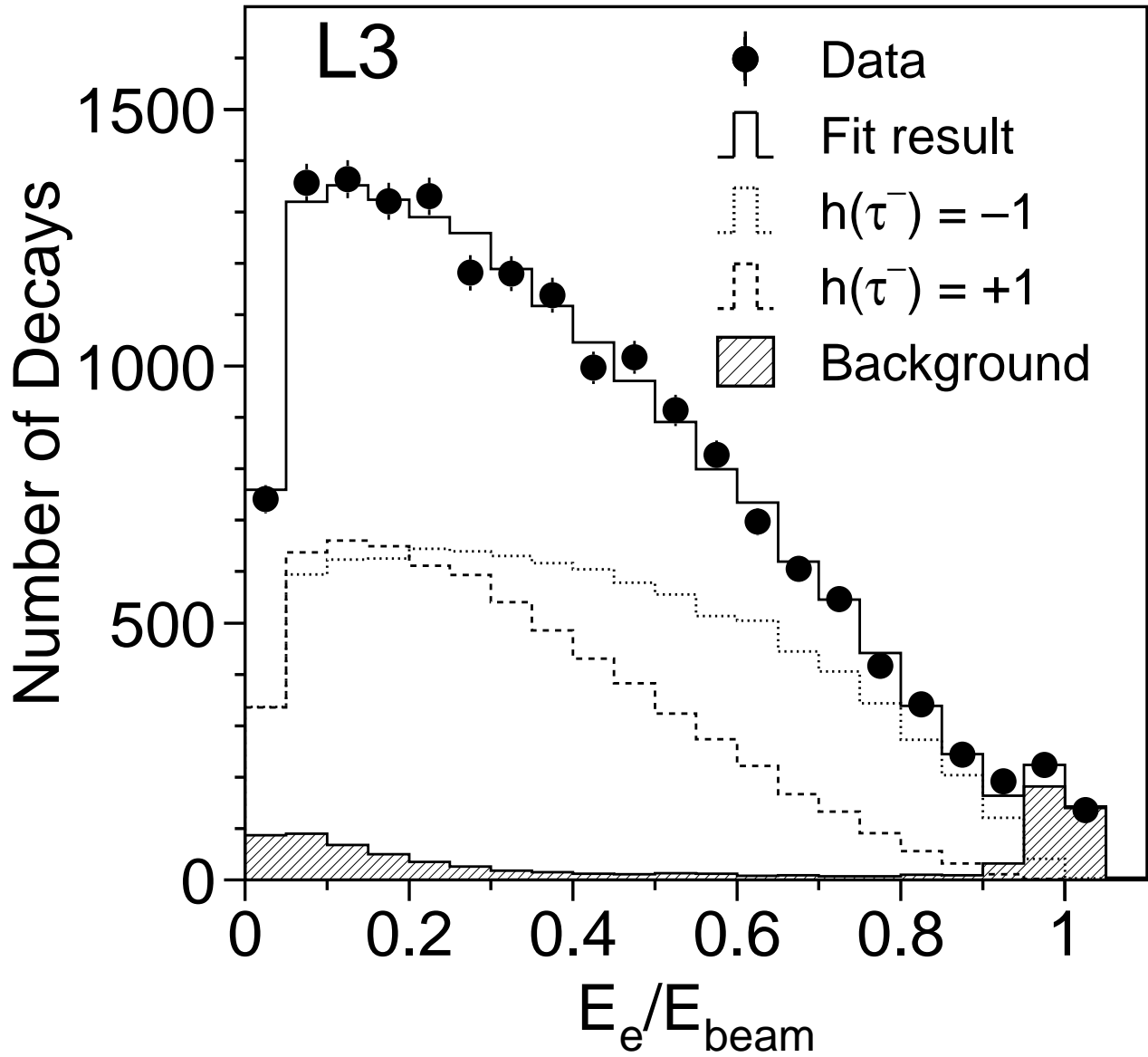


Figure 4.3: The measured spectrum of the polarisation-sensitive variable for the  $\tau$  decaying to electrons in the L3 experiment. The variable is the ratio of the measured electron energy to the beam energy. The data are compared to the results of the polarisation fit. The two helicity components and the background are shown separately.



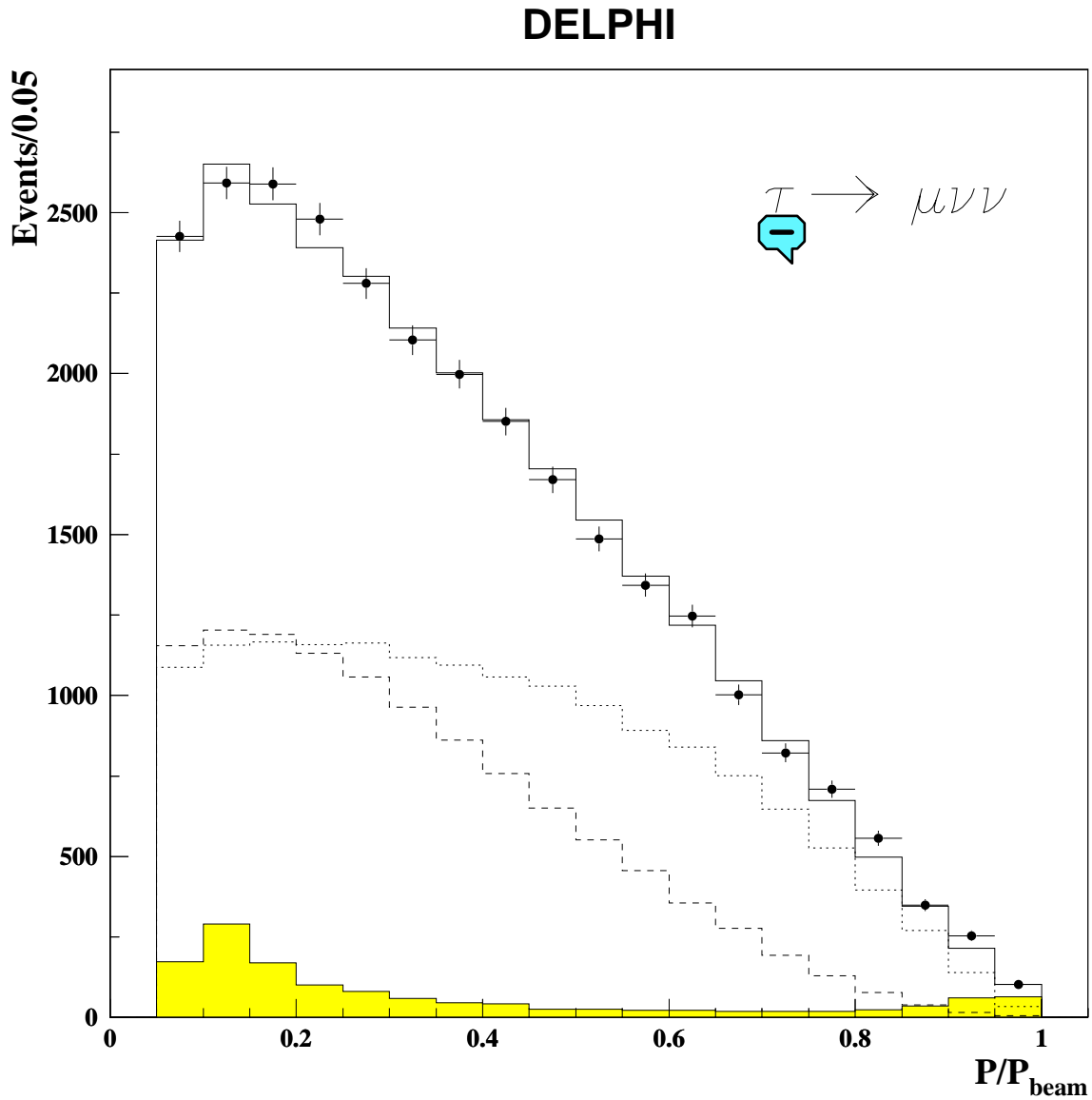


Figure 4.4: The measured spectrum of the polarisation-sensitive variable for the  $\tau \rightarrow \mu \nu \bar{\nu}$  decays in the DELPHI experiment. The variable is the ratio of the measured muon momentum to the beam energy. The data are compared to the results of the polarisation fit. The circles are data and the solid line is simulated data for the fitted values of  $\mathcal{A}_\tau$  and  $\mathcal{A}_e$ . The shaded area is background and the dashed and dotted lines correspond to the positive and negative polarisation contributions respectively.



In order to extract  $\mathcal{A}_\tau$  and  $\mathcal{A}_e$  from their data, ALEPH, DELPHI and L3 measure the average polarisation as a function of  $\cos\theta_{\tau^-}$  and then perform a `separate` fit for the two parameters using the theoretical expectation of the dependence. The results quoted by OPAL [69], which depend on a single maximum likelihood fit, do not explicitly use measurements of the average polarisation as a function of  $\cos\theta_{\tau^-}$ , although such fits are performed as cross checks and for graphical presentation. ALEPH, L3 and OPAL use Equation 4.1 in their fits but treat  $A_{FB}$  differently as discussed in section 4.3. Small corrections for the effects of initial state radiation, the photon propagator and  $\gamma$ -Z interference, and the fact that not all data are collected at the peak of the Z resonance are incorporated into the quoted values of  $\mathcal{A}_\tau$  and  $\mathcal{A}_e$ . These corrections, on the order of  $\mathcal{O}(0.005)$ , are calculated using ZFITTER [20]. DELPHI incorporates these corrections directly into the fit they perform by using the  $\mathcal{A}_\tau$  and  $\mathcal{A}_e$  dependent ZFITTER prediction as an estimation of  $\mathcal{P}_\tau(\cos\theta_{\tau^-})$  averaged over the luminosity-weighted centre-of-mass energies. This automatically includes the QED and weak effects as a function of  $\cos\theta_{\tau^-}$ , rather than as a `separate` correction as in the approach taken by the other three LEP experiments.

The LEP combination is made using the overall results from each experiment. This ensures that correlated errors between channels are properly taken into account since they are treated correctly by the individual experiments as discussed below.

Although the size of the event samples used by the four experiments are roughly equal, a smaller error is quoted by ALEPH. This is largely associated with the higher granularity of the ALEPH electromagnetic calorimeter. The tau ‘jets’ are tightly collimated at LEP energies which results in a substantial overlap of the energy deposited in the calorimeter by different particles. A calorimeter with a higher granularity is better able to identify the individual photons from  $\pi^0$  decay and therefore provides greater discrimination between hadronic decay channels of the tau. This results in improved signal-to-noise thereby providing greater polarisation sensitivity and lower systematic errors.

### 4.3 Systematic Errors

The combined statistical errors on  $\mathcal{A}_\tau$  and  $\mathcal{A}_e$  are 0.0035 and 0.0048, respectively. Systematic errors on these parameters which are less than 0.0003 will not alter the combined errors when two significant figures are quoted. Therefore, such systematic errors are considered to be negligible.

The systematic errors on  $\mathcal{A}_e$  are considerably smaller than the systematic errors on  $\mathcal{A}_\tau$  because, for the most part, the systematic effects are symmetric in  $q \times \cos(\theta)$ . This includes large cancellations of the Monte Carlo statistical errors which arise by using the same Monte Carlo samples in reflected  $\cos(\theta)$  bins. Different approaches to evaluating the degree of cancellation of the  $\mathcal{A}_e$  systematic errors are adopted by the four experiments and are detailed in References [66–69].

There are two broad categories of systematic error in these measurements: those associated with the uncertainty of the underlying physics assumptions and their treatment, and those associated with the modelling of the detector. The latter category of systematic error depend on the details of each of the individual detectors. Although three of the four experiments depend on the same detector simulation software, GEANT [26], the designs of the four detectors are sufficiently different that these detector related errors are uncorrelated between experiments. However, these uncertainties can be strongly correlated between measurements from different decay channels performed with the same detector. For example, the uncertainty in the momentum scale for one of the detectors is independent of that in the other three detectors, but the

momentum scale error is correlated between the  $\mathcal{P}_\tau$  measurements from different decay modes made with the same detector. Because each of the experiments takes these correlations into account when quoting a systematic error on the measurements of  $\mathcal{A}_\tau$  and  $\mathcal{A}_e$  using all channels, only the global results from each of the four experiments can be reliably combined to give a LEP average.

Turning now to the uncertainty of the treatment of the physics of  $\tau$  production and decay, there are a number of systematic uncertainties in this category that are common to all four experiments. One set of these uncertainties affect all decay modes in the same way whilst others are different for each  $\tau$  decay mode. The origins of some of the common uncertainties are the common software tools that are used to describe the production and decay of the  $\tau$  (KORALZ [31]); the major backgrounds [28,31,71–74]; and the tools used to interpret the data in terms of the Standard Model [20]. Another source of the common errors arise from reliance on the same physics input used in the analyses of the four experiments, such as the branching ratios of the  $\tau$ .

In the category of systematic uncertainty that affects all decay modes, the following have been identified as potential sources of error common to all experiments:

- ZFITTER treatment of  $\sqrt{s}$  dependence of  $\mathcal{P}_\tau$ , including the effects of initial state radiation, and of photon propagator and  $\gamma$ -Z interference. This amounts to the application of the Standard Model interpretation of  $\langle \mathcal{P}_\tau \rangle$  and  $A_{\text{FB}}^{\text{pol}}$  in terms of  $\mathcal{A}_\tau$  and  $\mathcal{A}_e$ . Although the experiments introduce this interpretation at different stages of their analyses, it effectively amounts to corrections of  $\mathcal{O}(0.005)$  to both  $\langle \mathcal{P}_\tau \rangle$  and  $A_{\text{FB}}^{\text{pol}}$  and it is estimated that the uncertainty on this correction is negligible. For example, variations of the unknown parameters in the model, such as the Higgs mass, alter this correction by  $\pm 0.0002$ . Since all experiments rely on ZFITTER for this treatment, the error is common across experiments as well as to  $\mathcal{A}_\tau$  and  $\mathcal{A}_e$ .
- Electromagnetic radiative corrections for initial state radiation from the  $e^+$  and  $e^-$  and final state radiation from the  $\tau^+$  and  $\tau^-$ . This radiation influences the measurement in two ways. The first relates to the fact that the experiments measure  $\langle \mathcal{P}_\tau \rangle$  and  $A_{\text{FB}}^{\text{pol}}$  which are integrated over  $s'$ ;  $s'$  being the centre-of-mass energy of the  $\tau$ -pair system excluding radiation. This effect is included in the  $\mathcal{O}(0.005)$  correction previously discussed. The second influence relates to changes to the kinematic distributions caused by initial and final state radiation. In this case, the four experiments rely on the KORALZ Monte Carlo event generator to take these effects into account. This radiation is calculated to  $\mathcal{O}(\alpha^2)$  and includes exclusive exponentiation in both initial and final state radiation. Although interference between the initial and final state radiation is not included in the generator when producing the simulated events, such effects have negligible impact on the  $\mathcal{P}_\tau$  measurements. Because of its precision, the treatment of initial and final state radiation, although common to all experiments, introduces no significant contribution to the systematic error.
- Born level mass terms leading to helicity flip configurations. This is a small effect  $\mathcal{O}(10^{-3})$  which has a negligible influence on the measurements, but which is included in the KORALZ treatment nonetheless.
- The value of  $A_{\text{FB}}$  used in the fit. The different experiments treat this differently. ALEPH and DELPHI use the Standard Model values of  $A_{\text{FB}}$  with appropriate  $\sqrt{s}$  dependence.



OPAL uses its measured values of  $A_{\text{FB}}$  for  $\tau$ -pairs at the different values of  $\sqrt{s}$ . L3 assumes the Standard Model relation  $A_{\text{FB}} \equiv \frac{3}{4} \mathcal{A}_\tau$  in the denominator of Equation 4.1. Since  $A_{\text{FB}}$  enters into the analysis as a small number in the normalisation, its uncertainty introduces a correspondingly small systematic error for each experiment. Although the Standard Model assumptions regarding  $A_{\text{FB}}$  by ALEPH, DELPHI and L3 imply that some correlation exists from this source between the measurements of these three experiments, it is negligible and consequently ignored in the combined LEP results. The OPAL treatment introduces a small correlation between between the  $\tau$ -polarisation measurement and the OPAL  $A_{\text{FB}}$  measurement. This introduces a negligible effect in the combined result.

In conclusion, all of these effects are theoretically well defined and have been calculated to adequate precision for the measurements at hand thereby contributing nearly negligible uncertainty to the common systematic error. Of these, the ZFITTER error of  $\pm 0.0002$  is included as a common error in the LEP combination.

Concerning the category of uncertainty that affects each decay mode separately, the following sources of potentially common systematic error have been identified:

- Branching ratios of the various  $\tau$  decay modes. These arise since the purity for selecting any particular decay mode for polarisation analysis is not unity. All experiments use the world average values of the branching ratios as determined by the Particle Data Group [75, 76], along with the quoted errors. Consequently, the components of the systematic error which are associated with the uncertainty in the branching ratios is an error correlated between experiments. These errors are taken into account in the combined error, and are shown in Table 4.2 for the combined error on  $\mathcal{A}_\tau$  and  $\mathcal{A}_e$  for each of the experiments.
- Radiative corrections for  $\tau$  leptonic final states. The radiation in the decays  $\tau \rightarrow e\nu\bar{\nu}$  and  $\tau \rightarrow \mu\nu\bar{\nu}$  are treated exactly to  $\mathcal{O}(\alpha)$  in KORALZ and negligible contributions to the systematic error are introduced by this treatment.
- Radiative corrections for  $\tau$  hadronic final states. Unlike radiation from leptons, there is no precise formalism for handling these corrections. The KORALZ generator uses an  $\mathcal{O}(\alpha)$  correction in the leading logarithmic approximation as implemented in the PHOTOS software package [77]. In the  $\tau \rightarrow \pi\nu$  channel, this radiation affects the polarisation at the 0.01 level whilst for the  $\tau \rightarrow \rho\nu$  the effects are less than half that. Theoretical work [78, 79] indicates that the treatment of radiation in the decay  $\tau \rightarrow \pi\nu\gamma$  is valid to the 5% level. Consequently, the uncertainties in the decay radiation treatment contribute at the 0.0005 level to the systematic error of the  $\tau \rightarrow \pi\nu$ , and much less than that to the error on the combined measurements. Unfortunately, no analogous theoretical studies have been performed for the  $\tau \rightarrow \rho\nu\gamma$  decay. Following reference [77], the error on the treatment of the radiation is approximately  $1/\ln(m_\tau/m_\rho)$  of the magnitude of the effect of the radiation on the measurement of  $\mathcal{P}_\tau$ . This results in an error of no more than 0.001 on  $\mathcal{A}_\tau$  and a negligible error on  $\mathcal{A}_e$ . The equivalent radiation effects for the other hadronic decay modes introduce a negligible contribution to the combined systematic error.
- Hadronic decay modelling. Model dependent uncertainties in  $a_1$  decay have been evaluated by all experiments. These uncertainties arise both in the analysis of the  $\tau \rightarrow a_1\nu$  channel itself and in the analysis of channels where backgrounds from the  $a_1$  can be significant, such as the  $\tau \rightarrow \rho\nu$ . These errors can be common to all experiments, but will



vary in sensitivity depending on the purity of the the samples and details of the analysis. The KORALZ [80] Monte Carlo simulation of the  $\tau \rightarrow \nu; \pi^0 \pi^0$  and  $\tau \rightarrow \nu; 3\pi^0$  decays, which are backgrounds to some of the  $\mathcal{P}_\tau$  analysing channels, also have model dependencies with a corresponding uncertainty. Consequently, the experiments estimate how much these deficiencies affect the  $\mathcal{P}_\tau$  measurements. These hadronic modelling errors are summarised in Table 4.2 and are found to contribute a small effect to the measurements over all channels.

- Bhabha background. ALEPH and OPAL use the BHWIDE Monte Carlo generator [71] to describe this background whilst L3 uses the generator described in reference [81] and DELPHI uses the BABAMC [34] and UNIBAB [35] in addition to BHWIDE. The use of BHWIDE by three of the experiments potentially introduces a common systematic error. The contributions from the use of this generator to the errors on the measurements from each experiment are shown in Table 4.2. In the case of experiments where there is very little Bhabha background, the errors are negligible. It should be noted that much of the uncertainty is detector-specific, and therefore does not constitute a large common systematic error.
- The background from two-photon events can be problematic since the Monte Carlo generators used by the experiments do not include initial state radiation. There is a potential danger that the measured event transverse momentum ( $p_T$ ), a quantity which discriminates between  $\tau$ -pair events, which have large  $p_T$ , and two-photon events which have small  $p_T$ , is sensitive to initial state radiation: low energy events, which can have a high  $\mathcal{P}_\tau$  analysing power, are not perfectly modelled in the simulation. This is common to all experiments, but the sensitivity of a given experiment to the effect depends on the effectiveness with which two-photon events are identified and removed from the sample. These errors are taken into account in the combined error with the contributions from each experiment shown in Table 4.2 but do not represent a significant correlation because some experiments make corrections to this background based on control samples in their own data.
- The modelling uncertainty of the multihadronic background introduces negligible errors in all channels but the  $\tau \rightarrow a_1\nu$ . However, because the background itself is small and the weight of the  $\tau \rightarrow a_1\nu$  measurement is not high, this is a negligible contribution to the error on  $\mathcal{P}_\tau$  from all channels.
- The modelling of  $\mu$ -pair background has a negligible error. Any uncertainty arising from  $\mu$ -pair events is evaluated as a detector-related systematic error.

## 4.4 Results

The results for  $\mathcal{A}_\tau$  and  $\mathcal{A}_e$  obtained by the four LEP collaborations [66–69] are shown in Table 4.3. Figure 4.5 shows the measured values of  $\mathcal{P}_\tau$  as a function of  $\cos\theta_{\tau^-}$  for all four LEP experiments. The measurements from all experiments are consistent with each other and are combined to give values of  $\mathcal{A}_\tau$  and  $\mathcal{A}_e$  from a fit which includes the effects of correlated errors. The combined results are included in Table 4.3. These results are also summarized in Figure 4.6.

	ALEPH		DELPHI		L3		OPAL	
	$\delta\mathcal{A}_\tau$	$\delta\mathcal{A}_e$	$\delta\mathcal{A}_\tau$	$\delta\mathcal{A}_e$	$\delta\mathcal{A}_\tau$	$\delta\mathcal{A}_e$	$\delta\mathcal{A}_\tau$	$\delta\mathcal{A}_e$
(1) ZFITTER	0.0002	0.0002	0.0002	0.0002	0.0002	0.0002	0.0002	0.0002
(2) $\tau$ branching ratios	0.0003	0.0000	0.0016	0.0000	0.0007	0.0012	0.0011	0.0003
(3) Bhabha background	0.0000	0.0000	0.0012	0.0000	0.0000	0.0000	0.0000	0.0000
(4) two-photon background	0.0000	0.0000	0.0005	0.0000	0.0007	0.0000	0.0000	0.0000
(5) radiative corrections	0.0000	0.0000	0.0010	0.0000			0.0001	0.0001
(6) hadronic decay modelling	0.0012	0.0008	0.0000	0.0000	0.0010*	0.0001*	0.0025	0.0005

Table 4.2: The magnitude of the major common systematic errors on  $\mathcal{A}_\tau$  and  $\mathcal{A}_e$  by category for each of the LEP experiments. \*L3 quotes a combined estimate of systematic errors from radiative corrections and  $a_1$  modelling which are in common with the other LEP experiments.

There are small ( $\leq 5\%$ ) statistical and, in some cases, systematic correlations between  $\mathcal{A}_\tau$  and  $\mathcal{A}_e$  performed by a single experiment. There are also systematic correlations between the different experimental values as discussed in the previous section. Therefore a single fit to all of the data using the complete  $8 \times 8$  error correlation matrix, given in Table 4.4, is used to obtain the LEP combined values of these two parameters.

We take the  $\pm 0.0002$  ZFITTER errors to be fully correlated between  $\mathcal{A}_\tau$  and  $\mathcal{A}_e$ . Other systematic errors listed in Table 4.2 are taken to be fully correlated between either  $\mathcal{A}_\tau$  or  $\mathcal{A}_e$  measurements. These are used to calculate the inter-experiment off-diagonal elements of the error correlation matrix. The correlated errors between  $\mathcal{A}_\tau$  and  $\mathcal{A}_e$  for a given experiment as quoted by the experiment are also included in the error correlation matrix.

The fitted values for  $\mathcal{A}_\tau$  and  $\mathcal{A}_e$  with no assumption of lepton universality are:

$$\mathcal{A}_\tau = 0.1439 \pm 0.0043 \quad (4.2)$$

$$\mathcal{A}_e = 0.1498 \pm 0.0049, \quad (4.3)$$

where the  $\chi^2$  is 3.9 for six degrees of freedom and the correlation is 0.014. These asymmetries are consistent with each other, in agreement with lepton universality. Assuming  $e - \tau$  universality, the values for  $\mathcal{A}_\tau$  and  $\mathcal{A}_e$  can be combined in a fit with a single lepton asymmetry parameter which yields a result of:

$$\mathcal{A}_\ell = 0.1465 \pm 0.0033. \quad (4.4)$$

where the  $\chi^2$  is 4.7 for seven degrees of freedom. This corresponds to a value of:

$$\sin^2 \theta_{\text{eff}}^{\text{lept}} = 0.23159 \pm 0.00041. \quad (4.5)$$

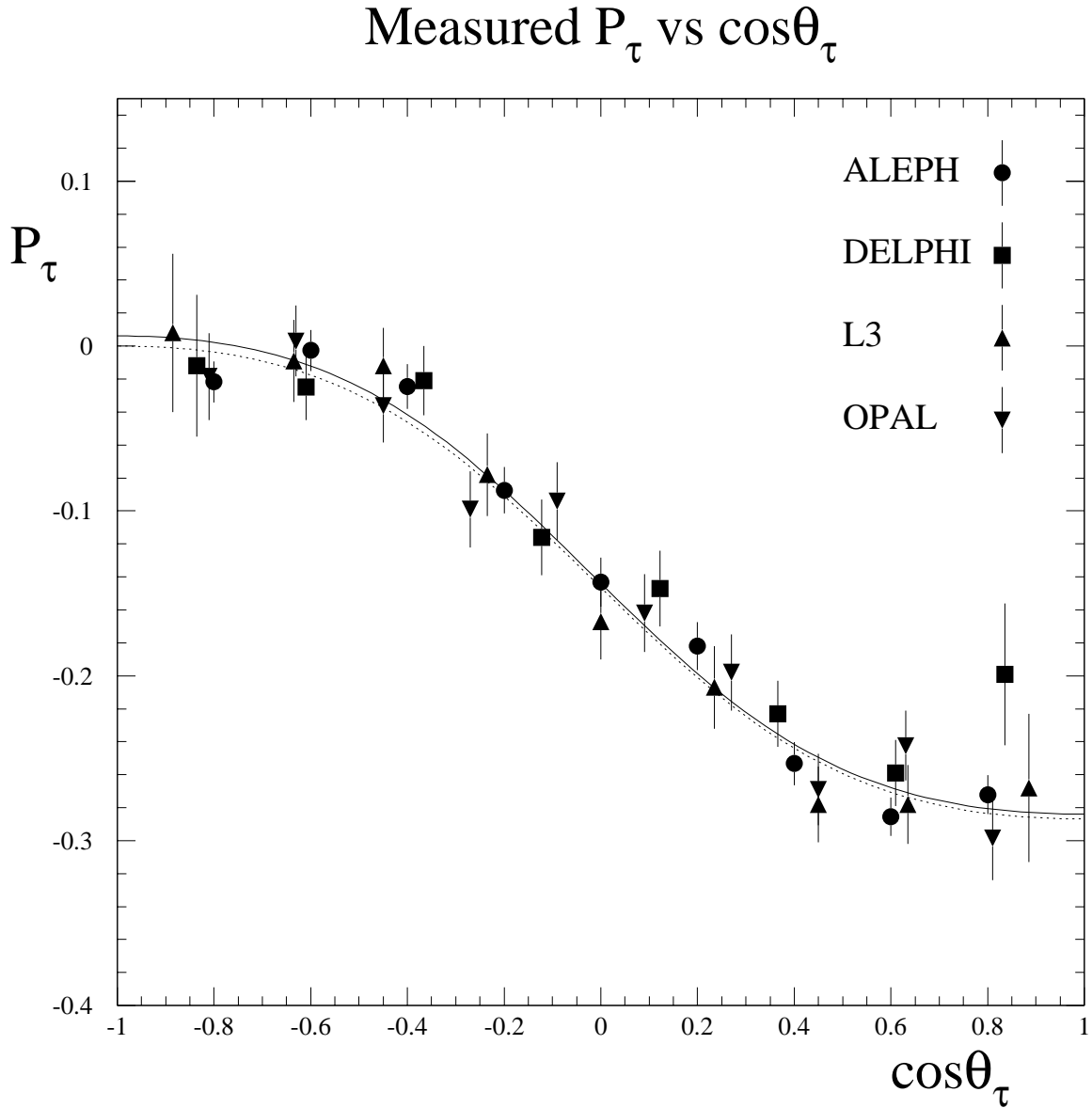


Figure 4.5: The values of  $\mathcal{P}_\tau$  as a function of  $\cos\theta_\tau$  as measured by each of the LEP experiments. Only the statistical errors are shown. The values are not corrected for radiation, interference or pure photon exchange. The solid curve overlays Equation 4.1 for the LEP values of  $\mathcal{A}_7$  and  $\mathcal{A}_e$ . The dashed curve overlays Equation 4.1 under the assumption of lepton universality for the LEP value of  $\mathcal{A}_e$ .



**$\mathcal{A}_l$  (LEP) =  $0.1465 \pm 0.0033$**

$\chi^2/\text{DoF} = 3.9/6$  **no lepton universality assumed**

$\chi^2/\text{DoF} = 4.7/7$  **lepton universality assumed**

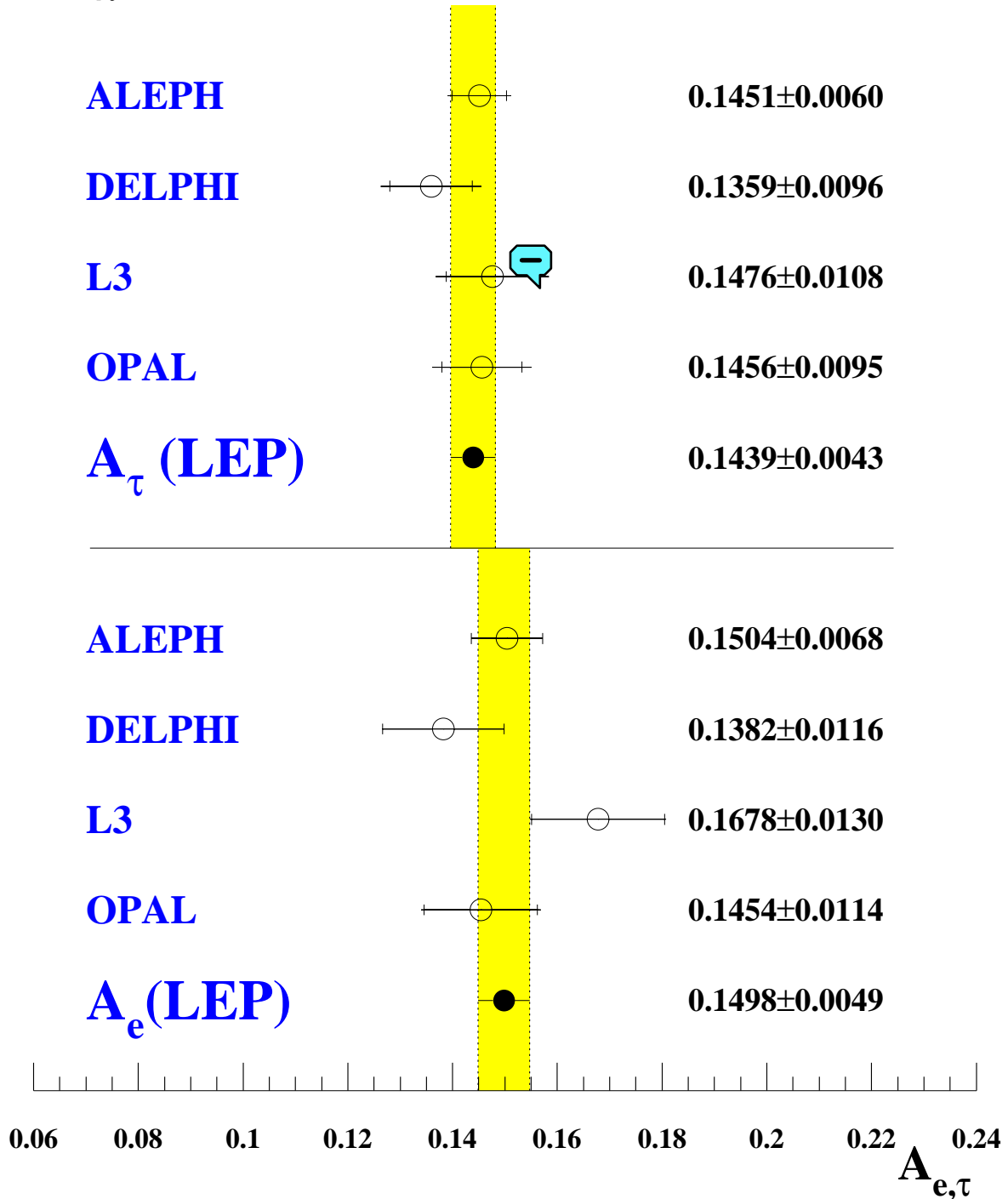


Figure 4.6: Measurements of  $\mathcal{A}_e$  and  $\mathcal{A}_\tau$  from the four LEP experiments. The error bars indicate the quadrature sum of the statistical and systematic errors. The magnitude of the statistical errors alone are indicated by the small tic marks on the error bar.

Experiment	$\mathcal{A}_\tau$	$\mathcal{A}_e$
ALEPH	$0.1451 \pm 0.0052 \pm 0.0029$	$0.1504 \pm 0.0068 \pm 0.0008$
DELPHI	$0.1359 \pm 0.0079 \pm 0.0055$	$0.1382 \pm 0.0116 \pm 0.0005$
L3	$0.1476 \pm 0.0088 \pm 0.0062$	$0.1678 \pm 0.0127 \pm 0.0030$
OPAL	$0.1456 \pm 0.0076 \pm 0.0057$	$0.1454 \pm 0.0108 \pm 0.0036$
LEP	$0.1439 \pm 0.0043$	$0.1498 \pm 0.0049$

Table 4.3: LEP results for  $\mathcal{A}_\tau$  and  $\mathcal{A}_e$ . The first error is statistical and the second systematic. To form the LEP combinations, statistical and systematic errors are combined in quadrature.

	$\mathcal{A}_\tau(\text{A})$	$\mathcal{A}_\tau(\text{D})$	$\mathcal{A}_\tau(\text{L})$	$\mathcal{A}_\tau(\text{O})$	$\mathcal{A}_e(\text{A})$	$\mathcal{A}_e(\text{D})$	$\mathcal{A}_e(\text{L})$	$\mathcal{A}_e(\text{O})$
$\mathcal{A}_\tau(\text{A})$	1.000							
$\mathcal{A}_\tau(\text{D})$	0.030	1.000						
$\mathcal{A}_\tau(\text{L})$	0.023	0.021	1.000					
$\mathcal{A}_\tau(\text{O})$	0.060	0.047	0.032	1.000				
$\mathcal{A}_e(\text{A})$	0.001	0.001	0.001	0.001	1.000			
$\mathcal{A}_e(\text{D})$	0.001	0.025	0.000	0.000	0.001	1.000		
$\mathcal{A}_e(\text{L})$	0.001	0.000	0.032	0.000	0.001	0.000	1.000	
$\mathcal{A}_e(\text{O})$	0.001	0.000	0.000	0.025	0.006	0.000	0.002	1.000

Table 4.4: Error correlation matrix used for the combination of the LEP results for  $\mathcal{A}_\tau$  and  $\mathcal{A}_e$ . The order is:  $\mathcal{A}_\tau$  for ALEPH, DELPHI, L3 and OPAL; followed by  $\mathcal{A}_e$  for ALEPH, DELPHI, L3 and OPAL.



# Chapter 5

## Results from b and c quarks

### 5.1 Introduction

Events resulting from the decay of the Z to b- and c-quarks can be tagged with high efficiency and purity and therefore can contribute to precision electroweak measurements. As already explained in chapter 1 their partial widths, normalised to the total hadronic width of the Z,  $R_b^0$ ,  $R_c^0$ , the forward-backward asymmetries with unpolarised beams,  $A_{\text{FB}}^{b\bar{b}}$ ,  $A_{\text{FB}}^{c\bar{c}}$ , and, with polarised beams, the left-right-forward-backward asymmetries,  $A_{\text{FB,LR}}^{b\bar{b}}$ ,  $A_{\text{FB,LR}}^{c\bar{c}}$ , can be measured.

The LEP experiments and SLD measure these quantities with a variety of methods. Since all the measurements make some assumptions about the fragmentation and decays of b- and c-quarks, there are many sources of systematic correlations between them. In addition, different observables are sometimes measured simultaneously, giving rise to statistical correlations between the results. For these two reasons a simple average of the different results is not sufficient. A more sophisticated procedure is needed and is described below.

In addition, several other quantities measured in both the LEP and SLD data are needed to derive the electroweak observables discussed here. They are sometimes measured at the same time as the electroweak observables, and depend on the same sources of systematic uncertainty. To derive consistent average values for the electroweak observables, these quantities are included in the electroweak heavy flavour fit. They are:

- the  $B\bar{B}$  effective mixing parameter  $\bar{\chi}$ , which is the probability for a semi-leptonically decaying b-quark to  $b\bar{c}$  produced as an anti-b-quark,
- the prompt and cascade semileptonic branching fraction of the b-hadrons  $\text{BR}(b \rightarrow \ell)^*$  and  $\text{BR}(b \rightarrow c \rightarrow \ell)$  and the prompt semileptonic branching fraction of the c-hadrons  $\text{BR}(c \rightarrow \ell)$ .
- the fraction of charm hemispheres fragmenting into a specified weakly decaying charmed hadron,  $f(D^+)$ ,  $f(D_s^+)$ ,  $f(c_{\text{baryon}})^\dagger$ ,
- the probability that a c-quark fragments into a  $D^{*+}$  that decays into  $D^0\pi^+$ ,  $\text{P}(c \rightarrow D^{*+}) \times \text{BR}(D^{*+} \rightarrow \pi^+D^0)$ .

---

\*Unless otherwise stated, charge conjugate modes are always included

† $f(D^0)$  is calculated from the constraint  $f(D^0) + f(D^+) + f(D_s^+) + f(c_{\text{baryon}}) = 1$ .

## 5.2 Heavy flavour tagging methods

In general there are two types of observables **with** heavy quarks at LEP and SLD, rate measurements  $R_q = \sigma_q/\sigma_{\text{had}}$  and forward-backward asymmetries. In principle, the measurement of  $R_q$  only requires a tag to separate the flavour  $q$  from other hadronic events. The tagging efficiency and backgrounds must be precisely known.

Asymmetry measurements do not require precise knowledge of the absolute tagging efficiency, except to evaluate background corrections. However, the separation power of the method used to distinguish the quark from the anti-quark must be understood.

### 5.2.1 Lifetime Tagging

The two most efficient and pure ways of selecting b-hadrons from Z decays are based on the reconstruction of secondary vertices and on the measurement of the large impact parameter of the b-hadron decay products. Since the average b lifetime is about 1.5 ps and the b-hadrons are produced with a most probable energy of 30 GeV at the Z peak, they travel for about 3 mm before decaying. Their mean charged multiplicity is  $\sim 5$  (see section 5.6.3). The silicon vertex detectors of the LEP experiments and SLD have a resolution for the secondary vertex position **of about** one order of magnitude smaller than the mean decay length.

Since the b-hadron decay vertex is separated from the interaction point, each of the tracks originating in the decay will in general appear to miss the primary vertex. The impact parameter is defined as the distance of closest approach of the reconstructed track to the interaction point. It is given by

$$\delta = \gamma\beta c\tau \sin \psi,$$

where  $\tau$  is the particle proper decay time and  $\psi$  is the angle between the secondary particle and the B hadron flight direction.

For a high momentum track,  $\sin \psi$  is proportional to  $1/\beta\gamma$ , and the average impact parameter is then proportional to the average lifetime  $\tau$ :  $\delta \propto c\tau$ , independent of the b-hadron energy. Since at LEP the b hadron momentum is high, the uncertainty on the b-hadron momentum distribution, i.e. the b fragmentation function, has only a small effect on the impact parameter distribution. The impact parameter of the b-hadrons is about  $300\mu\text{m}$ , to be compared with the experimental resolution of 20 to  $70\mu\text{m}$ , depending on the track momentum. ALEPH, L3, and SLD compute the impact parameter in 3D space, while DELPHI and OPAL compute the impact parameter separately in the two projections  $R\phi$  and  $Rz$ . The two projections are then treated as two separate variables.

The precise determination of the Z decay point, the so called primary vertex, is required in lifetime b-tagging techniques. It is determined separately for each hadronic event using the current envelope of such vertices (the beam spot) as a constraint. The beam spot is defined as the interaction region of the electron and the positron beams. At LEP the width along the x-axis varies with time but is typically 100 to  $150\mu\text{m}$ . The width along the y-axis is around  **$5\mu\text{m}$ , below the detector resolution and** the width along the z-axis is about 1 cm. **▲** Since the beam spot width in z is much larger than the detector resolution, the details do not influence the tagging efficiencies.

The event primary vertex is determined by a fit to all the tracks that are likely to have come from the primary interaction (i.e. after having excluded the decays of long lived particles and hadronic interaction products). The accuracy of the reconstructed primary vertex position



	ALEPH	DELPHI	L3	OPAL	SLD
Num. of layers	2	3	2	2	3
Radius of layers (cm)	6.5/11.3	6.3/9/11	6.4/7.9	6.1/7.5	2.9-4.1
$R\Phi$ imp. par. res. ( $\mu\text{m}$ )	25*	20	30	16	13
$z$ imp. par. res. ( $\mu\text{m}$ )		30	100	35	24
Primary Vertex res. $x \times y \times z$ ( $\mu\text{m}$ )	$58 \times 10$ $\times 60$	$22 \times 10$ $\times 22$	$42 \times 10$ $\times 100$	$80 \times 12$ $\times 85$	$6.4 \times 6.4$ $\times 15$

Table 5.1: Vertex detector characteristics and experimental resolutions.

The impact parameter resolution is given for 45 GeV muons and the vertex resolution is given for  $b\bar{b}$ -events when including the beam spot information.

\* for ALEPH the 3D impact parameter resolution is given.

depends on the algorithm used, on the geometry of silicon vertex detectors and on the size of the beam spot. At LEP the beam spot size in the horizontal direction ( $x$ ) is around  $150\mu\text{m}$ , which is significantly larger than the detector resolution while in the vertical direction its size is typically  $10\mu\text{m}$  and thus determines the vertex resolution. At SLC the beam spot is only a few microns wide in the transverse ( $xy$ ) plane giving an almost point-like primary vertex resolution. The parameters of the various vertex detectors and the resolution on the relevant quantity for a lifetime b-tag are summarised for the LEP and SLC experiments in Table 5.1.

A lifetime sign is assigned to each track impact parameter. This is positive if the extrapolated track is consistent with a secondary vertex which lies on the same side of the primary vertex as the track itself. Otherwise it is negative. In Figure 5.1 the projection in the  $R\phi$  plane of the lifetime signed impact parameter distribution is shown for tracks coming from the different quark flavours. Tracks coming from the decays of  $K_s^0$  and  $\Lambda$  are removed, so that the distribution of the light quark reflects the resolution of the apparatus (DELPHI in this case).

Due to the finite resolution of the detector, the relevant quantity for the identification of the b-quark is the impact parameter significance  $S$ , defined as the lifetime signed impact parameter divided by its error. A good description of  $S$  in the simulation is crucial for a reliable estimate of the tagging efficiencies. The negative part of the  $S$  distribution depends only on the impact parameter resolution, and can therefore be used for checking the simulation and ‘calibrating’ the tagging. A simple b-tag can use the number of tracks with a large positive significance. A better estimator is constructed by combining all the positive track significances: first the negative part of the significance distribution is fitted to a functional form that defines the resolution of the detector, then for each track the integral of this function is computed giving the probability that the track comes from the primary vertex. The probability that all tracks in a jet, hemisphere or event, come from the primary vertex is calculated by combining the probabilities for all tracks in that jet, hemisphere or event. By definition it is flat if all tracks originate from the primary vertex. The probability for a group of tracks coming from an  $uds$  event is then flat between zero and one, while the probability for a group of tracks coming from a b quark event is peaked at zero.

Figure 5.2 shows the distribution of the L3 b-tagging variable  $D$  which is the negative logarithm of the hemisphere impact parameter probability. It can be seen that at large values of  $D$  high tag purities can be achieved with impact parameters only.

An alternative lifetime-based tag uses the reconstruction of secondary vertices. OPAL fits all well-reconstructed high momentum tracks in a jet to a single secondary vertex, then

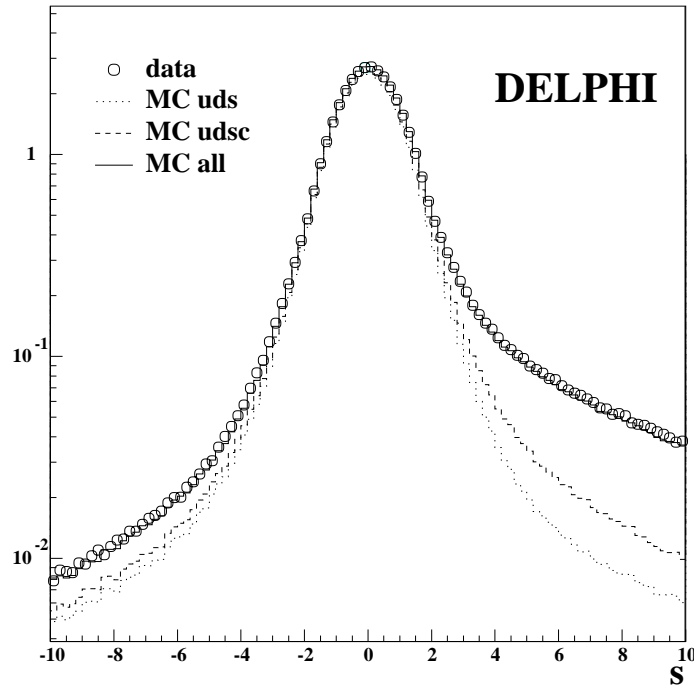


Figure 5.1: Impact parameter significance from DELPHI for data and simulation. The contributions of the different quark flavours are shown separately.

progressively removes those which do not fit well. The decay length significance  $L/\sigma_L$  (the reconstructed distance between the primary and secondary vertices divided by its error) is used as the  $b$ -tagging variable, signed depending on whether the secondary vertex is reconstructed in front of or behind the primary vertex (see Figure 5.3). This allows the background from light quark events with  $L/\sigma_L > 0$  to be estimated using the number of events with  $L/\sigma_L < 0$ .

The extremely precise SLD vertex detector and small stable SLC beam spot allow a novel approach to secondary vertex finding, based on representing tracks as Gaussian ‘probability tubes’. Spatial overlaps between the probability tubes give regions of high probability density corresponding to candidate vertices, to which tracks are finally attached. This topological vertex technique allows the efficient reconstruction of the primary, secondary and sometimes tertiary (D decay) vertices in  $b$ -quark jets, and the identification of the secondary D vertex in a large fraction of  $c$  quark jets.

The pure lifetime tags have an intrinsic limitation because D-mesons have a lifetime comparable to B-mesons. However this can be overcome if additional information is used. Since B-mesons are much heavier than D-mesons, the most obvious variable is the invariant mass of the particles fitted to the secondary vertex. In SLD this mass is used as a  $b$ -tag with an additional correction for the neutral decay products of the B. From the flight direction of the B, calculated from the primary and the B-decay vertex, and the momentum vector of the charged decay products of the B, fitted to the secondary vertex, the transverse momentum,  $p_t$ , of the sum of the neutral decay products can be calculated. Adding a massless pseudo particle with momentum  $p_t$  to the secondary vertex gives an improved lower limit for the mass of the decaying particle.

In Figure 5.4 the  $p_t$ -corrected mass of the secondary vertex is shown for  $b$  events and for the  $uds$  and  $c$  background. The high efficiency for assigning the correct tracks to the decay vertex

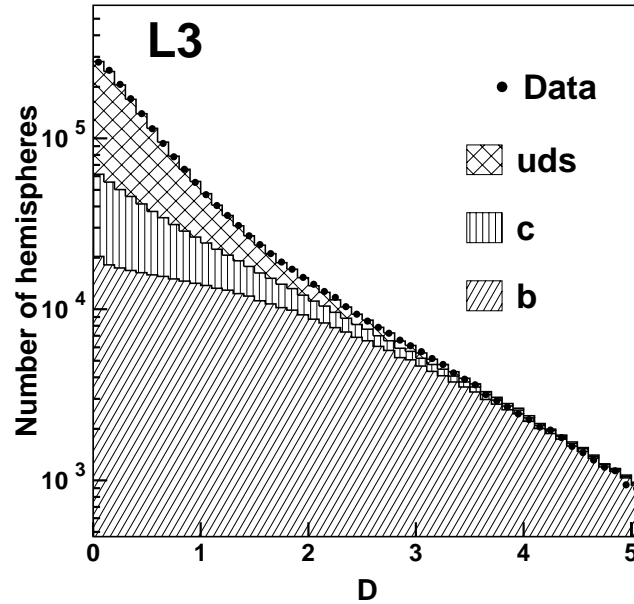


Figure 5.2: Impact parameter b-tag from L3.

results in a very high b-tagging purity of 98% for almost 50% efficiency, simply by requiring the  $p_t$ -corrected mass to be above the D-meson mass. A further improvement of the performance has been recently obtained with the introduction of a neural network to optimise the track to vertex association and a second neural network to improve the c-b separation by using the vertex decay length, multiplicity and momentum in addition to the  $p_t$ -corrected vertex mass.

At LEP the beam spot is one to two orders of magnitude larger in the y and x directions, and the first layer of silicon detector can be placed only at a radius twice that in SLD (see Table 5.1). These characteristics limit the performance of the b-tags in the LEP experiments. To reach the maximum possible performance the LEP experiments have developed sophisticated tagging techniques which combine different information.

DELPHI utilises a likelihood technique combining 4 variables: the probability that the tracks in the jet come from the primary vertex (see section 5.2.1), the mass of the reconstructed secondary vertex, the energy of the charged tracks belonging to the secondary vertex and their rapidity. Combining track properties with the information from the reconstructed secondary vertices makes the tag more robust against detector resolution effects. A considerable improvement can be obtained if the direction defined by the primary and secondary vertex is used as the b-hadron direction, instead of the jet axis.

ALEPH uses a linear combination of two lifetime-related variables. The first is the probability that the tracks from each **hemispheres** come from the primary vertex (as defined in section 5.2.1). The second variable is correlated with the mass of the hadron produced. In each jet the tracks are combined in order of decreasing inconsistency with the primary vertex until their mass exceeds  $1.8 \text{ GeV}/c^2$ . The variable is defined as the impact parameter probability of the last track added. ▲

L3 identify b-hemispheres using the impact parameter tag only.

OPAL uses a vertex tag based on a neural network combining five variables. The first four are derived from the reconstructed secondary vertex: the decay length significance  $L/\sigma_L$ , the decay length  $L$ , the number of tracks in the secondary vertex and a variable that measures the

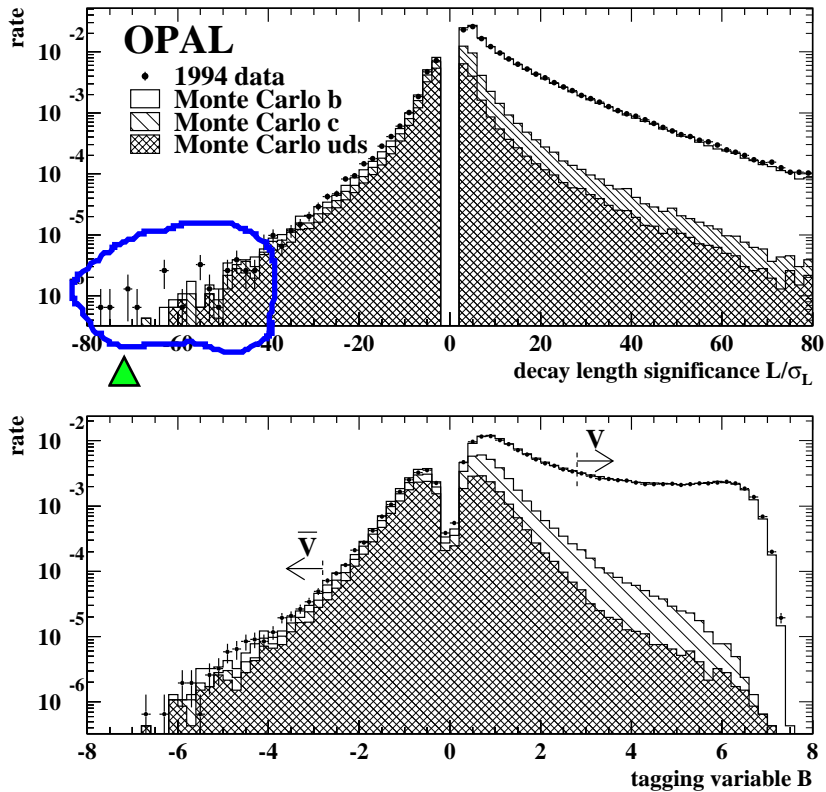


Figure 5.3: Decay length significance  $L/\sigma_L$  (top) and neural network tagging variable (bottom) for the OPAL secondary **vertex based** b-tag. The gaps around zero significance are due to neural network preselection cuts removing jets with no significant secondary vertex.

	ALEPH	DELPHI	L3	OPAL	SLD
b Purity %	97.8	98.6	84.3	96.7	98.3
b Efficiency %	22.7	29.6	23.7	25.5	61.8

Table 5.2: b-Tagging performance of the different experiments **at the working points** of the  $R_b$  analyses. The OPAL tag is an or of a secondary vertex and a lepton tag.

stability of the vertex against mismeasured tracks. The fifth variable exploits the high mass of b hadrons. For each track in the jet, the relative probabilities that it came from the primary and secondary vertex are calculated, using impact parameter and kinematic information. As in the ALEPH tag, these tracks are then combined in decreasing order of secondary vertex probability until the charm hadron mass is exceeded, and the secondary vertex probability of the last track added is used as input to the main neural network. The neural network output is signed according to the sign of  $L$ , preserving the ‘folding’ symmetry of the simple  $L/\sigma_L$  tag and allowing the light quark background to be subtracted (see Figure 5.3).

The b-tag performance of SLD and the LEP-experiments **at the  $R_b$  working point** is shown in Table 5.2.

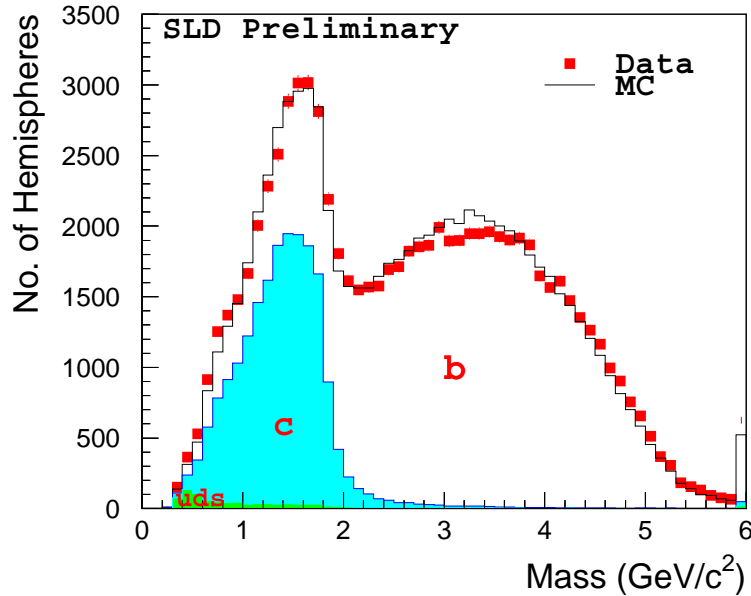


Figure 5.4: Reconstructed vertex mass from SLD for data and simulation.

## 5.2.2 Lepton tagging

One of the first methods to identify the flavour composition of a jet was based on the properties of the semileptonic decays of the heavy hadrons. Due to the hard fragmentation and the large mass, leptons from b-decays are characterised by large total and transverse momenta. Leptons from c-decays also have high momentum, but a significantly smaller transverse momentum. The charge of the lepton from a b- or c-decay is correlated to the charge of the decaying quark. Therefore in the asymmetry measurements the lepton tag can be used simultaneously to tag the quark flavour and to distinguish between the quark and the antiquark. b- and c-quarks decay semileptonically into electrons and muons with branching fractions around  $2 \times 10\%$ . For the decays  $b \rightarrow \ell^-$  and  $c \rightarrow \ell^+$  the lepton charge is the same as that of the decaying quark. However, because the charge of the b- and c-quark have opposite sign, the charge asymmetries for leptons from b- and c-quarks are opposite, leading to a large sensitivity of the asymmetry measurements with leptons to the sample composition. For the decay  $b \rightarrow c \rightarrow \ell^+$  the lepton charge is opposite to the b-quark charge. Apart from these three main sources there are also some other sources with different charge correlations, mainly  $b \rightarrow \bar{c} \rightarrow \ell^-$ ,  $b \rightarrow \tau^- \rightarrow \ell^-$  and  $b \rightarrow (J/\psi + \psi') \rightarrow \ell\ell$ . In addition there are misidentified hadrons and electrons from photon conversion.

The transverse momentum,  $p_t$ , of the decay lepton with respect to the decaying hadron direction is limited to half the hadron mass. Experimentally the direction of the jet containing the lepton is used, which provides a good approximation of the hadron direction. Since b-quarks fragment harder than c-quarks, additional separation power is given by the lepton momentum. Figure 5.5 shows the muon  $p$  and  $p_t$  spectrum from L3 compared to the simulation of the different sources.  $b \rightarrow \ell$  can be separated cleanly with a simple cut on  $p_t$ . However the other sources overlap strongly and can only be separated on a statistical basis.

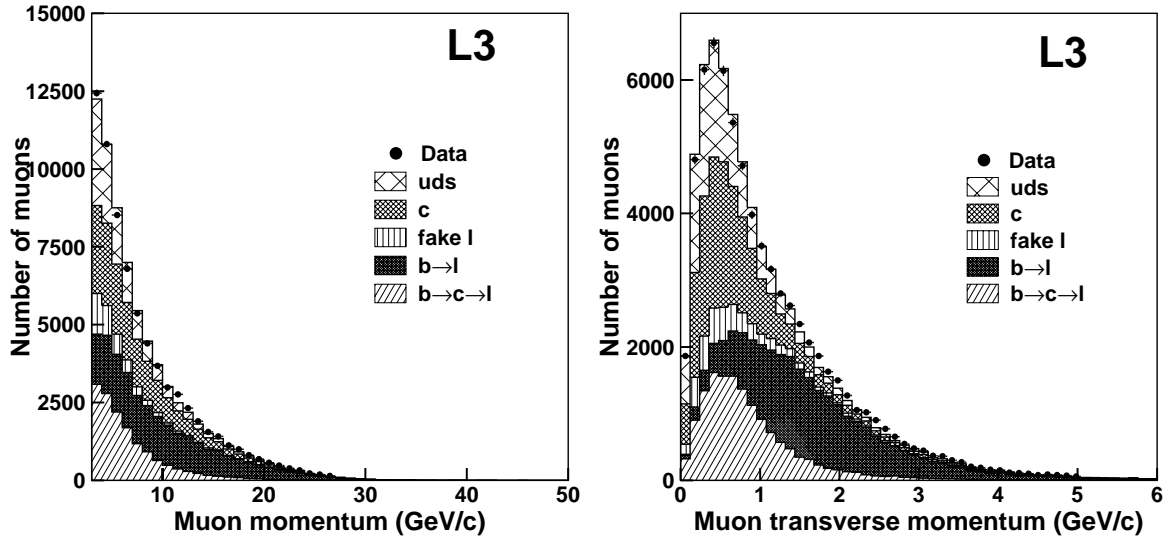


Figure 5.5: Momentum and transverse momentum spectrum from L3 compared to the different sources from simulation.

### 5.2.3 D-meson tags

Since charmed hadrons are only rarely produced during light quark fragmentation, their presence tags c-quarks either coming from the primary Z-decay or as decay products from a b-quark.

Charmed hadrons from a primary c-quark have on average a higher momentum than those from a b-decay (see Figure 5.6). In addition  $\Delta$  decay length information can be used to separate the two sources.

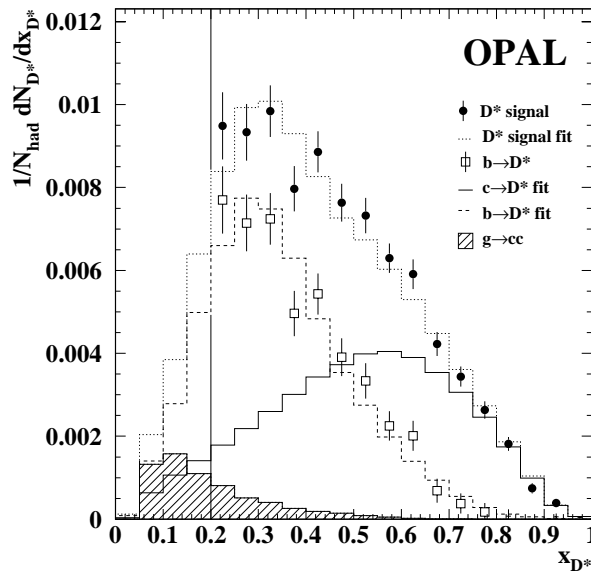


Figure 5.6:  $D^{*\pm}$  momentum spectrum for all events and for  $b\bar{b}$  and  $c\bar{c}$  events from OPAL normalised to the beam energy after subtraction of combinatorial background.

At LEP the weakly decaying charmed hadrons  $D^0$ ,  $D^+$ ,  $D_s^+$  and  $\Lambda_c$  can be reconstructed in particular exclusive final states (see Figure 5.7). The charm tagging efficiency is limited by the low branching fractions for these decay modes, which are typically only a few percent. The

decay  $D^{*+} \rightarrow \pi^+ D^0$  can be reconstructed particularly cleanly, due to the small mass difference  $\Delta m = m_{D^{*+}} - m_{D^0}$  leading to a characteristic narrow peak with little background, as shown in Figure 5.8. Because of the good resolution even  $D^0$  decays which are not fully reconstructed, such as  $D^0 \rightarrow \ell \nu X$  or  $D^0 \rightarrow K^- \pi^+ \pi^0$ , where the  $\pi^0$  is not seen, can be used.

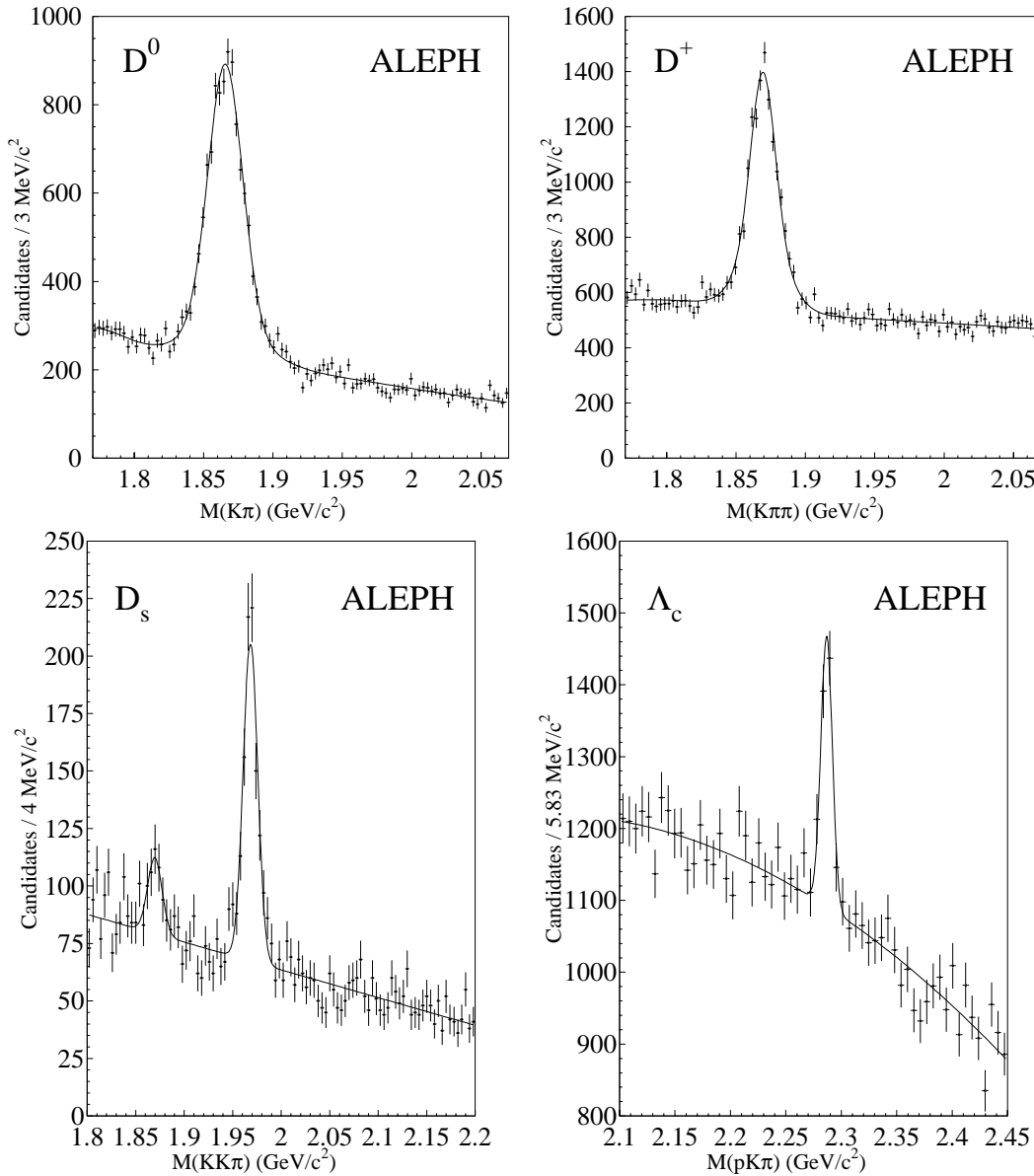


Figure 5.7: Mass spectra for  $D^0 \rightarrow K^- \pi^+$ ,  $D^+ \rightarrow K^- \pi^+ \pi^+$ ,  $D_s^+ \rightarrow K^+ K^- \pi^+$  and  $\Lambda_c \rightarrow p K^- \pi^+$  obtained by ALEPH.

The decay  $D^{*+} \rightarrow \pi^+ D^0$  can also be tagged inclusively. The small mass difference between the  $D^{*+}$  and  $D^0$  and the low mass of the pion result in a very low pion momentum in the  $D^{*+}$  restframe. Therefore in the laboratory frame the pion closely follows the  $D^{*+}$  and has a very low transverse momentum  $p_t$  with respect to the jet direction. As shown in Figure 5.9, the number of  $D^{*+}$  in a sample can thus be measured from the excess in the  $p_t^2$  spectrum at very low values. Because of the large background, this tag is typically used only in conjunction with other tags.

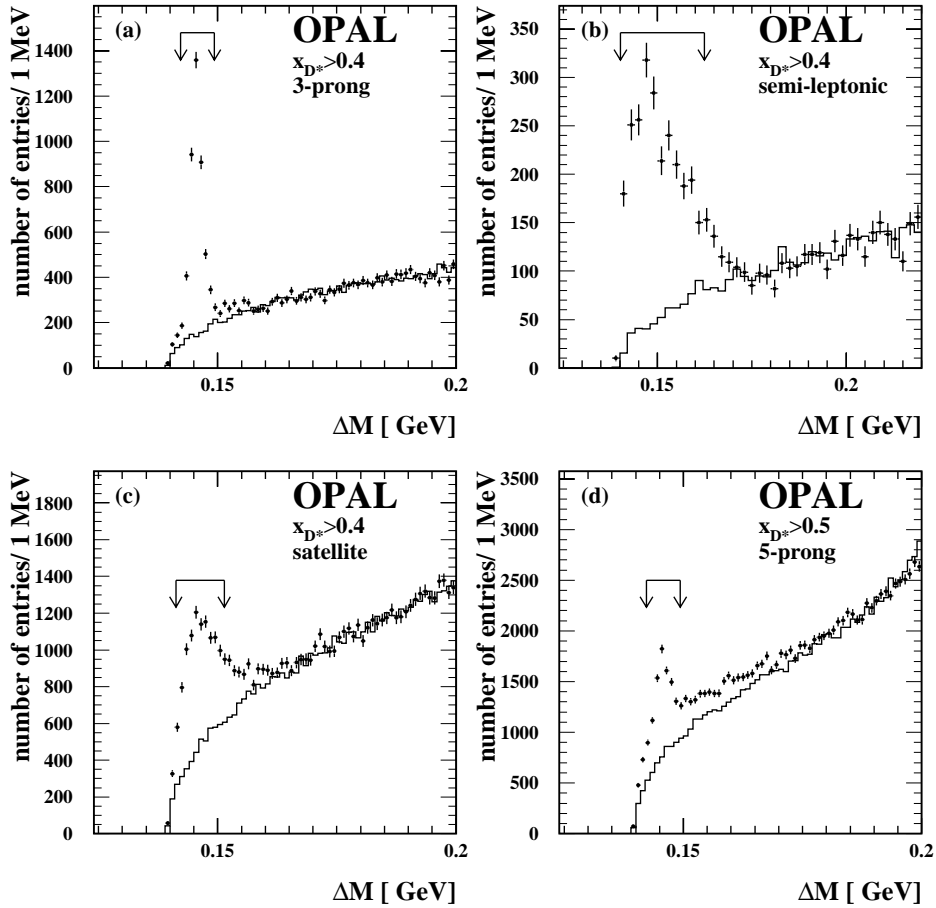


Figure 5.8:  $m(K^-\pi^+) - m(K^-\pi^+\pi^+)$  mass difference spectrum from OPAL in different channels. In the plot labelled “satellite” the decay mode  $D^0 \rightarrow K^-\pi^+\pi^0$  is used, where the  $\pi^0$  is not reconstructed. This  $K^-\pi^+$  mass peak is enhanced due to the large polarisation of the intermediate  $\rho^+$  produced in the  $D^0 \rightarrow K^-\rho^+ \rightarrow K^-\pi^+\pi^0$  decay.



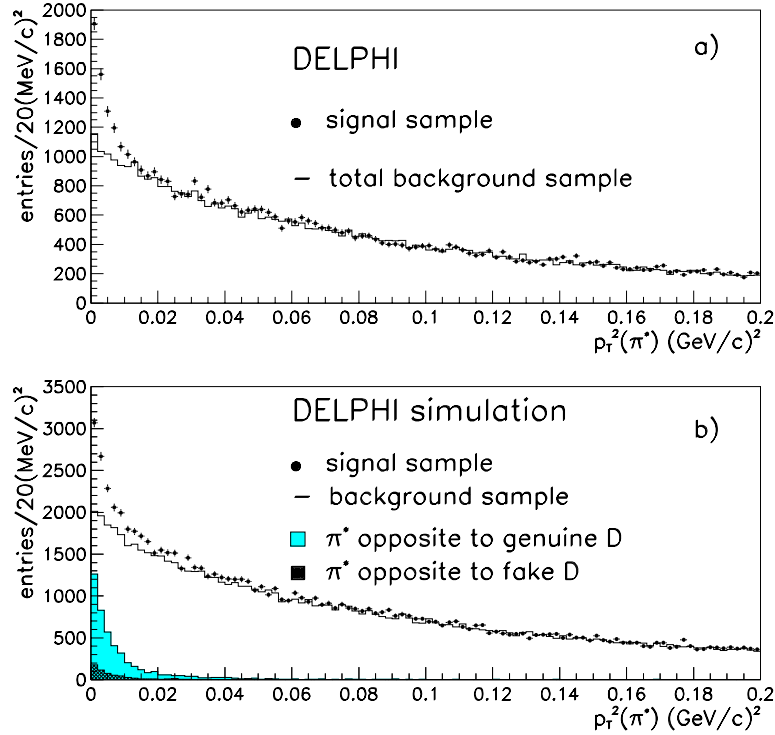


Figure 5.9:  $p_t$  spectrum opposite a high energy  $D^{*\pm}$  for pions with the opposite (points) and same (histogram) sign as the  $D^{*\pm}$ . The data is shown in a) and the simulation in b), with the signal component indicated separately.

The flavour of D-mesons is also correlated to the flavour of the original quark. Apart from the suppressed  $b \rightarrow \bar{c}$  decay there is only one source per flavour. Also the correlation for b- and c-quarks is the same leading to a reduced sensitivity of the asymmetry measurements to the sample composition. Since the absolute efficiency cancels in the asymmetries many different states can be used. Because of the low background the most sensitive decay, however, is  $D^{*+} \rightarrow \pi^+ D^0$  with  $D^0 \rightarrow K^- \pi^+$ .

### 5.3 Partial width measurements

To measure the fraction of a certain quark flavour within the hadronic event sample, it is in principle necessary only to count the number of flavour-tagged events and to understand the tagging efficiency and background. This method is generally called the single tag method and is used in some of the  $R_c$  measurements.

If the tag is very pure, backgrounds can generally be understood sufficiently using the single tag method, but it is difficult to determine the tagging efficiency for the flavour being measured with high enough precision using detector simulation techniques alone. The so called double tag method offers the advantage of determining this efficiency from the data itself. The double tag method relies on the fact that the decay products of each primary quark in a heavy quark pair event are well confined to separate hemispheres. By comparing the rates of events where either one or both hemispheres are tagged, both the tagging efficiency and the quark rate can be measured simultaneously. ▲

### 5.3.1 $R_b$ measurements

#### The double tag method

All precise measurements of  $R_b$  are primarily based on counting events with **single and** both hemispheres tagged. The fraction of hemispheres which are b-tagged  $f_s$  and fraction of events where both hemispheres are tagged  $f_d$  are given by:

$$\begin{aligned} f_s &= \varepsilon_b R_b + \varepsilon_c R_c + \varepsilon_{uds}(1 - R_b - R_c) \\ f_d &= \varepsilon_b^{(d)} R_b + \varepsilon_c^{(d)} R_c + \varepsilon_{uds}^{(d)}(1 - R_b - R_c), \end{aligned} \quad (5.1)$$

▲ where  $\varepsilon_f$  is the hemisphere tagging efficiency for flavour  $f$ . The double tagging efficiency  $\varepsilon_f^{(d)}$  can be written as  $\varepsilon_f^{(d)} = (1 + \mathcal{C}_f)\varepsilon_f^2$  where the correction factor  $\mathcal{C}_f \neq 0$  accounts for the fact that the two hemispheres in an event are slightly correlated. For the pure b-tags, **however**,  $\mathcal{C}_c$  and  $\mathcal{C}_{uds}$  can be safely neglected.

Neglecting ▲ hemisphere correlations and background,  $R_b = f_s^2/f_d$ , independent of the b-tagging efficiency  $\varepsilon_b$  which then does not need to be determined **from simulation**. In reality, corrections dependent on the background efficiencies  $\varepsilon_c$ ,  $\varepsilon_{uds}$  and hemisphere correlations  $\mathcal{C}_b$  must be applied and these have to be determined from Monte Carlo. The uncertainties on these parameters are included in the systematic errors. The effect of an uncertainty  $\Delta\varepsilon_x$  from a background source  $x$  is approximately given by  $\Delta R_b = 2\frac{\Delta\varepsilon_x}{\varepsilon_b} R_x$  and for an uncertainty on the correlation by  $\Delta R_b = \Delta\mathcal{C}_b R_b$ . Therefore it is essential to develop a high efficiency and high purity b-tag to enable the double tag scheme to achieve the necessary statistical and systematic precision. Details about the hemisphere correlations are explained in section 5.6.7.

OPAL [82] and SLD [83] measure  $R_b$  with a double tag scheme as described above. SLD uses only their efficient and pure vertex mass tag. OPAL uses **an or** of a secondary vertex and a lepton tag.

#### The multi tag method

In the double tag method, hemispheres are tagged simply as b or non-b. This leads to two equations and five unknowns,  $R_b$ ,  $R_c$ ,  $\varepsilon_c$ ,  $\varepsilon_{uds}$  and  $\mathcal{C}_b$ . Three of them ( $\varepsilon_c$ ,  $\varepsilon_{uds}$  and  $\mathcal{C}_b$ ) are taken from simulation and  $R_c$  is **fixed in the analyses**. The  **$R_c$ -dependence** is then accounted for in the systematic error of the experimental publications and in the combination procedure ▲ described in section 5.8. The method can be extended by adding more tags, *e.g.* additional b-tags with lower purity, or charm and light flavour tags. The tags are made exclusive, such that each hemisphere is counted as tagged by only one tag method, and the untagged hemispheres are counted as an extra ‘null’ tag.

With  $T$  separate hemisphere tags, there are then  $T(T+1)/2$  double tag fractions  $f_d^{ij}$  ( $i, j = 1, T$ ), given (analogously with Equations 5.2) by:

$$f_d^{ij} = \varepsilon_b^i \varepsilon_b^j (1 + \mathcal{C}_b^{ij}) R_b + \varepsilon_c^i \varepsilon_c^j (1 + \mathcal{C}_c^{ij}) R_c + \varepsilon_{uds}^i \varepsilon_{uds}^j (1 + \mathcal{C}_{uds}^{ij}) (1 - R_b - R_c), \quad (5.2)$$

where  $\varepsilon_f^i$  is the hemisphere tagging efficiency for flavour  $f$  with tag  $i$ , and  $\mathcal{C}_f^{ij}$  is the hemisphere correlation coefficient for tagging an event of flavour  $f$  with tag  $i$  in one hemisphere and  $j$  in the other. The single tag rates don’t give additional information in this case, since they can be written as sums over the appropriate double tag fractions.

With  $T$  tags and  $F$  event types, there are  $F(T-1)$  unknown efficiencies  $\varepsilon_q^j$  (since the  $T$  efficiencies for each flavour must add up to one) and  $F-1$  unknown partial widths ratios  $R_f$ .

If all the correlation coefficients  $\mathcal{C}_f^{ij}$  are taken from simulation, that leaves  $F(T-1) + (F-1) = TF - 1$  unknowns to be determined from  $T(T+1)/2 - 1$  independent double tag rates  $f_d^{ij}$ . With  $F = 3$  event types (b, c, uds), the minimum number of tags for an over-constrained system is six.

ALEPH [84, 85] and DELPHI [86] both use this multitag method for measuring  $R_b$ . The six tags used are: three b-tags with different purities, a charm tag, a light quark tag and the “untagged” hemispheres. However, even with these six tags, the solution for all efficiencies and partial widths is still not well determined. This problem is solved by exploiting the very high purity of the primary b-tag, taking the small background efficiencies for charm and light quark events from Monte Carlo, as in the simple double tag analysis.  $R_c$  is also fixed to its Standard Model value.

If the primary b-tag has the same efficiency and purity as in the double tag method, the statistical error is reduced, since the auxiliary b-tags also contribute to the measurement of  $R_b$ , their backgrounds being measured by the charm and light quark tags. The systematic error due to the backgrounds in the primary b-tag stays the same as in the double tag method. It can be reduced by changing the working point of the primary b-tag towards higher purity, thus sacrificing some of the gain in statistical error. Many additional hemisphere correlations have to be estimated from Monte Carlo, but the impact of the most important, between two hemispheres tagged with the primary b-tag, is reduced. The total systematic uncertainty from hemisphere correlations is therefore almost unchanged.

L3 [87] also use a multitag analysis for  $R_b$ , but with only two tags, based on lifetime and leptons, and determine the background efficiencies for both tags from simulation. The b-tagging efficiency for the lepton tag is used to provide a measurement of the semileptonic branching fraction  $\text{BR}(b \rightarrow \ell)$ .

### 5.3.2 $R_c$ measurements

#### ▲ Double tag measurements

In the normal double tag analyses the statistical error is determined by the size of the double tagged sample, which is proportional to the square of the tagging efficiency. Thus only SLD is able to present a high precision  $R_c$  measurement with the normal double tagging technique [88]. The tag has a very low uds-background, which can be estimated reliably from simulation. The b-background is relatively high, but can be measured accurately opposite to a high purity b-tag. ALEPH also presents a double tag measurement of  $R_c$  using fully reconstructed D-mesons. However due to the small branching fractions the efficiency is low and the statistical error relatively large [89].

#### Inclusive/exclusive double tags

At LEP more precise results can be obtained with the inclusive/exclusive double tag method. In the first step  $R_c \text{P}(c \rightarrow D^{*+}) \times \text{BR}(D^{*+} \rightarrow \pi^+ D^0)$  is measured from a sample of exclusively reconstructed  $D^{*+}$  (the ‘exclusive tag’). In the second step  $\text{P}(c \rightarrow D^{*+}) \times \text{BR}(D^{*+} \rightarrow \pi^+ D^0)$  is obtained using an inclusive  $D^{*+}$  tag where only the charged pion from the  $D^{*+}$  decay is identified (see section 5.2.3). A fit is made to the  $\pi^- p_t$  spectrum in hemispheres tagged as containing a charm quark by a high energy  $D^{*+}$  reconstructed in the other hemisphere of the event. The uds background in this tagged charm sample is estimated from the sidebands in the mass spectra of the high energy  $D^{*+}$ , and the b-background is measured using lifetime tags


and the  $D^{*+}$  momentum distribution. The fragmentation background under the low  $p_t$  pion  $D^{*+}$  signal can be estimated by exploiting the charge correlation between the pion and the  $D^*$  in the opposite hemisphere. Genuine signal pions have the opposite charge to that of the  $D^*$ , whilst background pions can have either charge (see Figure 5.9).

In this method the reconstruction efficiency for the  $D^0$  and the relevant decay branching fraction (normally  $D^0 \rightarrow K^-\pi^+$ ) still need to be known from simulation or external measurements. However the probability that a c-quark fragments into a  $D^{*+}$ , which is hard to calculate, is measured from the data. ALEPH [89], DELPHI [90,91] and OPAL [92] present such inclusive/exclusive double tag measurements. DELPHI and OPAL give both  $R_c$  and  $P(c \rightarrow D^{*+}) \times \text{BR}(D^{*+} \rightarrow \pi^+D^0)$  as results while ALEPH does the unfolding internally and presents only  $R_c$ .

### Charm counting

Another method for measuring  $R_c$  is known as charm counting. All charm quarks finally end up in a weakly decaying charmed hadron. The production rate of a single charmed hadron  $D_i$  is proportional to  $R_c f(D_i)$ , where  $f(D_i)$  is the fraction of charm quarks that eventually produce a  $D_i$ . However if all weakly decaying charmed hadrons can be reconstructed, the constraint  $\sum_i f(D_i) = 1$  can be exploited and  $R_c$  can be measured without the unknown fragmentation probabilities  $f(D_i)$ . In practice  $D^0$ ,  $D^+$ ,  $D_s^+$  and  $\Lambda_c$  are reconstructed and small corrections for unmeasured strange charmed baryons have to be applied:

$$f(D^0) + f(D^+) + f(D_s^+) + (1.15 \pm 0.05)f(\Lambda_c) = 1.$$

As a by-product these measurements obtain the production rates of the weakly decaying charmed hadrons  $f(D_i)$ , which are needed to calculate the charm tagging efficiency of the lifetime b-tags. ALEPH [93], DELPHI [91] and OPAL [94] present a charm counting  $R_c$  analysis. The method is however limited by the knowledge of the decay modes used, especially for the  $D_s^+$  and the  $\Lambda_c$ . 

### Lepton tag

ALEPH also measures  $R_c$  with leptons [89]. They measure the lepton total and transverse momentum spectrum and subtract the contribution from b decays. This is determined from the lepton spectra measured in b events tagged in the opposite hemisphere by a lifetime-based b-tag. The result is proportional to  $R_c \text{BR}(c \rightarrow \ell)$ , where  $\text{BR}(c \rightarrow \ell)$  is measured by DELPHI [90] and OPAL [95] in charm events tagged in the opposite hemisphere by a high energy  $D^{*+}$ .



## 5.4 Asymmetry measurements

The forward backward asymmetry for a quark flavour  $q$  is defined as

$$A_{\text{FB}}^{q\bar{q}} = \frac{\sigma_{\text{F}}^q - \sigma_{\text{B}}^q}{\sigma_{\text{F}}^q + \sigma_{\text{B}}^q}, \quad (5.3)$$

where the cross sections are integrated over the full hemisphere. The differential cross section with respect to the scattering angle is given by

$$\frac{\partial \sigma^q}{\partial \cos \theta} = \sigma_{\text{tot}}^q \left[ \frac{3}{8} (1 + \cos^2 \theta) + A_{\text{FB}}^{q\bar{q}} \cos \theta \right]. \quad (5.4)$$

This dependence can be used to [get the correction](#) for a non-uniform efficiency or can be fitted directly to the data. The differential asymmetry can be written as

$$A_{\text{FB}}^{\text{q,d}}(\cos\theta) = \frac{8}{3} A_{\text{FB}}^{\text{q}\bar{\text{q}}} \frac{\cos\theta}{1 + \cos^2\theta}. \quad (5.5)$$

Most experimental analyses measure  $A_{\text{FB}}^{\text{q,d}}(\cos\theta)$  and then use Equation (5.5) to fit  $A_{\text{FB}}^{\text{q}\bar{\text{q}}}$ . This is statistically slightly more powerful than simple event counting and all [angular](#) dependent efficiencies cancel. [Equation \(5.5\) is also valid for the left-right-forward-backward asymmetry.](#)

To define the direction  $\theta$  the thrust axis of the event is used, signed by the charge tagging methods described in the following. The thrust axis is infrared and collinear stable, so that it can be calculated in perturbative QCD and it is relatively insensitive to fragmentation effects.

In order to measure a quark asymmetry two ingredients are needed. The quark flavour needs to be tagged and the quark has to be separated from the antiquark. For the flavour tagging the methods described in section 5.2.1-5.2.3 can be used. For the charge tagging essentially five methods are in use: leptons, D-mesons, jet-charge, vertex-charge and Kaons. Some analyses also combine the information from the different methods.

In any analysis the measured asymmetry is given by

$$A_{\text{FB}}^{\text{meas}} = \sum_q (2\omega_q - 1) \eta_q A_{\text{FB}}^q, \quad (5.6)$$

where  $\eta_q$  is the fraction of  $q\bar{q}$  events in the sample,  $\omega_q$  is the probability to tag the quark charge correctly and the sum is taken over all quark flavours.

As an example, Figure 5.10 shows the reconstructed  $\cos\theta$  distribution from the ALEPH  $A_{\text{FB}}^{\text{b}\bar{\text{b}}}$  and  $A_{\text{FB}}^{\text{c}\bar{\text{c}}}$  measurement with leptons. The asymmetry of about 10% for  $A_{\text{FB}}^{\text{b}\bar{\text{b}}}$  and 6% for  $A_{\text{FB}}^{\text{c}\bar{\text{c}}}$  can clearly be seen. Figure 5.11 shows the angular distribution from the SLD vertex charge analysis with polarised beams. Here the asymmetries are much larger due to the beam polarisation.

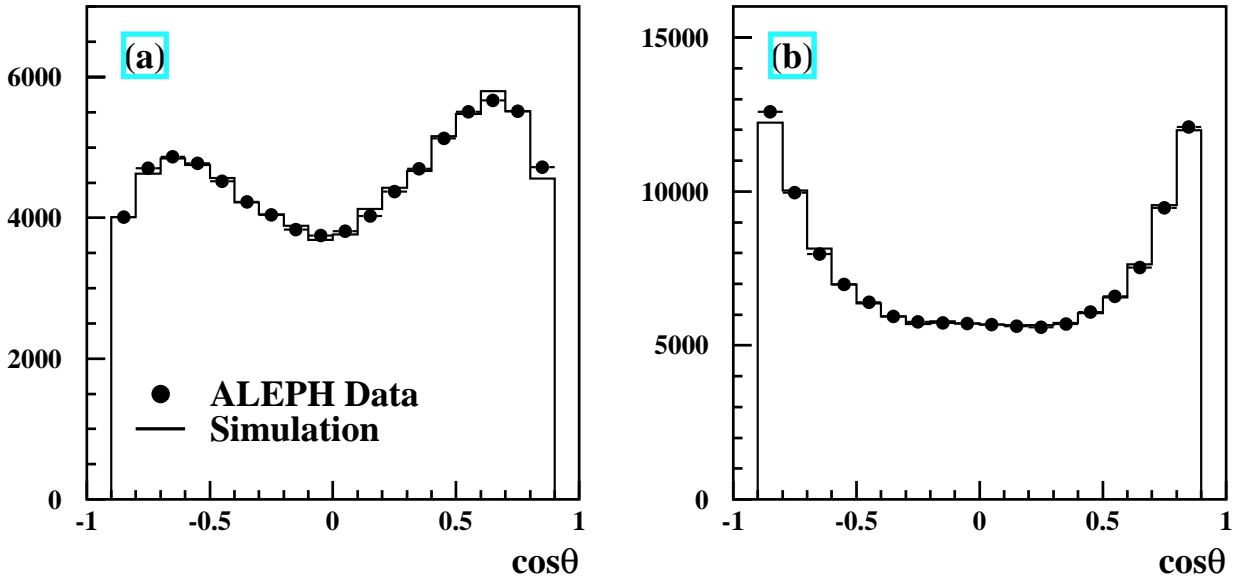


Figure 5.10: Reconstructed  $\cos\theta$  distribution from the ALEPH b-asymmetry measurement with leptons for [a\) the b-enriched and b\) the c-enriched sample.](#)

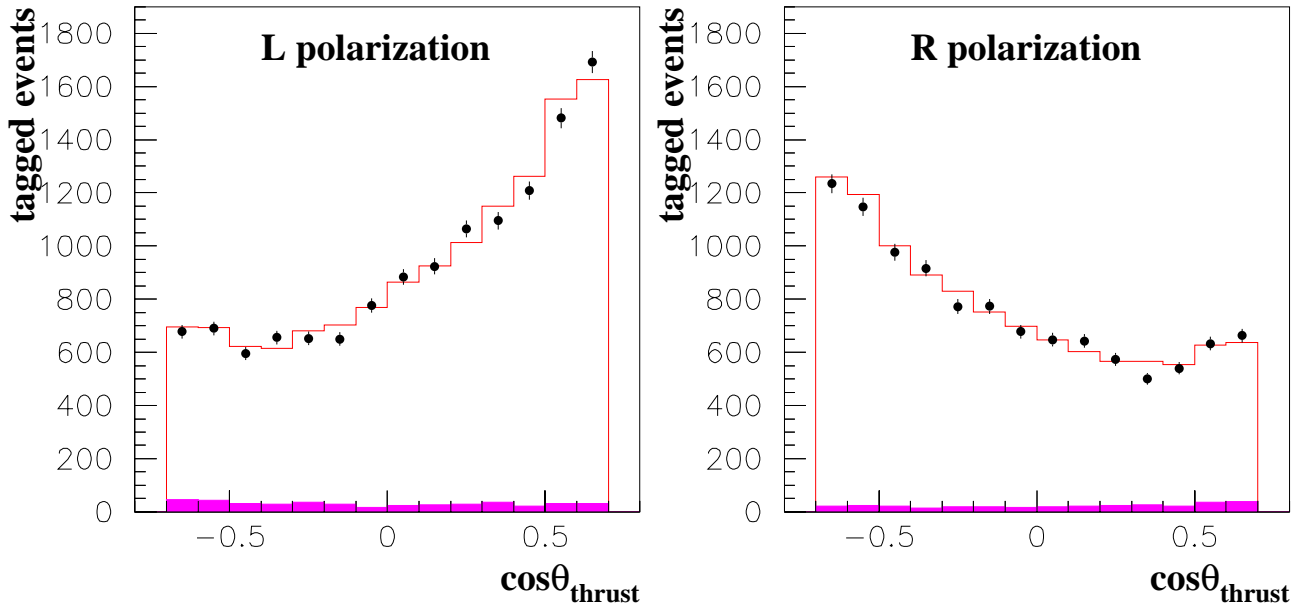


Figure 5.11: Reconstructed  $\cos\theta$  distribution from the SLD vertex charge analysis with left- and right-handed beam polarisation.

### Lepton and D meson measurements

As already described in sections 5.2.2 and 5.2.3 leptons and D-mesons can be used simultaneously for flavour and charge tagging.

$b \rightarrow \ell$  decays can be distinguished with a simple cut on the lepton transverse momentum but the leptons from other sources strongly overlap. As an example Table 5.3 shows the sample composition and the lepton-primary quark charge correlations for the ALEPH lepton sample with a transverse momentum cut of  $p_t > 1.25\text{GeV}$ . The charge correlations are given for the decaying quark, *i.e.* after any mixing of neutral B mesons. The relevant quantity for the asymmetry measurements is the quark charge at production, so corrections for the  $B\bar{B}$  effective mixing parameter  $\bar{\chi}$  have to be applied. To enhance the sensitivity of lepton-based analyses to  $A_{\text{FB}}^{c\bar{c}}$ , the experiments use additional information like lifetime tagging, jet charge in the opposite hemisphere or hadronic information from the lepton jet.

Lepton source	charge correlation	fraction for $p_t > 1.25\text{GeV}$
$b \rightarrow \ell^-, b \rightarrow \bar{c} \rightarrow \ell^-$	1	0.795
$b \rightarrow c \rightarrow \ell^+$	-1	0.046
$c \rightarrow \ell^+$	1	0.048
background	weak	0.111

Table 5.3: Correlation between the lepton charge and the quark charge at decay time. The sample composition for  $p_t > 1.25\text{GeV}$  in the ALEPH analysis is also shown.

A relatively pure charm sample can be obtained using high momentum reconstructed D-mesons, and additional b-tagging requirements are used to exchange the sensitivity to  $A_{\text{FB}}^{b\bar{b}}$ . ▲

In both cases the sample composition is usually taken from simulation. In lepton-tagged analyses, the uncertainties in the sample composition due to modelling of semileptonic b and c

decays are rather large. Therefore, in addition to the asymmetries, the experiments measure the  $B\bar{B}$  effective mixing parameter  $\bar{\chi}$ , the prompt and cascade semileptonic branching fraction of the b-hadrons  $\text{BR}(b \rightarrow \ell)$  and  $\text{BR}(b \rightarrow c \rightarrow \ell)$  and the prompt semileptonic branching fraction of the c-hadrons  $\text{BR}(c \rightarrow \ell)$ . As the same analysis cuts are used in both cases, these auxiliary measurements serve as an effective parametrisation of the lepton spectrum, greatly reducing the modelling errors.

In the same way, the fragmentation function is measured from data in the D-meson analyses. But since there is only one important source of D-mesons per quark flavour, and the correlation between the quark flavour and the D-meson flavour is the same for b- and c-quarks, the sensitivity to the sample composition is much smaller.

## Jet and vertex charge

The average charge of all particles in a jet contains information about the original quark charge.

Usually the jet charge is defined as

$$Q_h = \frac{\sum_i q_i p_{\parallel i}^\kappa}{\sum_i p_{\parallel i}^\kappa},$$

where the sum runs over all charged particles in a hemisphere with charge  $q_i$  and longitudinal momentum with respect to the thrust axis  $p_{\parallel i}$ , and  $\kappa$  is a tunable parameter with typical values between 0.3 and 1.

For B- and D-mesons the meson charge is correlated to the flavour of the b- or c-quark. If all charged particles of a jet can be uniquely assigned to the primary or the decay vertex, the charge sum of the decay vertex, if non zero, uniquely tags the quark charge. At SLD the b-asymmetry measurement with vertex charge is the most precise measurement of this quantity. At LEP vertex charge has also been used in conjunction with other tags, but its performance is much lower than at SLD due to the inferior impact parameter resolution and vertex reconstruction.

For both charge tagging methods, it is difficult estimate the charge tagging efficiency from simulation due to uncertainties from fragmentation and B-decays. However, the efficiency can be obtained reliably from data using double tags. If in a cut based analysis  $\omega_q$  is the efficiency to tag the quark charge correctly in a pure sample of q-quarks, the fraction of same sign double tags in the sample of all double tags is given by

$$f_{SS} = 2\omega_q(1 - \omega_q), \quad (5.7)$$

apart from small corrections due to hemisphere correlations. Equation 5.7 can then be used to obtain  $\omega_q$ . Corrections due to background and hemisphere correlations have to be applied using simulation.

Since the charge tagging efficiency for the jet charge is rather modest, a statistical method to extract the asymmetry is usually used. With  $Q_{F/B}$  being the jet charge of the forward/backward hemisphere and  $Q_{q/\bar{q}}$  the jet charge of the quark/antiquark hemisphere, one has

$$\begin{aligned} \langle Q_{FB} \rangle &= \langle Q_F - Q_B \rangle \\ &= \delta_q A_{FB}^{q\bar{q}} \\ \delta_q &= \langle Q_q - Q_{\bar{q}} \rangle, \end{aligned} \quad (5.8)$$

for a pure sample of  $q\bar{q}$ -events. The resolution parameter  $\delta_q$  can be measured from data using<sup>‡</sup>

$$\left(\frac{\delta_q}{2}\right)^2 = \frac{\langle Q_F \cdot Q_B \rangle + \rho_{q\bar{q}} \sigma(Q)^2 + \mu(Q)^2}{1 + \rho_{q\bar{q}}},$$

<sup>‡</sup>The exact formulae used by the experiments vary slightly, however the general formalism is identical.



where  $\mu(Q)$  is the mean value of  $Q$  for all hemispheres and  $\sigma(Q)$  its variance.  $\mu(Q)$  is slightly positive due to an excess of positive particles in secondary hadronic interactions. The hemisphere correlations,  $\rho_{q\bar{q}}$ , are coming from charge conservation, hard gluon radiation etc., and have to be taken from simulation.

The analyses select a relatively pure sample of  $b\bar{b}$  events using lifetime tagging techniques. Light quark background is always subtracted using Monte Carlo simulation. The charge separation for charm is either also taken from Monte Carlo or determined by performing the analysis in bins of different  $b$ -purities and fitting  $\delta_b$  and  $\delta_c$  from the data. It should be noted that dilution due to  $B\bar{B}$ -mixing is completely absorbed into the measured  $\delta_b$ . Effects from gluon radiation are also included to a large extent, so that the residual QCD correction is very small.

The above formalism can be generalised to any variable sensitive to the quark charge, including the combination of several different charge tagging techniques. As an example Figure 5.12 shows the charge tagging from ALEPH, which combines jet charge, vertex charge and charged Kaon information using a neural net to reach almost perfect tagging at high values. ▲

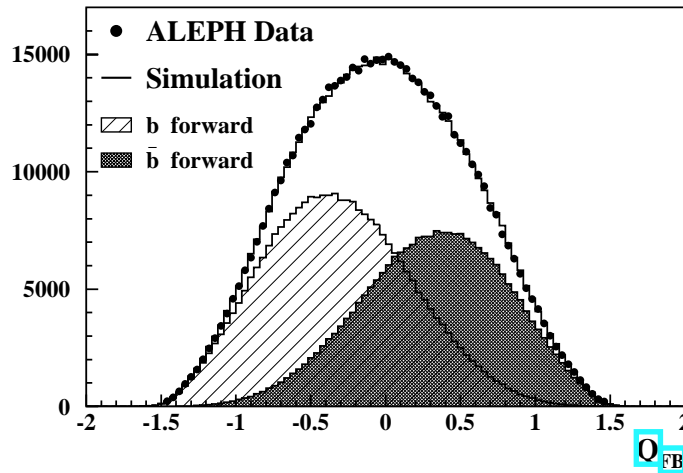


Figure 5.12: Charge separation of the ALEPH neural net tag using jet charge, vertex charge and charged Kaons. The asymmetry reflects  $A_{\text{FB}}^{b\bar{b}}$  diluted by the non-perfect charge tagging.

## Kaons

Charged Kaons from  $b$ - and  $c$ -decays are also sensitive to the quark flavour, via the decay chain  $(b \rightarrow)c \rightarrow s$ . Only Kaons with large impact parameters are used, to suppress those produced in the fragmentation process. As with other methods, the charge tagging efficiency is measured using the double tag technique.

### 5.4.1 Asymmetry measurements used in the combination

The forward-backward asymmetry measurements included in the average are:

- Lepton measurements from ALEPH [96], DELPHI [97], L3 [98] and OPAL [99]: L3 measures  $A_{\text{FB}}^{b\bar{b}}$  only from a sample of high  $p_t$  leptons. ALEPH, DELPHI and OPAL measure  $A_{\text{FB}}^{b\bar{b}}$  and  $A_{\text{FB}}^{c\bar{c}}$  using leptons combined with lifetime tagging and some additional information. ALEPH adds properties of hadrons in the events and information from the missing



energy due to escaping neutrinos. OPAL also uses hadronic properties while DELPHI includes the jet charge of the hemisphere opposite the lepton.

- Measurements of  $A_{\text{FB}}^{\text{b}\bar{\text{b}}}$  based on lifetime tagged events with a jet charge measurement using the weight method (see Equation 5.9 from DELPHI [100], L3 [101] and OPAL [102] and a similar analysis from ALEPH [103] with a charge tag combining jet charge vertex charge and Kaons in a neural net.
- Analyses with D mesons from ALEPH [104], DELPHI [105] and OPAL [106]: ALEPH measures  $A_{\text{FB}}^{\text{c}\bar{\text{c}}}$  only from a sample of high momentum D mesons. DELPHI and OPAL measure  $A_{\text{FB}}^{\text{b}\bar{\text{b}}}$  and  $A_{\text{FB}}^{\text{c}\bar{\text{c}}}$  by fitting the momentum spectrum of the D mesons and including lifetime information.
- A DELPHI analysis of  $A_{\text{FB}}^{\text{b}\bar{\text{b}}}$  combining jet charge, vertex charge, Kaons and some other variables sensitive to the b-quark charge in a neural net [107] using a cut on the charge estimator.


The left-right-forward-backward asymmetry measurements from SLD are directly quoted in terms of  $\mathcal{A}_b$  and  $\mathcal{A}_c$ . The following results are included:

- Measurements of  $\mathcal{A}_b$  and  $\mathcal{A}_c$  using leptons [108, 109];
- A measurement of  $\mathcal{A}_c$  using D mesons [110];
- A measurement of  $\mathcal{A}_b$  using vertex charge [111];
- A measurement of  $\mathcal{A}_b$  using Kaons [112];
- A measurement of  $\mathcal{A}_c$  using vertex charge and Kaons [113].



## 5.5 Auxiliary measurements

The measurements of the charmed hadron fractions  $P(c \rightarrow D^{*+}) \times \text{BR}(D^{*+} \rightarrow \pi^+ D^0)$ ,  $f(D^+)$ ,  $f(D_s^+)$  and  $f(c_{\text{baryon}})$  are included in the  $R_c$  analyses and are described there.

ALEPH [114], DELPHI [115], L3 [87, 116] and OPAL [117] measure  $\text{BR}(b \rightarrow \ell)$ ,  $\text{BR}(b \rightarrow c \rightarrow \ell)$  and  $\bar{\chi}$  or a subset from a sample of leptons opposite a b-tagged hemisphere and from a double lepton sample. DELPHI [90] and OPAL [95] measure  $\text{BR}(c \rightarrow \ell)$  from a sample opposite a high energy  $D^{*\pm}$ . 

## 5.6 External inputs to the heavy flavour combination

All the measurements contributing to the electroweak fit require some input from simulated events. Quantities derived from the simulation are affected by uncertainties related to the modelling of the detector response, as well as by the limited knowledge of the physics processes that are simulated. These latter sources are common to all experiments, and they have to be treated as correlated when averaging individual results. Furthermore, in order to produce consistent averages, the input physics parameters or models used in the simulation must be the same for all analyses in all experiments.

The choice of the input physics parameters and models relevant for electroweak heavy flavour analyses is discussed below. The relative importance of each input [on](#) the fitted partial widths and asymmetries can be seen from Table 5.9.

### 5.6.1 The heavy quark fragmentation

The process of hadron production is modelled as the convolution of a perturbative part (hard gluon radiation), and a non perturbative part, called fragmentation, described with phenomenological models.

In the JETSET [28] simulation the fragmentation model by Peterson *et al.* [118] is used, which describes the process in terms of the variable  $z = (E + p_{\parallel})_{\text{hadron}} / (E + p_{\parallel})_{\text{quark}}$ , where  $p_{\parallel}$  is the momentum component in the direction of the fragmenting quark. The model contains one free parameter,  $\varepsilon_Q$ , which is tuned to reproduce a given value of the mean energy of the heavy hadrons produced. Such tuning depends on the cut-off used for the transition between the perturbative and the non-perturbative part, therefore  $\varepsilon_Q$  can not be given an absolute meaning. The energy spectrum is more conveniently described in terms of the variable  $x_Q$ , defined as the energy of the weakly-decaying hadron containing the heavy quark  $Q$  normalised to the beam energy.

The analyses quoted in Reference [119–123], which provide a value for the mean energy of b hadrons, are averaged obtaining:

$$\langle x_b \rangle = 0.702 \pm 0.008$$

where the error includes the uncertainty due to the modelling of the fragmentation function. This uncertainty is estimated by using the functional forms proposed by Collins and Spiller [124], and by Kartvelishvili *et al.* [125] as alternatives to Peterson *et al.* when extracting  $\langle x_b \rangle$ .

The energy of charmed hadrons is measured in analyses which make use of lepton tags or inclusive reconstruction of  $D^0/D^+$  mesons [126,127], and in analyses with full reconstruction of  $D^{*+}$  mesons [128–130]. The former have a larger dependence on the modelling of the spectrum, while the latter need an additional correction to obtain the energy of the weakly-decaying hadron. In all cases the contribution from charmed hadrons produced by hard gluons splitting to heavy quarks is removed. The average energy of weakly-decaying c-hadrons is found to be

$$\langle x_c \rangle = 0.484 \pm 0.008$$

which again includes the estimated uncertainty from the modelling of the spectrum.

### 5.6.2 Heavy quarks from gluon splitting

Hard gluons can occasionally split to heavy quark pairs. In several analyses these contributions need to be subtracted. In particular the uncertainty on the rate of gluons splitting to  $b\bar{b}$  pairs is the single largest contribution to the systematic error on the  $R_b$  world average.

The rates  $g_{c\bar{c}}$  and  $g_{b\bar{b}}$  are defined as the number of hadronic Z decays containing a hard gluon splitting to a  $c\bar{c}$  or  $b\bar{b}$  pair, normalised to the total number of hadronic Z decays.

Measurements of  $g_{b\bar{b}}$  rely on an inclusive lifetime-based tag applied to the jets reconstructed in the event [131–135], while measurements of  $g_{c\bar{c}}$  make use of exclusive  $D^*$  reconstruction, final states containing leptons, or are based on the combination of event shape variables [93,136,137].

Averaging published results yields:

$$\begin{aligned} g_{c\bar{c}} &= 0.0296 \pm 0.0038, \\ g_{b\bar{b}} &= 0.00254 \pm 0.00051, \end{aligned}$$

with only a very small correlation between the two values.

### 5.6.3 Multiplicities in heavy flavour decays

Many analyses make use of inclusive b tagging methods which exploit the long lifetimes of b hadrons. The discrimination is based on the presence, in a jet, or a hemisphere, or the whole event, of charged tracks with significant impact parameter from the primary vertex of the events. Therefore the tagging efficiency is directly affected by the number of charged tracks produced in the long-lived hadron decay.

In  $R_b$  measurements the tag is applied to hemispheres, and the b efficiency is measured directly in the data from the fraction of events with both hemispheres tagged. The b charged multiplicity only enters through the hemisphere correlation, which is computed with the simulation. Measurements of the average b charged multiplicity performed at LEP are used. Results from lower energy experiments cannot be used because of the different b-hadron mixture.

However, the charm selection efficiency is taken from the simulation, **at least for the samples with highest purity.** It is therefore crucial to propagate correctly the **uncertainty due to the decay charged multiplicities of the various charmed hadrons.** This is done separately for each hadron species due to the significant differences in lifetimes.

The charm selection efficiency also depends on the number of neutral particles accompanying the charged particles in a given topological decay channel. The size of this effect depends on how invariant mass cuts are implemented and might vary substantially in different analyses. The uncertainty is evaluated varying the  $K^0$  and  $\pi^0$  production rates in charmed hadron decays.

#### Average charged multiplicity in b hadron decays

Inclusive measurements of the mean b-hadron charged multiplicity at LEP [138] are combined to obtain:

$$\langle n_b^{ch} \rangle = 4.955 \pm 0.062 .$$

Particles coming from the decay of  $B^{**}$  or other possible excited b states are excluded; the result is also corrected to exclude charged particles originating from the decay of  $K^0$  and  $\Lambda$ .

#### Charged multiplicities of c hadron decays

Inclusive topological branching fractions have been measured for  $D^0$ ,  $D^+$  and  $D_s^+$  [139]. For each species, each channel is varied within its uncertainty, except for the channel with the highest rate, which is used to compensate the variation. The resulting errors are combined using the corresponding correlation coefficients.

The values  $f_i$  of the branching fractions for the decays into  $i$  charged particles, the corresponding errors  $\sigma_i$  and correlation coefficients  $C_{ij}$  are given in Table 5.4.

#### Neutral particle production in c hadron decays

The procedure to estimate the residual dependence of the lifetime tag efficiency on the average rate of neutral particles produced in charm decays is tailored, case by case, on the specific properties of the tag and based on the measurements available [75]. Although the procedures differ somewhat between experiments, the resulting estimated uncertainties are taken as fully correlated.

$D^0$	$f_0 = 0.054$	$f_2 = 0.634$	$f_4 = 0.293$	$f_6 = 0.019$
	$\sigma_0 = 0.011$		$\sigma_4 = 0.023$	$\sigma_6 = 0.009$
	$C_{04} = 0.07$	$C_{46} = -0.46$	$C_{06} = 0$	
$D^+$	$f_1 = 0.384$	$f_3 = 0.541$	$f_5 = 0.075$	
	$\sigma_1 = 0.023$		$\sigma_5 = 0.015$	
	$C_{15} = -0.33$			
$D_s^+$	$f_1 = 0.37$	$f_3 = 0.42$	$f_5 = 0.21$	
	$\sigma_1 = 0.10$		$\sigma_5 = 0.11$	
	$C_{15} = -0.02$			

Table 5.4: Topological rates for the different charm meson species, with estimated errors and correlation coefficients. The subscripts indicate the number of charged particles produced.

### 5.6.4 Heavy flavour lifetimes

The lifetimes of heavy hadrons are relevant to many analyses, in particular all those which make use of lifetime-based b tagging methods. As for the charged multiplicity, in the case of the  $R_b$  analyses charm lifetimes enter directly in the estimate of the charm contamination in high purity samples, whereas b hadron lifetimes only affect the estimate of the hemisphere correlations.

#### Average b hadron lifetime

The average lifetime of b hadrons is taken to be [75]

$$\tau_b = 1.576 \pm 0.016 \text{ ps} ,$$

which is obtained from analyses of fully inclusive b final states. The lifetime difference between b species has in general little impact in all analyses. It is considered as a source of uncertainty in the  $R_b$  analyses either by using the individual lifetimes [75] or by enlarging the error to 0.05 ps.

#### Lifetimes of c hadrons

The lifetimes of the different c hadron species are considered as individual sources of uncertainties. The values and errors are [75]

$$\begin{aligned} \tau(D^0) &= 0.415 \pm 0.004 \text{ ps} , \\ \tau(D^+) &= 1.057 \pm 0.015 \text{ ps} , \\ \tau(D_s) &= 0.467 \pm 0.017 \text{ ps} , \\ \tau(\Lambda_c) &= 0.206 \pm 0.012 \text{ ps} . \end{aligned}$$

### 5.6.5 Charmed hadron decays to exclusive final states

Charm counting measurements determine the production rates of individual c-hadron species by tagging exclusive final states, using the branching fraction for the appropriate decay mode as input. The values and errors used are [75, 140]:

$$\begin{aligned}
\text{BR}(D^0 \rightarrow K^- \pi^+) &= 0.0385 \pm 0.0009, \\
\text{BR}(D^+ \rightarrow K^- \pi^+ \pi^+) &= 0.090 \pm 0.006, \\
\text{BR}(D_s^+ \rightarrow \phi \pi^+) &= 0.036 \pm 0.009, \\
\frac{\text{BR}(D_s^+ \rightarrow \bar{K}^{*0} K^+)}{\text{BR}(D_s^+ \rightarrow \phi \pi^+)} &= 0.92 \pm 0.09, \\
\text{BR}(\Lambda_c \rightarrow p K^- \pi^+) &= 0.050 \pm 0.013.
\end{aligned}$$

### 5.6.6 Heavy flavour leptonic decays

Many analyses rely on semileptonic final states in order to tag the presence of heavy hadrons and possibly their charge. Assessing the performance of such tags involves estimating the rates of the different sources of lepton candidates in hadronic events, and modelling the kinematics of the leptons produced in the decay of heavy hadrons.

The rates for the major sources (direct **b and c** decays  $b \rightarrow \ell^-$  and  $c \rightarrow \ell^+$ , cascade b decays  $b \rightarrow c \rightarrow \ell^+$ ) are measured at LEP, and included as fitted parameters. The modelling of the decay kinematics is a common source of systematic uncertainty. The rates for the other sources are taken from external measurements.

#### Modelling of direct semileptonic b decays

For the semileptonic decays of  $B^0$  and  $B^+$  mesons the CLEO collaboration has compared decay models to their data and measured the free parameters of the models. Based on the CLEO fits [141], the LEP experiments quote results for three different models.

- The model proposed by Altarelli *et al.* [142], is an extension of the free quark model which attempts to account for non-perturbative effects kinematically. The two free parameters of the model, the Fermi momentum of the constituent quarks inside the heavy meson and the mass of the final quark, are determined from CLEO data to be  $p_F = 298 \text{ MeV}/c$ ,  $m_c = 1673 \text{ MeV}/c^2$ .
- The form-factor model proposed by Isgur *et al.* [143], with the model prediction that 11% of semileptonic B meson decays result in an L=1 charm meson,  $D^{**}$ .
- The same model with the rate of  $D^{**}$  mesons increased to 32%, as preferred by the CLEO data [141, 143].

The model of Altarelli *et al.* is used to derive the central values of the analyses, while the two others, which give respectively harder and softer lepton spectra, are used to give an estimate of the associated uncertainty.

Reweighting functions are constructed to adjust the lepton spectrum of semileptonic  $B^0$  and  $B^+$  decays in the LEP Monte Carlo samples to the three models based on CLEO data. For use in Z decays, the same reweighting functions have been assumed to be valid for the  $B_s^0$  meson and b baryons. This would be correct in the simplest spectator model, and is thought more generally to be adequate for the  $B_s^0$ . The baryons contribution is only about 10%, and no additional systematic error is assigned.

## Modelling of direct semileptonic c decays

The measurements of DELCO [144] and MARK III [145] for  $D^0$  and  $D^+$  semileptonic decays have been combined and parameterised using the model of Altarelli *et al.* as a convenient functional form. The D boost and the experimental resolution are taken into account in the fit to the data. Based on this fit [146], the model parameters are fixed to  $p_F = 0.467$  GeV/ $c$ ,  $m_s = 0.001$  GeV/ $c^2$  and they are varied to  $p_F = 0.353$  GeV/ $c$ ,  $m_s = 0.001$  GeV/ $c^2$  and  $p_F = 0.467$  GeV/ $c$ ,  $m_s = 0.153$  GeV/ $c^2$  to derive an estimate of the associated uncertainty. The reweighting functions derived from  $D^0$  and  $D^+$  decays are assumed to be valid for all charm hadrons.

## Modelling of cascade semileptonic b decays

For the cascade decays,  $b \rightarrow c \rightarrow \ell^+$ , the three models used for  $c \rightarrow \ell^+$  decays are combined with the measured  $b \rightarrow D$  spectrum from CLEO [147] to generate three models for the lepton momentum spectrum in the rest frame of the b hadron. The CLEO  $b \rightarrow D$  spectrum can be conveniently modelled by a Peterson function [118] with free parameter  $\varepsilon = 0.42 \pm 0.07$ . The effect of this  $b \rightarrow D$  model uncertainty on the  $b \rightarrow c \rightarrow \ell^+$  spectrum is negligible compared to the uncertainty from the  $c \rightarrow \ell^+$  models.

## The rate of $b \rightarrow \bar{c} \rightarrow \ell^-$ transitions

Several quantities related to the rate of leptons from c hadrons produced from the “upper vertex” in b-hadron decays have been measured. An estimate of this rate is therefore possible, based upon experimental results.

The inclusive and flavour-specific  $B \rightarrow D$  and  $B \rightarrow \Lambda_c^+$  rates measured at CLEO [148] are combined with the  $B \rightarrow DD(X)$  rates measured in ALEPH [149] to extract the probabilities of producing the different c-hadrons from the upper vertex in b decays. These are combined with the c-hadron semileptonic branching fractions to obtain a value for the  $\text{BR}(b \rightarrow \bar{c} \rightarrow \ell^-)$ .

The estimate obtained is

$$\text{BR}(b \rightarrow \bar{c} \rightarrow \ell^-) = 0.0162_{-0.0036}^{+0.0044}.$$

## Other semileptonic decays

The rate for  $b \rightarrow \tau^- \rightarrow \ell^-$  decays derived from existing measurements of  $\text{BR}(b \rightarrow \tau)$  [150] combined with the  $\tau$  leptonic branching fraction [75]. The procedure yields:

$$\text{BR}(b \rightarrow \tau^- \rightarrow \ell^-) = 0.00419 \pm 0.00055.$$

The rate for  $b \rightarrow (J/\psi + \psi') \rightarrow \ell\ell$  decays calculated from the production rate of  $J/\psi$  and  $\psi'$  in  $Z \rightarrow b\bar{b}$  decays, and the  $J/\psi$  and  $\psi'$  leptonic branching fractions [75], yielding

$$\text{BR}(b \rightarrow (J/\psi + \psi') \rightarrow \ell\ell) = 0.00072 \pm 0.00006.$$

## 5.6.7 Hemisphere correlations in double-tag methods

In analyses where a b-tagging algorithm is applied in one hemisphere, the tagging efficiency can be measured from the data by comparing the fraction of hemispheres that are tagged and the fraction of events with both hemispheres tagged. However, the correlation between the tagging

efficiencies in the two hemispheres must then be estimated from simulation. This is particularly crucial for the precise  $R_b$  double tag measurements.

There are basically three physics sources for such a correlation:

- detector inhomogeneities,
- the use of a common primary [vertex](#).
- kinematic correlations, mainly due to gluon [radiation](#).

Detector effects are easily controllable from the data by measuring the tagging rate as a function of jet direction and then folding the two hemispheres in an event. This error source is clearly uncorrelated between the experiments.

The second of these sources is relatively small for algorithms based on the reconstruction of the b decay length, since this is dominated by the uncertainty on the position of the secondary vertex. However, it is a major issue for tags based on track impact parameters, and it is particularly difficult to control since it heavily influences the other sources. Therefore in the  $R_b$  analyses the primary vertex is generally reconstructed independently in the two hemispheres, rendering this source of correlation negligible.

The kinematic correlations are correlated between the experiments. They mainly arise from the fact that the tagging efficiency depends on the b-hadron momentum and that a gluon emitted at a large angle reduces the energy of both quarks.

If the efficiency is proportional to the b-hadron momentum the efficiency correlation is directly given by the momentum correlation. Analytic  $\mathcal{O}(\alpha_s)$  QCD calculations [predicts](#) effects of about 1.4% [151] for the correlation between the two b-quark momenta. At the parton level, fragmentation models agree to the 0.2% level with this number. At the hadron level HERWIG [29] gives an up to 0.8% larger correlation than the other models.

Since the proportionality between the B-momentum and the tagging efficiency is only approximate, in practice the experiments have derived test quantities that are sensitive to the kinematical correlations and the systematic uncertainties are derived from data/Monte Carlo comparisons. As an example the momentum of the fastest jet assuming a three jet topology can be calculated and the tagging rate for the hemisphere containing this jet and the opposite one is measured. Although these errors have a large statistical component, they are conservatively taken as fully correlated between the experiments.

Events where the radiated gluon is so hard that the two b-hadrons are in the same hemisphere are particularly relevant for the estimate of the correlation. The rate of such events (about 1% of all  $Z \rightarrow b\bar{b}$  events) is varied by 30%, motivated by a comparison of matrix element and parton shower models.

Furthermore, the hemisphere correlation also depends on b hadron production and decay properties. Such a dependence is a small second order effect for analyses which reconstruct the primary vertex independently in the two hemispheres, but can be substantial if a common primary vertex is used, due to the inclusion of tracks [from b-hadrons into](#) the primary vertex determination. The sources of uncertainty considered are:

- average charged track multiplicity in b-hadron decay,
- b fragmentation,
- b hadron lifetimes,

and the errors are evaluated according to [the prescription in this section](#).



### 5.6.8 Light quark background in lifetime tagged samples

The amount of light quark background in lifetime-tagged samples is mainly determined by the rate of long-lived light hadrons produced in the fragmentation. This is only a significant source of uncertainty for the precise  $R_b$  measurements. In the case of forward-backward asymmetry measurements, [other](#) details of light quark fragmentation are relevant in the extraction of the asymmetry from the measured charge flow.

#### The rate of long-lived light hadrons

All experiments have measured the rates of long-lived light hadrons and tuned their fragmentation model accordingly. Variations of 10% around the central value are used to estimate the uncertainty.

#### The fragmentation of light quarks

The JETSET model contains many free parameters, several of which influence the charge flow predictions. These parameters have been tuned individually by the experiments and it is not possible to define a common procedure to evaluate the errors due to light quark fragmentation. Fortunately these errors turn out to be relatively small, and they are assumed to be fully correlated even if the procedures to evaluate them vary [slightly](#) between the experiments.

## 5.7 Corrections to the measured electroweak parameters

### 5.7.1 Corrections to $R_b$ , $R_c$

Small corrections have to be applied to the [measurements performed by the experiments](#). The  $R_b$  and  $R_c$  analyses measure the ratio [of productions](#) cross sections  $R_q = \sigma_{q\bar{q}}/\sigma_{\text{had}}$ . To obtain the ratios of partial widths  $R_q^0 = \Gamma_{q\bar{q}}/\Gamma_{\text{had}}$ , small corrections for photon exchange and  $\gamma - Z$ -interference have to be applied. These corrections are typically +0.0002 for  $R_b$  and -0.0002 for  $R_c$ , and are applied by the experiments before the combination as their size depends slightly on the invariant mass cutoff of the  $q\bar{q}$ -system imposed in the analysis.

### 5.7.2 QCD corrections to the heavy flavour forward-backward asymmetries

The measured forward backward asymmetries do not correspond to the underlying quark asymmetries due to QCD effects. The dominant corrections are due to radiation of gluons from the final state quarks. The QCD corrections do not depend on the beam polarisation and are thus identical for the unpolarised forward-backward asymmetry and the left-right-forward-backward asymmetries.

Theoretical calculations use either the quark direction or the thrust direction to define the [axis relative to which the asymmetry is computed](#). Since the reconstructed thrust axis is generally used as the heavy quark direction estimator in experimental measurements, calculations based on the thrust axis are considered.



The effect on the asymmetry at the scale  $\mu^2 = m_Z^2$  is parametrised as [152]:

$$\left(A_{\text{FB}}^{\text{q}\bar{\text{q}}}\right)_{\text{meas}} = (1 - C_{\text{QCD}}) \left(A_{\text{FB}}^{\text{q}\bar{\text{q}}}\right)_{\text{no QCD}} = \left(1 - \frac{\alpha_s(m_Z^2)}{\pi} c_1 - \left(\frac{\alpha_s(m_Z^2)}{\pi}\right)^2 c_2\right) \left(A_{\text{FB}}^{\text{q}\bar{\text{q}}}\right)_{\text{no QCD}}. \quad (5.9)$$

The first-order corrections are known including mass effects [153]. Taking the thrust axis as the direction and using the pole mass, they are  $c_1 = 0.77$  for  $A_{\text{FB}}^{\text{b}\bar{\text{b}}}$  and  $c_1 = 0.86$  for  $A_{\text{FB}}^{\text{c}\bar{\text{c}}}$ .

The second order corrections have recently been recalculated [154, 155] and found to be in disagreement with previous results. The calculation of [155] is strictly massless and also neglects the corrections from triangle diagrams involving top quarks, given in [153]: corrections arising from diagrams which lead to two-parton final states are the largest, and they can be added to the results of [155], as they apply in the same way to calculations based either on the thrust or [and](#) the quark direction.

The second order coefficients used are  $c_2 = 5.93$  for  $A_{\text{FB}}^{\text{b}\bar{\text{b}}}$  and  $c_2 = 8.5$  for  $A_{\text{FB}}^{\text{c}\bar{\text{c}}}$ . The final QCD correction coefficients, including fragmentation effects, are  $C_{\text{QCD}}^{\text{had,T}} = 0.0354 \pm 0.0063$  for  $A_{\text{FB}}^{\text{b}\bar{\text{b}}}$  and  $C_{\text{QCD}}^{\text{had,T}} = 0.0413 \pm 0.0063$  for  $A_{\text{FB}}^{\text{c}\bar{\text{c}}}$ . The breakdown of the errors is given in Table 5.5.

Error on $C_{\text{QCD}}^{\text{had,T}}$		$\text{b}\bar{\text{b}}$	$\text{c}\bar{\text{c}}$
Higher orders	[155]	0.0025	0.0046
Mass effects	[152]	0.0015	0.0008
Higher order mass	[155]	0.005	0.002
$\alpha_s = 0.119 \pm 0.003$		0.0012	0.0015
Hadronisation	[152]	0.0023	0.0035
Total		0.0063	0.0063

Table 5.5: Error sources for the QCD corrections to the forward-backward asymmetries.

The procedure to implement QCD corrections in the experimental analyses is non-trivial. It is described in detail in [152] and briefly summarised in the following.

The corrections provided by theoretical calculations are not directly applicable to experimental measurements for two main reasons. First, the thrust axis used in theoretical calculations is defined using partons; a further smearing is caused by the hadronisation of partons into physical particles. This effect, typically ten times smaller than the correction itself, is taken from the simulation using the JETSET model, and its full size is taken as an additional uncertainty. Second, and much more important, the experimental selection and analysis method can introduce a bias in the topology of the events used, or intrinsically correct for the effects. It turns out that analyses based on semileptonic decays typically need between 50% and 70% of the full correction, while jet-charge based measurements intrinsically correct for the dilution induced by gluon radiation.

Because of the analysis dependence of the QCD corrections all asymmetries quoted in this chapter are corrected for QCD effects.

The uncertainty on the theoretical calculation of the corrections, as well as on the additional effect due to hadronisation, are taken as fully correlated between the different measurements. The ‘‘scaling factor’’ applied for each individual analysis to account for the experimental bias is instead evaluated case by case together with its associated uncertainty, and these errors are taken as uncorrelated.

### 5.7.3 Other corrections to the asymmetries

The forward backward asymmetries at LEP vary strongly as a function of the centre of mass energy because of  $\gamma - Z$ -interference. Since the mean energies at the different points vary slightly with time, the mean energies of the results of the different analyses are also not completely identical. The experiments quote the mean centre of mass energy for each asymmetry measurement. In a first fit the asymmetries are corrected to the closest of the three energies  $\sqrt{s} = 89.55\text{GeV}(-2)$ ,  $91.26\text{GeV}(\text{pk})$ ,  $92.94\text{GeV}(+2)$  assuming Standard Model energy dependence.

The slope of the asymmetries depends only on the well known fermion charges and axial couplings while the asymmetry value on the Z-pole is sensitive to the effective weak mixing angle. Once it is verified in the first fit that the energy dependence is indeed consistent with that expected in the Standard Model, in a second fit all asymmetries are corrected to the peak energy (91.26 GeV) before fitting.

To obtain the pole asymmetry,  $A_{\text{FB}}^{0,q}$ , which is defined as the asymmetry at the Z-mass for pure Z-exchange, the fitted asymmetries at the peak energy, denoted as  $A_{\text{FB}}^{\text{q}\bar{\text{q}}}(\text{pk})$  need to be corrected further as summarised in Table 5.6. These corrections are due to the energy shift from 91.26 GeV to  $m_Z$ , initial state radiation,  $\gamma$  exchange and  $\gamma$ -Z interference. A very small correction due to the nonzero value of the b quark mass is included in the correction called  $\gamma$ -Z interference. All corrections are calculated using ZFITTER.

Source	$\delta A_{\text{FB}}^{\text{bb}}$	$\delta A_{\text{FB}}^{\text{c}\bar{\text{c}}}$
$\sqrt{s} = m_Z$	-0.0013	-0.0034
QED corrections	+0.0041	+0.0104
$\gamma$ , $\gamma$ -Z, mass	-0.0003	-0.0008
Total	+0.0025	+0.0062

Table 5.6: Corrections to be applied to the quark asymmetries as  $A_{\text{FB}}^{0,q} = A_{\text{FB}}^{\text{q}\bar{\text{q}}}(\text{pk}) + \delta A_{\text{FB}}$ .

Similar corrections have to be applied to the left-right-forward-backward asymmetries. However they are directly presented in terms of  $\mathcal{A}_b$  and  $\mathcal{A}_c$  by SLD.

## 5.8 Combination procedure

The heavy flavour results are combined using a  $\chi^2$  minimisation technique [146]. In the case of the lineshape, each experiment measures the same 5 or 9 parameters. Here, the set of measurements is different for each experiment. Nonetheless, a  $\chi^2$  minimisation can be used to find the best estimates of each of the electroweak parameters. The formulation must be sufficiently flexible to allow any number of measurements of each electroweak parameter by each experiment. The measured values of closely related parameters are included in the averaging procedure, as mentioned above. Their treatment will be explained more fully below.

In order to write down an expression for this  $\chi^2$ , the average value, i.e. the best estimate of the set of electroweak parameters is denoted  $x^\mu$ , where the index  $\mu$  refers to the parameter.

$$x^\mu = \begin{matrix} R_b, \\ R_c, \\ A_{\text{FB}}^{\text{bb}}(-2), \end{matrix} \quad (5.10)$$

$$\begin{aligned}
& A_{\text{FB}}^{\text{c}\bar{\text{c}}}(-2), \\
& A_{\text{FB}}^{\text{b}\bar{\text{b}}}(\text{pk}), \\
& A_{\text{FB}}^{\text{c}\bar{\text{c}}}(\text{pk}), \\
& A_{\text{FB}}^{\text{b}\bar{\text{b}}}(+2), \\
& A_{\text{FB}}^{\text{c}\bar{\text{c}}}(+2), \\
& \mathcal{A}_{\text{b}}, \\
& \mathcal{A}_{\text{c}}, \\
& \text{BR}(\text{b} \rightarrow \ell), \\
& \text{BR}(\text{b} \rightarrow \text{c} \rightarrow \ell), \\
& \text{BR}(\text{c} \rightarrow \ell), \\
& \bar{\chi}, \\
& f(\text{D}^+), \\
& f(\text{D}_s^+), \\
& f(\text{c}_{\text{baryon}}), \\
& \text{P}(\text{c} \rightarrow \text{D}^{*+}) \times \text{BR}(\text{D}^{*+} \rightarrow \pi^+ \text{D}^0).
\end{aligned}$$

In this case the forward-backward asymmetries are averaged at three different centre-of-mass energies. Alternatively, they can all be interpreted as measurements of the asymmetry at the Z-peak,  $A_{\text{FB}}^{\text{b}\bar{\text{b}}}(\text{pk})$  and  $A_{\text{FB}}^{\text{c}\bar{\text{c}}}(\text{pk})$ , as described below.

Each experimental result is referred to as  $r_i^\mu$ . The  $i$ th result could be a measurement of any of the parameters,  $R_b$ , ( $\mu = 1$ ),  $R_c$  ( $\mu = 2$ ) and so on. A group of  $k$  results could be measured simultaneously in the same analysis to give:  $r_i^\mu, r_{i+1}^\nu \dots r_{i+k-1}^\rho$ .

The averages are given by minimising the  $\chi^2$ :

$$\chi^2 = \sum_{ij} (r_i^\mu - x^\mu) \mathcal{C}_{ij}^{-1} (r_j^\nu - x^\nu). \quad (5.11)$$

Almost all the complications in building the  $\chi^2$  are in calculating the  $n \times n$  covariance matrix,  $\mathcal{C}$ , relating the  $i = 1, n$  measurements. This matrix must take into account statistical and systematic correlations. Statistical errors arise from overlap of samples within an experiment, and for groups of measurements of closely related parameters in the same fit. Some systematic errors only lead to correlations between measurements made by the same experiment, for example errors due to the modelling of track resolutions in a particular detector. Others are potentially common to all the measurements. The experiments provide their measurements in the form of input tables, which list the central values, the statistical errors, any correlations between statistical errors and a detailed breakdown of the systematic errors. This breakdown is used to calculate the systematic error contribution to the covariance matrix by assuming that any particular systematic uncertainty, for example the uncertainty due to the lifetime of the  $\text{B}^0$  meson, is fully correlated for all measurements [146]. This assumption is legitimate if common values and uncertainties are used for those quantities taken from external experimental measurements. If necessary, older results are corrected to use the latest agreed set. The input parameters are discussed in section 5.6. In summary, the covariance matrix has the form:

$$\mathcal{C}_{ij} = \mathcal{C}_{ij}^{\text{stat}} + \sum_k \sigma_i^k \sigma_j^k, \quad (5.12)$$

where  $\mathcal{C}_{ij}^{\text{stat}}$  is the covariance matrix of statistical errors and  $\sigma_i^k$  is the systematic error in measurement  $i$ , due to the source of systematic uncertainty  $k$ .

It is also important to take into account that even when two electroweak parameters are not measured in the same fit, the measured value of one will depend on the value assumed for another. For example, a measurement of  $R_b$  often depends on the fraction of charm contamination in the sample, and therefore on the value of  $R_c$  that was assumed. The explicit first order dependence of the value of  $R_b$ ,  $r_i^{R_b}$ , on the average value of  $R_c$ ,  $x^{R_c}$ , is included as follows:

$$r_i^{R_b} = R_b^{\text{meas}} + a_i^{R_c} \frac{(x^{R_c} - R_c^{\text{used}})}{x^{R_c}}. \quad (5.13)$$

Here  $R_b^{\text{meas}}$  is the central value of  $R_b$  measured by the experiment, assuming a value for  $R_c = R_c^{\text{used}}$ . The constant  $a_i^{R_c}$  is given by

$$\frac{a_i^{R_c}}{x^{R_c}} = \left. \frac{dr_i^{R_b}}{dx^{R_c}} \right|_{x^{R_c}=R_c^{\text{used}}}. \quad (5.14)$$

The dependence of any measurement on any of the other fitted parameters can be expressed in the same way.

The system of including measurements by input tables has proved to be very flexible. Different subsets of results can be combined together in cross checks, to verify that the results are robust.

As an example Table 5.7 shows the **used measurements of  $R_b^0$** . The line “ $R_b$ (published)” shows the value published by the collaborations while in the line “ $R_b^0$ (used)” the values corrected for the agreed input parameters is given. The errors labelled “uncorrelated” are either internal to the analysis or to the experiment while the ones labelled “correlated” are potentially in common with other experiments. Also the dependencies of the  $R_b^0$  measurements on the other input parameters are given.

Since the uncertainties on the branching fractions of some of the decay modes used in the charm counting  $R_c$  analyses are rather large, two refinements are added to the fit to correct for non linear effects. The products  $R_c P(c \rightarrow D^{*+}) \times \text{BR}(D^{*+} \rightarrow \pi^+ D^0)$ ,  $R_c f(D^+)$ ,  $R_c f(D^0)$ ,  $R_c f(D_s^+)$  and  $R_c f(c_{\text{baryon}})$  are given as experimental results  $r_i^\mu$  and are compared to the product of the relevant fit parameters in the  $\chi^2$  calculation. In addition the errors on these parameters, again mainly the branching fraction errors, are more Gaussian if they are treated as relative errors. For this reason the logarithm of the products is fitted instead of the products themselves. **It has however been checked that only for  $R_c f(D_s^+)$  and  $R_c f(c_{\text{baryon}})$  the fit results depend on whether the logarithms or the values themselves are used.** However these two measurements are completely dominated by the branching fraction error for which it is clear that the logarithmic treatment is the better one.

## 5.9 Results

**This section contains the results of the winter01 conferences, they are not final!**

The results used in this combination have been described in sections 5.3, 5.4 and 5.5 and are summarised in tables A.1 - A.20. Figure 5.13 compares the main electroweak results of the different experiments.

In a first fit the different analyses have been combined with the asymmetries kept at the three different energies, yielding in total 18 free parameters. The results of this fit for the asymmetries are:

$$A_{\text{FB}}^{\text{b}\bar{\text{b}}}(-2) = 0.0521 \pm 0.0069,$$

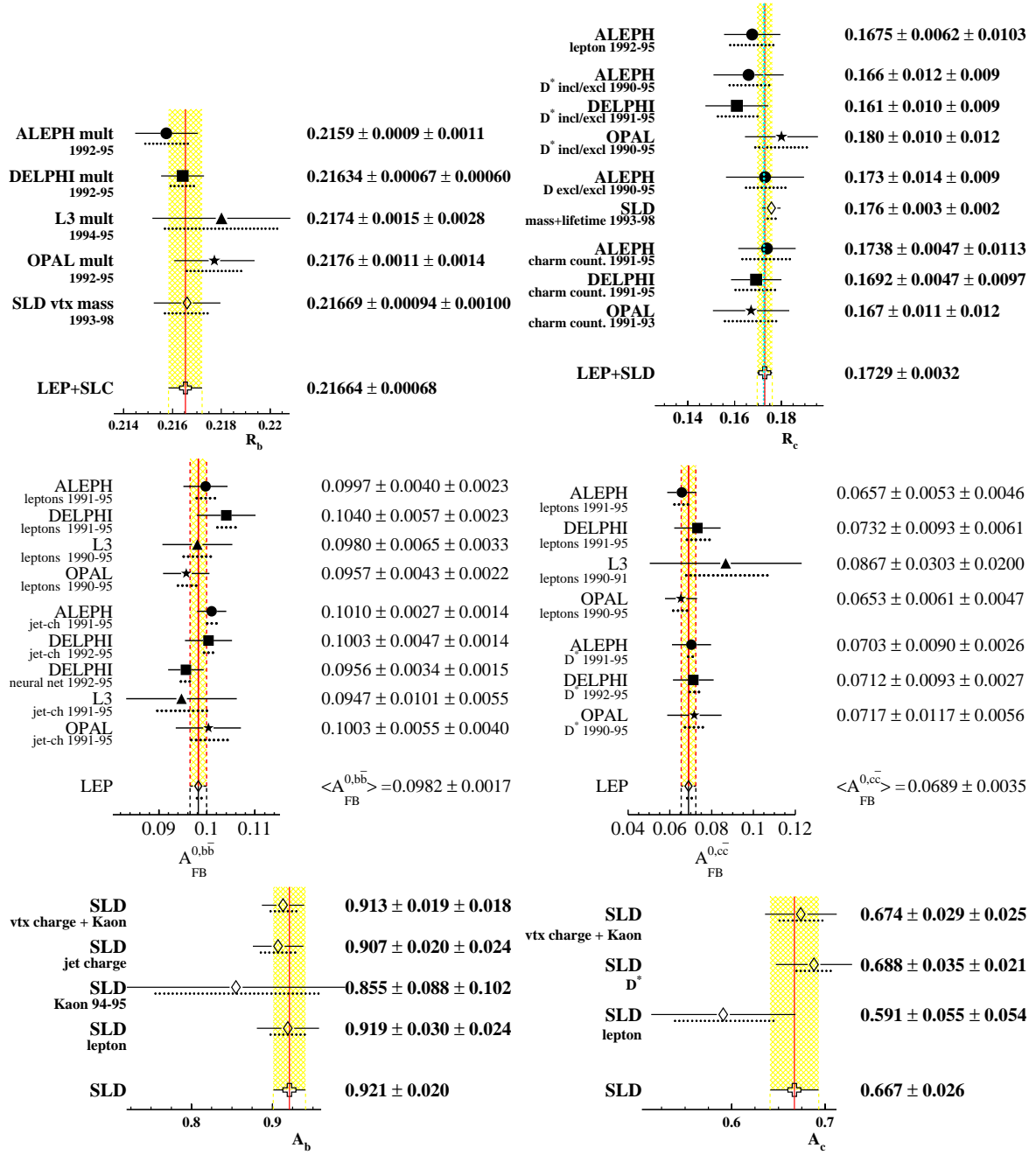


Figure 5.13:  $R_b^0$ ,  $R_c^0$ ,  $A_{FB}^{0,b}$ ,  $A_{FB}^{0,c}$ ,  $A_b$  and  $A_c$  measurements used in the heavy flavour combination. The  $A_{FB}^{0,b}$  measurements with D-mesons contribute only very little weight and are not shown in the plots. ▲

	ALEPH	DELPHI	L3	OPAL	SLD
	92-95 [85]	92-95 [86]	94-95 [87]	92-95 [82]	93-98† [83]
$R_b^0$ (published)	0.2159	0.2163	0.2174	0.2178	0.2171
$R_b^0$ (used)	0.2157	0.2163	0.2174	0.2174	0.2171
Statistical	0.0009	0.0007	0.0015	0.0011	0.0009
Uncorrelated	0.0007	0.0004	0.0015	0.0009	0.0005
Correlated	0.0007	0.0004	0.0018	0.0008	0.0005
Total Systematic	0.0009	0.0006	0.0023	0.0012	0.0008
$a(R_c)$	-0.0033	-0.0041	-0.0376	-0.0122	-0.0057
$R_c^{\text{used}}$	0.1720	0.1720	0.1734	0.1720	0.1710
$a(\text{BR}(c \rightarrow \ell))$			-0.0133	-0.0067	
$\text{BR}(c \rightarrow \ell)^{\text{used}}$			9.80	9.80	
$a(f(D^+))$	-0.0010	-0.0010	-0.0086	-0.0029	-0.0008
$f(D^+)^{\text{used}}$	0.2330	0.2330	0.2330	0.2380	0.2370
$a(f(D_s^+))$	-0.0001	0.0001	-0.0005	-0.0001	-0.0003
$f(D_s^+)^{\text{used}}$	0.1020	0.1030	0.1030	0.1020	0.1140
$a(f(\Lambda_c))$	0.0002	0.0003	0.0008	0.0003	-0.0003
$f(\Lambda_c)^{\text{used}}$	0.0650	0.0630	0.0630	0.0650	0.0730

Table 5.7: The measurements of  $R_b^0$ . All measurements use a lifetime tag enhanced by other features like invariant mass cuts or high  $p_T$  leptons.

$$\begin{aligned}
A_{\text{FB}}^{\text{c}\bar{\text{c}}}(-2) &= -0.026 \pm 0.015, \\
A_{\text{FB}}^{\text{b}\bar{\text{b}}}(\text{pk}) &= 0.0964 \pm 0.0018, \\
A_{\text{FB}}^{\text{c}\bar{\text{c}}}(\text{pk}) &= 0.0621 \pm 0.0036, \\
A_{\text{FB}}^{\text{b}\bar{\text{b}}}(+2) &= 0.1150 \pm 0.0058, \\
A_{\text{FB}}^{\text{c}\bar{\text{c}}}(+2) &= 0.131 \pm 0.013,
\end{aligned}$$

with a  $\chi^2/\text{d.o.f.}$  of  $48/(99 - 18)$ . All correlations between the asymmetries are below 15%.

Figure 5.14 shows the energy dependence of  $A_{\text{FB}}^{\text{b},\text{c}}$  compared to the Standard Model prediction. Since the model describes the energy dependence well, in a second fit all asymmetries are corrected to the peak energy before fitting, resulting in 14 free parameters. The results of this fit are:

$$\begin{aligned}
R_b^0 &= 0.21664 \pm 0.00068, \\
R_c^0 &= 0.1729 \pm 0.0032, \\
A_{\text{FB}}^{0,\text{b}} &= 0.0982 \pm 0.0017, \\
A_{\text{FB}}^{0,\text{c}} &= 0.0689 \pm 0.0035, \\
\mathcal{A}_b &= 0.921 \pm 0.020, \\
\mathcal{A}_c &= 0.667 \pm 0.026, \\
\text{BR}(b \rightarrow \ell) &= 0.1057 \pm 0.0019, \\
\text{BR}(b \rightarrow c \rightarrow \ell) &= 0.0801 \pm 0.0020,
\end{aligned} \tag{5.15}$$

$$\begin{aligned}
 \text{BR}(c \rightarrow \ell) &= 0.0974 \pm 0.0032, \\
 \bar{\chi} &= 0.1192 \pm 0.0043, \\
 f(D^+) &= 0.233 \pm 0.016, \\
 f(D_s^+) &= 0.130 \pm 0.027, \\
 f(c_{\text{baryon}}) &= 0.096 \pm 0.023, \\
 \text{P}(c \rightarrow D^{*+}) \times \text{BR}(D^{*+} \rightarrow \pi^+ D^0) &= 0.1608 \pm 0.0048,
 \end{aligned}$$

with a  $\chi^2/\text{d.o.f.}$  of  $50/(99 - 14)$ . The corresponding correlation matrix is given in Table 5.8. Note that this time the corrected pole asymmetries are given. The fit  $\chi^2$  is in all cases smaller than expected. As a cross check the fit has been repeated using statistical errors only. In this case the  $\chi^2/\text{d.o.f.}$  is  $103/(99 - 14)$ . A large contribution is coming from  $\text{BR}(b \rightarrow \ell)$  measurements, which get immediately consistent, if detector systematics are added. Subtracting the  $\text{BR}(b \rightarrow \ell)$  contribution one gets  $\chi^2/\text{d.o.f.} = 81/(93 - 13)$ . The low  $\chi^2$  for the main fit can be explained largely by conservatively estimated systematic errors. Many error sources are evaluated by comparing test quantities between data and simulation. The statistical errors of these tests are taken as systematic uncertainties although the central values are not changed by the actual difference because one has good reasons to believe that the Monte Carlo describes the truth better than suggested by the test. Also in some cases like the  $b \rightarrow \ell^-$  model fairly extreme assumptions are used for the error evaluation that are no longer really in agreement with data.

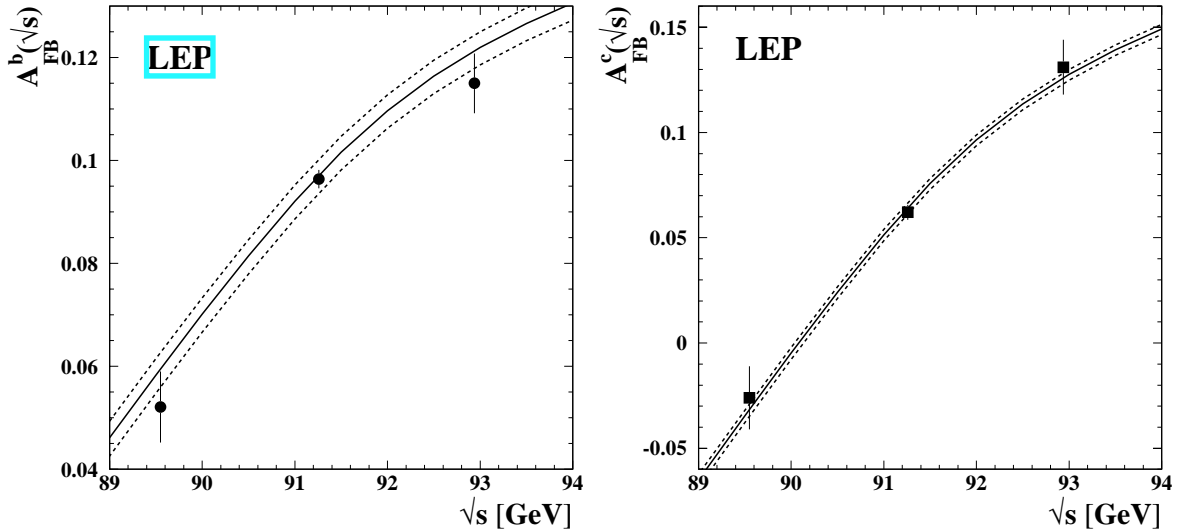


Figure 5.14: Energy dependence of  $A_{\text{FB}}^b$  and  $A_{\text{FB}}^c$ . The solid line represents the Standard Model prediction for  $m_t = 175\text{GeV}$ ,  $m_H = 300\text{GeV}$  the upper (lower) dashed line is the prediction for  $m_H = 100$  (1000) GeV.

Table 5.9 summarises the dominant errors for the electroweak parameters. In all cases the two largest error sources are statistics and systematics internal to the experiments. The error labelled “QCD effects” is due to hemisphere correlation for  $R_b^0$  and  $R_c^0$  and due to the theoretical knowledge of the QCD corrections, discussed in section 5.7.2, for the asymmetries. The uncertainties due the knowledge of the beam energy are negligible in all cases.

Figure 5.15 compares  $R_b^0$ ,  $R_c^0$  and  $A_b A_c$  with the Standard Model prediction. A good agree-

	1)	2)	3)	4)	5)	6)	7)	8)	9)	10)	11)	12)	13)	14)
	$R_b$	$R_c$	$A_{\text{FB}}^{0,b}$	$A_{\text{FB}}^{0,c}$	$A_b$	$\mathcal{A}_c$	$\text{BR}(1)$	$\text{BR}(2)$	$\text{BR}(3)$	$\bar{\chi}$	$f(D^+)$	$f(D_s^+)$	$f(c_{\text{var.}})$	$\text{PcDst}$
1)	1.00	-0.16	-0.09	0.01	-0.06	0.02	-0.08	-0.01	-0.02	-0.03	-0.15	-0.04	0.12	0.12
2)	-0.16	1.00	0.04	-0.02	0.03	-0.04	0.04	0.00	-0.30	0.03	-0.11	0.17	0.14	-0.43
3)	-0.09	0.04	1.00	0.16	0.02	0.00	0.03	-0.08	0.02	0.15	0.03	0.05	-0.04	-0.02
4)	0.01	-0.02	0.16	1.00	0.00	0.01	0.14	-0.17	-0.04	0.16	0.00	0.00	-0.01	0.01
5)	-0.06	0.03	0.02	0.00	1.00	0.12	-0.02	0.00	0.05	0.07	0.00	0.00	0.00	-0.02
6)	0.02	-0.04	0.00	0.01	0.12	1.00	0.02	-0.03	-0.03	0.00	0.00	0.00	0.00	0.01
7)	-0.08	0.04	0.03	0.14	-0.02	0.02	1.00	-0.33	0.15	0.43	0.04	0.01	-0.02	-0.02
8)	-0.01	0.00	-0.08	-0.17	0.00	-0.03	-0.33	1.00	-0.03	-0.40	0.01	-0.01	0.00	0.00
9)	-0.02	-0.30	0.02	-0.04	0.05	-0.03	0.15	-0.03	1.00	0.21	0.01	-0.03	-0.02	0.13
10)	-0.03	0.03	0.15	0.16	0.07	0.00	0.43	-0.40	0.21	1.00	0.02	0.02	-0.01	-0.02
11)	-0.15	-0.11	0.03	0.00	0.00	0.00	0.04	0.01	0.01	0.02	1.00	-0.39	-0.24	0.09
12)	-0.04	0.17	0.05	0.00	0.00	0.00	0.01	-0.01	-0.03	0.02	-0.39	1.00	-0.52	-0.09
13)	0.12	0.14	-0.04	-0.01	0.00	0.00	-0.02	0.00	-0.02	-0.01	-0.24	-0.52	1.00	-0.13
14)	0.12	-0.43	-0.02	0.01	-0.02	0.01	-0.02	0.00	0.13	-0.02	0.09	-0.09	-0.13	1.00

Table 5.8: The correlation matrix for the set of the 14 heavy flavour parameters.  $\text{BR}(1)$ ,  $\text{BR}(2)$  and  $\text{BR}(3)$  denote  $\text{BR}(b \rightarrow \ell)$ ,  $\text{BR}(b \rightarrow c \rightarrow \ell)$  and  $\text{BR}(c \rightarrow \ell)$  respectively,  $\text{PcDst}$  denotes  $\text{P}(c \rightarrow D^{*+}) \times \text{BR}(D^{*+} \rightarrow \pi^+ D^0)$ .



	$R_b^0$ ·10 <sup>-3</sup>	$R_c^0$ ·10 <sup>-3</sup>	$A_{FB}^{0,b}$ ·10 <sup>-3</sup>	$A_{FB}^{0,c}$ ·10 <sup>-3</sup>	$\mathcal{A}_b$ ·10 <sup>-2</sup>	$\mathcal{A}_c$ ·10 <sup>-2</sup>
statistics	0.44	2.4	1.5	3.0	1.5	2.1
internal systematics	0.29	1.4	0.7	1.4	1.3	1.6
QCD effects	0.18	0	0.2	0.1	0.4	0.2
BR(D → neut.)	0.14	0.1	0	0	0	0
D decay multiplicity	0.13	0.2	0	0	0	0
BR(D <sup>+</sup> → K <sup>-</sup> π <sup>+</sup> π <sup>+</sup> )	0.09	0.2	0.1	0	0	0
BR(D <sub>s</sub> <sup>+</sup> → φπ <sup>+</sup> )	0.03	0.6	0.1	0	0	0
BR(Λ <sub>c</sub> → p K <sup>-</sup> π <sup>+</sup> )	0.06	0.4	0.1	0.1	0	0
D lifetimes	0.06	0.1	0	0.1	0	0
gluon splitting	0.26	0.1	0	0.2	0.1	0.1
c fragmentation	0.10	0.2	0.1	0.2	0.1	0.1
light quarks	0.07	0.2	0.1	0.1	0	0
beam polarisation	0	0	0	0	0.5	0.4
total	0.68	3.2	1.7	3.5	2.0	2.6

Table 5.9: The dominant error sources for the electroweak parameters from the 14-parameter fit.

ment is found everywhere. The data are interpreted further, together with the leptonic observables in section 9.

Amongst the non-electroweak observables the B semileptonic branching fraction ( $BR(b \rightarrow \ell) = 0.1057 \pm 0.0019$ ) is of special interest. The dominant error sources on this quantity are the dependences on the semileptonic decay models  $b \rightarrow \ell^-$ ,  $c \rightarrow \ell^+$  with

$$\begin{aligned} \Delta BR(b \rightarrow \ell)(b \rightarrow \ell^- \text{ - modelling}) &= 0.0008, \\ \Delta BR(b \rightarrow \ell)(c \rightarrow \ell^+ \text{ - modelling}) &= 0.0005. \end{aligned}$$

Extensive studies have been made to understand the size of these errors. Amongst the electroweak quantities the quark asymmetries with leptons depend also on the assumptions on the decay model while the asymmetries using other methods usually do not. The fit implicitly requires that the different methods give consistent results. This effectively constrains the decay model and thus reduces the error from this source in the fit result for  $BR(b \rightarrow \ell)$ .

To get a conservative estimate of the modelling error in  $BR(b \rightarrow \ell)$  the fit has been repeated removing all asymmetry measurements. The result of this fit was

$$BR(b \rightarrow \ell) = 0.1065 \pm 0.0021 \tag{5.16}$$

with

$$\begin{aligned} \Delta BR(b \rightarrow \ell)(b \rightarrow \ell^- \text{ - modelling}) &= 0.0010, \\ \Delta BR(b \rightarrow \ell)(c \rightarrow \ell^+ \text{ - modelling}) &= 0.0006. \end{aligned}$$

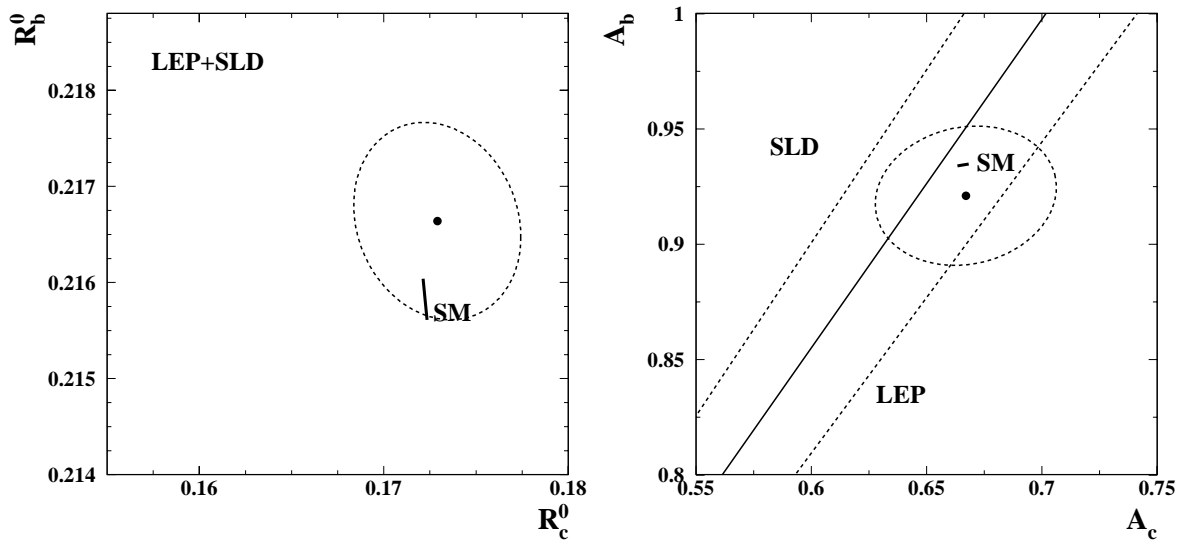


Figure 5.15: Contours in the  $R_c^0$ - $R_b^0$  and  $A_c$ - $A_b$  planes from the LEP and SLD data, corresponding to 68% confidence levels assuming Gaussian systematic errors. The Standard Model prediction for  $m_t = 174.1 \pm 5.4$  GeV is also shown. In case of  $A_c$ - $A_c$  for LEP the ratio  $A_{FB}^{0,b}/A_{FB}^{0,c}$  is shown which is equal to  $A_b/A_c$  without assumptions on the leptonic couplings of the Z. ▲

# Chapter 6

## Results from inclusive and light flavours

The first part of this chapter discusses inclusive results where no attempt to distinguish between quark flavours is made. In addition, tagging methods to identify specific light flavours have been developed. The results from these samples are rather less precise than those from heavy flavour or inclusive measurements, but they allow some checks of the light quark couplings. The rate of direct photons also gives information about the partial widths of the Z to up- and down-type quarks.

### 6.1 Inclusive flavour hadronic events

The ideas developed in the previous section can, in many cases, be extended and applied to an inclusive sample of  $Z^0 \rightarrow q\bar{q}$  decays. The inclusive samples have less enhancement from top quark corrections than beauty samples (which form a subset), but form a much larger dataset. The other reasons for interest mentioned in section 5 also apply to the inclusive case. In particular, the mean difference in jet charges measured in the forwards and backwards event hemispheres, or forward-backwards charge flow, of such an inclusive sample may be determined. This may be written as

$$\langle Q_{\text{FB}} \rangle = \sum_q R_q^0 A_{\text{FB}}^{q\bar{q}} \delta_q C_q s_q, \quad (6.1)$$

where the sum runs over the primary quark flavours, the charge separation,  $\delta_q = \langle Q_- - Q_+ \rangle$ , is the mean jet charge difference between the negative and positive parton hemispheres, the coefficients  $C_q$  reflect the acceptance for each flavour subsample, and the  $s_q$  are factors equal to +1 for down-like quarks and -1 for up like quarks (reflecting the opposite signs of the quark charges in the two cases). The way in which the mean charge separation between forward- and backward-going quark events combines with the forward-backward asymmetry for a single flavour is illustrated in Figure 6.1. The mean charge flow for an inclusive sample is then the sum of those for each flavour weighted by the fraction  $R_q^0$ .

As both  $R_q^0$  and  $A_{\text{FB}}^{q\bar{q}}$  are predicted by the Standard Model in terms of the effective weak mixing angle,  $\sin^2 \theta_{\text{eff}}^{\text{lept}}$ , these parameters may be determined by comparing the measured  $\langle Q_{\text{FB}} \rangle$  with that predicted, given a knowledge of the charge separations  $\delta_q$ . While a direct combination of the charge flow measurements from the different experiments is not possible as they embody

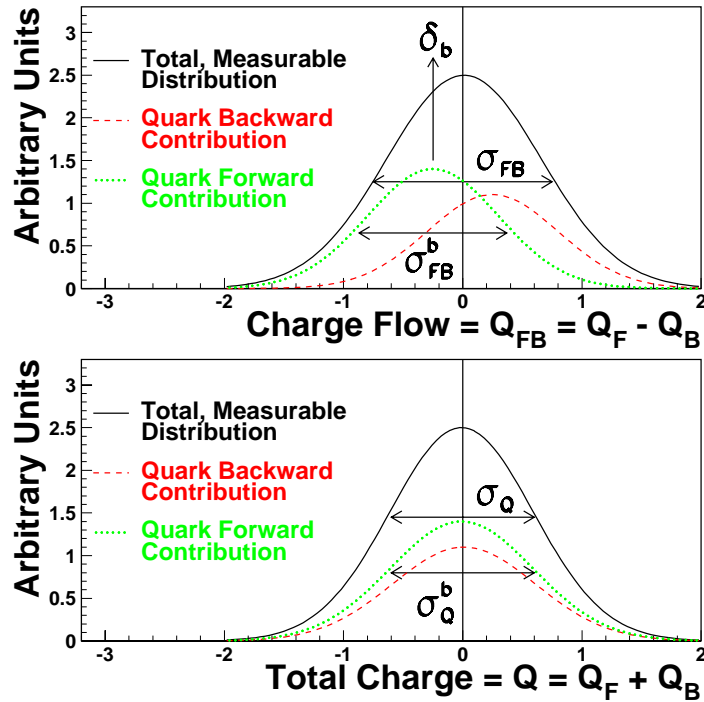


Figure 6.1: A schematic illustration of the charge flow for an individual flavour of  $Z^0 \rightarrow q\bar{q}$  decay. The sum of the hemisphere charges helps control any detector-induced biases, as this should be zero on average.

different acceptances and resolutions coming from the different detectors and analysis methods used. Thus, the strategy that will be adopted is the combination of the derived  $\sin^2 \theta_{\text{eff}}^{\text{lep}}$  values.

It should be noted that the results described in this section are completely within the context of the Standard Model. While various attempts have been made to allow the ratio of partial widths to take on non-Standard Model values, no consistent approach has been found. This is in contrast with, for example, the  $A_{\text{FB}}^{b\bar{b}}$  and  $R_b = \Gamma_{b\bar{b}}/\Gamma_{q\bar{q}}$  results, where the experimentally extracted values are not constrained to the context of the Standard Model.

As in the previously-described measurements of the forward-backwards asymmetry in  $Z^0 \rightarrow b\bar{b}$  events using jet charges, the mean charge separation for  $Z \rightarrow b\bar{b}$  events may be determined from the data; in a similar way, charm tagging may be used to determine the mean charge separation in  $Z^0 \rightarrow c\bar{c}$  events. However, in both cases the bias due to the tagging method employed must be evaluated, as the inclusive measurement is in the absence of such biases. For the charge separation in light-quark events, Monte Carlo models are employed. The mean charge separation for the inclusive sample may also be determined from the data, and while not directly applicable to the charge flow, it may be used as an additional constraint to the determined light-quark mean charge separations.

### 6.1.1 Systematic Uncertainties

The by far dominant systematic uncertainties in results from flavour-inclusive samples arise from the model input required to describe the light quark properties in the absence of high-purity and efficiency tags for specific light flavours. All experiments use the JETSET Monte Carlo as a reference fragmentation model, while the HERWIG model is used for systematic comparisons. The parameter set within JETSET is also typically varied as part of the assessment of the fragmentation model uncertainties. However, neither the parameter set used nor the method

for parameter variation is common to the experiments; indeed, there are typically code changes made to the Monte Carlo programs to improve the overall description in each experiment. Thus, there is far from 100% correlation between the quoted uncertainties. The remaining significant uncertainties are all specific to a given experiment.

Another possible source of common uncertainty is the QCD correction required to the forward-backwards asymmetries for each flavour. These are all essentially taken from JETSET, and a changed correction will introduce shifts in the derived  $\sin^2 \theta_{\text{eff}}^{\text{lept}}$ . However, the QCD correction uncertainties are all much smaller than the quoted fragmentation uncertainties and other experimental errors, and so will have little effect on the conclusions.

### 6.1.2 Combination Procedure

The derived values of the effective weak mixing angle,  $\sin^2 \theta_{\text{eff}}^{\text{lept}}$ , are combined by first forming the full covariance matrix of the results. As the dominant systematic uncertainties are clearly less than fully correlated, a more cautious approach is adopted and the pairwise-smaller of the two quoted correlated systematic uncertainties enters into the corresponding off-diagonal element of the matrix. The matrix is then inverted, and a  $\chi^2$  minimisation performed as for the heavy flavour results, although here there is only one free parameter. Different approaches have been considered for the construction of the covariance matrix, but the resulting weights for each input result and final combined  $\sin^2 \theta_{\text{eff}}^{\text{lept}}$  are little changed by the assumptions made. For example, taking in the off-diagonal elements only the smallest error common to all the inputs only changes the central value by 0.00005. The exception is the case when the common systematic errors are considered to be fully correlated, in which case there is an excessive pull towards the low-precision DELPHI result giving negative effective weights to the ALEPH and L3 contributions.

### 6.1.3 Results and Interpretation

There are published results on the inclusive charge flow from all four LEP experiments [101, 156–158]. These have been combined using the previously defined procedure. The input and the combination are given in Table 6.1; the correlation matrix for the total errors assumed for the averages is given in Table 6.2. The results and average are presented graphically in Figure 6.2.

Experiment	$\sin^2 \theta_{\text{eff}}^{\text{lept}}$
ALEPH (90-94)	$0.2322 \pm 0.0008 \pm 0.0011$
DELPHI (90-91)	$0.2345 \pm 0.0030 \pm 0.0027$
L3 (91-95)	$0.2327 \pm 0.0012 \pm 0.0013$
OPAL (90-91)	$0.2321 \pm 0.0017 \pm 0.0029$
LEP Average	$0.2324 \pm 0.0012$

Table 6.1: Summary of the determination of  $\sin^2 \theta_{\text{eff}}^{\text{lept}}$  from inclusive hadronic charge asymmetries at LEP. For each experiment, the first error is statistical and the second systematic. The latter is dominated by fragmentation and decay modelling uncertainties.

Experiment				
ALEPH	1.0	0.12	0.27	0.14
DELPHI	0.12	1.0	0.13	0.37
L3	0.27	0.13	1.0	0.15
OPAL	0.14	0.37	0.15	1.0

Table 6.2: The ‘minimum overlap’ correlation matrix for the total errors used in the final average of  $\langle Q_{\text{FB}} \rangle$  results.

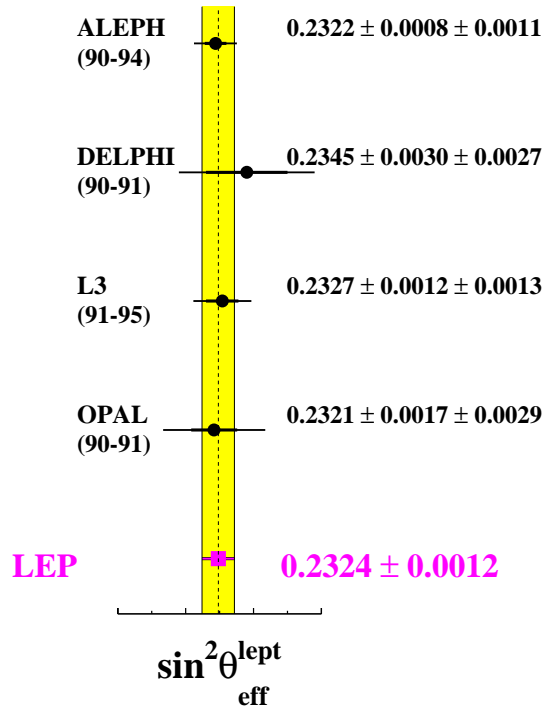


Figure 6.2: The input values and derived average of  $\sin^2 \theta_{\text{eff}}^{\text{lept}}$  from  $\langle Q_{\text{FB}} \rangle$  measurements.

The derived value of  $\sin^2 \theta_{\text{eff}}^{\text{lept}}$  has some correlation with that implicit in the corresponding measurement of  $A_{\text{FB}}^{\text{b}\bar{\text{b}}}$  using jet charges in the same experiment, the latter using similar techniques and a subset of the same data. This degree of correlation has been estimated in specific cases, and the typical degree of correlation is 20% to 25%. In addition, the jet charge results contribute only half of the information to the combined  $A_{\text{FB}}^{\text{b}\bar{\text{b}}}$  result, further diluting the correlation. This will lead to a negligible change in the relative weights of the  $A_{\text{FB}}^{\text{b}\bar{\text{b}}}$  and  $\langle Q_{\text{FB}} \rangle$  results in a combined determination of a global  $\sin^2 \theta_{\text{eff}}^{\text{lept}}$  value and the Standard Model fits.

## 6.2 Light flavour tagging

### 6.2.1 Asymmetry measurements

The first measurement of the strange quark forward-backward asymmetry was made by DELPHI [159], using 1992 data, and identifying strange quark events from kaons in the Ring Imaging Cherenkov detectors (RICH). The measurement was then updated with the full 1992-1995 data set [160]. The Barrel RICH covers  $40^\circ < \theta < 140^\circ$ , and was used for the full dataset. The Forward RICH covers  $15^\circ < \theta < 35^\circ$  plus  $145^\circ < \theta < 165^\circ$ , and was used for the 1994–1995

data. Kaons with momenta between 10 and 24 GeV/c are selected in the RICH detectors, with an average identification efficiency of 53% (42%) in the Barrel (Forward) region. At least two photoelectrons had to be identified in the ring, and the angle of the ring w.r.t. the track direction had to be consistent with the theoretical expectation for kaons within  $2.5\sigma$ , and at least  $2\sigma$  away from the pion expectation. The distribution of Cherenkov angle as a function of momentum is shown in Figure 6.3. The quark direction is taken to be the event thrust axis, signed according to the charge of the identified kaon. The strange fraction of the sample selected by the kaon tag is 43%. For events in the barrel region, which overlap with the microvertex acceptance, bottom and charm quark events are removed by a requirement on the event b-tagging probability, which increases the strange fraction to 55% and reduces the dependence of the result on modelling kaon production in heavy quark decays.

Place holder for DELPHI RICH plot

Figure 6.3: For DELPHI 1994 data, the reconstructed average Cherenkov angle in the gaseous radiator of (left) the barrel RICH and (right) the forward RICH as a function of the particle momentum. The two solid lines show the Cherenkov angle for the pion and kaon hypotheses.

The asymmetry of the selected event sample is a linear combination of five quark forward-backward asymmetries, weighted by the fraction of that flavour and a flavour dependent charge dilution factor, as in Equation ???. The asymmetry of the selected sample is estimated by a chisquared fit to the asymmetry in bins of  $\cos\theta$  of the event thrust axis, signed by the charge of the kaon. The sample asymmetry is corrected for background, dominated by misidentified pions.

This correction depends on the polar angle of the kaon candidate. The s-quark asymmetry is then evaluated, taking into account the fraction of each quark flavour in the kaon-tagged sample, and the probability that the charge is correctly tagged for each flavour. Corrections for QED radiation and QCD effects are also made. The analysis is somewhat model dependent, in that it assumes the Standard Model prediction for production fractions for each flavour, and for non-strange asymmetries, taken either from ZFITTER or from LEP combined measurements. The analysis also relies on the Monte Carlo simulation to compute the efficiencies and dilutions for each flavour. However, the explicit dependence on the other flavour asymmetries can be included in the result, which is:

$$A_{\text{FB}}^{0,s} = 0.1008 \pm 0.0113 \pm 0.0036 \quad (6.2)$$

$$+ 0.0292 \frac{A_{\text{FB}}^{0,c} - 0.0709}{0.0709} \quad (6.3)$$

$$+ 0.0121 \frac{A_{\text{FB}}^{0,d} - 0.1031}{0.1031} \quad (6.4)$$

$$+ 0.0115 \frac{A_{\text{FB}}^{0,u} - 0.0736}{0.0736} . \quad (6.5)$$

The dependence on the b-quark forward backward asymmetry is a factor 10 smaller and has been neglected.

OPAL [161] has also measured light quark asymmetries, using the full 1990-1995 dataset, and high-momentum stable particles as a tag for light flavour events. Their approach is quite different from that of DELPHI, aiming for the minimum model dependence. The tag method uses the fact that the leading particle in a jet tends to carry the quantum numbers of the primary quark, and that the decay of c- and b-hadrons does not usually yield very high momentum stable particles. Identified  $\pi^\pm$ ,  $K^\pm$ ,  $p(\bar{p})$ ,  $K_s^0$  or  $\lambda(\bar{\lambda})$  hadrons with momentum,  $p_h$ , satisfying  $2p_h/\sqrt{s} > 0.5$  are selected. Charged protons, pions and kaons are identified from the  $dE/dx$  measured in the OPAL jet chamber, while  $K_s^0$  and  $\lambda(\bar{\lambda})$  are selected by reconstructing their decay vertex and mass cuts. Only events where the polar angle of the thrust axis satisfies  $|\cos\theta| < 0.8$  are considered, and after all selection cuts about 110 thousand tagged hemispheres are retained out of 4.3 million events. The purities range from 89.5% for pions to 59% for protons.

With the 5 different tags, the analysis measures uses a system of 5 single and 15 double tag equations to derive the light flavour composition of the tagged hemispheres directly from data (see section 5 for a description of the double tag method). The unknowns are the 15  $\eta_q^h$ , the fractions of hemispheres of flavour  $q$  tagged by hadron  $h$ , and the three light flavour partial widths  $R_q$ , plus one correlation coefficient which is assumed to be the same for all tagging hadrons and flavours. The small heavy quark fractions are measured from data from a b-tagged sample for b-quarks, and from Monte Carlo simulation using measured uncertainties on their properties for c-quark events. To solve the system of equations, it is then also assumed that  $R_d = R_s$ , and that various hadronisation symmetries are valid, for example  $\eta_d^{\pi^\pm} = \eta_u^{\pi^\pm}$ . In order to measure the forward-backward asymmetry, the charge tagging probabilities are also measured from the double tagged events, and it is assumed that  $A_{\text{FB}}^{\text{dd}} = A_{\text{FB}}^{\text{ss}}$ .

The OPAL results are

$$A_{\text{FB}}^{0,d,s} = 0.072 \pm 0.035 \pm 0.011 \quad (6.6)$$

$$- 0.0119 \frac{A_{\text{FB}}^{0,c} - 0.0722}{0.0722} , \quad (6.7)$$



$$A_{\text{FB}}^{0,\text{u}} = 0.044 \pm 0.067 \pm 0.018 \quad (6.8)$$

$$- 0.0334 \frac{A_{\text{FB}}^{0,\text{c}} - 0.0722}{0.0722}. \quad (6.9)$$

The correlation between the two results is more than 90%, so only  $A_{\text{FB}}^{0,\text{d,s}}$  should be used for studying quark couplings. These pole asymmetries include corrections of +0.004 which have been applied to the measured  $A_{\text{FB}}^{\text{ss,dd}}$  and  $A_{\text{FB}}^{\text{u}\bar{\text{u}}}$  to account for QCD and ISR effects. The dependence on the c-quark forward backward asymmetry has been quoted explicitly, and the results have negligible dependence on other Standard Model parameters. Correlated systematic uncertainties with other measurements are also very small.

SLD have published a measurement of the strange quark coupling parameter,  $\mathcal{A}_s$ , from the left-right forward-backward asymmetry of events tagged by the presence in each hemisphere of a high momentum  $K^\pm$  or  $K_s^0$  [162]. The measurement uses the full sample of 550,000 Z decays recorded in 1993–1998. Charged kaons with momentum above 9 GeV/c are identified by the Cherenkov Ring Imaging Detector (CRID), with efficiency (purity) of 48% (91.5%). Background from kaons from heavy flavour events is suppressed by identifying B and D decay vertices. Requiring a strange tag in both hemispheres further suppresses the  $\text{u}\bar{\text{u}} + \text{d}\bar{\text{d}}$  events. The thrust axis is used to estimate the s-quark production angle, with the charge identified from a  $K^\pm$  in one hemisphere, which must be opposite to either a  $K^\mp$  or a  $K_s^0$ . For the two tagging cases, 1290 and 1580 events are selected, with  $\text{s}\bar{\text{s}}$  purities of 73% and 60% respectively. The corresponding analysing powers are 0.95 and 0.70, where analysing power is defined as  $(N_r - N_w)/(N_r + N_w)$ , and  $N_r(N_w)$  is the number of events where the thrust axis was signed correctly (incorrectly). The asymmetry is derived from a simultaneous maximum likelihood fit to the distributions shown in Figure 6.4, taking into account contributions from each flavour. As in the case of the OPAL measurement, this analysis is designed to be self-calibrating as much as possible. The analysing powers and the  $\text{u}\bar{\text{u}} + \text{d}\bar{\text{d}}$  backgrounds are constrained from the data, by examining the relative rates of single and multi-tagged hemispheres.

The result of the fit is

$$\mathcal{A}_s = 0.895 \pm 0.066 \pm 0.062. \quad (6.10)$$

The significant dependences of the result on other electroweak parameters *will be* given explicitly *as soon as I have checked the central values. So far I only have gradients.*

Common systematic uncertainties between any of these light quark results and the measurements in the heavy flavour sector, for example from QCD corrections, or the SLC electron beam polarization, can safely be neglected for all these results, since the total statistical and systematic errors are relatively much larger. Correlations between the light-quark results are also small, in particular because the OPAL and SLD results rely on data to constrain systematic uncertainties.

## 6.2.2 Partial width measurements

The OPAL analysis described above [161], using 1990-1995 data, and high-momentum stable particles as a light-flavour tag, also gives measurements of the ratios of partial widths:

$$\frac{R_{\text{d,s}}}{R_{\text{d}} + R_{\text{u}} + R_{\text{s}}} = 0.371 \pm 0.016 \pm 0.016 \quad (6.11)$$

$$\frac{R_{\text{u}}}{R_{\text{d}} + R_{\text{u}} + R_{\text{s}}} = 0.258 \pm 0.031 \pm 0.032. \quad (6.12)$$

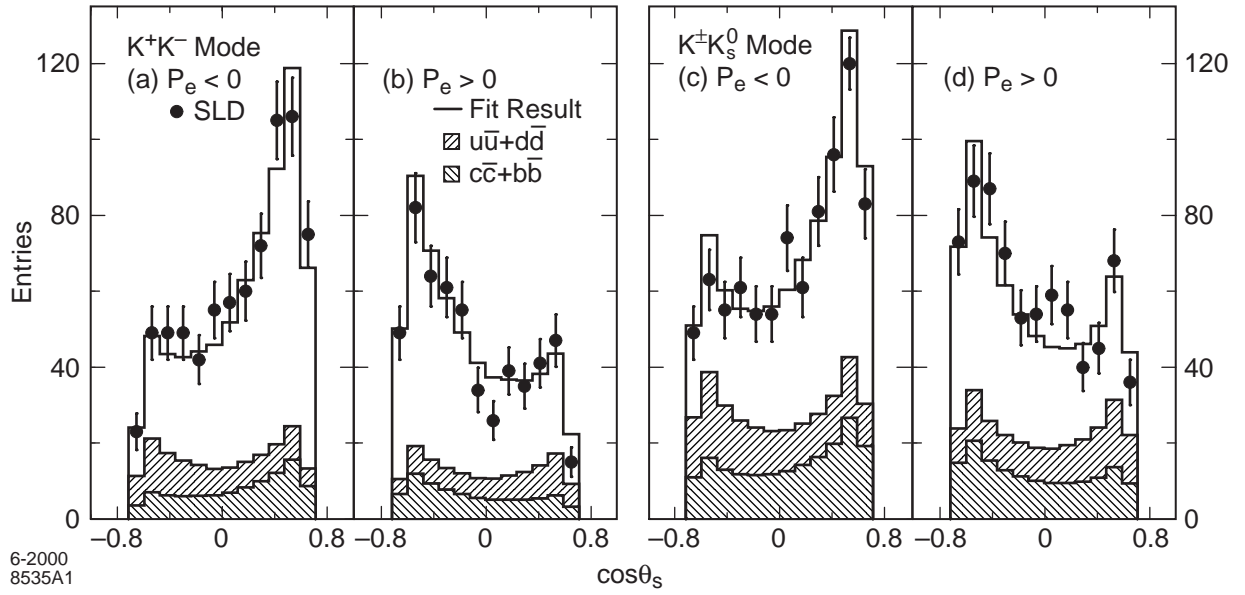


Figure 6.4: Measured  $s$ -quark polar angle distributions (dots) for selected SLD events in the  $a, b$ )  $K^+K^-$  modes, produced with  $a, c$ ) left- and  $b, d$ ) right-polarized electron beams. The histograms represent the result of a simultaneous fit to the four distributions, and the upper (lower) hatched areas indicate the estimated  $u\bar{u} + d\bar{d}(c\bar{c} + b\bar{b})$  backgrounds.

These two results are completely negatively correlated, so only one should be used to investigate quark couplings.

In addition, DELPHI [163], L3 [164] and OPAL [165] have used the rate of hadronic events with identified direct photons, interpreted as final state radiation from quarks, to access the effective couplings:

$$c_u = g_{V_u}^2 + g_{A_u}^2 \quad (6.13)$$

$$c_d = g_{V_d}^2 + g_{A_d}^2, \quad (6.14)$$

which are proportional to the up-type or down-type partial widths. The measured quantity is the fraction of hadronic events with an isolated photon, which is given by

$$\Gamma(Z \rightarrow \gamma + \text{jets})(y_{\text{cut}}) = \frac{h}{9} \frac{\alpha}{2\pi} F(y_{\text{cut}}) S_{\text{qq}\gamma}, \quad (6.15)$$

where  $h = 3G_F m_Z^3 / 24\pi\sqrt{2}$ ,  $F(y_{\text{cut}})$  expresses the theoretical matrix element calculation for the rate of  $\text{qq}\gamma$  events as a function of the jet resolution parameter  $y_{\text{cut}}$ , and  $S_{\text{qq}\gamma}$  is a function of the effective couplings given by:

$$S_{\text{qq}\gamma} = 8c_u + (3 - \epsilon)c_d. \quad (6.16)$$

This reflects the relative strengths of the up and down-type quark couplings to the photon. The quantity  $\epsilon$  takes into account the  $b$ -quark mass, and is also expected to depend on the jet resolution as discussed below. The total hadronic width of the  $Z$  can be expressed as

$$\Gamma_{\text{had}} = h \left[ 1 + \frac{\alpha_S^{(2)}}{\pi} + 1.41 \left( \frac{\alpha_S^{(2)}}{\pi} \right)^2 \right] S_{\text{qq}}, \quad (6.17)$$

where  $\alpha_s^{(2)} = 0.1220 \pm 0.0055$  is the strong coupling constant in second order and

$$S_{qq} = 2c_u + 3c_d. \quad (6.18)$$

The two Equations 6.16 and 6.18 can be solved to give the effective couplings,  $c_u$  and  $c_d$ . Although ALEPH have also investigated prompt photon production [166], the collaboration chose not to interpret these QCD studies in terms of electroweak couplings.

Experimentally, the photon is identified in hadronic events as an isolated calorimeter cluster, with no associated track. DELPHI and OPAL use shower shape variables to reduce the background from light neutral meson decays such as  $\pi^0 \rightarrow \gamma\gamma$ . The other dominant background is from initial state radiation. This is reduced by restricting the analysis to the central region of the detector. The event samples and the photon selection criteria are outlined in Table 6.3.

	DELPHI	L3	OPAL
Data set:			
Years	91–93	90–91	90–91
Multihadron events	1.5 M	320 k	350 k
Photon selection:			
$\theta_\gamma$ in range	25 – 155°	45 – 135°	$ \cos\theta_\gamma  < 0.72$
$E_\gamma$ satisfies	> 5.5 GeV	> 5.0 GeV	> 7.5 GeV
Isolation half angle	20°, $E > 400$ MeV	15°, $E > 500$ MeV	15°, $E > 250$ MeV
Jet scheme:	Durham, $y_{cut} = 0.02$	JADE, $y_{cut} = 0.05$	JADE, $y_{cut} = 0.06$
Photon–jet	same	same	$\gamma$ 20° from jet

Table 6.3: Comparison of direct photon analyses. The jet finding schemes and resolution parameters are those chosen for the central value of the electroweak couplings by each experiment.

The particles in the event excluding the photon are grouped into jets. The photon is then merged with the jets using the same jet resolution parameter (DELPHI, OPAL) or the angle between the photon and the jet (L3). The rate of isolated photons therefore depends on the jet resolution parameter that has been chosen. The rate as a function of  $y_{cut}$  is used in various QCD studies, but one working point is chosen for the calculation of electroweak parameters of relevance here. The rates are corrected for detector and fragmentation effects, and for the geometric acceptance. When compared with the predictions of matrix element calculations they yield a measurement of  $S_{qq\gamma}$ .

The correction to account for the b-quark mass was estimated by L3 to be  $\epsilon = 0.2 \pm 0.1$ . However this correction should depend on the effective mass of the photon-jet system. No correction was used by OPAL, while DELPHI adopted the same correction as L3, but in both cases the effective mass of the photon-jet system is constrained to be about an order of magnitude larger than for L3, where the relative impact of the b-quark mass should be much smaller. For this reason, the correction has been used here for the L3 result only.

The quoted values for  $S_{qq\gamma}$  from the three experiments are: for DELPHI,

$$S_{qq\gamma} = 11.71 \pm 0.43 \pm 0.78 \pm 0.50 \pm 0.25_{-1.78}^{+1.07}, \quad (6.19)$$

where the errors account for statistics, experimental effects, theory,  $\alpha_s$  and the  $y_{cut}$  range respectively; for L3

$$S_{qq\gamma} = 11.88 \pm 1.17 \pm 0.09 \pm 0.63, \quad (6.20)$$

where the errors represent statistical and experimental effects, hadronisation and variations of the photon-jet colinearity cut; and for OPAL,

$$S_{\text{qq}\gamma} = 12.36 \pm 0.78 \pm 0.64 \pm 0.29, \quad (6.21)$$

where the the first error is statistical plus experimental, the second covers photon energy and isolation requirements, and the third variations in  $\alpha_S$  and theory.

In order to derive the effective couplings,  $c_u$  and  $c_d$ , common uncertainties in  $S_{\text{qq}\gamma}$  have been assumed of 3% relative for possible common experimental effects (for example in the  $\eta$  and  $\pi^0$  background to the photon sample), and 5% relative for theoretical matrix element calculations,  $\alpha_S$  variations and hadronisation uncertainties. These are used to calculated the off-diagonal terms in the covariance matrix relating the three measurements of  $S_{\text{qq}\gamma}$ . From Equation 6.17, the value of  $S_{\text{qq}}$  is calculated to be

$$S_{\text{qq}} = 6.740 \pm 0.027. \quad (6.22)$$

The derived values of the couplings are

$$c_u = 0.89 \pm 0.14 \quad (6.23)$$

$$c_d = 1.65 \pm 0.10. \quad (6.24)$$

These values are more than 99% anti-correlated, so again only one should be used in studying quark couplings.

# Chapter 7

## Additional Correlations between Results

\$Id: physrep\_coupling.tex,v 1.54 2001/05/24 20:59:41 gruenew Exp \$

The previous Chapters present the measurements grouped according to closely related experimental analyses. This way all correlations within each set of Z-pole observables extracted from the corresponding group of measurements are easily incorporated. In addition, however, correlations also exist between results extracted from different groups of measurements, arising due to common uncertainties on:

- the centre-of-mass energy:  
shared between all LEP results; shared between all SLC results;
- the beam polarisation:  
shared between all SLC results;
- the QCD correction for quark-pair final states:  
shared between all results on quarks;

The resulting uncertainties on the individual Z-pole observables due to these sources is discussed in the corresponding Chapters. Non-negligible correlations between groups of measurements are caused only by the uncertainty on the SLC beam polarisation. Thus the following additional correlations coefficients  $C(\mathcal{A}_\ell, \mathcal{A}_q)$  between the measurements of  $\mathcal{A}_\ell$  (Chapter 3) and of  $\mathcal{A}_q$  (Chapter 5) must be taken into account in the joint analysis of all results, namely:

$$C(\mathcal{A}_\ell, \mathcal{A}_b) = +0.10 \quad (7.1)$$

$$C(\mathcal{A}_\ell, \mathcal{A}_c) = +0.06. \quad (7.2)$$

In addition, correlations between the jet-charge based heavy-flavour asymmetries (Chapter 5) and the inclusive hadronic charge asymmetries (Section 6.1) appear for the LEP-1 measurements. They are due to overlapping event samples and common systematic errors arising from the use of similar analysis techniques, yielding the following correlations for the combined results:

$$C(A_{\text{FB}}^{0,b}, \sin^2 \theta_{\text{eff}}^{\text{lept}}(\langle Q_{\text{FB}} \rangle)) = -0.?? \quad (7.3)$$

$$C(A_{\text{FB}}^{0,c}, \sin^2 \theta_{\text{eff}}^{\text{lept}}(\langle Q_{\text{FB}} \rangle)) = -0.?? \quad (7.4)$$

The additional correlations quantified here, **NOT YET** taken into account in following Chapters, modify values of quantities derived from these combined results at the level of up ??% of the respective total uncertainty.

# Chapter 8

## Effective Couplings of the Neutral Weak Current

\$Id: physrep\_coupling.tex,v 1.54 2001/05/24 20:59:41 gruenew Exp \$

### Numbers in this Chapter neither final nor consistent!

The experimental measurements and results on electroweak Z-pole observables are presented in the previous chapters. These measurements are now used to derive best values for various effective couplings of the neutral weak current at the Z pole, namely: the asymmetry parameters  $\mathcal{A}_f$ , the effective vector- and axial-vector coupling constants  $g_{Vf}$  and  $g_{Af}$ , the  $\rho_f$  parameters and the effective electroweak mixing angles,  $\sin^2 \theta_{\text{eff}}^f$ . The results of these model-independent analyses are compared to the expectations within the framework of the Minimal Standard Model, thereby testing its validity.

The inputs always consist of the results not assuming lepton universality, allowing to test this hypothesis. The newly derived couplings are determined in a fit to these input results, based on the simple expressions, listed in the Introduction, of the input variables in terms of the couplings to be determined. Those input results which cannot be expressed by the couplings to be determined, *e.g.*,  $m_Z$ ,  $\Gamma_Z$ ,  $\sigma_h^0$ , are left floating in the fit as well. When needed, lepton universality is imposed in the fit, then affecting all fit parameters where lepton universality is applicable.

For the determination of only leptonic couplings, the results of Chapter 2 (Table 2.13), Chapter 3 (Equation 3.10 and Table 3.6) and Chapter 4 (Table 4.3) are taken as input. For the determination of quark couplings, the results presented in Chapter 5 (Equation 5.15 and Table 5.8) are included as well and lepton universality is assumed. In the analysis for the effective electroweak mixing angle, its determination based on the hadronic charge asymmetry, Section 6.1 (Table 6.1), is also used.

### 8.1 The Asymmetry Parameters $\mathcal{A}_f$

Owing to polarised electron beams at SLC, the asymmetry parameters  $\mathcal{A}_f$  are measured directly by the SLD collaboration:  $A_{\text{LR}} = \mathcal{A}_e$  and  $A_{\text{FBLR}}^f = (3/4)\mathcal{A}_f$ . The analyses of tau polarisation at LEP determine  $\mathcal{A}_e$  and  $\mathcal{A}_\tau$  separately. The forward-backward pole asymmetries,  $A_{\text{FB}}^{0,f} = (3/4)\mathcal{A}_e\mathcal{A}_f$ , constrain the product of two asymmetry parameters. The measurements are performed separately for all three charged lepton species as well as the quarks flavours b

Parameter	Average	Correlations		
		$\mathcal{A}_e$	$\mathcal{A}_\mu$	$\mathcal{A}_\tau$
$\mathcal{A}_e$	$0.1514 \pm 0.0019$	+1.00	-0.10	-0.02
$\mathcal{A}_\mu$	$0.1456 \pm 0.0091$	-0.10	+1.00	+0.01
$\mathcal{A}_\tau$	$0.1448 \pm 0.0039$	-0.02	+0.01	+1.00

Table 8.1: Results on the leptonic asymmetry parameters  $\mathcal{A}_\ell$  not assuming neutral-current lepton universality and not including quark-related measurements. The combination has a  $\chi^2/dof$  of 3.6/5, corresponding to a probability of 61%.

and c (and s?) The results on the leptonic asymmetry parameters derived from measurements independent of quark asymmetry parameters are reported in Table 8.1.

The values of the asymmetry parameters obtained for the three lepton species agree well. Under the assumption of neutral-current lepton universality, the combined result is:

$$\mathcal{A}_\ell = 0.1500 \pm 0.0016. \quad (8.1)$$

This average has a  $\chi^2/dof$  of 6.2/9, corresponding to a probability of 72%.

As already discussed in Section 5.9 and shown in Figure 5.15, the ratios of the forward-backward pole asymmetries  $A_{\text{FB}}^{0,b}/A_{\text{FB}}^{0,c} = \mathcal{A}_b/\mathcal{A}_c$  agree well with the ratios of the direct measurements of the asymmetry parameters  $\mathcal{A}_b$  and  $\mathcal{A}_c$ . The mutual consistency of the measurements of  $\mathcal{A}_q$ ,  $A_{\text{FB}}^{0,q} = (3/4)\mathcal{A}_e\mathcal{A}_q$  and  $\mathcal{A}_\ell$  assuming lepton universality is shown in Figure 8.1 for b and c (and s?) quarks. The comparisons are valid since the results on both  $\mathcal{A}_q$  and  $A_{\text{FB}}^{0,q}$  have QCD corrections as expected in the Standard Model and as calculated with ZFITTER [20] removed, see Section 5.7.2.

Compared to the experimental uncertainties, the Standard Model predictions are nearly constant in  $\mathcal{A}_q$ , in contrast to the situation for  $\mathcal{A}_\ell$ . This is a consequence of the Standard-Model values of the electric charge and of the iso-spin for quarks, Table 1.3, leading to a small dependence of  $\mathcal{A}_q$ , which is a function of the ratio  $g_{Vq}/g_{Aq}$  (Equation 1.37) and thus of the effective electroweak mixing angle only (Equations 1.12 and 1.13), to this parameter. Therefore, the determinations of the quark asymmetry parameters  $\mathcal{A}_q$  allow for a robust test of the Standard Model.

The ratios  $(4/3)A_{\text{FB}}^{0,q}/\mathcal{A}_\ell$  also determine  $\mathcal{A}_q$ , with a precision comparable to that of the direct measurements of  $\mathcal{A}_q$ :

$$\frac{4}{3} \frac{A_{\text{FB}}^{0,b}}{\mathcal{A}_\ell} = 0.873 \pm 0.018 < 0.921 \pm 0.020 = \mathcal{A}_b \quad (\text{SM} : 0.935 \pm 0.001) \quad (8.2)$$

$$\frac{4}{3} \frac{A_{\text{FB}}^{0,c}}{\mathcal{A}_\ell} = 0.612 \pm 0.032 < 0.667 \pm 0.026 = \mathcal{A}_c \quad (\text{SM} : 0.665 \pm 0.002). \quad (8.3)$$

The ratios are lower than the direct measurements by 2.4 and 1.3 sigma for b and c quarks, respectively. Compared to the Standard Model expectations, the ratios are lower by 3.4 and 1.7 sigma, respectively, while the direct measurements agree very well with the Standard Model expectations.

Imposing lepton universality, the results of the joint analysis of the leptonic and heavy-flavour measurements in terms of the asymmetry parameters  $\mathcal{A}_f$  are reported in Table 8.2.

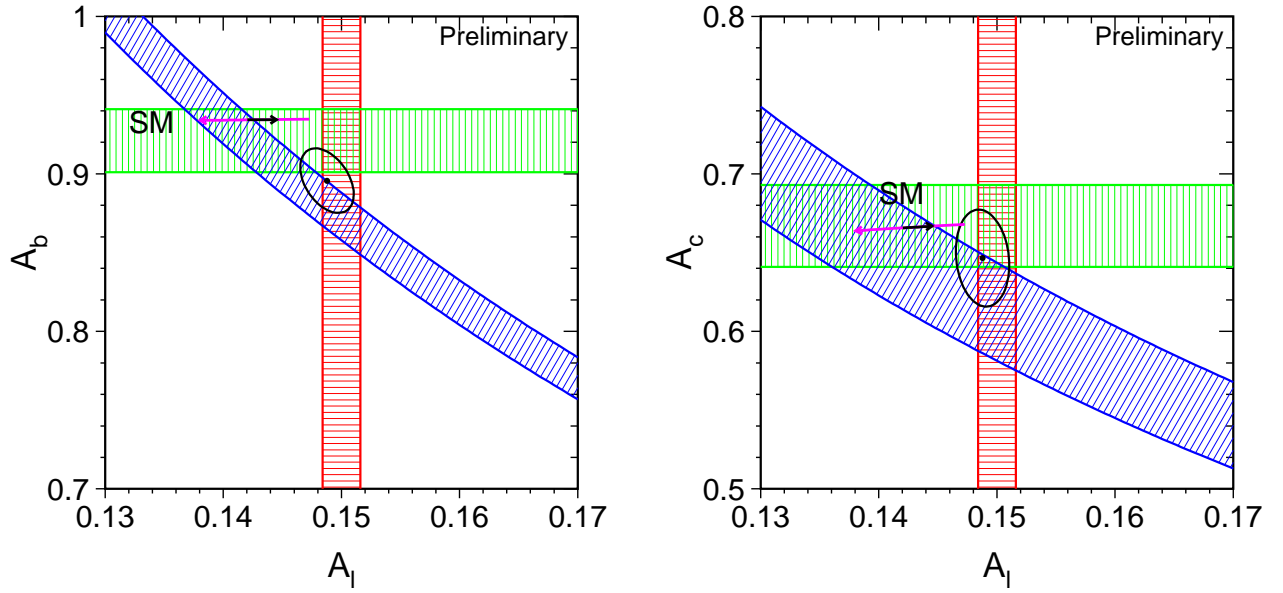


Figure 8.1: Comparison of the measurements of  $\mathcal{A}_\ell$ ,  $\mathcal{A}_q$  and  $A_{\text{FB}}^{0,q}$  for (a) b-quarks, (b) c-quarks, and (c) s-quarks? assuming lepton universality. Bands of  $\pm 1$  sigma widths in the  $(\mathcal{A}_\ell, \mathcal{A}_q)$  plane are shown for the measurements of  $\mathcal{A}_\ell$  (vertical band),  $\mathcal{A}_q$  (horizontal band), and  $A_{\text{FB}}^{0,q} = (3/4)\mathcal{A}_\ell\mathcal{A}_q$  (diagonal band). Also shown is the 68% confidence level contour for the two asymmetry parameters resulting from the joint analysis (Table 8.2). The arrows pointing to the right and to the left show the variation in the Standard-Model prediction for varying  $m_t$  in the range  $174.3 \pm 5.1$  GeV and  $m_H$  in the range of  $300^{+700}_{-187}$  GeV, respectively. Varying the hadronic vacuum polarisation by  $\Delta\alpha_{\text{had}}^{(5)}(m_Z^2) = 0.02761 \pm 0.00036$  yields an additional uncertainty on the Standard-Model prediction, oriented in direction of the Higgs arrow and size corresponding to the top arrow.

Since the leptonic asymmetry parameter  $\mathcal{A}_\ell$  is already well determined, the measurements of  $A_{\text{FB}}^{0,q}$  improve the determination of the quark asymmetry parameters  $\mathcal{A}_q$ . In the combined analysis, all of the resulting asymmetry parameters  $\mathcal{A}_f$  are decreased in value compared to their direct measurements, as shown in Figure 8.1. Compared to the Standard Model expectation, the combined extracted values for  $\mathcal{A}_b$  and  $\mathcal{A}_c$  are lower by 3.0 and 1.0 sigma, respectively.

## 8.2 The Effective Vector and Axial-Vector Coupling Constants

The asymmetry parameters  $\mathcal{A}_f$  depend only on the ratio  $g_{Vf}/g_{Af}$  of the effective vector and axial-vector coupling constants, Equation 1.37. In contrast, the partial decay widths of the Z boson determine the sum of the squares of these two coupling constants, Equation 1.26. It is thus possible to disentangle the effective coupling constants  $g_{Vf}$  and  $g_{Af}$  by analysing both the asymmetry measurements as well as the partial Z decay widths

For charged leptons, the results on  $g_{V\ell}$  and  $g_{A\ell}$  are reported in Table 8.3. The comparison



Parameter	Average	Correlations			
		$\mathcal{A}_\ell$	$\mathcal{A}_b$	$\mathcal{A}_c$	$\mathcal{A}_s$
$\mathcal{A}_\ell$	$0.1488 \pm 0.0015$	+1.00	-0.42	-0.14	
$\mathcal{A}_b$	$0.896 \pm 0.013$	-0.42	+1.00	+0.18	
$\mathcal{A}_c$	$0.647 \pm 0.020$	-0.14	+0.18	+1.00	
$\mathcal{A}_s$	$\pm$				+1.00

Table 8.2: Results on the quark asymmetry parameters  $\mathcal{A}_q$  and the leptonic asymmetry parameter  $\mathcal{A}_\ell$  assuming neutral-current lepton universality and including quark-related measurements containing also information on  $\mathcal{A}_\ell$ . The combination has a  $\chi^2/dof$  of 10.4/11, corresponding to a probability of 49%.

of different lepton species in the  $(g_{V\ell}, g_{A\ell})$  plane is also shown in Figure 8.2a. Good agreement is observed.

Parameter	Average	Correlations					
		$g_{Ae}$	$g_{A\mu}$	$g_{A\tau}$	$g_{Ve}$	$g_{V\mu}$	$g_{V\tau}$
$g_{Ae}$	$-0.50111 \pm 0.00035$	+1.00	-0.13	-0.12	+0.01	-0.00	-0.01
$g_{A\mu}$	$-0.50120 \pm 0.00054$	-0.13	+1.00	+0.35	-0.01	-0.30	+0.02
$g_{A\tau}$	$-0.50204 \pm 0.00064$	-0.12	+0.35	+1.00	-0.03	+0.01	-0.07
$g_{Ve}$	$-0.03816 \pm 0.00047$	+0.01	-0.01	-0.03	+1.00	-0.10	-0.02
$g_{V\mu}$	$-0.0367 \pm 0.0023$	-0.00	-0.30	+0.01	-0.10	+1.00	+0.01
$g_{V\tau}$	$-0.03654 \pm 0.00097$	-0.01	+0.02	-0.07	-0.02	+0.01	+1.00

Table 8.3: Results on the effective vector and axial-vector coupling constants for leptons not assuming neutral-current lepton universality. The combination has a  $\chi^2/dof$  of 3.6/5, corresponding to a probability of 61%.

The combined result under the assumption of neutral-current lepton universality is:

$$g_{V\ell} = -0.03781 \pm 0.00041 \tag{8.4}$$

$$g_{A\ell} = -0.50123 \pm 0.00026, \tag{8.5}$$

with a correlation of  $-0.06$ . This average has a  $\chi^2/dof$  of 6.6/7, corresponding to a probability of 47%. The value of  $g_{A\ell}$  is different from the corresponding Born-level value of  $-1/2$  by 4.7 standard deviations, indicating the presence of non-trivial electroweak radiative corrections.

The effective coupling constant of the Z boson to neutrinos is derived from the partial decay width of the Z into invisible particles, attributing it solely to decays into neutrino pairs. Assuming three neutrino families with equal effective coupling constants, the result is:

$$|g_{A\nu}| = |g_{V\nu}| = 0.50068 \pm 0.00075. \tag{8.6}$$

Including the heavy-quark measurements and assuming lepton universality, the results are reported in Table 8.4, assuming lepton universality. Note that the QCD corrections absorbed

in the partial widths for quark-pair final states are taken from the Standard Model and are calculated with ZFITTER [20] when extracting effective quark couplings from partial widths. This is consistent with the treatment of the various asymmetries in quark-pair production, see Section 5.7.2, which also have QCD effects as expected in the Standard Model removed.

Parameter	Average	Correlations					
		$g_{A\ell}$	$g_{Ab}$	$g_{Ac}$	$g_{V\ell}$	$g_{Vb}$	$g_{Vc}$
$g_{A\ell}$	$-0.50125 \pm 0.00026$	+1.00	-0.02	-0.01	-0.05	+0.05	-0.02
$g_{Ab}$	$-0.5162 \pm 0.0051$	-0.02	+1.00	-0.02	+0.41	-0.97	+0.18
$g_{Ac}$	$+0.5055 \pm 0.0054$	-0.01	-0.02	+1.00	-0.07	+0.05	-0.26
$g_{V\ell}$	$-0.03750 \pm 0.00038$	-0.05	+0.41	-0.07	+1.00	-0.43	+0.14
$g_{Vb}$	$-0.3200 \pm 0.0078$	+0.05	-0.97	+0.05	-0.43	+1.00	-0.19
$g_{Vc}$	$+0.1854 \pm 0.0069$	-0.02	+0.18	-0.26	+0.14	-0.19	+1.00

Table 8.4: Results on the effective coupling constants for leptons and quarks assuming neutral-current lepton universality. The combination has a  $\chi^2/dof$  of 12.3/11, corresponding to a probability of 34%.

The leptonic vector coupling constant is decreased in magnitude compared to Equation 8.4 as already observed for the asymmetry parameter  $\mathcal{A}_\ell$  in the previous section. For the quark flavours b and c (and s?), the results are also shown in Figure 8.2. The strong anti-correlation between the b-quark couplings arises from the tight constraint on the sum of the squares of the couplings due to the measurement of  $R_b$ . The apparent deviation of the measured b-quark coupling constants from the Standard-Model expectation is a direct consequence of the combined result on  $\mathcal{A}_b$  being lower than the Standard-Model expectation discussed in the previous section.

### 8.3 The $\rho_f$ Parameters and the Effective Electroweak Mixing Angles

The effective vector and axial-vector coupling constants obey a simple relation with the  $\rho$  parameter and the effective electroweak mixing angle, see Equations 1.12 and 1.13. For the following analyses, the electric charge  $Q_f$  and the third component of the weak iso-spin  $I_f^3$  are assumed to be given by the Standard-Model assignments as listed in Table 1.3. Tests of fermion universality, *i.e.*, a comparison between leptons and quarks in terms of  $\rho_f$  and  $\sin^2 \theta_{\text{eff}}^f$ , now become possible.

Considering the leptonic measurements alone and assuming lepton universality, the combined results on  $\rho_\ell$  and  $\sin^2 \theta_{\text{eff}}^{\text{lept}}$  are found to be:

$$\rho_\ell = 1.0049 \pm 0.0010 \quad (8.7)$$

$$\sin^2 \theta_{\text{eff}}^{\text{lept}} = 0.23114 \pm 0.00020, \quad (8.8)$$

with a correlation of +0.10. For neutrinos, based on Equation 8.6, the  $\rho$  parameter is determined to be:

$$\rho_\nu = 1.0027 \pm 0.0030. \quad (8.9)$$

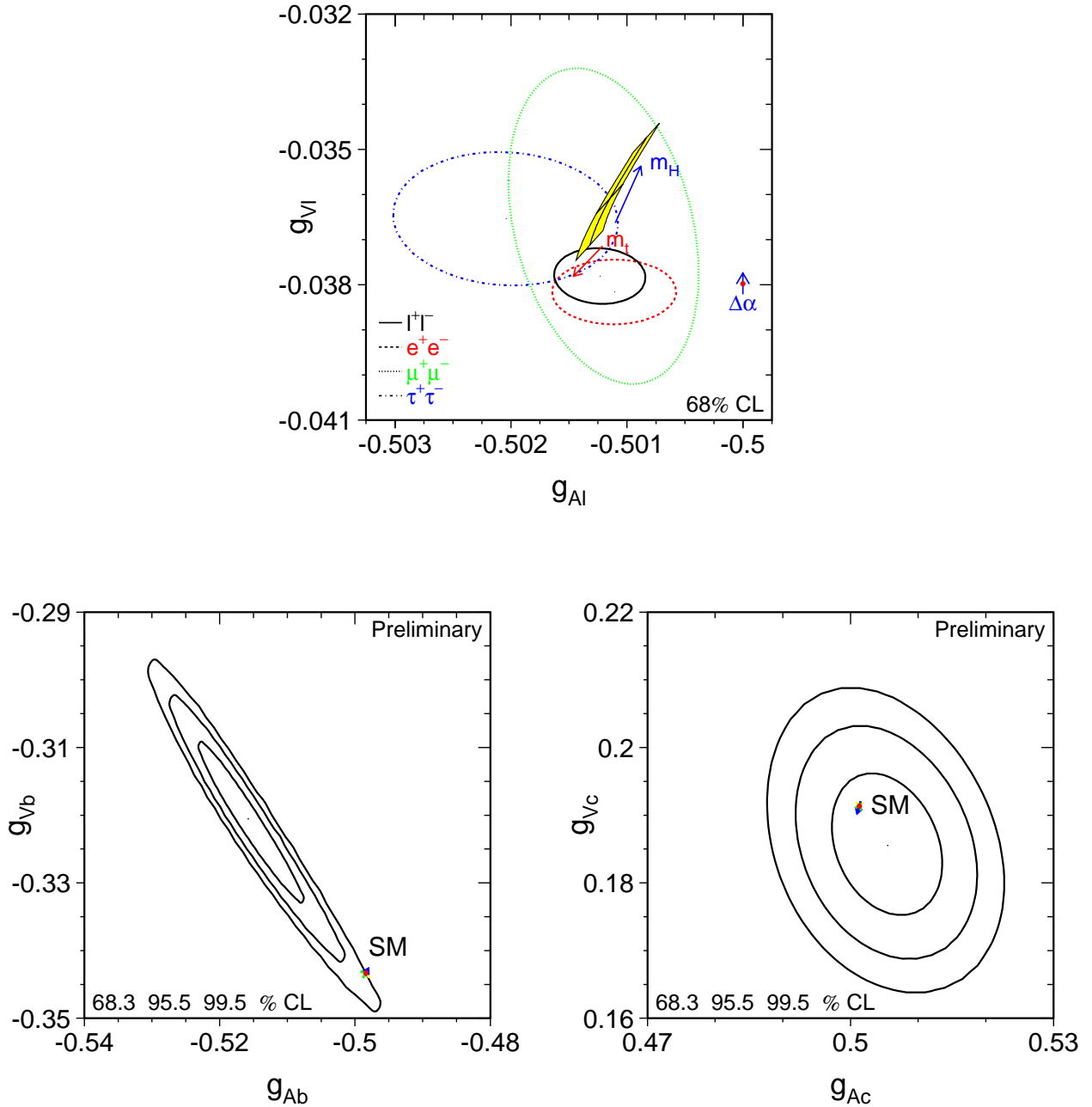


Figure 8.2: Comparison of the effective vector and axial-vector coupling constants for fermions: (a) charged leptons; (b) b quarks; (c) b quarks; (d) s quarks?. The shaded region in (a) shows the predictions within the Standard Model for  $m_t = 174.3 \pm 5.1$  GeV and  $m_H = 300^{+700}_{-187}$  GeV; varying the hadronic vacuum polarisation by  $\Delta\alpha_{\text{had}}^{(5)}(m_Z^2) = 0.02761 \pm 0.00036$  yields an additional uncertainty on the Standard-Model prediction shown by the arrow labelled  $\Delta\alpha$ . Compared to the experimental uncertainties, the Standard Model predictions in (b) and (c) are nearly constant for the quark coupling constants.

Adding the heavy-quark measurements, the results on  $\rho_f$  and the effective electroweak mixing angle for leptons and quarks are reported in Table 8.5 and shown in Figure 8.3. The measurement of  $\sin^2 \theta_{\text{eff}}^{\text{lept}}$  based on the hadronic charge asymmetry as discussed in Section 6.1 (Table 6.1) is included here. As before, neutral-current lepton universality is assumed. The value of  $\rho_\ell$  is different from the corresponding Born-level value of unity by 5.0 standard deviations, again indicating the presence of non-trivial electroweak radiative corrections. The strong anti-correlation between  $\rho_b$  and  $\sin^2 \theta_{\text{eff}}^b$  arises, as for  $g_{Vb}$  and  $g_{Ab}$  above, from the tight constraint given by the measurement of  $R_b$ .

Parameter	Average	Correlations					
		$\rho_\ell$	$\rho_b$	$\rho_c$	$\sin^2 \theta_{\text{eff}}^{\text{lept}}$	$\sin^2 \theta_{\text{eff}}^b$	$\sin^2 \theta_{\text{eff}}^c$
$\rho_\ell$	$1.0050 \pm 0.0010$	+1.00	-0.02	+0.01	+0.09	-0.04	-0.01
$\rho_b$	$1.064 \pm 0.021$	-0.02	+1.00	+0.02	-0.41	+0.99	+0.17
$\rho_c$	$1.022 \pm 0.022$	+0.01	+0.02	+1.00	-0.06	+0.04	+0.49
$\sin^2 \theta_{\text{eff}}^{\text{lept}}$	$0.23133 \pm 0.00019$	+0.09	-0.41	-0.06	+1.00	-0.42	-0.14
$\sin^2 \theta_{\text{eff}}^b$	$0.284 \pm 0.016$	-0.04	+0.99	+0.04	-0.42	+1.00	+0.18
$\sin^2 \theta_{\text{eff}}^c$	$0.2373 \pm 0.0057$	-0.01	+0.17	+0.49	-0.14	+0.18	+1.00

Table 8.5: Results on the  $\rho$  parameter and the effective electroweak mixing angle  $\sin^2 \theta_{\text{eff}}^f$  assuming neutral-current lepton universality. The combination has a  $\chi^2/dof$  of 13.1/12, corresponding to a probability of 36%.

Within the Standard Model, slightly different values for both  $\rho_f$  and  $\sin^2 \theta_{\text{eff}}^f$  are expected for different fermions due to non-universal flavour-specific electroweak radiative corrections. These specific corrections are largest for b quarks,  $\rho_b - \rho_\ell \approx -0.011$  and  $\sin^2 \theta_{\text{eff}}^b - \sin^2 \theta_{\text{eff}}^{\text{lept}} \approx 0.0014$ , and more than a factor of five smaller for the other quark flavours, as shown in Figure 8.3. For all fermions the non-universal flavour-specific corrections expected in the Standard Model are small compared to the experimental errors.

## 8.4 The Leptonic Effective Electroweak Mixing Angle

The measurements of the various asymmetries determine  $\sin^2 \theta_{\text{eff}}^f$  independently of  $\rho_f$  as they depend only on the ratio of the effective coupling constants,  $g_{Vf}/g_{Af}$ . Because of the values of the electric charge  $Q_f$  and the third component of the weak iso-spin  $I_f^3$  as listed in Table 1.3, the sensitivity of the quark vector coupling  $g_{Vq}$ , and hence of  $\mathcal{A}_q$  and of  $A_{\text{FB}}^{0,q}$ , to  $\sin^2 \theta_{\text{eff}}^q$  is smaller than that for leptons. This is also visible in Figures 8.1 and 8.2, showing that for up-type quarks as well as down-type quarks both the asymmetry parameters  $\mathcal{A}_q$  and the effective coupling constants  $g_{Aq}$  and  $g_{Vq}$  are, on the scale of the experimental uncertainties, nearly constant within the Standard Model. Therefore, the heavy quark forward-backward asymmetries  $A_{\text{FB}}^{0,q} = (3/4)\mathcal{A}_e\mathcal{A}_q$  as well as the hadronic charge asymmetry  $\langle Q_{\text{FB}} \rangle$ , being sensitive to  $\sin^2 \theta_{\text{eff}}^{\text{lept}}$  through the factor  $\mathcal{A}_e$  rather than to  $\sin^2 \theta_{\text{eff}}^q$ , can be interpreted as a measurement of  $\sin^2 \theta_{\text{eff}}^{\text{lept}}$ .

Assuming the Standard-Model structure of the effective coupling constants in terms of  $\rho_f$  and  $\sin^2 \theta_{\text{eff}}^f$ , the measurements of the various asymmetries are compared in terms of  $\sin^2 \theta_{\text{eff}}^{\text{lept}}$  in

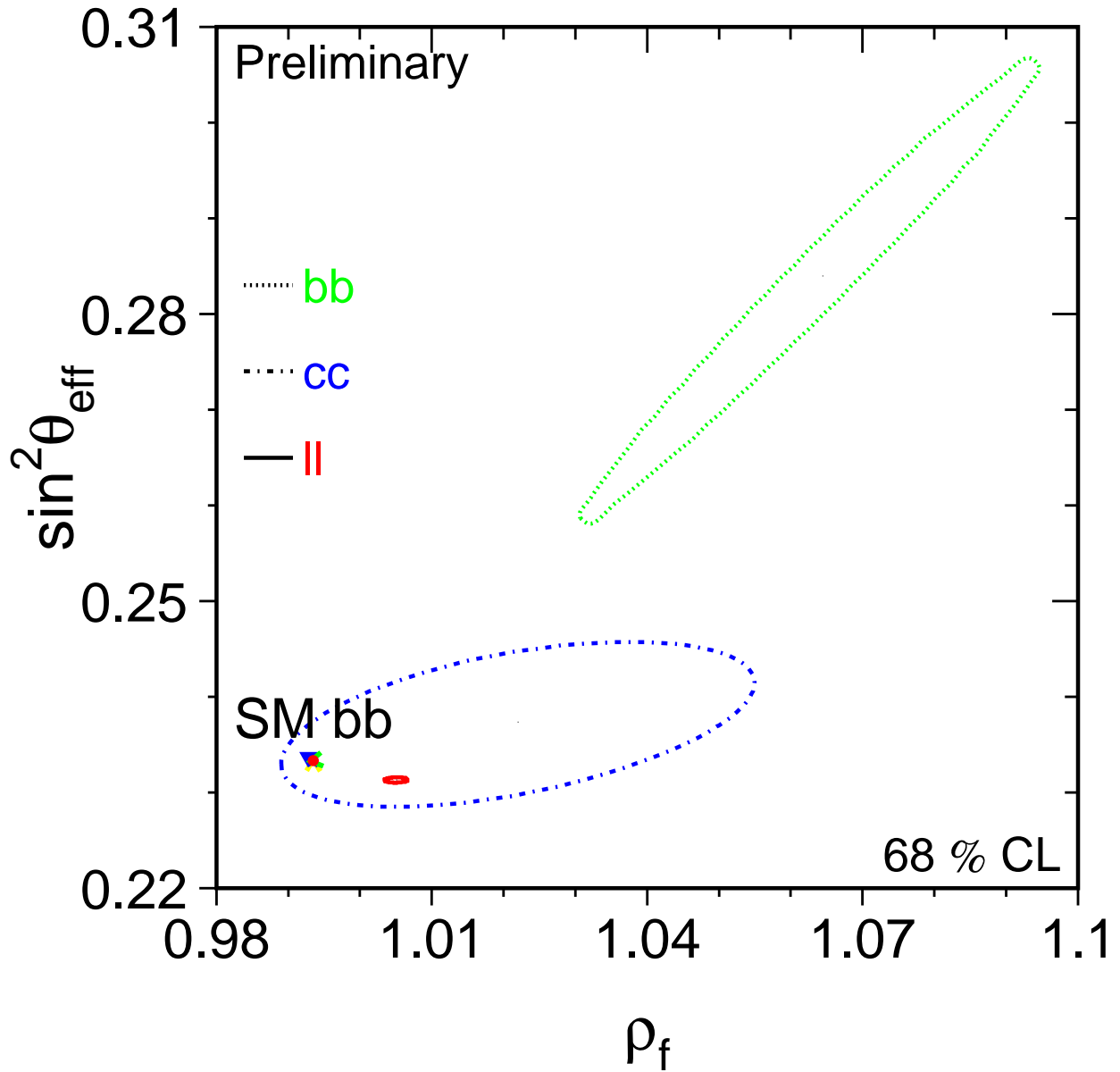


Figure 8.3: Comparison of  $\rho_f$  and the effective electroweak mixing angle  $\sin^2 \theta_{\text{eff}}^f$  for leptons, b and c quarks. The Standard Model expectation for b quarks is shown as the dot ( $\rho_b < 1$ ); those of c quarks and of leptons is not drawn as they lie at the same place as the experimental contour curve for leptons ( $\rho_\ell > 1$ ).

Figure 8.4. The measurements are grouped into two sets of three results each. In the first set, the results on  $\sin^2 \theta_{\text{eff}}^{\text{lept}}$  are derived from measurements depending on leptonic couplings only,  $A_{\text{FB}}^{0,\ell}$ ,  $\mathcal{A}_\ell(\text{SLD})$  and  $\mathcal{A}_\ell(P_\tau)$ . In this case, only lepton universality is assumed, and no further corrections are necessary. In the second set, consisting of  $A_{\text{FB}}^{0,b}$ ,  $A_{\text{FB}}^{0,c}$  and  $\langle Q_{\text{FB}} \rangle$ , quark couplings are involved. In this case, the small non-universal flavour-specific electroweak corrections, making  $\sin^2 \theta_{\text{eff}}^{\text{lept}}$  different from  $\sin^2 \theta_{\text{eff}}^{\text{q}}$ , must be taken from the Standard Model. The effect of these corrections and their uncertainties on the extracted value of  $\sin^2 \theta_{\text{eff}}^{\text{lept}}$  is, however, negligible.

The two sets of measurements yield averages values for  $\sin^2 \theta_{\text{eff}}^{\text{lept}}$  of  $0.23114 \pm 0.00020$  ( $\chi^2/dof = 1.7/2$ ) and  $0.23240 \pm 0.00029$  ( $\chi^2/dof = 0.12/2$ ), respectively, which differ by about 3.6 sigma. As a consequence, the average of all six  $\sin^2 \theta_{\text{eff}}^{\text{lept}}$  determinations, yielding  $\sin^2 \theta_{\text{eff}}^{\text{lept}} = 0.23156 \pm 0.00017$ , has a  $\chi^2/dof$  of 14.7/5, corresponding to a probability of only 1.2%. The two most precise determinations of  $\sin^2 \theta_{\text{eff}}^{\text{lept}}$ , namely those derived from the measurements of  $\mathcal{A}_\ell$  by SLD, dominated by the  $A_{\text{LR}}$  result, and of  $A_{\text{FB}}^{0,b}$  at LEP, yield the largest pulls and fall on opposite sides of the  $\sin^2 \theta_{\text{eff}}^{\text{lept}}$  average. This is a consequence of the same effect as discussed in the previous sections: the deviation in  $\mathcal{A}_b$  as extracted from  $A_{\text{FB}}^{0,b}$  discussed previously is reflected in the value of  $\sin^2 \theta_{\text{eff}}^{\text{lept}}$  extracted from  $A_{\text{FB}}^{0,b}$  in this analysis here.

## 8.5 Discussion

The unexpectedly large shifts observed in the various analyses for asymmetry parameters, effective coupling constants,  $\rho_f$  and  $\sin^2 \theta_{\text{eff}}^{\text{lept}}$  are all showing the consequences of the same effect. It is most clearly visible in the effective couplings and  $\sin^2 \theta_{\text{eff}}^{\text{lept}}$  averages.

The results as shown in Figure 8.2 suggest that the effective couplings for b-quarks cause the main effect; both  $g_{\text{Vb}}$  and  $g_{\text{Ab}}$  deviate from the expectation. In terms of the left- and right-handed couplings  $g_{\text{Lb}}$  and  $g_{\text{Rb}}$ , however, only  $g_{\text{Rb}}$  shows a significant deviation. Since for b-quarks with electric charge  $-1/3$  and weak isospin  $-1/2$  one has  $|g_{\text{Rb}}| \ll |g_{\text{Lb}}|$ , the effect could be explained by a change in the right-handed b-quark coupling already at Born level. This would affect  $\mathcal{A}_b$  and  $A_{\text{FB}}^{0,b}$ , both depending only on the ratio  $g_{\text{Rb}}/g_{\text{Lb}}$ , more strongly than  $R_b \propto g_{\text{Rb}}^2 + g_{\text{Lb}}^2$ .

From the experimental point of view, no systematic effect potentially explaining such large shifts could be identified. Within the Standard Model, flavour specific electroweak radiative corrections and their uncertainties are likewise too small to explain the difference in the extracted  $\sin^2 \theta_{\text{eff}}^{\text{lept}}$  values. All uncertainties are taken into account in the analyses.

Thus the effect is either a sign for new physics, invalidating the simple relations to convert between the effective parameters used in this Chapter, or a fluctuation in one or more of the input measurements. In the following we assume the latter and thus neither modify nor exclude any of the measurements. As a direct consequence, the  $\chi^2/dof$  in all analyses including these measurements will be rather large due to the contribution of at least 14.7 units from the six asymmetry measurements.

Preliminary

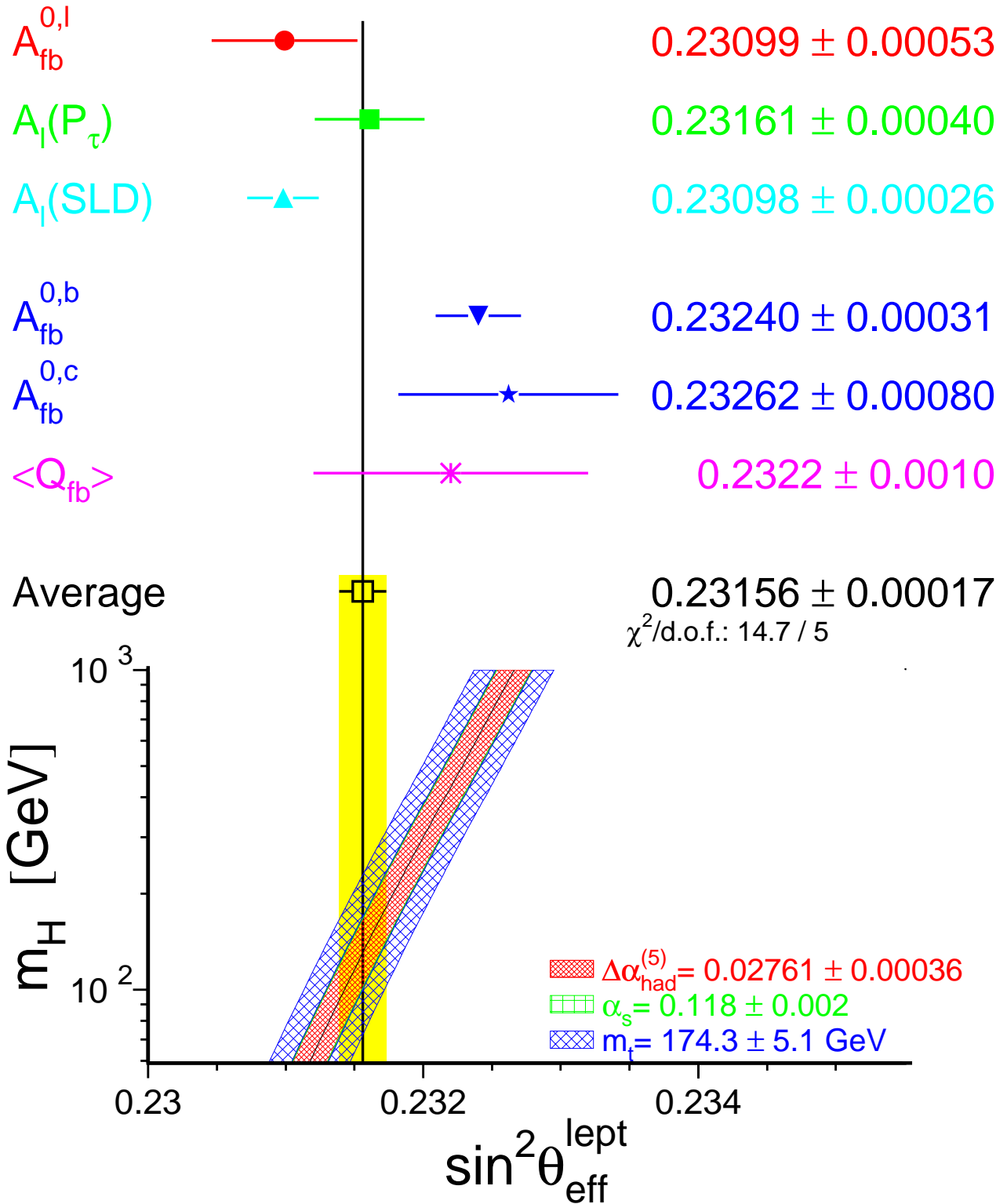


Figure 8.4: Comparison of the effective electroweak mixing angle  $\sin^2 \theta_{\text{eff}}^{\text{lept}}$  derived from measurement results depending on lepton couplings only (top) and also quark couplings (bottom). Also shown is the prediction of  $\sin^2 \theta_{\text{eff}}^{\text{lept}}$  in the Standard Model as a function of  $m_H$ . The additional uncertainty of the Standard Model prediction shown is parametric and dominated by the uncertainties in  $\Delta\alpha_{\text{had}}^{(5)}(m_Z^2)$  and  $m_t$ , shown as the bands. The total width of the band is the linear sum of these effects.

# Chapter 9

## Constraints on the Standard Model

\$Id: physrep\_sm.tex,v 1.65 2001/05/24 20:59:41 gruenew Exp \$

### Numbers in this Chapter neither final nor consistent!

In the previous sections, several figures have already shown comparisons between the experimental results and the expectations from the Standard Model [4]. As discussed in the Introduction, the Standard Model prediction for each Z-pole observable depends on free parameters which are not predicted by the theory, such as the coupling constants of the various interactions and the masses of the fundamental fermions (quarks and leptons) and heavy bosons (Z, W, and H). Owing to this dependence, directly at Born level or through electroweak radiative corrections, the experimental measurements of Z-pole and other observables allow us to constrain these free parameters. Most importantly it is possible to determine the masses of the top quark precisely and also that of Higgs boson, both fundamental particles of the Standard Model.

### 9.1 Parameters of the Minimal Standard Model

The masses of all known fundamental fermions with the exception of the top quark are small compared to the Z mass, 91 GeV, and precisely enough measured so that their influence on Z-pole observables through kinematic effects is both rather small and calculable to more than adequate precision. The only exception is the top quark with a mass of about 175 GeV, which it is too heavy to be produced directly in  $e^+e^-$  collisions at LEP1/SLC centre-of-mass energies close to the Z pole,  $\sqrt{s} < 100$  GeV. However, as discussed in the Introduction, it controls the size of the electroweak radiative corrections, because to leading order these corrections depend quadratically on the fermion mass. The top-quark mass is therefore one of the parameters of the Standard Model which will be determined in the following, while the masses of all other fundamental fermions are fixed. The comparison of such an indirect determination of the top-quark mass with the direct measurement obtained from  $t\bar{t}$  production in proton-antiproton collisions at the TEVATRON constitutes an important test of the Standard Model.

For the electromagnetic, weak and strong interactions described by the Standard Model, the corresponding three coupling constants are also not predicted, but must be inferred from measurements. Because the Higgs mechanism gives an integrated description of the electromagnetic and the weak interaction in the form of the electroweak theory, the weak coupling is related to the electromagnetic coupling and the masses of the charged and neutral heavy gauge bosons W and Z. Therefore, just two coupling constants, those of the electromagnetic



and the strong interaction,  $\alpha$  and  $\alpha_S$ , are considered, together with the masses of the heavy gauge bosons  $W$  and  $Z$ . The mass of the electromagnetic gauge boson, the photon, is fixed at zero as required by the theory of QED.

The mass of the  $Z$  boson is precisely measured as described in Chapter 2. When calculating radiative corrections for  $Z$  pole observables, it is advantageous to replace the mass of the  $W$  boson by the Fermi constant,  $G_F = 1.16639(1) \cdot 10^{-5} \text{ GeV}^{-2}$  [167]. The reason is twofold: first, radiative corrections are smaller and more easily calculated and expressed in terms of  $G_F$ . Second, the experimental precision on  $G_F$  of 9 ppm is by far higher than that on the mass of the  $W$  boson will be in the foreseeable future.\* Indeed,  $G_F$  is treated as a constant in the following analyses. The mass of the  $W$  boson,  $m_W$ , is then predicted within the Standard Model as a function of  $G_F$  and the other Standard-Model parameters. Comparing this prediction with the direct measurements of  $m_W$  performed at the TEVATRON and at the LEP-2 colliders yields a second stringent test of the Standard Model.

At tree level, the  $Z$ -pole observables depend on just three of the five parameters discussed above, namely  $\alpha$  and  $m_Z$ , and, in case of quark production,  $\alpha_S$ , (see Equations 1.23 and 1.26). Electroweak radiative corrections such as those shown in Figure 1.9 modify this simple picture. They induce a running of the coupling constants  $\alpha$  and  $\alpha_S$  with momentum transfer or  $s$ . For  $Z$ -pole observables, it is a very good approximation to use a fixed  $s = m_Z^2$ , called  $Z$ -pole approximation, so that the relevant coupling constants are  $\alpha(m_Z^2)$  and  $\alpha_S(m_Z^2)$ . In addition, loop corrections involving virtual top quarks and Higgs bosons introduce a dependence on the masses of these particles.

The five parameters of the Standard Model relevant for the calculation of  $Z$ -pole observables are therefore the coupling constants of QED and QCD at the  $Z$  pole,  $\alpha(m_Z^2)$  and  $\alpha_S(m_Z^2)$ , and the masses of the  $Z$  boson, the top quark and the Higgs boson. The measurements of electroweak observables presented in the previous Chapters are used to extract and constrain these five parameters. Besides the mass of the  $Z$  boson, the interesting parameters of the Standard Model are the mass of the top quark and of course the mass of the Higgs Boson. The hadronic  $Z$ -pole observables will give rise to one of the most precise determinations of  $\alpha_S(m_Z^2)$ . The treatment of  $\alpha(m_Z^2)$  is discussed in the following Section. The programs TOPAZ0 [19] and ZFITTER [20] are used to calculate all  $Z$ -pole observables including radiative corrections in the framework of the Standard Model and as a function of these Standard Model parameters. They include the Equations shown in the Introduction, supplemented by more complicated high-order expressions for improved theoretical accuracy.

## 9.2 Hadronic Vacuum Polarisation

The running of the electromagnetic coupling with momentum transfer,  $\alpha(0) \rightarrow \alpha(s)$ , caused by fermion-pair loop insertions in the photon propagator, is customarily written as:

$$\alpha(s) = \frac{\alpha(0)}{1 - \Delta\alpha_{e\mu\tau}(s) - \Delta\alpha_{\text{top}}(s) - \Delta\alpha_{\text{had}}^{(5)}(s)}, \quad (9.1)$$

with  $\alpha(0) = 1/137.036$  [76]. The contribution of leptons is calculated diagrammatically up to third order:  $\Delta\alpha_{e\mu\tau}(m_Z^2) = 0.03150$  with negligible uncertainty [168]. Since heavy particles decouple in QED, the top-quark contribution is small:  $\Delta\alpha_{\text{top}}(m_Z^2) = -0.00007(1)$ ; it is

---

\*Note, however, that this replacement is in some sense purely technical: the constraints on the Standard-Model parameters derived from the measurements are independent of whether  $m_W$  is replaced by the measured value of  $G_F$ , or  $G_F$  is included as an additional measurement instead.

calculated by TOPAZ0 and ZFITTER as a function of  $m_t$ . The running electromagnetic coupling is insensitive to new particles with high masses. For light-quark loops the diagrammatic calculations have very large uncertainties due to sizeable QCD corrections at low quark-mass scales. Therefore, the total contribution of the five light quark flavours to the vacuum polarisation,  $\Delta\alpha_{\text{had}}^{(5)}(m_Z^2)$ , is more accurately obtained through a dispersion integral over the measured hadronic cross section in electron-positron annihilations at low centre-of-mass energies. In this case the uncertainty on  $\Delta\alpha_{\text{had}}^{(5)}(m_Z^2)$  is given by the experimental uncertainties in the measured hadronic cross section at low centre-of-mass energies. Until recently, this uncertainty was quite large, leading to [169, 170]:

$$\Delta\alpha_{\text{had}}^{(5)}(m_Z^2) = 0.02804 \pm 0.00065, \quad (9.2)$$

as used in Chapter 2. Based on the same analysis technique but including recent new measurements of the hadronic cross section at low energies, in particular the precise measurements of the BES collaboration in the range  $2 \text{ GeV} < \sqrt{s} < 5 \text{ GeV}$  [171], the uncertainty is much reduced [172]:

$$\Delta\alpha_{\text{had}}^{(5)}(m_Z^2) = 0.02761 \pm 0.00036, \quad (9.3)$$

Since a few years, more theory-driven determinations of  $\Delta\alpha_{\text{had}}^{(5)}(m_Z^2)$  have appeared [173–180], which employ perturbative QCD to calculate the hadronic cross section in the continuum region at low  $\sqrt{s}$ , outside the region populated by the hadronic resonances. As the theoretical uncertainty on the predicted cross section is assumed to be smaller than that of the experimental measurements, a reduced error on  $\Delta\alpha_{\text{had}}^{(5)}(m_Z^2)$  is achieved, for example [179]:

$$\Delta\alpha_{\text{had}}^{(5)}(m_Z^2) = 0.02738 \pm 0.00020, \quad (9.4)$$

also taking the new results from BES into account. All recent evaluations of  $\Delta\alpha_{\text{had}}^{(5)}(m_Z^2)$  are consistent with but lower than the previous evaluation of Equation 9.2. In the following, the experiment-driven value of  $\Delta\alpha_{\text{had}}^{(5)}(m_Z^2)$  as given in Equation 9.3 will be used for the analyses presented here, on the same footing as any other experimental measurement with associated uncertainty.

### 9.3 Additional Measurements

Obviously, a wealth of other measurements are performed in particle physics experiments at high energies, using various particle beams and targets. The results of these experiments are crucial to explore the predictive power of the Standard Model in as large a breadth as possible. Of all these measurements, those are particularly interesting here which have a high sensitivity to the Standard Model parameters as introduced above.

For simplicity, only such additional measurements are considered here which directly or indirectly increase the precision in the determination of the Standard-Model parameters, in particular the mass of the Higgs boson. In decreasing order of importance, the results considered in some of the analyses presented in the following are: the mass of the top quark, the mass of the W boson, the on-shell electroweak mixing angle, and the atomic parity violation parameters.

### 9.3.1 Mass of the Top Quark

A few years ago the top quark was discovered in proton-antiproton collisions at the TEVATRON by the experiments CDF [181] and DØ [182]. Since then both experiments measure its mass exploiting various decay chains. Combining the results from CDF [183] and DØ [184], the current world average value for the pole mass of the top quark is:  $m_t = 174.3 \pm 5.1$  GeV [76].

### 9.3.2 Mass of the W Boson

Initially, the mass of the W boson is measured in proton-antiproton collisions, first by the experiments UA1 [185] and UA2 [186] at the SPS collider, and nowadays by CDF [187] and DØ [188] at the TEVATRON, with a combined result of:  $m_W = 80.452 \pm 0.062$  GeV [189].

Since a few years, also the LEP experiments ALEPH, DELPHI, L3 and OPAL measure the W-boson mass directly, made possible by more than doubling the centre-of-mass energy of the LEP accelerator (LEP-2). Combining all published [190–193] and *preliminary* LEP-2 measurements, the LEP-2 result is:  $m_W = 80.446 \pm 0.040$  GeV [194]. As for the Z boson, the mass of the W boson is defined according to a Breit-Wigner with  $s$ -dependent width.

### 9.3.3 On-Shell Electroweak Mixing Angle

The measurement of the neutrino-nucleon neutral-to-charged current cross-section ratio also determines the electroweak mixing angle. Note that the electroweak mixing angle determined here is different from the Z-pole equivalent due to the different momentum-transfer scale in  $t$ -channel neutrino-nucleon scattering as opposed to  $s$ -channel electron-positron interactions. The result is quoted in terms of the on-shell mixing angle, adding small electroweak radiative corrections.

Combining the measurement of CCFR [195] and the *preliminary* measurement from NUTEV [196], the combined result is:  $\sin^2 \theta_W = 1 - m_W^2/m_Z^2 = 0.2255 \pm 0.0021 - 0.0014 \frac{m_t^2 - (175 \text{ GeV})^2}{(100 \text{ GeV})^2} + 0.00048 \ln \frac{m_H}{150 \text{ GeV}}$ , where the residual dependence of the result on the Standard-Model electroweak radiative corrections is explicitly parametrised. Using  $m_Z$  from LEP-1, Table 2.13, this result corresponds to a W-boson mass of  $m_W = 80.25 \pm 0.11$  GeV.

### 9.3.4 Atomic Parity Violation Parameters

The measurement of parity violation in atoms determines the weak charge of the atomic nucleus as probed by the electron,  $Q_W(N, Z) = -2[(2Z + N)C_{1u} + (Z + 2N)C_{1d}]$  for a nucleus with  $Z$  protons and  $N$  neutrons. The weak charges of up and down quarks as seen by the electron through the parity-violating  $t$ -channel Z exchange are expressed in terms of effective vector and axial-vector coupling constants,  $C_{1q} = 2g_{Ae}g_{Vq}$ . Including electroweak radiative corrections, these couplings are different from their Z-pole equivalents due to the momentum-transfer being zero in atomic-parity violation experiments.

Precise measurements of  $Q_W$  are performed for cesium [197, 198] and thallium [199, 200]. However, certain aspects in nuclear many-body perturbation theory needed in the experimental analyses are still under discussion and only very recently addressed for cesium [201, 202], being the most precise measurement. Thus only the newly corrected experimental result for cesium,  $Q_W(\text{Cs}) = -72.5 \pm 0.7$  [202], will **NOT YET** be used in the following.

## 9.4 Sensitivities and Uncertainties

Since the interesting electroweak radiative corrections involving top-quark and Higgs-boson masses are typically in the order of 1% or less at the Z pole, all other effects must be controlled at the per-mille level in order to extract quantitatively these interesting Standard-Model parameters. The uncertainties affecting the observables as calculated within the framework of the Standard Model fall into two classes discussed in the following. Numerical results for several observables are reported in Table 9.1.

First, there are uncertainties in the values of the five Standard-Model parameters themselves, which of course lead to uncertainties in any observable calculated as a function of these parameters. This dependence on the five Standard-Model parameters allows their determination in the Standard-Model analysis of the measurements. As all five parameters are determined in parallel, these so-called parametric uncertainties are properly accounted for automatically by the analysis procedure discussed in the next Section. For the determination of the interesting parameters, namely the mass of the top-quark and the mass of the Higgs boson, a high sensitivity is advantageous, while the dependence on the other Standard-Model parameters, in particular the hadronic vacuum polarisation, should be small.

Many theorists perform the various calculations of radiative corrections. In order to make the calculations accessible to experimentalists in a consistent way, the relevant calculations are incorporated in programs such as TOPAZ0, using the modified minimal subtraction renormalisation scheme, and ZFITTER, using the on-mass-shell renormalisation scheme.

For cross sections and asymmetries, the following corrections are included in TOPAZ0 and ZFITTER: up to  $\mathcal{O}(\alpha^2)$  [?] and leading  $\mathcal{O}(\alpha^3)$  [?] for initial-state QED radiation including pairs [?],  $\mathcal{O}(\alpha)$  for final-state QED radiation and QED initial-final interference [?],  $\mathcal{O}(\alpha_S^3)$  for final-state QCD radiation [?] and  $\mathcal{O}(\alpha\alpha_S)$  for mixed QED/QCD final-state radiation [?]. These corrections are needed to extract the observables discussed in this report from the measured cross sections and asymmetries. For the calculation of the extracted observables discussed in this report, the final-state corrections listed above are also available for the Z decay widths. Furthermore, complete one-loop electroweak radiative corrections are included as well as (leading) two-loop corrections up to  $\mathcal{O}(\alpha\alpha_S)$  [?],  $\alpha\alpha_S^2$  [?],  $G_F^2 m_t^4$  [?],  $G_F^2 m_t^2 m_Z^2$  [?],  $G_F m_t^2 \alpha_S$  [?],  $G_F m_t^2 \alpha_S^2$  [?].

Recently, complete fermionic electroweak two-loop corrections were calculated [203]. These are not yet included as the effect on  $m_W$  turns out to be small compared to the current experimental uncertainty on  $m_W$  and the corresponding calculations of the effective weak mixing angle and the partial Z widths are not yet available.

Uncertainties in radiative corrections arise due to the fact that the perturbative expansion is known and calculated only up to a finite order. Missing higher-order electroweak, strong and mixed corrections cause the calculations of observables to be incomplete and thus approximative. Equivalently, ambiguities due to the choice of renormalisation schemes, resummation schemes, momentum-transfer scales in loop corrections, and schemes to implement the factorisation of various corrections are introduced which reflect and are of the order of the missing higher-order corrections. The uncertainty on the predicted observables due to this effect is thus estimated by comparing results obtained under such different but to the order of calculated corrections equivalent approaches [21, 204].

As shown in Table 9.1, the uncertainties due to missing higher-orders are in general small compared to the leading parametric uncertainties. In the case of the effective electroweak mixing angle it is already shown in Figure 8.4 that the parametric uncertainty on the Standard-Model prediction arising from  $\Delta\alpha_{\text{had}}^{(5)}(m_Z^2)$  is non-negligible compared to the experimental uncertainty

Source	$\delta$	$\Gamma_{\text{tot}}$ [MeV]	$\sigma_{\text{h}}^0$ [nb]	$R_{\ell}^0$	$R_b$	$\rho_{\ell}$	$\sin^2 \theta_{\text{eff}}^{\text{lept}}$	$m_{\text{W}}$ [MeV]
$\Delta\alpha_{\text{had}}^{(5)}(m_{\text{Z}}^2)$	0.00036	0.3	0.001	0.002	—	—	0.00013	7
$\alpha_{\text{S}}(m_{\text{Z}}^2)$	0.002	1.1	0.011	0.013	—	—	0.00001	1
$m_{\text{Z}}/\text{MeV}$	2.1	0.2	0.002	—	—	—	0.00002	3
$m_{\text{t}}/\text{GeV}$	5.0	1.2	0.003	0.002	0.00018	0.0005	0.00016	31
$\log_{10}(m_{\text{H}}/\text{GeV})$	0.3	1.9	0.001	0.006	0.00002	0.0004	0.00036	44
Theory	FHWW excl.	0.3	0.001	0.002	0.00007	0.0001	0.00003	4
Theory	FHWW incl.	0.3	0.001	0.002	0.00007	0.0001	0.00008	4

Table 9.1: Theoretical uncertainties on selected Z-pole observables and  $m_{\text{W}}$ . Top: parametric uncertainties, *i.e.*, sensitivities to Standard-Model parameters. For each observable, the change is shown when varying the Standard-Model parameter listed in the first column by the amount  $\delta$  listed in the second column. Bottom: uncertainties due to missing higher-order corrections estimated through variation of calculational schemes implemented in TOPAZ0 and ZFITTER (half of full range of values). In case no number is listed, the effect is smaller than half a unit in the number of digits quoted.

of the average. As a consequence, the uncertainty on the hadronic vacuum polarisation is one of the limiting factors in the extraction of the mass of the Higgs boson. This situation underlines the importance of further improved determinations of the hadronic vacuum polarisation through measurements of the hadronic cross section in electron-positron annihilations at low centre-of-mass energies.

### 9.4.1 QCD Uncertainties

The largest QCD correction on Z-pole observables arises through the final-state QCD radiation factor in quark-pair production, Equation 1.26, modifying the decay width of the Z into hadrons,  $\Gamma_{\text{had}}$ , and thus also the Z-pole observables  $\Gamma_{\text{tot}}$ ,  $\sigma_{\text{h}}^0$ ,  $\sigma_{\ell}^0$ , and  $R_{\ell}^0$ . The theoretical uncertainty in the calculation of these observables due to unknown higher-order QCD effects, and thus in the  $\alpha_{\text{S}}(m_{\text{Z}}^2)$  values extracted from measurements of these quantities, is a subject of discussion. Estimates of the corresponding theoretical uncertainty on  $\alpha_{\text{S}}(m_{\text{Z}}^2)$  are under discussion and vary by a factor of six, ranging from 0.0005 to 0.003 [205–207], where the larger value is larger than the uncertainty on  $\alpha_{\text{S}}(m_{\text{Z}}^2)$  caused by the experimental errors on the measured observables.

A much smaller  $\alpha_{\text{S}}$  dependence is induced by propagator corrections, virtual quark loops with additional gluon exchange, in the calculation of any Z-pole observable. As it is a two-loop correction, even uncertainties on  $\alpha_{\text{S}}$  in the range quoted above cause only negligible uncertainties on the prediction of any Z-pole observable.

This has several consequences: The extracted value of  $\alpha_{\text{S}}(m_{\text{Z}}^2)$  is solely given by the dependence of the hadronic Z-pole observables on the final-state QCD radiation factor. As it is the very same final-state QCD correction factor entering the calculation of all hadronic Z-pole observables, the theoretical uncertainties are fully correlated and affect the extracted  $\alpha_{\text{S}}(m_{\text{Z}}^2)$  value independent of which observable is used. Because of this correlation, the extracted values of the other Standard-Model parameters are not affected by the unknown theoretical uncertainty

due to unknown higher-order QCD effects.<sup>†</sup>

## 9.5 Analysis Procedure

In order to determine the five relevant Standard-Model parameters a  $\chi^2$  minimisation is performed using the program MINUIT [208]. The  $\chi^2$  is calculated as usual by comparing the measurements of Z-pole and other observables, their errors and correlations including those discussed in Section 7, with the predictions calculated in the framework of the Standard Model. For measurements on leptonic Z-pole observables, the results combined in the previous Chapters under the hypothesis of lepton universality, inherent to the Standard Model, are used. All are reported in Table 9.6. The predictions are calculated as a function of the five Standard-Model parameters by the programs TOPAZ0 and ZFITTER, which include all relevant electroweak radiative corrections. All five Standard-Model parameters are allowed to vary in the fit, so that parametric uncertainties are correctly treated and propagated.

This analysis procedure allows to test quantitatively how well the Standard Model is able to describe the complete set of all measurements with just one value for each of the five parameters. For this, however, the large contribution to the  $\chi^2$  arising from the asymmetry measurements as discussed in the previous Chapter has to be taken into account in the interpretation.

In addition, the mass of the remaining particle of the Standard Model without significant direct experimental evidence, the mass of the Higgs boson, will be constrained. For this part, the additional measurements presented in Section 9.3, such as the direct measurements of  $m_W$  and  $m_t$  at LEP-2 and the TEVATRON, are also included, in order to obtain the best precision.

Uncertainties due to missing higher order corrections as discussed above are typically implemented by offering various choices or options in the programs TOPAZ0 and ZFITTER calculating radiative corrections. As these choices correspond to discrete options (flags), they cannot be varied during a fit. Rather, the analysis is repeated with different flag settings. The change in the extracted Standard Model parameters is taken as an estimate of the theoretical uncertainty for the option studied. Effectively, the theoretical uncertainty in the calculation of observables is propagated back to the extracted Standard Model parameters. Since this uncertainty is usually much smaller than the uncertainty arising from the experimental uncertainties in the measured Z-pole observables, it is not included in the results presented in the following.

## 9.6 Sensitivity to Radiative Corrections Beyond QED

A fundamental question is whether the experimental Z-pole results show indeed evidence for the existence of electroweak radiative corrections beyond those solely predicted by the well known and tested theory of QED. The predictions based on Born-term expressions, including only the running of  $\alpha$ , for the  $\rho$  parameter and the electroweak mixing angle are:

$$\rho_0 = 1 \tag{9.5}$$

$$\sin^2 \theta_0 = \frac{1}{2} \left( 1 - \sqrt{1 - 4 \frac{\pi \alpha(m_Z^2)}{\sqrt{2} G_F m_Z^2}} \right) = 0.23101 \pm 0.00012, \tag{9.6}$$

---

<sup>†</sup>Note that this theoretical uncertainty would have to be known quantitatively and included explicitly if external measurements of  $\alpha_S(m_Z^2)$  were included in the analyses. For the Standard-Model analyses presented here, however, this is not necessary as external constraints on  $\alpha_S(m_Z^2)$ , even without any uncertainty, do not lead to reduced uncertainties on the other Standard-Model parameters.

where the uncertainty on  $\sin^2 \theta_0$  arises due to the uncertainty in the hadronic vacuum polarisation, Equation 9.3. When these predictions are compared to the results derived from the measurement of Z-pole observables, essentially the leptonic partial decay width and the leptonic asymmetries, Table 8.5:

$$\rho_\ell = 1.0050 \pm 0.0010 \quad (9.7)$$

$$\sin^2 \theta_{\text{eff}}^{\text{lept}} = 0.23133 \pm 0.00019, \quad (9.8)$$

it becomes evident, in particular in the case of the  $\rho$  parameter, that electroweak radiative corrections beyond QED are needed to describe the measurements. This is also shown in Figure 9.1.

In the case of the effective electroweak mixing angle, the uncertainty on the prediction of  $\sin^2 \theta_{\text{eff}}^{\text{lept}}$  within the Standard Model due to the uncertainty on  $\Delta\alpha_{\text{had}}^{(5)}(m_Z^2)$  is non-negligible compared to the accuracy of experimental measurement of  $\sin^2 \theta_{\text{eff}}^{\text{lept}}$ . This observation underlines the importance of a precise cross-section measurement of electron-positron annihilation into hadrons at low centre-of-mass energies. In contrast to  $\sin^2 \theta_{\text{eff}}^{\text{lept}}$ , the  $\rho$  parameter is not affected by the uncertainty of  $\Delta\alpha_{\text{had}}^{(5)}(m_Z^2)$ .

## 9.7 Tests of Electroweak Radiative Corrections

### 9.7.1 Parametrisations

As discussed above, the expected structure of electroweak radiative corrections in the Standard model shows contributions quadratic in the fermion masses and only logarithmic in the Higgs-boson mass. It has been studied how the small Higgs-mass dependence can be disentangled from the large top-quark mass dependence. For this purpose, four new effective parameters,  $\epsilon_1$ ,  $\epsilon_2$ ,  $\epsilon_3$  and  $\epsilon_b$  are introduced. They are defined such that they vanish in the approximation when only effects due to pure QED and QCD are taken into account. In terms of the auxiliary quantities  $\sin^2 \theta_0$  defined above and  $\Delta\kappa'$  relating  $\sin^2 \theta_{\text{eff}}^{\text{lept}}$  to  $\sin^2 \theta_0$  as:

$$\sin^2 \theta_{\text{eff}}^{\text{lept}} = (1 + \Delta\kappa') \sin^2 \theta_0, \quad (9.9)$$

the  $\epsilon$  parameters are given by:

$$\epsilon_1 = \Delta\rho \quad (9.10)$$

$$\epsilon_2 = \cos^2 \theta_0 \Delta\rho + \frac{\sin^2 \theta_0}{\cos^2 \theta_0 - \sin^2 \theta_0} \Delta r_w - 2 \sin^2 \theta_0 \Delta\kappa' \quad (9.11)$$

$$\epsilon_3 = \cos^2 \theta_0 \Delta\rho + (\cos^2 \theta_0 - \sin^2 \theta_0) \Delta\kappa' \quad (9.12)$$

$$\epsilon_b = \frac{1}{2} \Delta\rho_b. \quad (9.13)$$

Within the Standard Model the leading contributions in terms of  $m_t$  and  $m_H$  are:

$$\epsilon_1 = \frac{3G_F m_t^2}{8\sqrt{2}\pi^2} - \frac{3G_F m_W^2}{4\sqrt{2}\pi} \tan^2 \theta_W \ln \frac{m_H}{m_Z} + \dots \quad (9.14)$$

$$\epsilon_2 = -\frac{G_F m_W^2}{2\sqrt{2}\pi^2} \ln \frac{m_t}{m_Z} + \dots \quad (9.15)$$

$$\epsilon_3 = \frac{G_F m_W^2}{12\sqrt{2}\pi^2} \ln \frac{m_H}{m_Z} - \frac{G_F m_W^2}{6\sqrt{2}\pi^2} \ln \frac{m_t}{m_Z} + \dots \quad (9.16)$$

$$\epsilon_b = -\frac{G_F m_t^2}{4\sqrt{2}\pi^2} + \dots \quad (9.17)$$

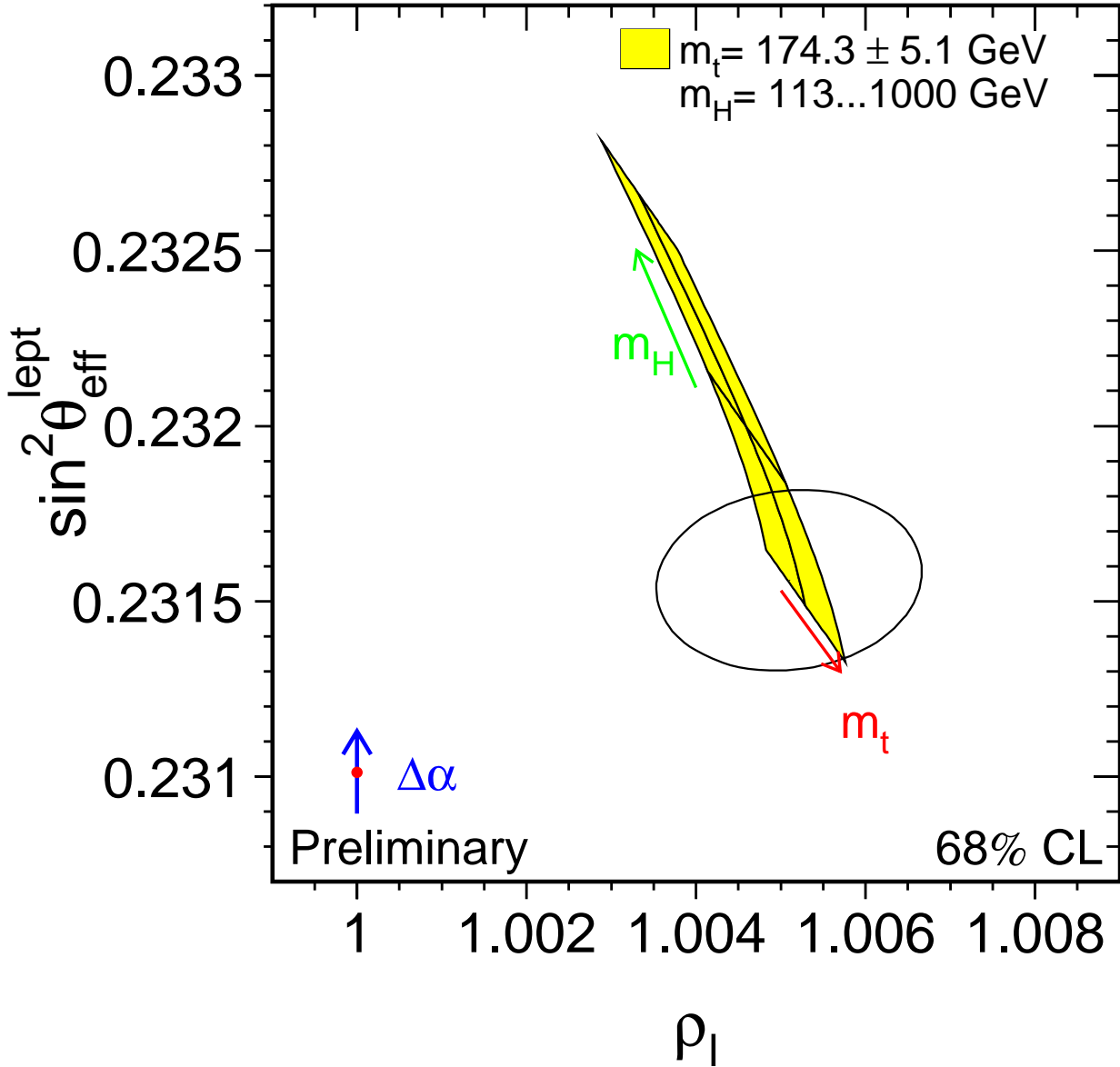


Figure 9.1: Contour curve of 68% probability in the  $(\rho_l, \sin^2 \theta_{\text{eff}}^{\text{lept}})$  plane. The prediction of a theory based on Born and QED with running  $\alpha$  is shown as the dot, with the arrow representing the uncertainty due to the hadronic vacuum polarisation. The same uncertainty also affects the Standard Model prediction, shown as the shaded region drawn for a fixed  $\Delta\alpha_{\text{had}}^{(5)}(m_Z^2)$  and values of  $m_t$  and  $m_H$  varied in the ranges indicated.



Thus the  $\epsilon$  parameters separate electroweak radiative corrections in quadratic  $m_t$  effects and logarithmic  $m_H$  effects. Such a rearrangement is also useful in the search for new physics effects in precision measurements.

Another commonly used description is based on the so-called  $STU$  parameters [209], extended by an additional parameter,  $\gamma_b$ , for the b-quark sector [75]. Approximate linear relations between these two sets of parameters exist:

$$S \simeq +\epsilon_3 \frac{4 \sin^2 \theta_0}{\alpha(m_Z^2)} - c_S \quad (9.18)$$

$$T \simeq \epsilon_1 \frac{1}{\alpha(m_Z^2)} - c_T \quad (9.19)$$

$$U \simeq -\epsilon_2 \frac{4 \sin^2 \theta_0}{\alpha(m_Z^2)} - c_U \quad (9.20)$$

$$\gamma_b \simeq 2\epsilon_b - c_\gamma. \quad (9.21)$$

In the literature, these parameters are in fact defined as shifts relative to a fixed set of Standard-Model values  $c$ , so that  $S = T = U = \gamma_b = 0$  at that point. Thus these parameters measure deviations from the electroweak radiative corrections expected in the Standard Model, in particular new physics effects in oblique electroweak corrections, *i.e.*, those entering through vacuum polarisation diagrams. For numerical results presented in the following, we use as the fixed subtraction point the values corresponding to:  $\Delta\alpha_{\text{had}}^{(5)}(m_Z^2) = 0.02761$ ,  $\alpha_S(m_Z^2) = 0.118$ ,  $m_Z = 91.1875$  GeV,  $m_t = 175$  GeV,  $m_H = 150$  GeV.

## 9.7.2 Results

The Z-pole measurements performed by SLD and at LEP-1 constrain the parameters  $\epsilon_1$  ( $T$ ),  $\epsilon_3$  ( $S$ ) and  $\epsilon_b$  ( $\gamma_b$ ). Given these, the measurements of the W-boson mass or of the on-shell electroweak mixing angle are solely determining  $\epsilon_2$  ( $U$ ). The other additional measurements discussed in Section 9.3 are not included here as they can be expressed in terms of neither the  $\epsilon$  nor the  $STU$  parameters without additional assumptions. In both analyses, the largest contribution to the  $\chi^2$  arises from the asymmetry measurements as discussed in Section 8.3.

The results of the fit of all  $\epsilon$  parameters to all LEP and SLD results are reported in Table 9.2, and are shown as a contour curve in the  $(\epsilon_3, \epsilon_1)$  plane in Figure 9.2. All  $\epsilon$  parameters are significantly different from zero, showing again that genuine electroweak radiative corrections beyond the running of  $\alpha$  and  $\alpha_S$  are observed.

The results of the fit of the  $STU$  parameters to the same data set, imposing the constraint  $U = 0$ , are shown in Table 9.3. In the  $(T, S)$  plane, the overall result as well as bands corresponding to the most precise measurements are shown in Figure 9.3. The  $STU$  analyses show that there are no large unexpected electroweak radiative corrections, as the values of the  $STU$  parameters are in agreement with zero.

Parameter	Value	Correlations						
		$\Delta\alpha_{\text{had}}^{(5)}(m_Z^2)$	$\alpha_S(m_Z^2)$	$m_Z$	$\epsilon_1$	$\epsilon_2$	$\epsilon_3$	$\epsilon_b$
$\Delta\alpha_{\text{had}}^{(5)}(m_Z^2)$	$0.02761 \pm 0.00036$	1.00	0.00	0.00	0.00	0.06	-0.31	0.00
$\alpha_S(m_Z^2)$	$0.1173 \pm 0.0040$	0.00	1.00	0.02	-0.37	-0.25	-0.27	-0.65
$m_Z$ [GeV]	$91.1873 \pm 0.0021$	0.00	0.02	1.00	-0.10	-0.03	-0.06	0.00
$\epsilon_1$	$+0.0055 \pm 0.0010$	0.00	-0.37	-0.10	1.00	0.60	0.86	0.00
$\epsilon_2$	$-0.0096 \pm 0.0012$	0.06	-0.25	-0.03	0.60	1.00	0.39	-0.01
$\epsilon_3$	$+0.0055 \pm 0.0009$	-0.31	-0.27	-0.06	0.86	0.39	1.00	0.02
$\epsilon_b$	$-0.0041 \pm 0.0017$	0.00	-0.65	0.00	0.00	-0.01	0.02	1.00

Table 9.2: Results on the  $\epsilon$  parameters including their correlations derived from a fit to all LEP and SLD measurements and including the measurement of the W-boson mass. The  $\chi^2/dof$  has a value of 19.6/11, corresponding to a probability of 5%. See Section 9.4 for a discussion on theoretical uncertainties not included here.

Parameter	Value	Correlations					
		$\Delta\alpha_{\text{had}}^{(5)}(m_Z^2)$	$\alpha_S(m_Z^2)$	$m_Z$	$S$	$T$	$\gamma_b$
$\Delta\alpha_{\text{had}}^{(5)}(m_Z^2)$	$0.02764 \pm 0.00036$	1.00	0.02	0.00	-0.37	-0.05	0.00
$\alpha_S(m_Z^2)$	$0.1157 \pm 0.0039$	0.02	1.00	0.01	-0.19	-0.28	-0.67
$m_Z$ [GeV]	$91.1872 \pm 0.0021$	0.00	0.01	1.00	-0.05	-0.11	0.00
$S$	$+0.08 \pm 0.10$	-0.37	-0.19	-0.05	1.00	0.85	0.03
$T$	$+0.16 \pm 0.10$	-0.05	-0.28	-0.11	0.85	1.00	0.01
$\gamma_b$	$+0.0036 \pm 0.0034$	0.00	-0.67	0.00	0.03	0.01	1.00

Table 9.3: Results on the  $STU\gamma_b$  parameters including their correlations derived from a fit to all LEP and SLD measurements and including the measurement of the W-boson mass. The parameter  $U$  is fixed to 0. The  $\chi^2/dof$  has a value of 22.1/12, corresponding to a probability of 4%. See Section 9.4 for a discussion on theoretical uncertainties not included here.

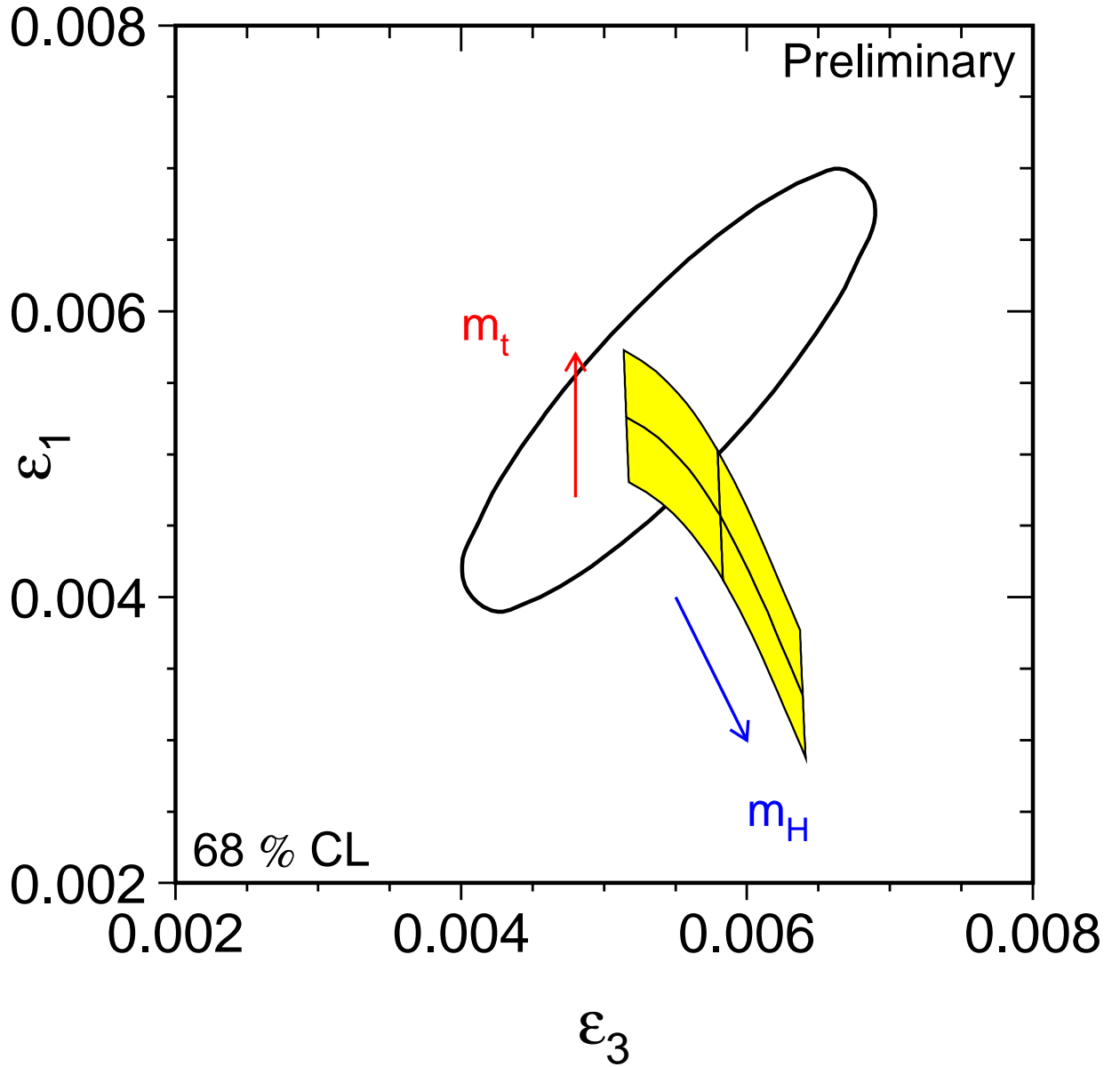


Figure 9.2: Contour curve of 68% probability in the  $(\epsilon_3, \epsilon_1)$  plane. The shaded region shows the predictions within the Standard Model for  $m_t = 174.3 \pm 5.1$  GeV and  $m_H = 300^{+700}_{-187}$  GeV for a fixed hadronic vacuum polarisation of  $\Delta\alpha_{\text{had}}^{(5)}(m_Z^2) = 0.02761$ .

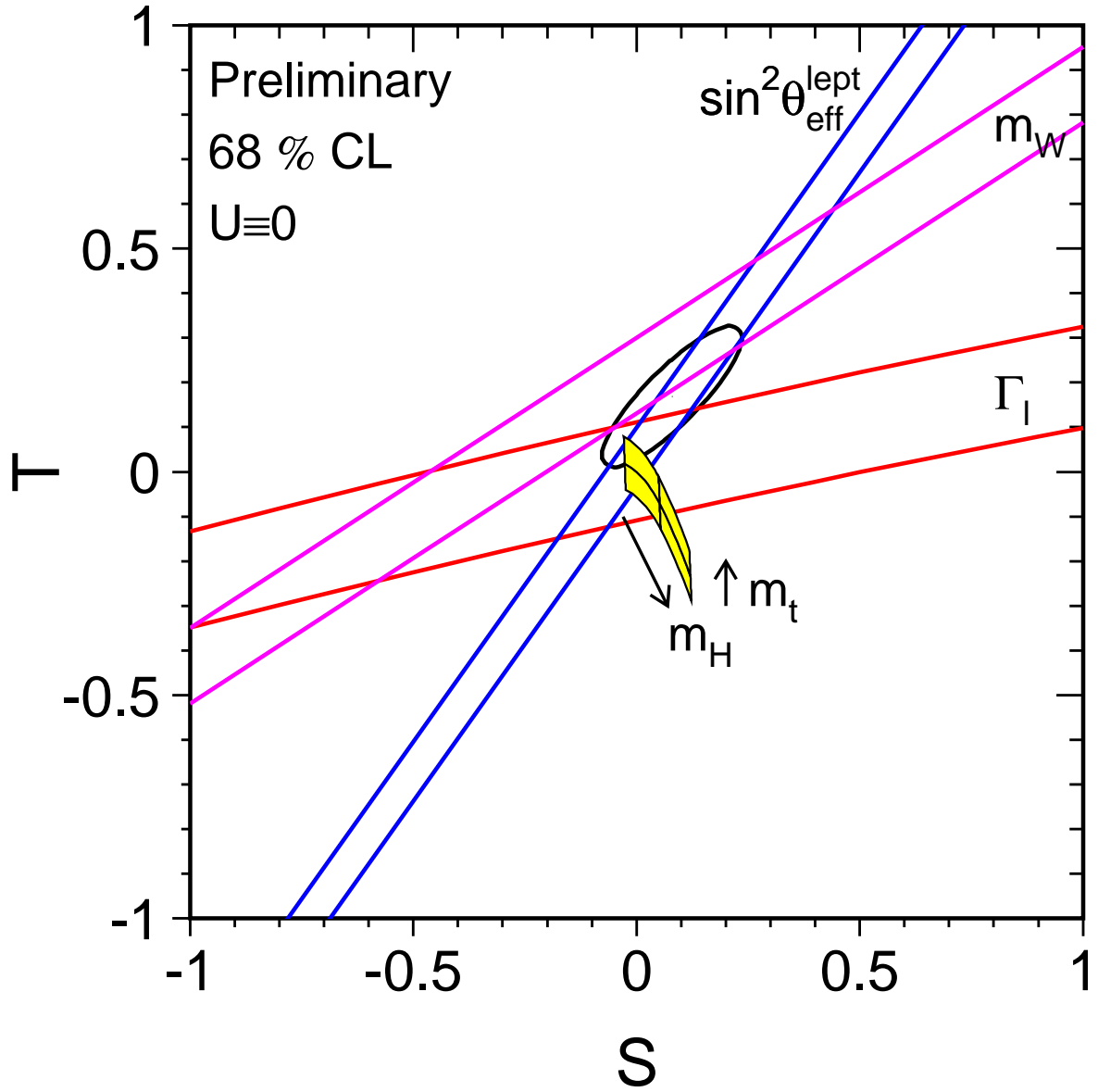


Figure 9.3: Contour curve of 68% probability in the  $(T, S)$  plane. Also shown are  $\pm 1$  sigma bands corresponding to the measurements of  $\Gamma_{\ell\ell}$ ,  $m_W$  and  $\sin^2 \theta_{\text{eff}}^{\text{lept}}$  in increasing slope of  $\Delta T/\Delta S$ . The shaded region shows the predictions within the Standard Model for  $m_t = 174.3 \pm 5.1$  GeV and  $m_H = 300_{-187}^{+700}$  GeV for a fixed hadronic vacuum polarisation of  $\Delta\alpha_{\text{had}}^{(5)}(m_Z^2) = 0.02761$ . The Standard-Model reference point at which all  $STU$  parameters vanish is chosen to be:  $\Delta\alpha_{\text{had}}^{(5)}(m_Z^2) = 0.02761$ ,  $\alpha_S(m_Z^2) = 0.118$ ,  $m_Z = 91.1875$  GeV,  $m_t = 175$  GeV,  $m_H = 150$  GeV. The constraint  $U = 0$  is always applied.

## 9.8 Standard-Model Analyses

### 9.8.1 Z-Pole Results

Based on the electroweak observables measured at LEP-1 and by SLD and presented before, a fit is performed in order to determine the five parameters of the Standard Model. The result is reported in Table 9.4. A  $\chi^2/dof$  of 21.5/12 is obtained, corresponding to a probability of 4%. The largest contribution to the  $\chi^2$  arises from the asymmetry measurements as discussed in Section 8.5. The Standard Model describes the complete set of measurements with a unique set of values for the free parameters. Note that the inclusion of a direct measurement of  $\alpha_S(m_Z^2)$ , or even fixing  $\alpha_S(m_Z^2)$ , introduces negligible improvements in the determination of the other Standard-Model parameters, as correlation coefficients between  $\alpha_S(m_Z^2)$  and all other parameters are small.

Parameter	Value	Correlations				
		$\Delta\alpha_{\text{had}}^{(5)}(m_Z^2)$	$\alpha_S(m_Z^2)$	$m_Z$	$m_t$	$\log_{10}(m_H/\text{GeV})$
$\Delta\alpha_{\text{had}}^{(5)}(m_Z^2)$	$0.02762 \pm 0.00035$	+1.00	-0.02	0.00	+0.02	-0.30
$\alpha_S(m_Z^2)$	$0.1188 \pm 0.0027$	-0.02	+1.00	-0.03	+0.10	+0.16
$m_Z$	$91.1874 \pm 0.0021$	0.00	-0.03	+1.00	-0.08	-0.03
$m_t$	$168 \pm_9^{12}$	+0.02	+0.10	-0.08	+1.00	+0.85
$\log_{10}(m_H/\text{GeV})$	$1.94 \pm_{0.30}^{0.37}$	-0.30	+0.16	-0.03	+0.85	+1.00
$m_H$	$87 \pm_{43}^{119}$	-0.30	+0.16	-0.03	+0.85	+1.00

Table 9.4: Results on the five Standard Model parameters derived from a fit to the electroweak results obtained at LEP-1 and by SLD. The fit has a  $\chi^2/dof$  of 21.5/12, corresponding to a probability of 4%. See Section 9.4 for a discussion on theoretical uncertainties not included here.

### Discussion

The Z-pole data alone is not able to improve significantly on the determination of  $\Delta\alpha_{\text{had}}^{(5)}(m_Z^2)$  compared to the direct determination presented in Section 9.2. The role of the mass of the Z boson is now changed from that of a model-independent parameter unrelated to other input measurements, Chapter 2, to a fundamental parameter of the Standard Model affecting the calculation of all observables. The uncertainty on  $m_Z$  remains unchanged. The strong coupling constant,  $\alpha_S(m_Z^2)$ , essentially determined by the leptonic pole cross section  $\sigma_\ell^0 \sigma_n^0 / R_\ell^0$  as discussed in Section 2.5, is one of the most precise determinations of this quantity [76].

The mass of the top quark is predicted with an accuracy of about 10 GeV. This precise prediction for a fundamental particle of the Standard Model not directly accessible at the Z pole emphasizes clearly the predictive power of the Standard Model as well as the precision of the experimental results.

Despite the logarithmic dependence of the electroweak radiative corrections on the mass of the Higgs boson, its value is nevertheless predicted with an uncertainty of about 100%. The value obtained shows the self-consistency of the Standard-Model analysis presented here, as such an analysis would be inconsistent and invalid for resulting Higgs masses close to or larger

than 1 TeV. The large correlation coefficient of  $m_H$  with  $m_t$  shows that the precision of the  $m_H$  prediction will drastically improve when including the direct measurement of  $m_t$ , as shown in the following.

### 9.8.2 The mass of the top quark and of the W boson

The above indirect constraint on the mass of the top quark, Table 9.4, must be compared with the result of the direct measurement of  $m_t$  at the TEVATRON,  $m_t = 174.3 \pm 5.1$  GeV [76]. The indirect determination is slightly lower but in good agreement with the direct measurement. The accuracy of the indirect constraint on  $m_t$  is improved by including the direct measurements of the W boson mass at the TEVATRON and LEP-2,  $m_W = 80.448 \pm 0.034$  GeV (Section 9.3), increasing the value to:

$$m_t = 180_{-9}^{+12} \text{ GeV}, \quad (9.22)$$

now in even better agreement with the direct measurement. In the case of the top quark, the direct measurement of its mass is already more precise than the indirect determination within the framework of the Standard Model.

Having determined the five Standard Model parameters as in Table 9.4, the mass of the W boson is then predicted to be:

$$m_W = 80.357 \pm 0.033 \text{ GeV}, \quad (9.23)$$

which is in agreement with the direct measurement. The accuracy of the  $m_W$  prediction is improved when the direct measurement of  $m_t$  is included in the fit, yielding:

$$m_W = 80.368 \pm 0.023 \text{ GeV}. \quad (9.24)$$

The Standard Model constraint on  $m_W$  is more precise than the current direct measurements. For a stringent test of the Standard Model, the mass of the W boson should thus be measured to an accuracy of 20 MeV or better. The different determinations of  $m_W$  are compared in Figure 9.4. All are in agreement.

### 9.8.3 The mass of the Higgs boson

The comparison between the indirect constraints and the direct measurements of  $m_t$  and  $m_W$  in the  $(m_t, m_W)$  plane is shown in Figure 9.5. The agreement is a crucial test of the Standard Model. Both contours prefer low values for the mass of the Higgs boson. As the Standard Model is so successful in predicting the values of  $m_W$  and  $m_t$ , this type of analysis is now extended to predict the mass of the Higgs Boson. The relative importance of including the direct measurements of  $m_t$  and  $m_W$  in constraining  $m_H$  is shown in Figure 9.6a and b. At the current level of experimental precision, the direct measurement of  $m_t$  is more important. A measurement of  $m_W$  with increased precision, however, will become very valuable.

The analysis is performed including all SLD and LEP-1 results as well as the additional measurements discussed in Section 9.3. The results are shown in Table 9.5. A  $\chi^2/dof$  of 25.5/15 is obtained, corresponding to a probability of 4%. The largest contribution to the  $\chi^2$  arises from the asymmetry measurements as discussed in Section 8.5. The unchanged  $\chi^2/ndof$  probability shows that also the complete set of measurements is accommodated by the Standard Model. Compared to the results shown in Table 9.4, the relative uncertainty on  $m_H$  decreases by more than a third, mainly by including the direct measurements of  $m_t$  and  $m_W$ . The

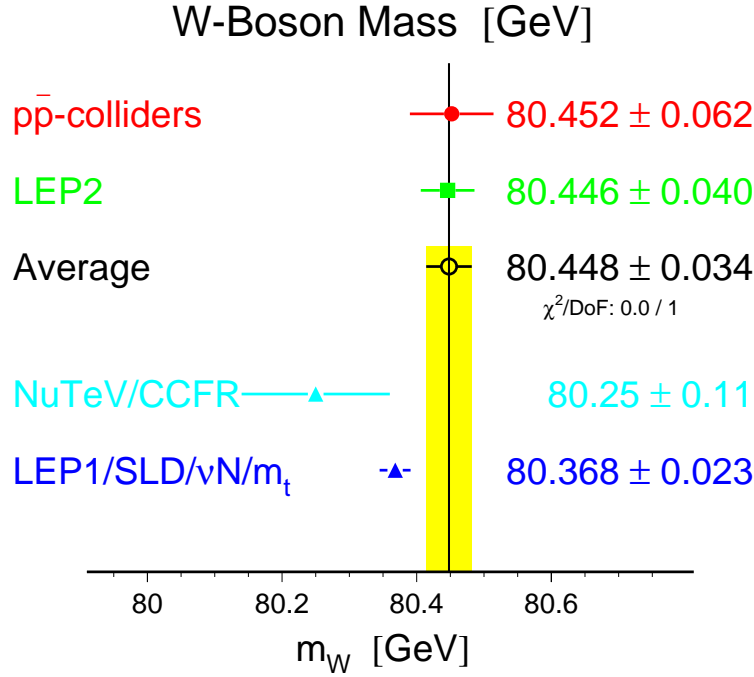


Figure 9.4: Results on the mass of the W boson,  $m_W$ . The direct measurements of  $m_W$  at the TEVATRON and at LEP-2 are compared with the indirect determinations.

importance of the external  $\Delta\alpha_{\text{had}}^{(5)}(m_Z^2) = 0.02761 \pm 0.00036$  determination for the constraint on  $m_H$  is shown in Figure 9.6c. Without the external  $\Delta\alpha_{\text{had}}^{(5)}(m_Z^2)$  constraint, the fit results are  $\Delta\alpha_{\text{had}}^{(5)}(m_Z^2) = 0.02978_{-0.00122}^{+0.00092}$  and  $m_H = 25_{-12}^{+37}$  GeV.

The  $\Delta\chi_{\text{min}}^2$  curve is shown in Figure 9.7. The effect of the theoretical uncertainties in the Standard-Model calculations due to missing higher-order corrections as discussed in Section 9.4 is shown by the width of the curve. Including these errors, the one-sided 95%CL upper limit on the mass of the Higgs boson at  $\Delta\chi^2 = 2.7$  is given by:

$$m_H < 212 \text{ GeV} . \tag{9.25}$$

In case the theory-driven  $\Delta\alpha_{\text{had}}^{(5)}(m_Z^2)$  determination of Equation 9.4 is used, the central value of  $m_H$  increases while the uncertainty on  $m_H$  is reduced. The upper limit becomes:

$$m_H < 236 \text{ GeV} . \tag{9.26}$$

Both results are in good agreement with the 95% confidence level lower limit on  $m_H$  of 113.5 GeV based on the direct search performed at LEP-2 [?].

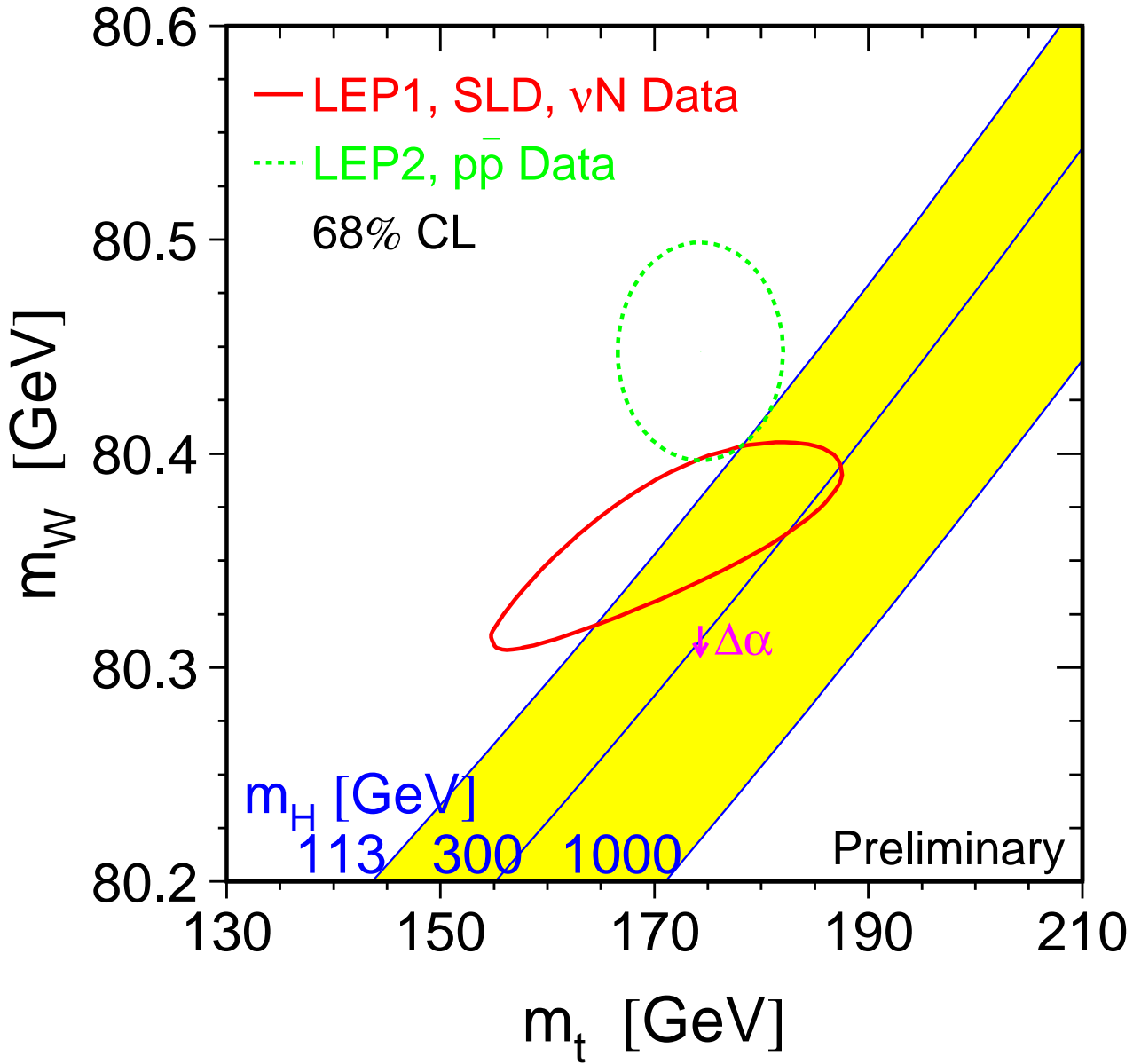


Figure 9.5: Contour curves of 68% probability in the  $(m_t, m_W)$  plane. The shaded band shows the Standard-Model prediction based on the value for  $G_F$  for various values of the Higgs mass and fixed  $\Delta\alpha_{\text{had}}^{(5)}(m_Z^2)$ ; varying the hadronic vacuum polarisation by  $\Delta\alpha_{\text{had}}^{(5)}(m_Z^2) = 0.02761 \pm 0.00036$  yields an additional uncertainty on the Standard-Model prediction shown by the arrow labelled  $\Delta\alpha$ .



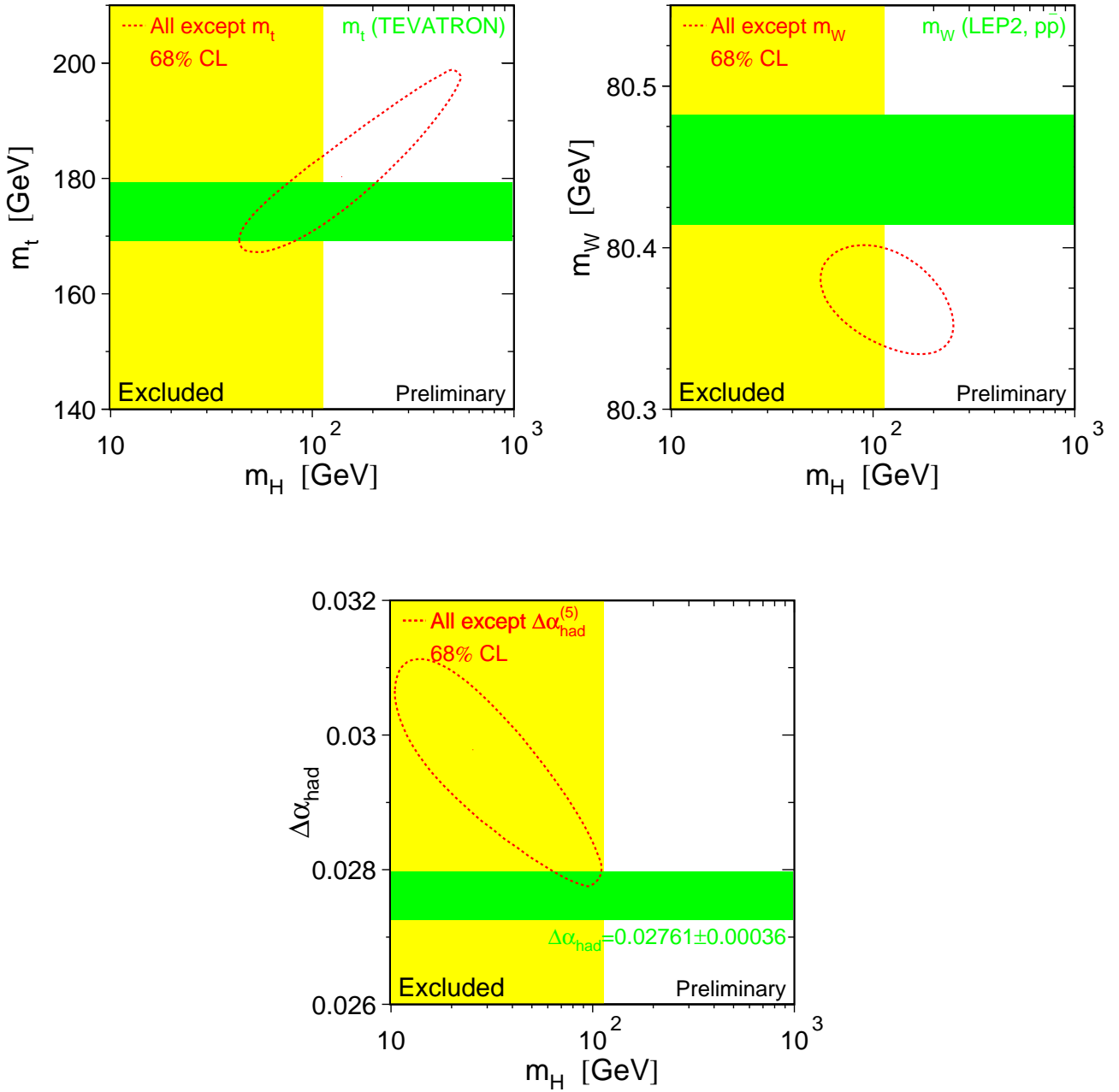


Figure 9.6: Contour curves of 68% probability in (a) the  $(m_t, m_H)$  plane, (b) the  $(m_W, m_H)$  plane, and (c) the  $(\Delta\alpha_{\text{had}}^{(5)}(m_Z^2), m_H)$  plane, based on all measurements except (a) the direct measurement of  $m_t$ , (b) the direct measurement of  $m_W$ , and (c) the external constraint on  $\Delta\alpha_{\text{had}}^{(5)}(m_Z^2)$ , in each case shown as the horizontal band of width  $\pm 1$  sigma. The region on  $m_H$  excluded at 95% confidence level by the direct search is also shown.

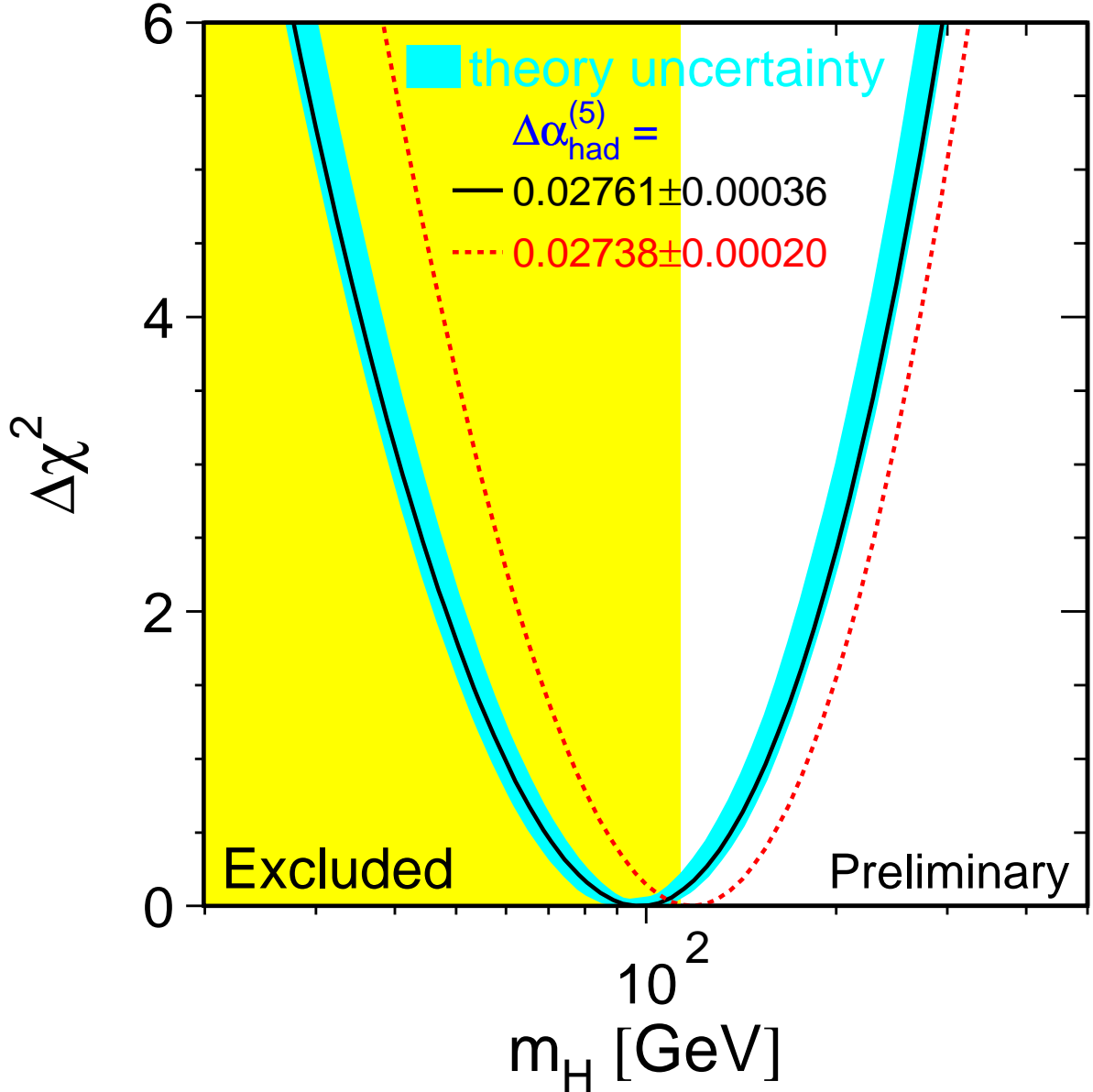


Figure 9.7:  $\Delta\chi^2(m_H) = \chi_{min}^2(m_H) - \chi_{min}^2$  as a function of  $m_H$ . The line is the result of the fit using all data. The associated band represents the estimate of the theoretical uncertainty due to missing higher-order corrections as discussed in Section 9.4. The vertical band shows the 95% confidence level exclusion limit on  $m_H$  of 113 GeV derived from the direct search at LEP-2. The dashed curve is the result obtained using the theory-driven  $\Delta\alpha_{\text{had}}^{(5)}(m_Z^2)$  determination of Equation 9.4.

Parameter	Value	Correlations				
		$\Delta\alpha_{\text{had}}^{(5)}(m_Z^2)$	$\alpha_S(m_Z^2)$	$m_Z$	$m_t$	$\log_{10}(m_H/\text{GeV})$
$\Delta\alpha_{\text{had}}^{(5)}(m_Z^2)$	$0.02774\pm 0.00035$	+1.00	-0.01	-0.01	-0.05	-0.45
$\alpha_S(m_Z^2)$	$0.1184\pm 0.0027$	-0.01	+1.00	-0.02	+0.09	+0.14
$m_Z$	$91.1874\pm 0.0021$	-0.01	-0.02	+1.00	-0.04	+0.05
$m_t$	$175.7\pm 4.4$	-0.05	+0.09	-0.04	+1.00	+0.70
$\log_{10}(m_H/\text{GeV})$	$1.99\pm 0.21$	-0.45	+0.14	+0.05	+0.70	+1.00
$m_H$	$98\pm_{38}^{58}$	-0.45	+0.14	+0.05	+0.70	+1.00

Table 9.5: Results on the five Standard Model parameters derived from a fit to all electroweak results. The fit has a  $\chi^2/dof$  of 25.5/15, corresponding to a probability of 4%. See Section 9.4 for a discussion on theoretical uncertainties not included here.

## 9.9 Discussion

The global  $\chi^2/dof$  of the Standard-Model fit is 25.5/15, corresponding to a probability of 4%. The contributions of the individual measurements to the global  $\chi^2$  are reported in Table 9.6 and shown in Figure 9.8 in terms of the pull of each measurement. The pull is defined as the difference between measured value and predicted value, calculated for the values of the five Standard-Model parameters corresponding to the global minimum of the  $\chi^2$ , in units of the measurement uncertainty.

The by far largest contribution to the overall  $\chi^2$  has already been discussed, namely the b-quark forward-backward asymmetry measured at LEP-1. The second and third largest pulls are caused by the left-right asymmetry measured by SLD, dominating  $\mathcal{A}_\ell(\text{SLD})$ , and the hadronic Z pole cross section measured at LEP-1. Compared to the uncertainty of the measurement,  $\sigma_h^0$  exhibits only a weak dependence on any of the five Standard-Model parameters. Nearly the same pull is caused by the combined result on the direct measurement of the W-boson mass.

As far as the mass of the Higgs boson is concerned, both  $A_{\text{FB}}^{0,b}$  and  $\mathcal{A}_\ell(\text{SLD})$  exhibit a high sensitivity to it, but prefer a high and a low value, respectively, as shown in Figures 9.9 to 9.11. Within the Standard-Model analysis, the other observables also prefer low values for  $m_H$ , in particular the leptonic asymmetry measurements and the measurements of the mass of the W boson. Thus the pull of the  $A_{\text{FB}}^{0,b}$  measurement is enlarged compared to the  $\sin^2 \theta_{\text{eff}}^{\text{lept}}$  combination discussed in Section 8.4, while that of  $\mathcal{A}_\ell(\text{SLD})$  is reduced, pointing to  $A_{\text{FB}}^{0,b}$  as the deviating measurement. Given the size of the experimental errors on the b-quark couplings compared to the size of their radiative corrections as expected in the Standard Model, a potential explanation in terms of new physics phenomena would require modifications of the b-quark couplings already at the level of the Born-term values, as also discussed in Section 8.5. It is thus interesting to repeat the Standard-Model analysis excluding the combined result on  $A_{\text{FB}}^{0,b}$ . With a  $\chi^2/dof$  of 15/14 (38%) a Higgs mass of  $m_H = 55_{-24}^{+41}$  GeV is obtained, corresponding to a 95% confidence level upper limit on  $m_H$  of 134 GeV.

The sensitivity of the observables to the mass of the Higgs boson within the framework of the Standard Model is shown in Figures 9.9 to 9.11 and quantified in Table 9.6. Note in particular, that compared to the Z-pole asymmetry measurements, the W-boson mass sensitivity to  $m_t$  and  $m_H$  relative to that to  $\Delta\alpha_{\text{had}}^{(5)}(m_Z^2)$  is larger, making  $m_W$ , measured at the TEVATRON and at LEP-2, an ideal observable to further reduce the error on the Higgs mass prediction.

In the data collected in the year 2000, the last year of LEP-2 operation, indications for the production of the Higgs boson were found [?]. Combining all four LEP experiments, the observations, compared to the expected background, correspond to a significance of 2.9 standard deviations [?]. Attributing this excess to the production of the Standard Model Higgs boson, a mass of about 115 GeV is found. More data is needed to confirm or exclude this indication and its interpretation. Such a value for  $m_H$  is in good agreement with the value predicted within the Standard Model, Table 9.5, based on the analysis of precision electroweak observables.

	Measurement with Total Error	Systematic Error	Standard Model fit	Pull	Higgs Sens.
$\Delta\alpha_{\text{had}}^{(5)}(m_Z^2)$ [172]	$0.02761 \pm 0.00036$	0.00035	0.02774	-0.4	—
$m_Z$ [GeV]	$91.1875 \pm 0.0021$	<sup>(a)</sup> 0.0017	91.1874	0.0	—
$\Gamma_Z$ [GeV]	$2.4952 \pm 0.0023$	<sup>(a)</sup> 0.0013	2.4963	-0.5	2.8
$\sigma_h^0$ [nb]	$41.540 \pm 0.037$	<sup>(b)</sup> 0.028	41.480	1.6	0.10
$R_\ell^0$	$20.767 \pm 0.025$	<sup>(b)</sup> 0.007	20.740	1.1	0.80
$A_{\text{FB}}^{0,\ell}$	$0.0171 \pm 0.0010$	<sup>(b)</sup> 0.0003	0.0164	0.8	2.1
$\mathcal{A}_\ell$ (SLD)	$0.1513 \pm 0.0021$	0.0010	0.1478	1.6	4.4
$\mathcal{A}_e$ ( $P_\tau$ )	$0.1498 \pm 0.0048$	0.0009	0.1478	0.4	1.9
$\mathcal{A}_\tau$ ( $P_\tau$ )	$0.1439 \pm 0.0041$	0.0026	0.1478	-1.0	2.3
$R_b^0$	$0.21664 \pm 0.00068$	0.00056	0.21574	1.3	0.11
$R_c^0$	$0.1729 \pm 0.0032$	0.0028	0.1723	0.2	0.024
$A_{\text{FB}}^{0,b}$	$0.0982 \pm 0.0017$	0.0010	0.1036	-3.2	3.9
$A_{\text{FB}}^{0,c}$	$0.0689 \pm 0.0035$	0.0019	0.0741	-1.5	1.5
$\mathcal{A}_b$	$0.921 \pm 0.020$	0.017	0.935	-0.7	0.037
$\mathcal{A}_c$	$0.667 \pm 0.026$	0.016	0.668	-0.4	0.16
$\sin^2 \theta_{\text{eff}}^{\text{lept}}$ ( $\langle Q_{\text{FB}} \rangle$ )	$0.2322 \pm 0.0010$	0.0008	0.23142	0.8	1.2
$m_t$ [GeV] ( $p\bar{p}$ [76])	$174.3 \pm 5.1$	4.0	175.7	-0.3	—
$m_W$ [GeV] ( $p\bar{p}$ [189])	$80.452 \pm 0.062$	0.050	80.393	0.9	2.4
$m_W$ [GeV] (LEP-2 [194])	$80.446 \pm 0.040$	0.030	80.393	1.3	3.7
$\sin^2 \theta_W$ ( $\nu N$ [196])	$0.2255 \pm 0.0021$	0.0010	0.2227	1.2	1.4
$Q_W(\text{Cs})$ [202]	$-72.5 \pm 0.7$	0.6	-73.09	?.?	0.55

Table 9.6: Summary of measurements included in the combined analysis of Standard Model parameters. See Chapters 2 to 7 for the correlations between these results not reported in this table. The total errors in column 2 include the systematic errors listed in column 3. Although the systematic errors include both correlated and uncorrelated sources, the determination of the systematic part of each error is approximate. The Standard Model results in column 4 and the pulls (difference between measurement and fit in units of the total measurement error) in column 5 are derived from the Standard-Model analysis including all data. These analyses include all correlations between the results. The last column shows the Standard-Model Higgs sensitivity, defined as the partial derivative of the Standard-Model calculation of the observable w.r.t.  $\log_{10}(m_H/\text{GeV})$ , divided by the total measurement error.

<sup>(a)</sup> Only systematic errors arising from the uncertainties in the LEP beam energy are indicated.

<sup>(b)</sup> Only common systematic errors are indicated.

## Winter 2001

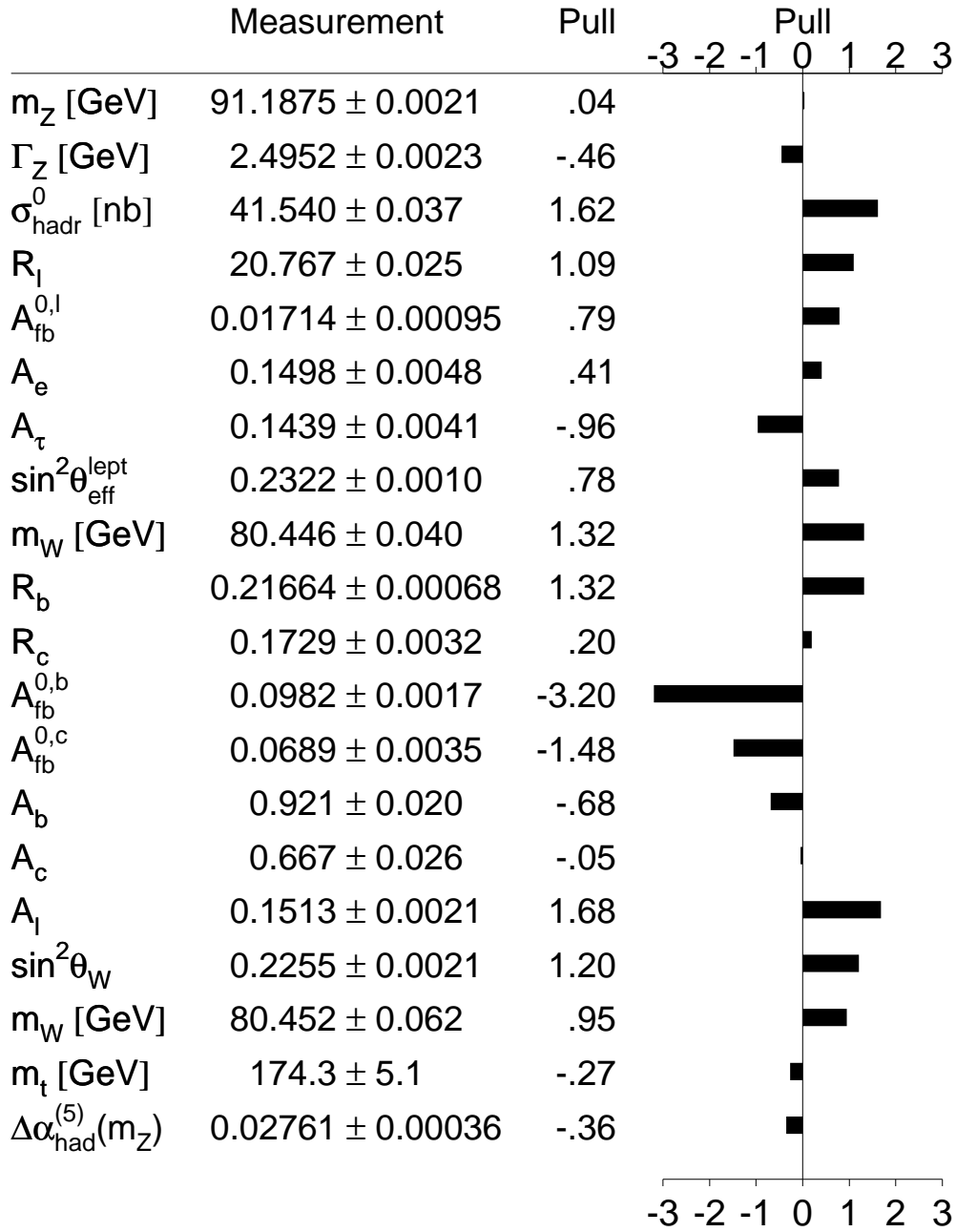


Figure 9.8: Comparison of the measurements with the expectation of the Standard Model, calculated for the Standard-Model parameter values in the minimum of the global  $\chi^2$ . Also shown is the pull of each measurement, where pull is defined as the difference of measurement and expectation in units of the measurement uncertainty.

# Preliminary

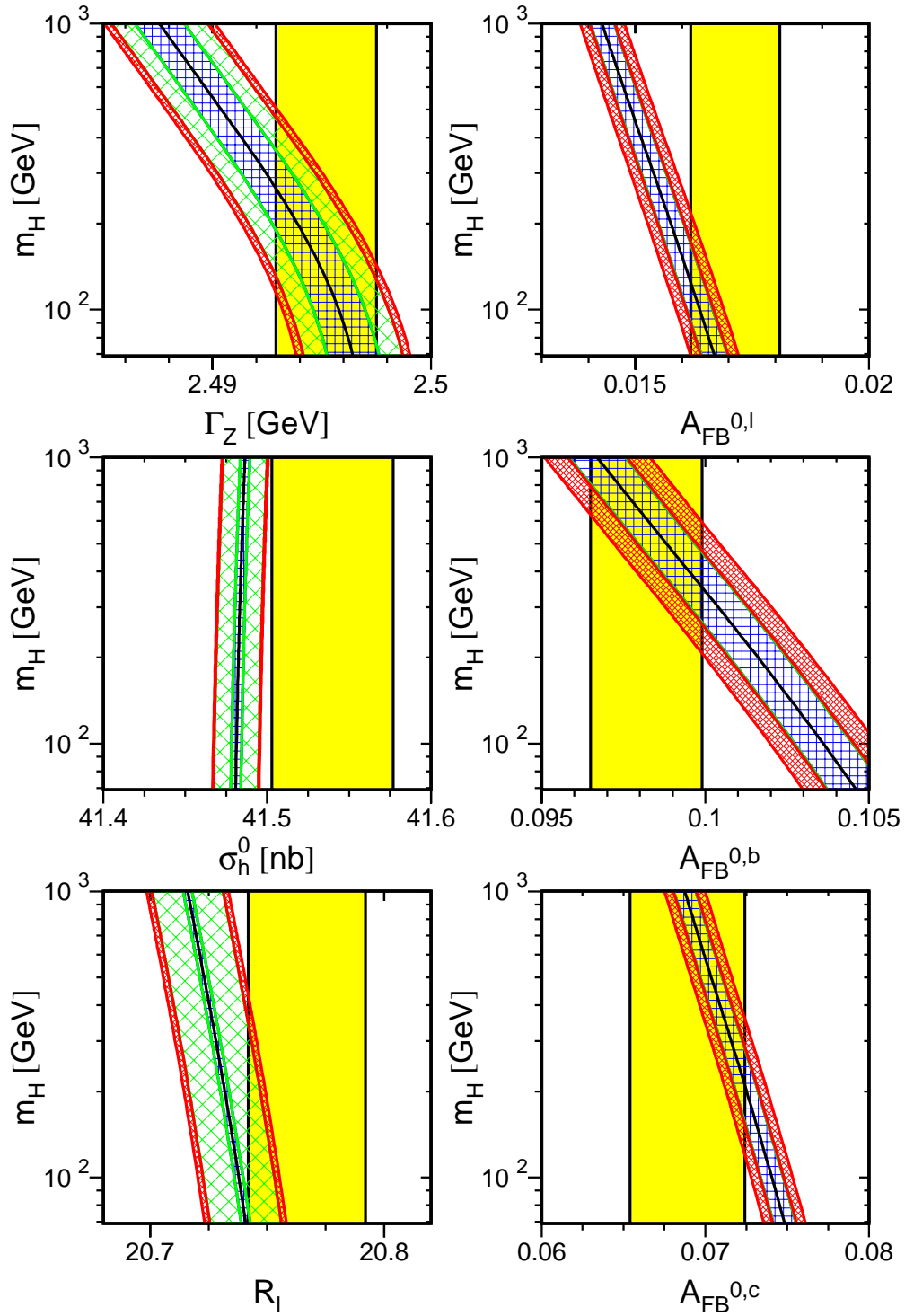


Figure 9.9: Comparison of the LEP/SLD combined measurements of  $\Gamma_Z$ ,  $\sigma_h^0$ ,  $R_\ell^0$ ,  $A_{\text{FB}}^{0,\ell}$ ,  $A_{\text{FB}}^{0,b}$  and  $A_{\text{FB}}^{0,c}$  with the Standard-Model prediction as a function of the mass of the Higgs boson. The measurement with its uncertainty is shown as the vertical band. The width of the Standard Model band arises due to the uncertainties in  $\Delta\alpha_{\text{had}}^{(5)}(m_Z^2)$ ,  $\alpha_S(m_Z^2)$  and  $m_t$ . The total width of the band is the linear sum of these effects. See Figure 9.10 for the definition of these parametric uncertainties.

Preliminary

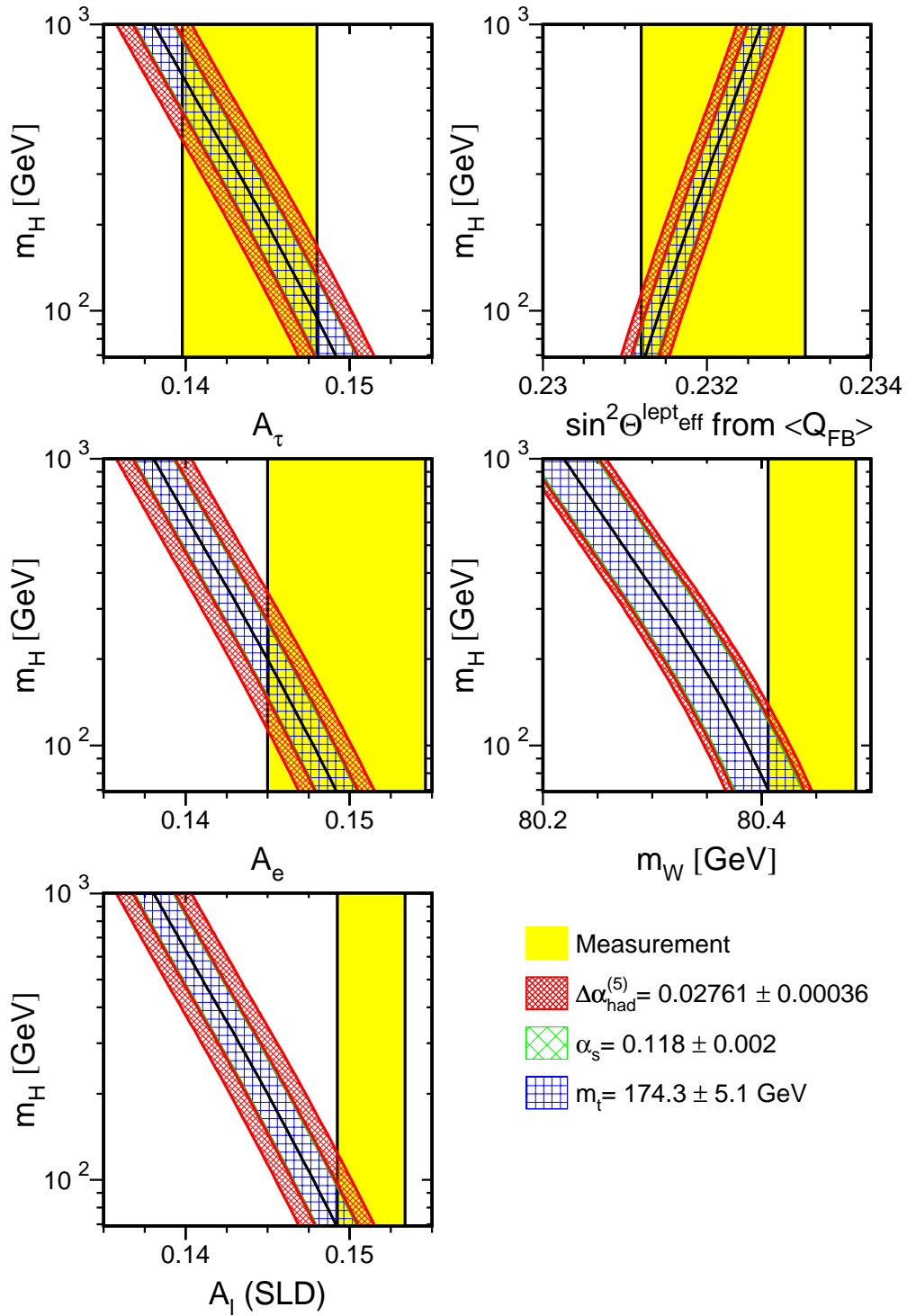


Figure 9.10: Comparison of the LEP/SLD combined measurements of  $\mathcal{A}_\tau(P_\tau)$ ,  $\mathcal{A}_e(P_\tau)$ ,  $\mathcal{A}_\ell(\text{SLD})$ ,  $\sin^2 \theta_{\text{eff}}^{\text{lept}}(\langle Q_{\text{FB}} \rangle)$  and  $m_W$  (LEP-2) with the Standard-Model prediction as a function of the mass of the Higgs boson (see Figure 9.9).



# Preliminary

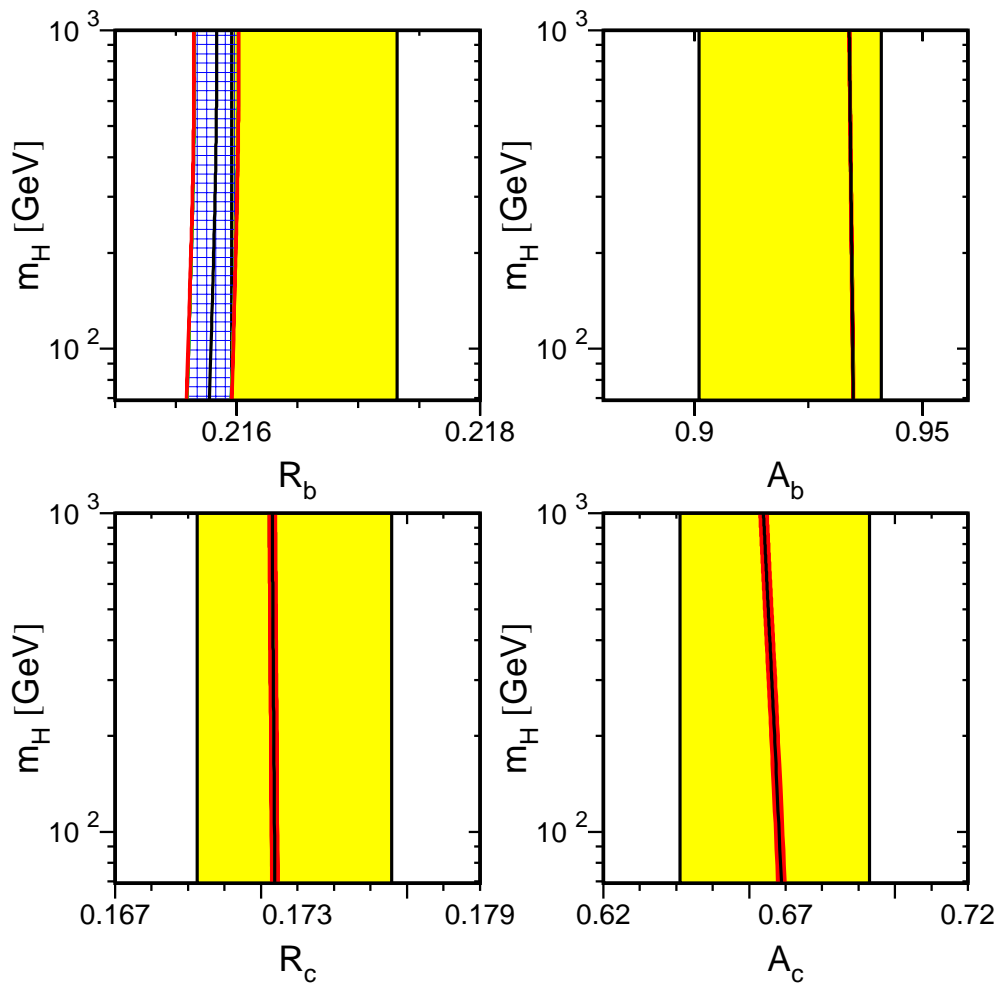


Figure 9.11: Comparison of the LEP/SLD combined measurements of  $R_b$ ,  $R_c$ ,  $A_b$  and  $A_c$  with the Standard-Model prediction as a function of the mass of the Higgs boson (see Figure 9.9).

# Chapter 10

## Summary and Conclusions

\$Id: physrep\_summary.tex,v 1.10 2001/05/25 12:18:25 gruenew Exp \$

The four LEP experiments ALEPH, DELPHI, L3 and OPAL and the SLD experiment at the SLC perform measurements in electron-positron collisions at centre-of-mass energies corresponding to the mass of the Z boson. Accumulating about 18 million Z decays with excellent detectors, the measurements are of unprecedented accuracy in high-energy particle physics. In particular, the pair-production of charged leptons and heavy quarks as well as inclusive hadron production is analysed by measuring production cross sections and various cross-section asymmetries. The measurements are used to determine the mass of the Z boson, its decay widths and its couplings to the various fermion species. In addition, the large number of precise results on many different observables allows both stringent tests of many relations inspired by the Standard Model and to constrain its free parameters.

While most measurements are well accommodated, the various measurements of forward-backward and polarised asymmetries, when interpreted in terms of a single quantity, the leptonic effective electroweak mixing angle, show a dispersion larger than expected with a  $\chi^2/dof$  of 14.7/5. Within the Standard-Model framework, the large  $\chi^2/dof$  is mainly caused by the measurement of the forward-backward asymmetry in  $b\bar{b}$  production, which could be explained by new physics, for example, modifying the right-handed b-quark coupling, or simply by a fluctuation of one or more of the asymmetry measurements. Further improvements on the precision of Z-pole observables, essential to shed light on this, is expected from a linear collider taking data at the Z-pole.

Analysing all results in the framework of the Standard Model, the predicted masses of the top quark and of the W boson agree with the direct measurements of these quantities, successfully testing the Standard Model at the level of its radiative corrections. The mass of the Higgs boson is predicted with a precision of about 50% and constrained to be less than 212 GeV at 95% confidence level, in agreement with the lower limit obtained from direct searches at LEP-2.

In the next years, improvements to three other important electroweak observables will become available, namely the masses of the top quark and of the W boson, and the hadronic vacuum polarisation. Assuming future world-average uncertainties of 2 GeV on  $m_t$ , 25 MeV on  $m_W$ , and 0.01 on  $\Delta\alpha_{\text{had}}^{(5)}(m_Z^2)$ , the mass of the Higgs boson can be predicted with an uncertainty of about 3X%, while the direct observation of Higgs-boson production will eventually allow to measure its mass at the GeV level, allowing another crucial test of the Standard Model through a comparison of the two.

# Appendix A

## The Measurements used in the Heavy Flavour Averages

**This appendix contains the results of the winter01 conferences, they are not final!**

In the following 20 tables the results used in the combination are listed. In each case an indication of the dataset used and the type of analysis is given. Preliminary results are indicated by the symbol “†”. The values of centre-of-mass energy are given where relevant. In each table, the result used as input to the average procedure is given followed by the statistical error, the correlated and uncorrelated systematic errors, the total systematic error, and any dependence on other electroweak parameters. In the case of the asymmetries, the measurement moved to a common energy (89.55 GeV, 91.26 GeV and 92.94 GeV, respectively, for peak−2, peak and peak+2 results) is quoted as *corrected* asymmetry.

Contributions to the correlated systematic error quoted here are from any sources of error shared with one or more other results from different experiments in the same table, and the uncorrelated errors from the remaining sources. In the case of  $\mathcal{A}_c$  and  $\mathcal{A}_b$  from SLD the quoted correlated systematic error has contributions from any source shared with one or more other measurements from LEP experiments. Constants such as  $a(x)$  denote the dependence on the assumed value of  $x^{\text{used}}$ , which is also given.

	ALEPH	DELPHI	L3	OPAL	SLD
	92-95 [85]	92-95 [86]	94-95 [87]	92-95 [82]	93-98† [83]
$R_b^0$	0.2157	0.2163	0.2174	0.2174	0.2171
Statistical	0.0009	0.0007	0.0015	0.0011	0.0009
Uncorrelated	0.0007	0.0004	0.0015	0.0009	0.0005
Correlated	0.0007	0.0004	0.0018	0.0008	0.0005
Total Systematic	0.0009	0.0006	0.0023	0.0012	0.0008
$a(R_c)$	-0.0033	-0.0041	-0.0376	-0.0122	-0.0057
$R_c^{\text{used}}$	0.1720	0.1720	0.1734	0.1720	0.1710
$a(\text{BR}(c \rightarrow \ell))$ $\text{BR}(c \rightarrow \ell)^{\text{used}}$			-0.0133 9.80	-0.0067 9.80	
$a(f(D^+))$ $f(D^+)^{\text{used}}$	-0.0010 0.2330	-0.0010 0.2330	-0.0086 0.2330	-0.0029 0.2380	-0.0008 0.2370
$a(f(D_s^+))$ $f(D_s^+)^{\text{used}}$	-0.0001 0.1020	0.0001 0.1030	-0.0005 0.1030	-0.0001 0.1020	-0.0003 0.1140
$a(f(\Lambda_c))$ $f(\Lambda_c)^{\text{used}}$	0.0002 0.0650	0.0003 0.0630	0.0008 0.0630	0.0003 0.0650	-0.0003 0.0730

Table A.1: The measurements of  $R_b^0$ . All measurements use a lifetime tag enhanced by other features like invariant mass cuts or high  $p_T$  leptons.

	ALEPH			DELPHI		OPAL		SLD
	91-95 c-count [93]	91-95 D meson [89]	92-95 lepton [89]	92-95 c-count [91]	92-95 D meson [91]	91-94 c-count [94]	90-95 D meson [92]	93-97† vtx-mass [88]
$R_c^0$	0.1734	0.1679	0.1668	0.1692	0.1610	0.164	0.1760	0.1754
Statistical	0.0049	0.0082	0.0062	0.0047	0.0104	0.011	0.0095	0.0032
Uncorrelated	0.0057	0.0078	0.0059	0.0050	0.0064	0.012	0.0102	0.0018
Correlated	0.0101	0.0026	0.0010	0.0083	0.0060	0.010	0.0062	0.0013
Total Systematic	0.0116	0.0082	0.0059	0.0097	0.0088	0.016	0.0120	0.0022
$a(R_b)$ $R_b^{\text{used}}$		-0.0050 0.2159						-0.1170 0.2166
$a(\text{BR}(c \rightarrow \ell))$ $\text{BR}(c \rightarrow \ell)^{\text{used}}$			-0.1646 9.80					

Table A.2: The measurements of  $R_c^0$ . “c-count” denotes the determination of  $R_c^0$  from the sum of production rates of weakly decaying charmed hadrons. “D meson” denotes any single/double tag analysis using exclusive and/or inclusive D meson reconstruction.

	ALEPH				DELPHI			L3		OPAL	
	90-95 lepton [96]	90-95 lepton [96]	90-95 lepton [96]	91-95† jet charge [103]	93-95† lepton [97]	92-95 <i>D</i> -meson [105]	92-95 jet charge [100]	90-95 lepton [210]	91-95 jet charge [102]	90-95† lepton [99]	90-95 <i>D</i> -meson [106]
$\sqrt{s}$ (GeV)	88.380	89.380	90.210	89.420	89.433	89.434	89.550	89.500	89.440	89.490	89.490
$A_{\text{FB}}^{\text{bb}}(-2)$	-3.53	5.47	9.11	4.66	5.90	5.65	6.80	6.14	4.10	3.56	-9.30
$A_{\text{FB}}^{\text{bb}}(-2)$ Corrected	5.87			4.97	6.18	5.93	6.80	6.26	4.36	3.70	-9.16
Statistical	1.90			1.26	2.20	7.59	1.80	2.93	2.10	1.73	10.80
Uncorrelated	0.39			0.06	0.08	0.91	0.12	0.37	0.25	0.16	2.51
Correlated	0.70			0.01	0.08	0.08	0.01	0.19	0.02	0.04	1.41
Total Systematic	0.80			0.06	0.12	0.91	0.13	0.41	0.25	0.16	2.88
$a(R_b)$	-0.3069			-9.5	-1.1543		-0.1962	-1.4467	-0.7300	-0.1000	
$R_b^{\text{used}}$	0.2192			0.2150	0.2164		0.2158	0.2170	0.2150	0.2155	
$a(R_c)$	0.0362			0.3100	1.0444		0.3200	0.3612	0.0700	0.1000	
$R_c^{\text{used}}$	0.1710			0.1725	0.1671		0.1720	0.1734	0.1730	0.1720	
$a(A_{\text{FB}}^{\text{cc}}(-2))$	-0.2244			-0.2644				-0.1000	-0.3156		
$A_{\text{FB}}^{\text{cc}}(-2)^{\text{used}}$	-2.34			-2.57				-2.50	-2.81		
$a(\text{BR}(b \rightarrow \ell))$	-0.2486				-1.0154			-1.0290		0.3406	
$\text{BR}(b \rightarrow \ell)^{\text{used}}$	11.34				10.56			10.50		10.90	
$a(\text{BR}(b \rightarrow c \rightarrow \ell))$	-0.1074				-0.1424			-0.1440		-0.5298	
$\text{BR}(b \rightarrow c \rightarrow \ell)^{\text{used}}$	7.86				8.07			8.00		8.30	
$a(\text{BR}(c \rightarrow \ell))$	-0.0474				0.7224			0.5096		0.1960	
$\text{BR}(c \rightarrow \ell)^{\text{used}}$	9.80				9.90			9.80		9.80	
$a(\bar{\chi})$	5.259				1.3054						
$\bar{\chi}^{\text{used}}$	0.12460				0.11770						
$a(f(D^+))$						0.5083	0.0949				
$f(D^+)^{\text{used}}$						0.2210	0.2330				
$a(f(D_s^+))$						0.1742	0.0035				
$f(D_s^+)^{\text{used}}$						0.1120	0.1020				
$a(f(A_c))$						-0.0191	-0.0225				
$f(A_c)^{\text{used}}$						0.0840	0.0630				

Table A.3: The measurements of  $A_{\text{FB}}^{\text{bb}}(-2)$ . All numbers are given in %.

	ALEPH	DELPHI		OPAL	
	91-95 <i>D</i> -meson [104]	93-95† lepton [97]	92-95 <i>D</i> -meson [105]	90-95† lepton [99]	90-95 <i>D</i> -meson [106]
$\sqrt{s}$ (GeV)	89.370	89.433	89.434	89.490	89.490
$A_{\text{FB}}^{\text{cc}}(-2)$	-1.10	1.11	-5.04	-6.92	3.90
$A_{\text{FB}}^{\text{cc}}(-2)$ Corrected	-0.02	1.81	-4.35	-6.56	4.26
Statistical	4.30	3.60	3.69	2.44	5.10
Uncorrelated	1.00	0.53	0.40	0.38	0.80
Correlated	0.09	0.16	0.09	0.23	0.30
Total Systematic	1.00	0.55	0.41	0.44	0.86
$a(R_b)$ $R_b^{\text{used}}$		-0.2886 0.2164		-3.4000 0.2155	
$a(R_c)$ $R_c^{\text{used}}$		1.0096 0.1671		3.2000 0.1720	
$a(A_{\text{FB}}^{\text{bb}}(-2))$ $A_{\text{FB}}^{\text{bb}}(-2)^{\text{used}}$	-1.3365 6.13				
$a(\text{BR}(b \rightarrow \ell))$ $\text{BR}(b \rightarrow \ell)^{\text{used}}$		-1.0966 10.56		-1.7031 10.90	
$a(\text{BR}(b \rightarrow c \rightarrow \ell))$ $\text{BR}(b \rightarrow c \rightarrow \ell)^{\text{used}}$		1.1156 8.07		-1.4128 8.30	
$a(\text{BR}(c \rightarrow \ell))$ $\text{BR}(c \rightarrow \ell)^{\text{used}}$		1.0703 9.90		3.3320 9.80	
$a(\overline{\chi})$ $\overline{\chi}^{\text{used}}$		-0.0856 0.11770			
$a(f(D^+))$ $f(D^+)^{\text{used}}$			-0.3868 0.2210		
$a(f(D_s^+))$ $f(D_s^+)^{\text{used}}$			-0.1742 0.1120		
$a(f(\Lambda_c))$ $f(\Lambda_c)^{\text{used}}$			-0.0878 0.0840		

Table A.4: The measurements of  $A_{\text{FB}}^{\text{cc}}(-2)$ . All numbers are given in %.

	ALEPH				DELPHI					L3			OPAL	
	91-95† lepton [96]	91-95† jet charge [103]	91-92 lepton [97]	93-95† lepton [97]	92-95 $D$ -meson [105]	92-95 jet charge [100]	92-95† multi [107]	91-95 jet charge [101]	90-95 lepton [210]	91-95 jet charge [102]	90-95† lepton [99]	90-95 $D$ -meson [106]		
$\sqrt{s}$ (GeV)	91.210	91.230	91.270	91.223	91.235	91.260	91.260	91.240	91.260	91.210	91.240	91.240		
$A_{\text{FB}}^{\text{bb}}$ (pk)	9.71	9.90	10.89	9.86	7.59	9.83	9.31	9.31	9.85	10.06	9.14	8.90		
$A_{\text{FB}}^{\text{bb}}$ (pk) Corrected	9.81	9.96	10.87	9.93	7.63	9.83	9.31	9.35	9.85	10.15	9.18	8.94		
Statistical	0.40	0.27	1.30	0.64	1.97	0.47	0.34	1.01	0.67	0.52	0.44	2.70		
Uncorrelated	0.16	0.14	0.33	0.15	0.76	0.13	0.15	0.51	0.27	0.41	0.14	2.15		
Correlated	0.12	0.01	0.27	0.14	0.10	0.04	0.02	0.21	0.14	0.20	0.15	0.45		
Total Systematic	0.20	0.14	0.43	0.20	0.77	0.14	0.15	0.55	0.31	0.46	0.20	2.20		
$a(R_b)$	-0.9545	-9.5	-2.8933	-2.0201		-0.1962	-0.2824	-9.1622	-2.1700	-7.6300	-0.7000			
$R_b^{\text{used}}$	0.2172	0.2158	0.2170	0.2164		0.2158	0.2165	0.2170	0.2170	0.2150	0.2155			
$a(R_c)$	0.6450	0.3100	1.0993	1.1488		0.8400	0.1558	1.0831	1.3005	0.4600	0.6000			
$R_c^{\text{used}}$	0.1720	0.1715	0.1710	0.1671		0.1720	0.1709	0.1733	0.1734	0.1730	0.1720			
$a(A_{\text{FB}}^{\text{cc}}(\text{pk}))$		0.6849					0.4173	1.1603	0.9262	0.6870				
$A_{\text{FB}}^{\text{cc}}(\text{pk})^{\text{used}}$		6.66					6.89	6.91	7.41	6.19				
$a(\text{BR}(b \rightarrow \ell))$	-1.8480		-3.8824	-2.0308					-2.0160		-0.3406			
$\text{BR}(b \rightarrow \ell)^{\text{used}}$	10.78		11.00	10.56					10.50		10.90			
$a(\text{BR}(b \rightarrow c \rightarrow \ell))$	0.4233		0.4740	-0.3798					-0.1280		-0.3532			
$\text{BR}(b \rightarrow c \rightarrow \ell)^{\text{used}}$	8.14		7.90	8.07					8.00		8.30			
$a(\text{BR}(c \rightarrow \ell))$	0.5096		0.7840	1.0703					1.5288		0.5880			
$\text{BR}(c \rightarrow \ell)^{\text{used}}$	9.80		9.80	9.90					9.80		9.80			
$a(\bar{\chi})$	2.9904		3.4467	1.6692										
$\bar{\chi}^{\text{used}}$	0.12460		0.12100	0.11770										
$a(f(D^+))$					0.0442	0.2761	0.4539							
$f(D^+)^{\text{used}}$					0.2210	0.2330	0.2330							
$a(f(D_s^+))$					-0.0788	0.0106	0.1432							
$f(D_s^+)^{\text{used}}$					0.1120	0.1020	0.1020							
$a(f(A_c))$					-0.0115	-0.0495	-0.0468							
$f(A_c)^{\text{used}}$					0.0840	0.0630	0.0930							

Table A.5: The measurements of  $A_{\text{FB}}^{\text{bb}}$ (pk). All numbers are given in %.

	ALEPH		DELPHI			L3	OPAL	
	91-95† lepton [96]	91-95 <i>D</i> -meson [104]	91-92 lepton [97]	93-95† lepton [97]	92-95 <i>D</i> -meson [105]	90-95 lepton [210]	90-95† lepton [99]	90-95 <i>D</i> -meson [106]
$\sqrt{s}$ (GeV)	91.210	91.220	91.270	91.223	91.235	91.240	91.240	91.240
$A_{\text{FB}}^{\text{cc}}$ (pk)	5.69	6.20	8.05	6.28	6.58	7.94	5.97	6.60
$A_{\text{FB}}^{\text{cc}}$ (pk) Corrected	5.94	6.39	8.00	6.46	6.70	8.04	6.07	6.70
Statistical	0.53	0.90	2.26	1.00	0.97	3.70	0.59	1.20
Uncorrelated	0.24	0.23	1.25	0.53	0.25	2.40	0.37	0.49
Correlated	0.36	0.17	0.49	0.27	0.04	0.49	0.32	0.24
Total Systematic	0.44	0.28	1.35	0.60	0.25	2.45	0.49	0.54
$a(R_b)$	1.4318		2.8933	-2.3087		4.3200	4.1000	
$R_b^{\text{used}}$	0.2172		0.2170	0.2164		0.2160	0.2155	
$a(R_c)$	-2.9383		-6.4736	5.4307		-6.7600	-3.8000	
$R_c^{\text{used}}$	0.1720		0.1710	0.1671		0.1690	0.1720	
$a(A_{\text{FB}}^{\text{bb}})$		-2.1333				6.4274		
$A_{\text{FB}}^{\text{bb}}$ (pk) <sup>used</sup>		9.79				8.84		
$a(\text{BR}(b \rightarrow \ell))$	1.8993		4.8529	-2.7618		3.5007	5.1094	
$\text{BR}(b \rightarrow \ell)^{\text{used}}$	10.78		11.00	10.56		10.50	10.90	
$a(\text{BR}(b \rightarrow c \rightarrow \ell))$	-1.0745		-3.9500	2.2786		-3.2917	-1.7660	
$\text{BR}(b \rightarrow c \rightarrow \ell)^{\text{used}}$	8.14		7.90	8.07		7.90	8.30	
$a(\text{BR}(c \rightarrow \ell))$	-3.2732		-7.2520	4.8965		-6.5327	-3.9200	
$\text{BR}(c \rightarrow \ell)^{\text{used}}$	9.80		9.80	9.90		9.80	9.80	
$a(\bar{\chi})$	0.0453			0.3852				
$\bar{\chi}^{\text{used}}$	0.12460			0.11770				
$a(f(D^+))$					-0.0221			
$f(D^+)^{\text{used}}$					0.2210			
$a(f(D_s^+))$					0.0788			
$f(D_s^+)^{\text{used}}$					0.1120			
$a(f(\Lambda_c))$					0.0115			
$f(\Lambda_c)^{\text{used}}$					0.0840			

Table A.6: The measurements of  $A_{\text{FB}}^{\text{cc}}$  (pk). All numbers are given in %.



	ALEPH				DELPHI			L3		OPAL	
	90-95 lepton [96]	90-95 lepton [96]	90-95 lepton [96]	91-95† jet charge [103]	93-95† lepton [97]	92-95 $D$ -meson [105]	92-95 jet charge [100]	90-95 lepton [210]	91-95 jet charge [102]	90-95† lepton [99]	90-95 $D$ -meson [106]
$\sqrt{s}$ (GeV)	92.050	92.940	93.900	92.950	92.990	92.990	92.940	93.100	92.910	92.950	92.950
$A_{\text{FB}}^{\text{bb}}(+2)$	3.93	10.60	9.03	11.82	10.10	8.78	12.30	13.78	14.60	10.75	-3.40
$A_{\text{FB}}^{\text{bb}}(+2)$ Corrected	10.03			11.81	10.05	8.73	12.30	13.62	14.63	10.74	-3.41
Statistical	1.51			0.99	1.80	6.37	1.60	2.40	1.70	1.43	9.00
Uncorrelated	0.14			0.16	0.14	0.97	0.25	0.34	0.64	0.25	2.03
Correlated	0.24			0.01	0.16	0.13	0.05	0.20	0.34	0.28	1.74
Total Systematic	0.28			0.16	0.21	0.98	0.26	0.40	0.73	0.37	2.68
$a(R_b)$	-1.964			-9.5	-2.8859		-0.1962	-3.3756	-12.9000	-0.8000	
$R_b^{\text{used}}$	0.2192			0.2156	0.2164		0.2158	0.2170	0.2150	0.2155	
$a(R_c)$	1.575			0.3100	1.3577		1.2000	1.9869	0.6900	0.8000	
$R_c^{\text{used}}$	0.1710			0.1719	0.1671		0.1720	0.1734	0.1730	0.1720	
$a(A_{\text{FB}}^{\text{cc}}(+2))$	1.081			1.2793				0.5206	1.3287		
$A_{\text{FB}}^{\text{cc}}(+2)^{\text{used}}$	12.51			12.42				12.39	12.08		
$a(\text{BR}(b \rightarrow \ell))$	-1.762				-2.3557			-2.0790		-1.3625	
$\text{BR}(b \rightarrow \ell)^{\text{used}}$	11.34				10.56			10.50		10.90	
$a(\text{BR}(b \rightarrow c \rightarrow \ell))$	-0.2478				-0.7595			-1.1200		0.7064	
$\text{BR}(b \rightarrow c \rightarrow \ell)^{\text{used}}$	7.86				8.07			8.00		8.30	
$a(\text{BR}(c \rightarrow \ell))$	1.524				1.0703			1.9796		0.7840	
$\text{BR}(c \rightarrow \ell)^{\text{used}}$	9.80				9.90			9.80		9.80	
$a(\bar{\chi})$	6.584				1.6050						
$\bar{\chi}^{\text{used}}$	0.12460				0.11770						
$a(f(D^+))$											
$f(D^+)^{\text{used}}$											
$a(f(D_s^+))$											
$f(D_s^+)^{\text{used}}$											
$a(f(A_c))$											
$f(A_c)^{\text{used}}$											

Table A.7: The measurements of  $A_{\text{FB}}^{\text{bb}}(+2)$ . All numbers are given in %.

	ALEPH	DELPHI		OPAL	
	91-95 <i>D</i> -meson [104]	93-95† lepton [97]	92-95 <i>D</i> -meson [105]	90-95† lepton [99]	90-95 <i>D</i> -meson [106]
$\sqrt{s}$ (GeV)	92.960	92.990	92.990	92.950	92.950
$A_{\text{FB}}^{\text{cc}}(+2)$	10.94	10.50	11.78	15.65	16.70
$A_{\text{FB}}^{\text{cc}}(+2)$ Corrected	10.89	10.37	11.65	15.62	16.67
Statistical	3.30	2.90	3.20	2.02	4.10
Uncorrelated	0.79	0.41	0.52	0.57	0.92
Correlated	0.18	0.29	0.07	0.62	0.51
Total Systematic	0.81	0.50	0.52	0.84	1.05
$a(R_b)$ $R_b^{\text{used}}$		-4.0402 0.2164		9.6000 0.2155	
$a(R_c)$ $R_c^{\text{used}}$		7.5891 0.1671		-8.9000 0.1720	
$a(A_{\text{FB}}^{\text{bb}}(+2))$ $A_{\text{FB}}^{\text{bb}}(+2)^{\text{used}}$	-2.6333 12.08				
$a(\text{BR}(b \rightarrow \ell))$ $\text{BR}(b \rightarrow \ell)^{\text{used}}$		-3.2492 10.56		9.5375 10.90	
$a(\text{BR}(b \rightarrow c \rightarrow \ell))$ $\text{BR}(b \rightarrow c \rightarrow \ell)^{\text{used}}$		1.5191 8.07		-1.5894 8.30	
$a(\text{BR}(c \rightarrow \ell))$ $\text{BR}(c \rightarrow \ell)^{\text{used}}$		8.1341 9.90		-9.2120 9.80	
$a(\overline{\chi})$ $\overline{\chi}^{\text{used}}$		-0.2140 0.11770			
$a(f(D^+))$ $f(D^+)^{\text{used}}$			-0.2984 0.2210		
$a(f(D_s^+))$ $f(D_s^+)^{\text{used}}$			0.0539 0.1120		
$a(f(\Lambda_c))$ $f(\Lambda_c)^{\text{used}}$			0.0764 0.0840		

Table A.8: The measurements of  $A_{\text{FB}}^{\text{cc}}(+2)$ . All numbers are given in %.



	SLD			
	93-98† lepton [108]	93-98† jet charge [211]	94-95† $K^\pm$ [112]	96-98† multi [111]
$\sqrt{s}$ (GeV)	91.280	91.280	91.280	91.280
$\mathcal{A}_b$	0.922	0.907	0.855	0.913
Statistical	0.029	0.020	0.088	0.019
Uncorrelated	0.019	0.023	0.102	0.018
Correlated	0.008	0.001	0.006	0.001
Total Systematic	0.021	0.024	0.102	0.018
$a(R_b)$	-0.0542		-0.0139	-0.4586
$R_b^{\text{used}}$	0.2168		0.2180	0.2158
$a(R_c)$	0.0424		0.0060	0.0215
$R_c^{\text{used}}$	0.1697		0.1710	0.1722
$a(\mathcal{A}_c)$	0.0449	0.0211	-0.0112	0.0076
$\mathcal{A}_c^{\text{used}}$	0.667	0.670	0.666	0.667
$a(\text{BR}(b \rightarrow \ell))$	-0.2160			
$\text{BR}(b \rightarrow \ell)^{\text{used}}$	10.80			
$a(\text{BR}(b \rightarrow c \rightarrow \ell))$	0.0888			
$\text{BR}(b \rightarrow c \rightarrow \ell)^{\text{used}}$	8.05			
$a(\text{BR}(c \rightarrow \ell))$	0.0479			
$\text{BR}(c \rightarrow \ell)^{\text{used}}$	9.83			
$a(\overline{\chi})$	0.3052			
$\overline{\chi}^{\text{used}}$	0.11990			

Table A.9: The measurements of  $\mathcal{A}_b$ .

	SLD		
	93-98† lepton [109]	93-98† <i>D</i> -meson [110]	96-98† K+vertex [113]
$\sqrt{s}$ (GeV)	91.280	91.280	91.280
$\mathcal{A}_c$	0.567	0.688	0.674
Statistical	0.051	0.035	0.029
Uncorrelated	0.056	0.020	0.025
Correlated	0.018	0.003	0.002
Total Systematic	0.059	0.021	0.025
$a(R_b)$	0.2173		0.1888
$R_b^{\text{used}}$	0.2173		0.2158
$a(R_c)$	-0.4089		-0.0430
$R_c^{\text{used}}$	0.1730		0.1722
$a(\mathcal{A}_b)$	0.2151	-0.0673	-0.0160
$\mathcal{A}_b^{\text{used}}$	0.935	0.935	0.935
$a(\text{BR}(b \rightarrow \ell))$	0.2328		
$\text{BR}(b \rightarrow \ell)^{\text{used}}$	11.06		
$a(\text{BR}(b \rightarrow c \rightarrow \ell))$	-0.1178		
$\text{BR}(b \rightarrow c \rightarrow \ell)^{\text{used}}$	8.02		
$a(\text{BR}(c \rightarrow \ell))$	-0.4077		
$\text{BR}(c \rightarrow \ell)^{\text{used}}$	9.80		
$a(\bar{\chi})$	0.1138		
$\bar{\chi}^{\text{used}}$	0.12170		

Table A.10: The measurements of  $\mathcal{A}_c$ .

	ALEPH	DELPHI	L3		OPAL
	91-95† multi [114]	94-95† multi [115]	92 lepton [116]	94-95† multi [87]	92-95 multi [117]
BR( $b \rightarrow \ell$ )	10.55	10.65	10.68	10.21	10.83
Statistical	0.09	0.07	0.11	0.13	0.10
Uncorrelated	0.17	0.23	0.36	0.20	0.20
Correlated	0.22	0.42	0.22	0.31	0.21
Total Systematic	0.27	0.48	0.42	0.36	0.29
$a(R_b)$ $R_b^{\text{used}}$			-9.2571 0.2160		-0.1808 0.2169
$a(R_c)$ $R_c^{\text{used}}$				1.4450 0.1734	0.4867 0.1770
$a(\text{BR}(b \rightarrow c \rightarrow \ell))$ $\text{BR}(b \rightarrow c \rightarrow \ell)^{\text{used}}$			-1.1700 9.00	0.1618 8.09	
$a(\text{BR}(c \rightarrow \ell))$ $\text{BR}(c \rightarrow \ell)^{\text{used}}$	-0.3078 9.85	-0.1960 9.80	-2.5480 9.80	0.9212 9.80	
$a(\bar{\chi})$ $\bar{\chi}^{\text{used}}$	0.7683 0.1178				
$a(f(D^+))$ $f(D^+)^{\text{used}}$				0.5523 0.2330	0.1445 0.2380
$a(f(D_s^+))$ $f(D_s^+)^{\text{used}}$				0.0213 0.1030	0.0055 0.1020
$a(f(\Lambda_c))$ $f(\Lambda_c)^{\text{used}}$				-0.0427 0.0630	-0.0157 0.0650

Table A.11: The measurements of BR( $b \rightarrow \ell$ ). All numbers are given in %.

	ALEPH	DELPHI	OPAL
	91-95† multi [114]	94-95† multi [115]	92-95 multi [117]
BR( $b \rightarrow c \rightarrow \ell$ )	8.04	7.88	8.40
Statistical	0.14	0.13	0.16
Uncorrelated	0.20	0.26	0.19
Correlated	0.14	0.36	0.34
Total Systematic	0.25	0.45	0.39
$a(R_b)$ $R_b^{\text{used}}$			-0.1808 0.2169
$a(R_c)$ $R_c^{\text{used}}$	0.8916 0.1694		0.3761 0.1770
$a(\text{BR}(c \rightarrow \ell))$ $\text{BR}(c \rightarrow \ell)^{\text{used}}$	0.3078 9.85	-0.1960 9.80	
$a(\bar{\chi})$ $\bar{\chi}^{\text{used}}$	-1.2804 0.11780		
$a(f(D^+))$ $f(D^+)^{\text{used}}$			0.1190 0.2380
$a(f(D_s^+))$ $f(D_s^+)^{\text{used}}$			0.0028 0.1020
$a(f(\Lambda_c))$ $f(\Lambda_c)^{\text{used}}$			-0.0110 0.0660

Table A.12: The measurements of  $\text{BR}(b \rightarrow c \rightarrow \ell)$ . All numbers are given in %.

	DELPHI	OPAL
	92-95 $D$ +lepton [90]	90-95 $D$ +lepton [95]
BR( $c \rightarrow \ell$ )	9.59	9.60
Statistical	0.42	0.60
Uncorrelated	0.24	0.49
Correlated	0.14	0.43
Total Systematic	0.27	0.65
$a(\text{BR}(b \rightarrow \ell))$ $\text{BR}(b \rightarrow \ell)^{\text{used}}$	-0.5600 11.20	-1.4335 10.99
$a(\text{BR}(b \rightarrow c \rightarrow \ell))$ $\text{BR}(b \rightarrow c \rightarrow \ell)^{\text{used}}$	-0.4100 8.20	-0.7800 7.80

Table A.13: The measurements of  $\text{BR}(c \rightarrow \ell)$ . All numbers are given in %.

	ALEPH	DELPHI	L3	OPAL
	90-95 multi [96]	94-95† multi [115]	90-95 lepton [210]	90-95† lepton [99]
$\bar{\chi}$	0.12461	0.12700	0.11920	0.11390
Statistical	0.00515	0.01300	0.00680	0.00540
Uncorrelated	0.00252	0.00566	0.00214	0.00306
Correlated	0.00397	0.00554	0.00252	0.00324
Total Systematic	0.00470	0.00792	0.00330	0.00446
$a(R_b)$	0.0341		0.0000	
$R_b^{\text{used}}$	0.2192		0.2170	
$a(R_c)$	0.0009		0.0004	
$R_c^{\text{used}}$	0.1710		0.1734	
$a(\text{BR}(b \rightarrow \ell))$	0.0524		0.0550	0.0170
$\text{BR}(b \rightarrow \ell)^{\text{used}}$	11.34		10.50	10.90
$a(\text{BR}(b \rightarrow c \rightarrow \ell))$	-0.0440		-0.0466	-0.0318
$\text{BR}(b \rightarrow c \rightarrow \ell)^{\text{used}}$	7.86		8.00	8.30
$a(\text{BR}(c \rightarrow \ell))$	0.0035	-0.0020	0.0006	0.0039
$\text{BR}(c \rightarrow \ell)^{\text{used}}$	9.80	9.80	9.80	9.80

Table A.14: The measurements of  $\bar{\chi}$ .

	DELPHI	OPAL
	92-95 $D$ -meson [90]	90-95 $D$ -meson [92]
$P(c \rightarrow D^{*+}) \times \text{BR}(D^{*+} \rightarrow \pi^+ D^0)$	0.1740	0.1513
Statistical	0.0100	0.0096
Uncorrelated	0.0040	0.0088
Correlated	0.0007	0.0011
Total Systematic	0.0041	0.0089
$a(R_b)$	0.0293	
$R_b^{\text{used}}$	0.2166	
$a(R_c)$	-0.0158	
$R_c^{\text{used}}$	0.1735	

Table A.15: The measurements of  $P(c \rightarrow D^{*+}) \times \text{BR}(D^{*+} \rightarrow \pi^+ D^0)$ .

	ALEPH	DELPHI	OPAL
	91-95 <i>D</i> meson [93]	92-95 <i>D</i> meson [91]	91-94 <i>D</i> meson [94]
$R_c f_{D^+}$	0.0406	0.0384	0.0390
Statistical	0.0013	0.0013	0.0050
Uncorrelated	0.0014	0.0015	0.0042
Correlated	0.0032	0.0025	0.0031
Total Systematic	0.0035	0.0030	0.0052
$a(f(D^+))$ $f(D^+)^{\text{used}}$		0.0008 0.2210	
$a(f(D_s^+))$ $f(D_s^+)^{\text{used}}$		-0.0002 0.1120	
$a(f(\Lambda_c))$ $f(\Lambda_c)^{\text{used}}$		0.0000 0.0840	

Table A.16: The measurements of  $R_c f_{D^+}$ .



	ALEPH	DELPHI	OPAL
	91-95 <i>D</i> meson [93]	92-95 <i>D</i> meson [91]	91-94 <i>D</i> meson [94]
$R_c f_{D_s}$	0.0207	0.0213	0.0160
Statistical	0.0033	0.0017	0.0042
Uncorrelated	0.0011	0.0010	0.0016
Correlated	0.0053	0.0054	0.0043
Total Systematic	0.0054	0.0055	0.0046
$a(f(D^+))$ $f(D^+)^{\text{used}}$		0.0007 0.2210	
$a(f(D_s^+))$ $f(D_s^+)^{\text{used}}$		-0.0009 0.1120	
$a(f(\Lambda_c))$ $f(\Lambda_c)^{\text{used}}$		-0.0001 0.0840	

Table A.17: The measurements of  $R_c f_{D_s}$ .

	ALEPH	DELPHI	OPAL
	91-95 <i>D</i> meson [93]	92-95 <i>D</i> meson [91]	91-94 <i>D</i> meson [94]
$R_c f_{\Lambda_c}$	0.0157	0.0169	0.0091
Statistical	0.0016	0.0035	0.0050
Uncorrelated	0.0005	0.0016	0.0015
Correlated	0.0044	0.0045	0.0035
Total Systematic	0.0045	0.0048	0.0038
$a(f(D^+))$ $f(D^+)^{\text{used}}$		0.0002 0.2210	
$a(f(D_s^+))$ $f(D_s^+)^{\text{used}}$		-0.0001 0.1120	
$a(f(\Lambda_c))$ $f(\Lambda_c)^{\text{used}}$		-0.0002 0.0840	

Table A.18: The measurements of  $R_c f_{\Lambda_c}$ .

	ALEPH	DELPHI	OPAL
	91-95 <i>D</i> meson [93]	92-95 <i>D</i> meson [91]	91-94 <i>D</i> meson [94]
$R_c f_{D^0}$	0.0964	0.0926	0.0997
Statistical	0.0029	0.0026	0.0070
Uncorrelated	0.0040	0.0038	0.0057
Correlated	0.0045	0.0023	0.0041
Total Systematic	0.0060	0.0044	0.0070
$a(f(D^+))$ $f(D^+)^{\text{used}}$		0.0020 0.2210	
$a(f(D_s^+))$ $f(D_s^+)^{\text{used}}$		-0.0004 0.1120	
$a(f(\Lambda_c))$ $f(\Lambda_c)^{\text{used}}$		-0.0004 0.0840	

Table A.19: The measurements of  $R_c f_{D^0}$ .

	DELPHI	OPAL
	92-95 <i>D</i> meson [91]	90-95 <i>D</i> -meson [92]
$R_c P(c \rightarrow D^{*+}) \times \text{BR}(D^{*+} \rightarrow \pi^+ D^0)$	0.0282	0.0266
Statistical	0.0007	0.0005
Uncorrelated	0.0010	0.0010
Correlated	0.0007	0.0009
Total Systematic	0.0012	0.0014
$a(f(D^+))$ $f(D^+)^{\text{used}}$	0.0006 0.2210	
$a(f(D_s^+))$ $f(D_s^+)^{\text{used}}$	-0.0001 0.1120	
$a(f(\Lambda_c))$ $f(\Lambda_c)^{\text{used}}$	-0.0004 0.0840	

Table A.20: The measurements of  $R_c P(c \rightarrow D^{*+}) \times \text{BR}(D^{*+} \rightarrow \pi^+ D^0)$ .

# Bibliography

- [1] Gargamelle Neutrino Collaboration, F. J. Hasert *et al.*, Phys. Lett. **B46** (1973) 138.
- [2] UA1 Collaboration, G. Arnison *et al.*, Phys. Lett. **B122** (1983) 103;  
UA2 Collaboration, M. Banner *et al.*, Phys. Lett. **B122** (1983) 476.
- [3] UA1 Collaboration, G. Arnison *et al.*, Phys. Lett. **B126** (1983) 398;  
UA2 Collaboration, P. Bagnaia *et al.*, Phys. Lett. **B129** (1983) 130.
- [4] S. L. Glashow, Nucl. Phys. **22** (1961) 579;  
S. Weinberg, Phys. Rev. Lett. **19** (1967) 1264;  
A. Salam, Weak and Electromagnetic Interactions, p. 367, in Elementary Particle Theory, Proceedings of the 1968 Nobel Symposium, ed. N. Svartholm, (Almquist and Wiksells, Stockholm, 1968).
- [5] *LEP Design Report*, CERN-LEP/84-01, June 1984;  
The main features of LEP have been reviewed by:  
S. Myers and E. Picasso, Contemp. Phys. **31** (1990) 387;  
D. Brandt *et al.*, Rep. Prog. Phys. **63** (2000) 939.
- [6] *SLAC Linear Collider Conceptual Design Report*, SLAC-R-229, June 1980.
- [7] ALEPH Collaboration, D. Decamp *et al.*, Nucl. Inst. Meth. **A294** (1990) 121;  
ALEPH Collaboration, D. Buskulic *et al.*, Nucl. Inst. Meth. **A360** (1995) 481.
- [8] DELPHI Collaboration, P. Aarnio *et al.*, Nucl. Inst. Meth. **A303** (1991) 233;  
P. Abreu *et al.*, Nucl. Inst. Meth. **A378** (1996) 57.
- [9] L3 Collaboration, B. Adeva *et al.*, Nucl. Inst. Meth. **A289** (1990) 35;  
L3 Collaboration, M. Acciarri *et al.*, Nucl. Inst. Meth. **A351** (1994) 300;  
L3 Collaboration, M. Chemarin *et al.*, Nucl. Inst. Meth. **A349** (1994) 345;  
L3 Collaboration, A. Adam *et al.*, Nucl. Inst. Meth. **A383** (1996) 342;  
L3 Collaboration, I.C. Brock *et al.*, Nucl. Inst. Meth. **A381** (1996) 236.
- [10] OPAL Collaboration, K. Ahmet *et al.*, Nucl. Inst. Meth. **A305** (1991) 275;  
OPAL Collaboration, P. Allport *et al.*, Nucl. Inst. Meth. **A324** (1993) 34;  
OPAL Collaboration, P. Allport *et al.*, Nucl. Inst. Meth. **A346** (1994) 476;  
OPAL Collaboration, B.E. Anderson *et al.*, IEEE Trans. Nucl. Sci. **41** (1994) 845.
- [11] Mark-II Collaboration, G. S. Abrams *et al.*, Phys. Rev. Lett. **63** (1989) 724.

- [12] SLD Collaboration, M. J. Fero *et al.*, Nucl. Instrum. Meth. **A367** (1995) 111;  
SLD Collaboration, D. Axen *et al.*, Nucl. Instrum. Meth. **A328** (1993) 472;  
SLD Collaboration, K. Abe *et al.*, Nucl. Instrum. Meth. **A343** (1994) 74;  
SLD Collaboration, S. C. Berridge *et al.*, IEEE Trans. Nucl. Sci. **39** (1992) 1242.
- [13] SLD Collaboration, K. Abe *et al.*, Nucl. Instrum. Meth. **A400** (1997) 287.
- [14] SLD Collaboration, A. C. Benvenuti *et al.*, Nucl. Instr. Meth. **A276** (1989) 94.
- [15] The working group on LEP energy and the Collaborations ALEPH, DELPHI, L3 and OPAL, L. Arnaudon *et al.*, Phys. Lett. **B307** (1993) 187–193.
- [16] Working group on LEP energy (L. Arnaudon *et al.*), *The Energy Calibration of LEP in 1992*, Preprint CERN SL/93-21 (DI), CERN, 1993.
- [17] Working group on LEP energy (R. Assmann *et al.*), Z. Phys. **C66** (1995) 567–582.
- [18] Working group on LEP energy (R. Assmann *et al.*), Eur. Phys. J. **C6** (1999) 187.
- [19] G. Montagna, O. Nicrosini, G. Passarino, F. Piccinni and R. Pittau, Nucl. Phys. **B401** (1993) 3; Comp. Phys. Comm. **76** (1993) 328; Comp. Phys. Comm. **93** (1996) 120;  
G. Montagna, O. Nicrosini, G. Passarino and F. Piccinini, hep-ph/9804211, recently updated to include initial state pair radiation (G. Passarino, priv. comm.).
- [20] D. Bardin *et al.*, Z. Phys. **C44** (1989) 493; Comp. Phys. Comm. **59** (1990) 303;  
Nucl. Phys. **B351**(1991) 1; Phys. Lett. **B255** (1991) 290; CERN-TH 6443/92 (May 1992) and Comp. Phys. Com. **133** (2001), 229-395, recently updated with results from [43].
- [21] M. G. D. Bardin and G. Passarino, *Precision calculation project report*, Preprint hep-ph/9902452, 1999.
- [22] ALEPH Collaboration, D. Decamp *et al.*, Z. Phys. **C48** (1990) 365;  
ALEPH Collaboration, D. Decamp *et al.*, Z. Phys. **C53** (1992) 1;  
ALEPH Collaboration, D. Buskulic *et al.*, Z. Phys. **C60** (1993) 71;  
ALEPH Collaboration, D. Buskulic *et al.*, Z. Phys. **C62** (1994) 539;  
ALEPH Collaboration, R. Barate *et al.*, Europ. Phys. J. **C 14** (2000) 1.
- [23] DELPHI Collaboration, P. Aarnio *et al.*, Nucl. Phys. **B367** (1991) 511;  
DELPHI Collaboration, P. Abreu *et al.*, Nucl. Phys. **B417** (1994) 3;  
DELPHI Collaboration, P. Abreu *et al.*, Nucl. Phys. **B418** (1994) 403;  
Europ. Phys. J. **C 16** (2000) 371.
- [24] L3 Collaboration, B. Adeva *et al.*, Z. Phys. **C51** (1991) 179;  
L3 Collaboration, O. Adriani *et al.*, Phys. Rep. **236** (1993) 1;  
L3 Collaboration, M. Acciarri *et al.*, Z. Phys. **C62** (1994) 551;  
Eur. Phys. J. **C16** (2000) 1.
- [25] OPAL Collaboration, G. Alexander *et al.*, Z. Phys. **C52** (1991) 175;  
OPAL Collaboration, P.D. Acton *et al.*, Z. Phys. **C58** (1993) 219;  
OPAL Collaboration, R. Akers *et al.*, Z. Phys. **C61** (1994) 19;  
OPAL Collaboration (G. Abbiendi *et al.*), Eur. Phys. J. **C14** (2000) 373;  
*Precise Determination of the Z Resonance Parameters at LEP : Zedometry*, CERN-EP-2000-148 (Nov. 2000), subm. to Eur. Phys. J. **C**.

- [26] R. Brun *et al.*, *GEANT3*, Preprint CERN DD/EE/84-1, CERN, 1987.
- [27] DELPHI internal note *DELSIM*, 87-96/PROG 99 and 87-98/PROG 100 (1989);  
J. Allison *et al.*, *The Detector Simulation Program for the OPAL experiment at LEP*,  
Nucl. Inst. Meth. **A317** (1992) 47;  
the simulations are all based on [26]; more details may be found in the references on the  
detectors, [7], [8] and [9].
- [28] T. Sjostrand, *Comput. Phys. Commun.* **82** (1994) 74.
- [29] G. Marchesini *et al.*, *Comput. Phys. Commun.* **67** (1992) 465.
- [30] L. Lonnblad, *Comp. Phys. Comm.* **71** (1992) 15.
- [31] S. Jadach, B. Ward, and Z. Wcas, *Comp. Phys. Comm.* **79** (1994) 503, (KORALZ 4.0).
- [32] S. Jadach, B.F.L. Ward and Z. Wcas, *Comput. Phys. Commun.* **130** (2000) 260.
- [33] W. Beenakker, F.A. Berends and S.C. van der Marck, *Nucl. Phys.* **B349** (1991) 323–368,  
(ALIBABA).
- [34] F.A. Berends, R. Kleiss and W. Hollik, *Nucl. Phys.* **B304** (1988) 712, (BABAMC).
- [35] H. Anlauf *et al.*, *Comput. Phys. Commun.* **79** (1994) 466–486, (UNIBAB).
- [36] S. Jadach, W. Placzek, E. Richter-Wcas, B.F.L. Ward and Z. Wcas, *Comput. Phys.  
Commun.* **102** (1997) 229, (BHLUMI 4.04).
- [37] J. Hilgart, R. Kleiss and F. Le Diberder, *Comput. Phys. Commun.* **75** (1993) 191.
- [38] J. Fujimoto *et al.*, *Comput. Phys. Commun.* **100** (1997) 128–156.
- [39] LEP Polarization Collaboration, L. Arnaudon *et al.*, *Phys. Lett.* **B284** (1992) 431–439.
- [40] L. Arnaudon *et al.*, *Z. Phys.* **C66** (1995) 45–62.
- [41] L. Knudsen *et al.*, *Phys. Lett.* **B270** (1991) 97–104.
- [42] M. Placidi and M. Rossmannith, *Nucl. Inst. Meth.* **A274** (1989) 79..
- [43] A. B. Arbuzov, *Light pair corrections to electron positron annihilation at LEP/SLC*,  
Preprint hep-ph/9907500, 1999.
- [44] W. Beenakker and G. Passarino, *Phys. Lett.* **B425** (1998) 199.
- [45] W. Beenakker and G. Passarino, private communication.
- [46] B.F.L. Ward, S. Jadach, M. Melles and S.A. Yost, *Phys. Lett.* **B450** (1999) 262.
- [47] G. Montagna, M. Moretti, O. Nicrosini, A. Pallavicini and F. Piccinini, *Phys. Lett.* **B459**  
(1999) 649.
- [48] F.A. Berends, W.L. van Neerven and G.J.H. Burgers, *Nucl. Phys.* **B297** (1988) 429,  
erratum: B304 (1988) 921.

- [49] E. A. Kuraev and V. S. Fadin, *Sov. J. Nucl. Phys.* **41** (1985) 466–472.
- [50] G. Montagna, O. Nicrosini and F. Piccinini, *Phys. Lett.* **B406** (1997) 243–248.
- [51] M. Skrzypek, *Acta Phys. Polon.* **B23** (1992) 135.
- [52] S. Jadach, M. Skrzypek and B.F.L. Ward, *Phys. Lett.* **B257** (1991) 173–178.
- [53] D.R. Yennie, S.C. Frautschi and H. Suura, *Ann. Phys.* **13** (1961) 379–452.
- [54] S. Jadach, M. Skrzypek and B. Pietrzyk, *Phys. Lett.* **B456** (1999) 77.
- [55] L. Garrido *et al.*, *Z. Phys.* **C49** (1991) 645;  
M. Martinez and F. Teubert, *Z. Phys.* **C65** (1995) 267, updated with results summarized in [54] and [204].
- [56] S. Jadach, B. Pietrzyk, E. Tournefier, B.F.L. Ward and Z. Wcas, *Phys. Lett.* **B465** (1999) 254.
- [57] B.A. Kniehl, M. Krawczyk, J.H. Kühn and R.G. Stuart, *Phys. Lett.* **B209** (1988) 337.
- [58] S. Jadach, M. Skrzypek and M. Martinez, *Phys. Lett.* **B280** (1992) 129–136.
- [59] A. Leike, T. Riemann, J. Rose, *Phys. Lett.* **B273** (1991) 513;  
T. Riemann, *Phys. Lett.* **B293** (1992) 451;  
S. Krisch, T. Riemann, *Comp. Phys. Comm.* **88** (1995) 89.
- [60] TOPAZ Collaboration, K. Miyabayashi *et al.*, *Phys. Lett.* **B347** (1995) 171.
- [61] VENUS Collaboration, K. Yusa *et al.*, *Phys. Lett.* **B447** (1999) 167.
- [62] ALEPH Collaboration, D. Buskulic *et al.*, *Z. Phys.* **C 71** (1996) 179.
- [63] DELPHI Coll. (P. Abreu *et al.*), *Eur. Phys. J.* **C11** (1999) 383.
- [64] L3 Collaboration (O Adriani *et al.*), *Phys. Lett.* **B 315** (1993) 637;  
L3 Coll. (M. Acciarri *et al.*), *Phys. Lett.* **B 479** (2000) 101;  
*Phys. Lett.* **B 489** (2000) 93..
- [65] OPAL Coll. (K. Ackerstaff *et al.*), *Eur. Phys. J.* **C2** (1998) 441.
- [66] ALEPH Collaboration, A. Heister *et al.*, *Measurement of the tau polarisation at LEP*, Preprint CERN-EP/2001-027, CERN, 2001;  
ALEPH Collaboration, D. Buskulic *et al.*, *Z. Phys.* **C69** (1996) 183–194;  
ALEPH Collaboration, D. Buskulic *et al.*, *Z. Phys.* **C59** (1993) 369–386;  
ALEPH Collaboration, D. Decamp *et al.*, *Phys. Lett.* **B265** (1991) 430–444.
- [67] DELPHI Collaboration, P. Abreu *et al.*, *Eur. Phys. J.* **C14** (2000) 585–611;  
DELPHI Collaboration, P. Abreu *et al.*, *Z. Phys.* **C67** (1995) 183–202.
- [68] L3 Collaboration, M. Acciarri *et al.*, *Phys. Lett.* **B 429** (1998) 387;  
L3 Collaboration, M. Acciarri *et al.*, *Phys. Lett.* **B341** (1994) 245–256;  
L3 Collaboration, O. Adriani *et al.*, *Phys. Lett.* **B294** (1992) 466–478.

- [69] OPAL Collaboration, G. Abbiendi, *Precision neutral current asymmetry parameter measurements from the tau polarization at LEP*, Preprint CERN-EP-2001-023, CERN, 2001; OPAL Collaboration, G. Alexander *et al.*, *Z. Phys.* **C72** (1996) 365–375; OPAL Collaboration, R. Akers *et al.*, *Z. Phys.* **C65** (1995) 1–16; OPAL Collaboration, G. Alexander *et al.*, *Phys. Lett.* **B266** (1991) 201–217.
- [70] M. Davier *et al.*, *Phys. Lett.* **B306** (1993) 411–417.
- [71] S. Jadach, W. Placzek, and B. F. L. Ward, *Phys. Lett.* **B390** (1997) 298–308.
- [72] J. Smith, J. A. M. Vermaseren, and J. G. Grammer, *Phys. Rev.* **D15** (1977) 3280.
- [73] F. A. Berends, P. H. Daverveldt, and R. Kleiss, *Phys. Lett.* **B148** (1984) 489.
- [74] F. A. Berends, P. H. Daverveldt, and R. Kleiss, *Nucl. Phys.* **B253** (1985) 441.
- [75] Particle Data Group Collaboration, C. Caso *et al.*, *Eur. Phys. J.* **C3** (1998) 1–794.
- [76] Particle Data Group Collaboration, D. E. Groom *et al.*, *Eur. Phys. J.* **C15** (2000) 1.
- [77] E. Barbiero, B. van Eijk, and Z. Wcas, *Comp. Phys. Comm.* **66** (1991) 115, CERN-TH 7033/93, (PHOTOS).
- [78] R. Decker and M. Finkemeier, *Phys. Rev.* **D48** (1993) 4203.
- [79] M. Finkemeier, Radiative corrections to the decay  $\tau \rightarrow \pi\nu$ , Ph.D. thesis, University of Karlsruhe, Feb 1994.
- [80] S. Jadach, J.H. Kühn and Z. Wcas, *Comp. Phys. Comm.* **64** (1990) 275; S. Jadach, Z. Wcas, R. Decker and J.H. Kühn, *Comp. Phys. Comm.* **76** (1993) 361 (TAUOLA).
- [81] J. H. Field and T. Riemann, *Comput. Phys. Commun.* **94** (1996) 53–87.
- [82] OPAL Collaboration, G. Abbiendi *et al.*, *E. Phys. J.* **C8** (1999) 217.
- [83] SLD Collaboration, SLAC-PUB-7585, contributed paper to EPS-HEP-97, Jerusalem, **EPS-118**;  
V.Serbo, *Electroweak measurements with heavy quarks at SLD*, III International conference on Hyperons, Charm and Beauty Hadrons, Genova, Italy, June/30–July/3/1998..
- [84] ALEPH Collaboration, R. Barate *et al.*, *Phys. Lett.* **B401** (1997) 150.
- [85] ALEPH Collaboration, R. Barate *et al.*, *Phys. Lett.* **B401** (1997) 163.
- [86] DELPHI Collaboration, P. Abreu *et al.*, *E. Phys. J.* **C10** (1999) 415.
- [87] L3 Collaboration, M. Acciarri *et al.*, *Z. Phys.* **C71** (1996) 379.
- [88] SLD Collaboration, *A Measurement of  $R_c$  with the SLD Detector* SLAC-PUB-7880, contributed paper to ICHEP 98 Vancouver **ICHEP'98 #174** ;  
N. de Groot, *Electroweak results from SLD*, talk presented at XXXIVth Rencontres de Moriond, Electroweak Interactions and Unified Theories, Les Arcs, March 13-20 1999..

- [89] ALEPH Collaboration, R. Barate *et al.*, EPJ **C4** (1998) 557.
- [90] DELPHI Collaboration, P. Abreu *et al.*, EPJ **C12** (2000) 209.
- [91] DELPHI Collaboration, P. Abreu *et al.*, EPJ **C12** (2000) 225.
- [92] OPAL Collaboration, K. Ackerstaff *et al.*, Eur. Phys. J. **C1** (1998) 439.
- [93] ALEPH Collaboration, R. Barate *et al.*, EPJ **C16** (2000) 597.
- [94] OPAL Collaboration, G. Alexander *et al.*, Zeit. Phys. **C72** (1996) 1.
- [95] OPAL Collaboration, G. Abbiendi *et al.*, Eur. Phys. J. **C8** (1999) 573.
- [96] ALEPH Collaboration, D. Buskulic *et al.*, Phys. Lett. **B384** (1996)414;  
ALEPH Collaboration, *Measurement of the b and c forward-backward asymmetries using leptons* ALEPH 99-076 CONF 99-048, contributed paper to EPS 99 Tampere **HEP'99 #6-65**..
- [97] DELPHI Collaboration, P. Abreu *et al.*, Z. Phys **C65** (1995) 569;  
DELPHI Collaboration, *Measurement of the Forward-Backward Asymmetries of  $e^+e^- \rightarrow Z \rightarrow b\bar{b}$  and  $e^+e^- \rightarrow Z \rightarrow c\bar{c}$  using prompt leptons* DELPHI 98-143 CONF 204, contributed paper to ICHEP 98 Vancouver **ICHEP'98 #124** .  
Delphi notes are available at <http://wwwcn.cern.ch/~pubxx/www/delsec/delnote/>..
- [98] L3 Collaboration, O. Adriani *et al.*, Phys. Lett. **B292** (1992) 454;  
L3 Collaboration, M. Acciarri *et al.*, Phys. Lett. **B448** (1996) 152.
- [99] OPAL Collaboration, G. Alexander *et al.*, Zeit. Phys. **C70** (1996) 357.
- [100] DELPHI Collaboration, P. Abreu *et al.*, EPJ **C9** (1999) 367.
- [101] L3 Collaboration, M. Acciarri *et al.*, Phys. Lett. **B439** (1998) 225.
- [102] OPAL Collaboration, K. Ackerstaff *et al.*, Zeit. Phys. **C75** (1997) 385.
- [103] ALEPH Collaboration, R. Barate *et al.*, Phys. Lett. **B426** (1998) 217.
- [104] ALEPH Collaboration, R. Barate *et al.*, Phys. Lett. **B434** (1999) 415.
- [105] DELPHI Collaboration, P. Abreu *et al.*, EPJ **C10** (1999) 219.
- [106] OPAL Collaboration, G. Alexander *et al.*, Zeit. Phys. **C73** (1997) 379.
- [107] DELPHI Collaboration, *Determination of  $A_{FB}^b$  using inclusive charge reconstruction and lifetime tagging at LEP 1*, DELPHI 2001-027 CONF 468..
- [108] SLD Collaboration, *Direct measurement of  $A_b$  at the  $Z^0$  Pole using a lepton tag*, SLAC-PUB-8516, Contributed Paper to ICHEP2000 , # **741**..
- [109] SLD Collaboration, SLAC-PUB-7637, contributed paper to EPS-HEP-97, Jerusalem, **EPS-124**;  
S. Fahey, *Measurements of Quark Coupling Asymmetries at the SLD* , talk presented at ICHEP 98 Vancouver..



- [110] SLD Collaboration, K. Abe, *et al.*, *Measurement of  $\mathcal{A}_c$  with charmed mesons at SLD*, SLAC-PUB-8195, contributed paper to EPS-HEP-99, Tampere, **6-474**..
- [111] SLD Collaboration, K. Abe *et al.*, *New measurement of  $\mathcal{A}_b$  at the  $Z^0$  resonance using a vertex-charge technique*, SLAC-PUB-8201, contributed paper to EPS-HEP-99, Tampere, **6-473**..
- [112] SLD Collaboration, K. Abe *et al.*, Phys. Rev. Lett. **83** (1999) 1902;  
SLD Collaboration, K. Abe *et al.*, *Direct measurement of  $\mathcal{A}_b$  using charged kaons at the SLD detector*, SLAC-PUB-8200, contributed paper to EPS-HEP-99, Tampere, **6-473**..
- [113] SLD Collaboration, K. Abe *et al.*, *Direct measurement of  $\mathcal{A}_c$  using inclusive charm tagging at the SLD detector*, SLAC-PUB-8199, contributed paper to EPS-HEP-99, Tampere, **6-474**..
- [114] ALEPH Collaboration., D. Buskulic *et al.*, *Measurement of the semileptonic  $b$  branching ratios from inclusive leptons in  $Z$  decays*, Contributed Paper to EPS-HEP-95 Brussels, **eps0404**.  
This note may be found at <http://alephwww.cern.ch/ALPUB/oldconf/HEP95/HEP95.html>..
- [115] DELPHI Collaboration, *Measurement of the semileptonic  $b$  branching ratios in  $Z$  decays* DELPHI 99-111 CONF 298, contributed paper to EPS 99 Tampere **HEP'99 #5.522** ..
- [116] L3 Collaboration, M. Acciarri *et al.*, Z. Phys. **C71** (1996) 379.
- [117] OPAL Collaboration, G. Abbiendi *et al.*, EPJ **C13** (2000) 225.
- [118] I. S. C. Peterson, D. Schlatter and P. Zerwas, Phys. Rev. **D27** (1983) 105.
- [119] ALEPH Collaboration, D. Buskulic *et al.*, Phys. Lett. **B357** (1995) 699.
- [120] ALEPH Collaboration, D. Buskulic *et al.*, Zeit. Phys. **C62** (1994) 179.
- [121] DELPHI Collaboration, P. Abreu *et al.*, Zeit. Phys. **C66** (1995) 323.
- [122] OPAL Collaboration, G. Alexander *et al.*, Phys. Lett. **B364** (1995) 93.
- [123] OPAL Collaboration, R. Akers *et al.*, Zeit. Phys. **C60** (1993) 199.
- [124] P. Collins and T. Spiller, J. Phys. **G 11** (1985) 1289..
- [125] V.G. Kartvelishvili, A.K. Likehoded and V.A. Petrov, Phys. Lett. **B 78** (1978) 615..
- [126] ALEPH Collaboration, D. Buskulic *et al.*, Z. Phys. **C62** (1994) 179.
- [127] OPAL Collaboration, G. Alexander *et al.*, Z. Phys. **C72** (1996) 1.
- [128] ALEPH Collaboration, D. Buskulic *et al.*, Z. Phys. **C62** (1994) 1.
- [129] DELPHI Collaboration, P. Abreu *et al.*, Z. Phys. **C59** (1993) 533, erratum: Z. Phys. **C65** (1995) 709.
- [130] OPAL Collaboration, G. Alexander *et al.*, Z. Phys. **C67** (1995) 27.

- [131] ALEPH Collab., R. Barate *et al.*, Phys. Lett. **B 434** (1998) 437.
- [132] DELPHI Collab., P. Abreu *et al.*, Phys. Lett. **B 405** (1997) 202.
- [133] DELPHI Collab., P. Abreu *et al.*, Phys. Lett. **B 462** (1999) 425.
- [134] OPAL Collab., G. Abbiendi *et al.*, CERN-EP/2000-123, accepted by E. Phys. J. **C**.
- [135] SLD Collab., K. Abe, *et al.*, SLAC-PUB-8737, accepted by Phys. Lett. **B**..
- [136] L3 Collab., M. Acciarri *et al.*, Phys. Lett. **B476** (2000) 243..
- [137] OPAL Collab., G. Abbiendi *et al.*, E. Phys. J. **C13** (2000) 1..
- [138] DELPHI Collab., P. Abreu *et al.*, Phys. Lett. **B 425** (1998) 399. L3 Collab., M. Acciarri *et al.*, Phys. Lett. **B 416** (1998) 220. OPAL Collab., R. Akers *et al.*, Z. Phys. **C 61** (1994) 209..
- [139] MARK III Collab., D. Coffman *et al.*, Phys. Lett. **B263** (1991) 135..
- [140] CLEO Collaboration, D. E. Jaffe *et al.*, Phys. Rev. **D62** (2000) 072005.
- [141] CLEO Collab., D. Bortoletto *et al.*, Phys. Rev. **D 45** (1992) 2212..
- [142] G. Altarelli *et al.*, Nucl. Phys. **B 208** (1982) 365..
- [143] N. Isgur, D. Scora, B. Grinstein and M. Wise, Phys. Rev. **D 39** (1989) 799..
- [144] DELCO Collab., W. Bacino *et al.*, Phys. Rev. Lett. **43** (1979) 1073..
- [145] MARK III Collab., R.M. Baltrusaitis *et al.*, Phys. Rev. Lett. **54** (1985) 1976..
- [146] The LEP collaborations, Nucl. Instrum. Meth. **A378** (1996) 101.
- [147] CLEO Collab., D. Bortoletto *et al.*, Phys. Rev. **D 45** (1992) 21..
- [148] CLEO Collab., T.E. Coan *et al.*, Phys. Rev. Lett. **80** (1998) 1150.  
CLEO Collab., D. Gibaut *et al.*, Phys. Rev. **D 53** (1996) 4734.  
CLEO Collab., R. Ammar *et al.*, Phys. Rev. **D 55** (1997) 13..
- [149] ALEPH Collab., R. Barate *et al.*, E. Phys. J. **C 4** (1998) 37..
- [150] ALEPH Collab., R. Barate *et al.*, CERN-EP/2000-126, accepted by E. Phys. J. **C**.  
DELPHI Collab., P. Abreu *et al.*, Phys. Lett. **B 496** (2000) 43.  
L3 Collab., M. Acciarri *et al.*, Phys. Lett. **B 332** (1994) 201.  
L3 Collab., M. Acciarri *et al.*, Z. Phys. **C 71** (1996) 379..
- [151] P. Nason and C. Oleari, Phys. Lett. **B407** (1997) 57.
- [152] D. Abbaneo *et al.*, Eur. Phys. J. **C4** (1998) 185.
- [153] G. Altarelli and B. Lampe, Nucl. Phys. **B 391** (1993) 3..
- [154] V. Ravindran and W.L. van Neerven, Phys. Lett. **B 445** (1998) 206..

- [155] S. Catani and M. Seymour, JHEP 9907:023 (1999)..
- [156] ALEPH Collaboration, D. Buskulic *et al.*, Z. Phys. **C71** (1996) 357..
- [157] DELPHI Collaboration, P. Abreu *et al.*, Phys. Lett. **B277** (1992) 371..
- [158] OPAL Collaboration, P. D. Acton *et al.*, Phys. Lett. **B294** (1992) 436..
- [159] DELPHI Collaboration, P. Abreu *et al.*, *First measurement of the strange quark asymmetry at the Z peak*, CERN-PPE/94-219, Z.Phys.C67 (1995) 1..
- [160] DELPHI Collaboration, P. Abreu *et al.*, CERN-EP/99-134, *Measurement of the strange quark forward-backward asymmetry around the Z peak*, Submitted to E. Phys. J. C.
- [161] OPAL Collaboration, K. Ackerstaff *et al.*, *Measurement of the branching fractions and forward-backward asymmetries of the Z into light quarks*, CERN-EP/97-063, Z.Phys.C76 (1997) 387..
- [162] SLD Collaboration, K. Abe *et al.*, Phys. Rev. Lett. **85** (2000) 5059.
- [163] DELPHI Collaboration, P. Abreu *et al.*, *Study of prompt photon production in hadronic Z decays*, CERN-PPE/95-101, Z.Phys.C69 (1995) 1..
- [164] L3 Collaboration, O. Adriani *et al.*, *Determination of quark electroweak couplings from direct photon production in hadronic Z decays*, CERN-PPE/92-209, Phys.Lett.B301 (1993) 136..
- [165] OPAL Collaboration, P.D.Acton *et al.*, *Studies of strong and electroweak interactions using final state photon emission in hadronic Z decays*, CERN-PPE/92-215, Z.Phys.C58 (1993) 405..
- [166] ALEPH Collaboration, D. Buskulic *et al.*, Z. Phys. **C57** (1993) 17–36.
- [167] T. van Ritbergen and R.G. Stuart, Phys. Rev. Lett. **82** (1999) 488..
- [168] M. Steinhauser, Phys. Lett. **B429** (1998) 158..
- [169] S. Eidelmann and F. Jegerlehner, Z. Phys. **C67** (1995) 585.
- [170] H. Burkhardt and B. Pietrzyk, Phys. Lett. **B356** (1995) 398..
- [171] The BES Collaboration, J.Z.Bai *et al.*, *Measurements of the Cross Section for  $e^+e^- \rightarrow$  hadrons at Center-of-Mass Energies from 2 to 5 GeV*, hep-ex/0102003..
- [172] H. Burkhardt and B. Pietrzyk, *Update of the hadronic contribution to the QED vacuum polarisation* Preprint LAPP-EXP 2001-03, accepted by Phys. Lett. **B**..
- [173] M. L. Swartz, Phys. Rev. **D53** (1996) 5268.
- [174] A.D. Martin and D. Zeppenfeld, Phys. Lett. **B345** (1994) 558.
- [175] R. Alemany, *et al.*, Eur. Phys. J. **C2** (1998) 123.
- [176] M. Davier and A. Höcker, Phys. Lett. **B419** (1998) 419.

- [177] J.H. Kühn and M. Steinhauser, Phys. Lett. **B437** (1998) 425.
- [178] J. Erler, Phys. Rev. **D59**, (1999) 054008.
- [179] A. D. Martin, J. Outhwaite, and M. G. Ryskin, Phys. Lett. **B492** (2000) 69–73.
- [180] F. Jegerlehner, *Hadronic Effects in  $(g-2)$  and  $\alpha_{QED}(M_Z)$  : Status and Perspectives*, Proc. of Int. Symp. on Radiative Corrections, Barcelona, Sept. 1998, page 75..
- [181] CDF Collaboration, F. Abe *et al.*, Phys. Rev. Lett. **73** (1994) 225–231;  
CDF Collaboration, F. Abe *et al.*, Phys. Rev. Lett. **74** (1995) 2626–2631.
- [182] D0 Collaboration, S. Abachi *et al.*, Phys. Rev. Lett. **74** (1995) 2632–2637.
- [183] CDF Collaboration, F. Abe *et al.*, Phys. Rev. Lett. **82** (1999) 271–276;  
CDF Collaboration, T. Affolder *et al.*, Phys. Rev. **D63** (2001) 032003;  
CDF Collaboration, F. Abe *et al.*, Phys. Rev. Lett. **79** (1997) 1992–1997.
- [184] D0 Collaboration, B. Abbott *et al.*, Phys. Rev. Lett. **80** (1998) 2063–2068;  
D0 Collaboration, B. Abbott *et al.*, Phys. Rev. **D60** (1999) 052001;  
D0 Collaboration, S. Abachi *et al.*, Phys. Rev. Lett. **79** (1997) 1197–1202;  
D0 Collaboration, B. Abbott *et al.*, Phys. Rev. **D58** (1998) 052001.
- [185] UA1 Collaboration, C. Albajar *et al.*, Z. Phys. **C44** (1989) 15.
- [186] UA2 Collaboration, J. Alitti *et al.*, Phys. Lett. **B276** (1992) 354–364.
- [187] CDF Collaboration, T. Affolder *et al.*, (2000).
- [188] D0 Collaboration, B. Abbott *et al.*, Phys. Rev. Lett. **80** (1998) 3008;  
D0 Collaboration, B. Abbott *et al.*, Phys. Rev. **LETT.** (2000) 84:222–227.
- [189] The results on the W-boson mass from UA2 [186], CDF [187] and DØ [188] are combined assuming 25 MeV correlated uncertainty, see also [http://www-cdf.fnal.gov/physics/ewk/wmass\\_global.html](http://www-cdf.fnal.gov/physics/ewk/wmass_global.html).
- [190] ALEPH Collaboration, R. Barate *et al.*, Eur. Phys. J. **C17** (2000) 241–261.
- [191] DELPHI Collaboration, P. Abreu *et al.*, (2001).
- [192] L3 Collaboration, M. Acciarri *et al.*, Phys. Lett. **B454** (1999) 386–398.
- [193] OPAL Collaboration, G. Abbiendi *et al.*, Phys. Lett. **B507** (2001) 29–46.
- [194] The LEP Collaborations ALEPH, DELPHI, L3, OPAL and the LEP W Working Group, *Combined Preliminary Results on the Mass and Width of the W Boson Measured by the LEP Experiments*, LEPEWWG/MASS/2001-01, March 15th, 2001; see also <http://www.cern.ch/LEPEWWG/lepww/mw/Winter01/>.
- [195] CCFR/NuTeV Collaboration, K. McFarland *et al.*, Eur. Phys. Jour. **C1** (1998) 509.
- [196] NuTeV Collaboration, K. McFarland, talk presented at the XXXIIIth Rencontres de Moriond, Les Arcs, France, 15-21 March, 1998, hep-ex/9806013. The result quoted is a combination of the NuTeV and CCFR results.

- [197] C. S. Wood *et al.*, *Science* **275** (1997) 1759.
- [198] S. C. Bennett and C. E. Wieman, *Phys. Rev. Lett.* **82** (1999) 2484–2487.
- [199] N. H. Edwards *et al.*, *Phys. Rev. Lett.* **74** (1995) 2654–2657.
- [200] P. A. Vetter *et al.*, *Phys. Rev. Lett.* **74** (1995) 2658–2661.
- [201] A. Derevianko, *Phys. Rev. Lett.* **85** (2000) 1618–1621.
- [202] M. G. Kozlov, S. G. Porsev, and I. I. Tupitsyn, *Phys. Rev. Lett.* **86** (2001) 3260–3263.
- [203] A. Freitas *et al.*, *Phys. Lett.* **B495** (2000) 338–346.
- [204] *Reports of the working group on precision calculations for the Z resonance*, eds. D. Bardin, W. Hollik and G. Passarino, CERN Report: CERN 95-03, (1995).
- [205] K. G. Chetyrkin, J. H. Kuhn, and A. Kwiatkowski, *Phys. Rept.* **277** (1996) 189–281.
- [206] D. E. Soper and L. R. Surguladze, *Phys. Rev.* **D54** (1996) 4566–4577.
- [207] S. Bethke, *J. Phys.* **G26** (2000) R27.
- [208] F. James and M. Roos, *Comput. Phys. Commun.* **10** (1975) 343.
- [209] M. E. Peskin and T. Takeuchi, *Phys. Rev. Lett.* **65** (1990) 964–967;  
M. E. Peskin and T. Takeuchi, *Phys. Rev.* **D46** (1992) 381–409.
- [210] L3 Collaboration, O. Adriani *et al.*, *Phys. Lett.* **B292** (1992) 454;  
L3 Collaboration, *L3 Results on  $A_{FB}^{b\bar{b}}$ ,  $A_{FB}^{c\bar{c}}$  and  $\chi$  for the Glasgow Conference*, L3 Note 1624;  
L3 Collaboration, M. Acciarri *et al.*, *Phys. Lett.* **B448** (1999) 152..
- [211] SLD Collaboration, *Measurement of  $\mathcal{A}_b$  at the Z resonance using a Jet-Charge Technique* SLAC-PUB-7886, contributed paper to ICHEP 98 Vancouver **ICHEP'98 #179** ;  
N. de Groot, *Electroweak results from SLD*, talk presented at XXXIVth Rencontres de Moriond, Electroweak Interactions and Unified Theories, Les Arcs, March 13-20 1999.